Skolkovo Institute of Science and Technology

A STUDY OF CHEMICAL BONDING THROUGH QUANTUM CHEMICAL TOPOLOGY

Doctoral Thesis

by

CHRISTIAN TANTARDINI

DOCTORAL PROGRAM IN MATERIAL SCIENCES AND ENGINEERING

Supervisor

Professor Artem R. Oganov

Moscow 31-01 2020

© Christian Tantardini 2020

To my father Giuseppe died during my PhD

«*What does not destroy me makes me stronger*»

cit. Friedrich Nietzsche

The secret of human existence lies not only in living, but also in knowing what we are living for»

cit. Fyodor Mihajlovic Dostoevsky

CONTENTS

1.0 ABSTRACT

The chemical behavior of atoms and molecules is entirely defined by the distribution of their electron density. It is by studying the electron density in the field of Quantum Chemical Topology that such key concept as *chemical bonding* can be used to explain reactivity, atomic hybridization, and the existence of electric multipole moments. In such direction the work here presented is principally focused on development of Quantum Chemical Topology Theory introducing new different concepts, which a new equation style of real gases other that a “energy border” between hydrogen bond and van der Waals interaction with consequent limit of long range interactions, and the investigation of different compounds to investigate the correlations between solubility (oxicams) and reactivity (Dess-martin periodinane) with electronic structure with data supported by literature and experiments.

2.0 PUBLICATIONS

2.1 Thesis Work

1_**Christian Tantardini*** A new equation of state for real gases developed into the framework of Bader's Theory. *Theoretical Chemistry Accounts*, 2018, 137, 93.

2_**Christian Tantardini***, Sergey G. Arkipov*, Kseniya A. Cherkashina, Alexander S. Kil'met'ev, Elena V. Boldyreva* Synthesis and crystal structure of a meloxicam co-crystal with benzoic acid. *Structural Chemistry*, 2018, 29 (6), 1867-1874.

3_**Christian Tantardini***, Adam A. L. Michalchuk Dess-martin periodinane: The reactivity of a λ^5-iodane catalyst explained by topological analysis. *International Journal of Quantum Chemistry*, 2018, 119 (6), e25838.

4_**Christian Tantardini*** When does a hydrogen bond become a van der Waals interaction? A topological answer. *Journal of Computational Chemistry*, 2019, 40 (8), 937-943.

5_ Alexey Yu. Fedorov, Tatiana N. Drebushchak and **Christian Tantardini*** Seeking the best model for non-covalent interactions within the crystal structure of meloxicam. *Computational and Theoretical Chemistry*, 2019, 1157, 47-53.

6_Sergey G. Arkhipov, Peter S. Sherin*, Alexey S. Kiryutin, Vladimir A. Lazarenk and **Christian Tantardini*** The Role of S-bond in Tenoxicam Keto-Enolic Tautomerization. *CrystEngComm*, 2019, 21, 5392-5401.

2.1 Other Publications

- Christian Tantardini*, Davide Ceresoli, Enrico Benassi, Source Function and Plane Waves: Toward Complete Bader Analysis, *Journal of Computational Chemistry* (2016), DOI: 10.1002/jcc.24433.

- **Christian Tantardini***, Sergey G. Arkhipov*, Ksenya A. Cherkashina, Alexander S. Kil'met'eva and Elena V. Boldyreva*, Crystal structure of a 2:1 co-crystal of meloxicam with acetylendicarboxylic acid, *Acta Cryst E* (2016), DOI: https://doi.org/10.1107/S2056989016018909.

- **Christian Tantardini***, Elena V. Boldyreva, and Enrico Benassi*, Hypervalency in Organic Crystals: A Case Study of the Oxicam Sulfonamide Group, *J. Phys. Chem. A* (2016), DOI: 10.1021/acs.jpca.6b10703.

- **Christian Tantardini***, Enrico Benassi Topology vs Thermodynamics in Chemical Reactions: The Instability of PH_5, *Phys. Chem. Chem. Phys.* (2017), DOI: 10.1039/C7CP06130G.

- Christian Tantardini, Enrico Benassi* Crystal Structure Resolution of a Mott Insulator through Bader's Theory: The Challenging Case of Cobaltite Oxide Y114, *Dalton Transaction* (2018), DOI: 10.1039/C8DT00073E

** corresponding author*

3.0 INTRODUCTION

The PhD thesis is mainly devoted to the study of fundamental insights on/into chemical bonding within the field of Quantum Chemical Topology using first-principles simulations of different states of matter with both local basis set and plane wave basis set calculations. Some of the chosen systems were investigated not only with a computational approach but also through experimental structural analyses to confirm theoretical results. Great part of the work was focused on non-covalent interactions (NCIs) formulating a new equation of state for describing real gases in the field of theory of atoms in molecules (QTAIM) to overcome the old concept of spherical atoms and in the same field the “energy border” between hydrogen bond (H-bond) and van der Waals (vdW) interaction to fulfill the lacuna of H-bond IUPAC definition based on experimental techniques are not able to discriminate between blurry H-bond and vdW interactions. One important question about the correlation between the intramolecular interactions and the solubility of crystals is also highlighted through first-principles simulations on co-crystals, salts, solvates as compared with pure component solids. In this way, it is possible to explore several issues

(i) A first important property to be investigated is the so-called interaction density, i.e. the charge density redistribution that takes place both in the intermolecular region and within the covalent bonding framework of the individual molecules upon 'switching on' their interaction. This charge density rearrangement will be different according to whether cocrystal, salts solvates or pure component crystals are formed.

(ii) By applying the topological descriptors that are provided by the wavefunctions, it is possible to explore the different kinds of non-covalent interactions taking place within the examined systems. At the same time, the effect of different crystal fields on the intramolecular interactions can be investigated. Besides the change affecting local properties, also the molecular properties like dipole moments, polarizability and so on, are worth of being monitored when different crystal forms are compared. The role of the symmetry on such properties will be also investigated. It should be noted that molecular properties find their definition in crystals by using topological methods.

(iii) As different crystal forms exploit also different thermodynamic stabilities as a function of their environment, how the component molecules vary their energies and their energy decompositions in dependence of the crystal field they experience will be evaluated. It should be noted that energy decomposition may be also afforded in terms of contributions of individual atomic atoms or groups. This is done through QTAIM by exploring the energy landscape through both empirical and quantum mechanical methods eventually gaining insights into thermodynamics of competing polymorphs and with the possibility to predict what kind of structure it will be expected if the crystallization takes place under thermodynamic control.

An ulterior employment of QTAIM was focused in order to correlate *chemical bonding* with molecular reactivity. In the specific case through the study of Dess-Martin periodinane (DMP), which derivatives are popular organic catalysts. DMP is extremely reactive in the presence of alcohols, catalyzing their oxidative conversion into ketones. This work seeks to better understand the intrinsic electronic factors that drive the reactivity of the DMP molecule.

Furthermore, the *chemical bonding* was investigated at high pressure through the analysis of one very well-known property: electronegativity, which is a property of bonded atom defined as the capacity of an atom to attract on itself the shared electron cloud in the bond. This property as defined by Pauling represents a definition of ionicity of bond and it is calculated on arbitrarily electronegativity value associated to fluorine of 4.0. During this work such property is evaluated with variation of pressure to understand the hellish chemistry at high pressure. High-Pressure is responsible to modify different atomic properties with repercussion on chemical bonding. The understanding of how pressure modifies chemical bonding, hence properties will give important information for future prediction of new structures knowing *a priori* the type of bond and consequent oxidation number.

4.0 THEORETICAL BACKGROUND

4.1 Introduction

Since from their discover in the 1875 by English physicist William Crookes, the electrons have been object of interest in the field of physical chemistry and not only. This interest was born simply by the fact, that the atoms are made by electrons that surround a nucleus. Electrons determine the chemical (i.e. reactivity), and physical (i.e. solubility) properties of atom. These properties are explained through the displacement of electrons around the nucleus, and their state of the motion in an electronic field created by stationary nucleus is so called atomic electronic structure. In nature it is difficult to find atoms alone, but in the major part of cases they are found with other atoms of same or different nature to make molecules, salts, rocks, oxides and so on. The forces acting between two or a group of atoms are such as to lead to the formation of an aggregate with sufficient stability to make it convenient for the chemist to consider it as an independent molecular species is the definition of *chemical bond* as introduced by Lewis in the 1916 [1] and it is actually adopted as it is by IUPAC, albeit, it leaves too much subjective interpretation. The concept of *chemical bond* was subsequently investigated by Pauling [2] introducing such terms as covalent bond corresponding to shared pair of electrons between two atoms, and ionic bond generated by two atoms with high electronegative difference. The nature of *chemical bond* between atoms changes the initial atomic electronic structure and the result of this change gives information on chemical and physical properties of atoms within a compound. The resulting electronic structure of compound is made by an adaptation of atomic electronic structures, which generate the global chemical and physical proprieties of compound. So, the chemical behaviour of atoms and molecules is entirely defined by the distribution of their electron density. It is by studying the electron density that key concepts of chemical importance come about, such as reactivity, atomic hybridisation, and the existence of electric multiple moments [3-58] allowing to overcome the hold Lewis-Pauling concepts of *chemical bond* to fulfil the lacunas as the description of multicentre bonds as 3-center-2-electrons and 3-center-4-electrons which appear in different theoretical and experimental studies [59-63]. The importance to decode the electron density has led to the development of the field of quantum chemical topology (QCT), so named by Popelier [64]. Within QCT, a number of techniques have been developed, all of which rely solely on topological features of the electron density function to derive chemically relevant information [3].

4.2 Bader's Theory

While many theories exist within QCT, the most influential to date has been the quantum theory of atoms in molecules (QTAIM), developed by R. W. Bader and colleagues in the 1980s [65]. At the heart of QTAIM there exists the central concept of atomic basins, which subdivide a molecule into regions that encase an atomic nucleus: an atom. An atomic basin is delimitated by surface, S, so called zero flux surface (ZFS) by R. W. Bader, and is defined by all points in space, $\mathbf{r}_S$, for which the product of the gradient of ED, $\nabla\rho$, and the normal vector, $\hat{\boldsymbol{n}}$, is zero:

$$\boldsymbol{\nabla}\rho(\mathbf{r}) \cdot \hat{\boldsymbol{n}}(\mathbf{r}) = 0, \forall \mathbf{r} \in \mathrm{S}(\mathbf{r}_S) \qquad (1)$$

Such arbitrary definition of atomic basin doesn't allow to define unambiguously the atomic domains, , because the interatomic surfaces, along with the surfaces found at infinity, are the only closed surfaces of $\mathbb{R}^3$, which satisfy the zero-flux condition [65]. Thus, in the calculus the ZFS is numerically approximated for the bound against vacuum with a threshold of ED value of 10^{-3} a.u. This was selected by Bader [65] just to define a volume for those basins that extend to infinity considering that ED tends to 0 when its distance from nucleus tends to infinity. Bader showed that the accuracy of numerical integration of kinetic energy within atomic basin, Ω, allows to obtain the partition of molecular electron energy in atomic energies through the observance of virial theorem $\gamma = -\langle\hat{V}\rangle/\langle\hat{T}\rangle = 2$ [65]. Thus, under these conditions, the expectation values of $\langle\hat{V}\rangle$ and $\langle\hat{T}\rangle$ must be multiplied by a factor $(1+\gamma)$ and $(1 + 1/\gamma)$, respectively, in order to obtain the correct results $\mathrm{E} = \langle\hat{T}\rangle = -\langle\hat{V}\rangle/2$. Thus, it exists a quantity by Bader called Lagrangian, $L(\Omega)$, so defined as:

$$L(\Omega) = -\left(\frac{\hbar^2}{4m}\right)\int_{\Omega} \nabla^2\rho(\mathbf{r})d\tau = -\left(\frac{\hbar^2}{4m}\right)\oint dS(\Omega,\mathbf{r})\boldsymbol{\nabla}\rho(\mathbf{r})\cdot\hat{\boldsymbol{n}}(\mathbf{r}) \tag{2}$$

If $L(\Omega)$falls in the range 10^{-4} to $10^{-5}$the error in the estimation of kinetic energy was demonstrated to be less than 0.4 kJ/mol [65].

A unique subdivision of space through ZFS is not always possible, because there is not a family of mapping of $\boldsymbol{\nabla}_\Phi$ of the local ZFS, $\partial\Omega(\Phi)$, defined by the wave-function Φ of a neighborhood of a given wave-function Ψ, onto that defined by Ψ, $\partial\Omega(\Psi)$, because the $\boldsymbol{\nabla}_\Phi$ is not bijective and differentiable for all Φ, but only the $\lim\limits_{\Phi\to\Psi} \boldsymbol{\nabla}_\Phi$ equal to identity [66]. Furthermore, the vanishing of atomic domains at the vibrational nodes is another problem that affects QTAIM [66]. Such failure can be explained by a vibrational state for a nuclear configuration $\mathbf{R}^0$, where the nuclear wave-function $\Psi_n(\mathbf{R}^0) = 0$ implies that the reduced electron density defined as

$$\rho(\mathbf{r},\mathbf{R}) = \rho_e(\mathbf{r},\mathbf{R})\rho_n(\mathbf{R}) \tag{3}$$

it will be $\rho(\mathbf{r},\mathbf{R}^0) = 0$, $\forall\mathbf{r}$; and for such system the exact wave-function, $\Psi(\mathbf{r},\mathbf{R})$, is a linear combination of product between nuclear wave-function, $\Psi_n(\mathbf{R})$, and electron wave-function, $\Psi_e(\mathbf{r},\mathbf{R})$. Thus, in according with QTAIM at such nuclear configuration $\mathbf{R}^0$ there is not atom, bond or structure. So despite the few cases where QTAIM fails: electronic or vibrational (in the harmonicity or close to anharmonicity approximation) exited states making not valid the application of Schwinger principle under the condition of Courant and Hilbert for a subsystem delimitated by ZFS; it has been successfully applied in most other cases, especially for its adaptation to the multipole model, giving a detailed description of electronic structure. Even if QTAIM in its feasible application on ground state systems [67] it is accused by Dunitz & Gavezzotti (2005) [68] to be only a descriptive approach to ED without any reference to predictivity. QTAIM introduces the concept of *chemical bonding* as a shared interatomic surface with associated critical point so called bond critical point (BCP) and bond path. The bond path is is a unique trajectory in ρ between two atoms, where the density is maximal compared with any normal displacement from the line. The used BCP as indicator of *chemical bonding* is matter of question if such assumption can be used also for non-covalent interactions. In presence of van der Waals interactions no BCPs are seen, even if such inter-molecular interactions are present. While, in intra-molecular H-bonds at closed angles it makes difficult to use the presence or not of BCP like a feasible indicator of present or absence for such chemical bonding. As reported by Galvão *et al.* [69] in some cases the BCP is absent between acceptor (A) and hydrogen (H) for intra-molecular H-bond angle lesser than 122.5 deg. But BCP is present between A and donor (D) due to the overlapping of their big electronic clouds that interact too much each other making impossible a H...A bond path with associated BCP [69]. Thus, below a certain angle, one should probably not talk of an H-Bond, but simply of an D—H bond and of an A...D interaction, as the topology itself reveals.

To describe the non-covalent interactions (NCIs) [70] in the field of QTAIM a fundamental quantity defined within density functional theory formalism from the electron density at point $\mathbf{r}$, $\rho(\mathbf{r})$, and its first derivative, $\nabla\rho(\mathbf{r})$, and is so called reduced density gradient (RDG) [71-73]

$$s(\mathbf{r}) = \frac{|\nabla\rho(\mathbf{r})|}{2(3\pi^2)^{1/3}\rho(\mathbf{r})^{4/3}} \tag{4}$$

For regions far from the various nuclei of a system (i.e. where density decays exponentially to zero), the RDG adopts large positive values. In contrast, the RDG values approach zero for regions of covalent and non-covalent bonding. Hence, the magnitude of *s* offers a good indication of the position of NCIs. The nature of the NCI is subsequently defined by analyzing the Laplacian of ED, $\nabla^2\rho(\mathbf{r})$. To characterize interactions, $\nabla^2\rho(\mathbf{r})$ is often decomposed into its three principal axes of maximum variation, the three eigenvalues λ_n of the Hessian of ED, $\nabla^2\rho(\mathbf{r}) = \lambda_1 + \lambda_2 + \lambda_3$ $(\lambda_1 \leq \lambda_2 \leq \lambda_3)$. Where $\lambda_1 < 0$ and $\lambda_3 > 0$, it has been found that bonding interactions are defined by a negative value of λ_2, and non-bonding interactions by its positive value. vdW interactions typically have $\lambda_2 \approx 0$. Hence the nature of interactions at points of $s(\mathbf{r}) \rightarrow 0$ can be defined by the corresponding value of $\rho(\mathbf{r}) \cdot \mathrm{sign}(\lambda_2)$. It is generally accepted that the magnitude of $\rho(\mathbf{r})$ corresponds to the relative strength of interaction. As a rule of thumb, it has been suggested that the limits ±0.02 be used to distinguish between bonding regimes,with bonding interactions found at $\rho(\mathbf{r}) \cdot \mathrm{sign}(\lambda_2)$ <-0.02, vdW interaction in regions where -0.02 <$\rho(\mathbf{r}) \cdot \mathrm{sign}(\lambda_2)$<0.02, and steric repulsion in region with $\rho(\mathbf{r}) \cdot \mathrm{sign}(\lambda_2) >$ 0.02 [71-73].

BCP is not the only critical point of topological interest in QTAIM but a full topological analysis consists in a mathematically analysis of the function $\rho_e(\mathbf{r}, \mathbf{R})$ through a research of all its critical points, which can be maximum, minimum or saddles [65]. In such points the gradient of function, $\boldsymbol{\nabla}\rho_e(\mathbf{r}, \mathbf{R})$, must be null

$$\boldsymbol{\nabla}\rho_e(\mathbf{r}, \mathbf{R}) = \hat{\mathbf{i}}\frac{\partial\rho_e(\mathbf{r}, \mathbf{R})}{\partial x} + \hat{\mathbf{j}}\frac{\partial\rho_e(\mathbf{r}, \mathbf{R})}{\partial y} + \hat{\mathbf{k}}\frac{\partial\rho_e(\mathbf{r}, \mathbf{R})}{\partial z} \tag{5}$$

In such points the Hessian matrix of function, $\boldsymbol{\mathcal{H}}\big(\rho_e(\mathbf{r},\mathbf{R})\big)$, which is very well known to be correlated at the Jacobian matrix of function, $\boldsymbol{J}\big(\boldsymbol{\nabla}\rho_e(\mathbf{r},\mathbf{R})\big)$ by the relation

$$\boldsymbol{\mathcal{H}}\big(\rho_e(\mathbf{r},\mathbf{R})\big) = \boldsymbol{J}\big(\boldsymbol{\nabla}\rho_e(\mathbf{r},\mathbf{R})\big)^{\mathrm{T}} \tag{6}$$

Corresponds to the trace of Hessian matrix, $tr(\boldsymbol{\mathcal{H}})$, being the $\boldsymbol{\mathcal{H}}$ matrix diagonalizable with all mixed partial second derivates equal to zero. Thus, the $\nabla^2\rho_e(\mathbf{r},\mathbf{R})$ so called Laplacian of electron density or Laplacian of charge density is invariant to the choice of coordinate axes.

$$\nabla^2\rho_e(\mathbf{r},\mathbf{R}) = \boldsymbol{\nabla}\cdot\boldsymbol{\nabla}\rho_e(\mathbf{r},\mathbf{R}) = \frac{\partial^2\rho_e(\mathbf{r},\mathbf{R})}{\partial x^2} + \frac{\partial^2\rho_e(\mathbf{r},\mathbf{R})}{\partial y^2} + \frac{\partial^2\rho_e(\mathbf{r},\mathbf{R})}{\partial z^2} \tag{7}$$

The Hessian Matrix represents the linear transformation of gradient vector (eigenvector) and the Laplacian of electron density is the correspondent scale factor (eigenvalue).

$$\boldsymbol{\mathcal{H}}\boldsymbol{\nabla}\rho_e = \nabla^2\rho_e\boldsymbol{\nabla}\rho_e \tag{8}$$

The *rank* of $\boldsymbol{\mathcal{H}}$ is 3 being for a generical linear application is the dimension of vectoral space given by its image. While, the *signature* of $\boldsymbol{\mathcal{H}}$ corresponds to the algebraical sum of the signs of eigenvalues. These values are respectively used to classify a critical point with the label (3, X), where the first number correspond to *rank* and the second to the *signature*. Thus, a study of curvature of ρ_e allows to identify: a bond critical point (3, -1), with a positive eigenvalue associated to an eigenvector along the bond path and two negative eigenvalues associated to two eigenvectors perpendicular to the bond path; a nucleus (3, -3), with three negative eigenvalues; a ring critical point (3, 1), with two positive eigenvalues associated to two eigenvectors which lie in a plane (i.e. center of aromatic rings) and one negative eigenvalue associated to an eigenvector perpendicular at the that plane; a cage (3, 3), with three positive eigenvalues [65].

Subsequently a research of ρ_e critical points to understand the regions of electronic depletion and concentration it is very useful a study of critical points of a new defined function $\mathrm{L}(\mathbf{r})$ corresponding to

$$\mathrm{L}(\mathbf{r}) = -\nabla^2\rho_e \tag{9}$$

The Laplacian of electron density is the second derivate of function ρ_e representing its curvature, which it is interesting look in the valence shell of each atom being the region of space subjected to variation influenced by chemical surrounding to make different types of interaction with the closest atoms. The valence shell is generally made by two shells, one internal of charge concentration (negative Laplacian), named valence shell charge concentration (VSCC), and one more external of charge depletion (positive Laplacian). Bader focused the research of $\mathrm{L}(\mathbf{r})$ critical points in the VSCC, which provide chemical insight on atomic hybridization and chemical bonding. For example in the VSCC a critical point associated to function $\mathrm{L}(\mathbf{r})$ of major interest are: minimum (3, 3), which represents a depletion of ED; maximum (3, -3), which represents a concentration of ED typically associated to a bonded charge concentration or to a lone pair.

4.3 Source Function

In any point of ρ_e and $\mathrm{L}(\mathbf{r})$ it is possible to calculate the different contributions to ρ_e coming from each atom within a molecule through a topological tool so called source function (SF). SF from its birth in the 1998 [74] was employed to reveal subtle electron-delocalization effects within molecules and more recently to periodic systems, proving a powerful tool for solving a number of difficult chemical questions. Bader and Gatti showed that ρ_e in a c point $\mathbf{r}$ from an atomic basin, Ω, is given by the sum of integrated $\nabla^2\rho_e$ on all points $\mathbf{r}' \in \Omega$ weighted by Green function, $|\mathbf{r}-\mathbf{r}'|^{-1}$, with the integrated flux of electric field density, $\boldsymbol{\varepsilon}(\mathbf{r}-\mathbf{r}_S)$, on all points of ZFS, $S(\mathbf{r}_S)$.

$$\rho_e(\mathbf{r}) = -\frac{1}{4\pi}\left\{\int_{\Omega} d\mathbf{r}'\frac{\nabla^2\rho(\mathbf{r}')}{|\mathbf{r}-\mathbf{r}'|} + \int_{S_\Omega} dS(\mathbf{r}_S)\cdot\boldsymbol{\varepsilon}(\mathbf{r}-\mathbf{r}_S)\right\} \tag{10}$$

The second term of eq.10 is zero if all zero-flux surfaces are at the infinite where the electric field density is decaying to zero. One may move from Eq. 10 to 11, just by replacing the integral over the basin Ω and its bounding surface, with an integral over the whole space or as a sum of integrals over the disjoint and exhaustive partitioning of the space in QTAIM basins.

$$\rho_e(\mathbf{r}) = -\frac{1}{4\pi}\sum_{\Omega}\int_{\Omega} d\mathbf{r}'\frac{\nabla^2\rho(\mathbf{r}')}{|\mathbf{r}-\mathbf{r}'|} = -\frac{1}{4\pi}\sum_{\Omega}\int_{\Omega} d\mathbf{r}'\, LS(\mathbf{r},\mathbf{r}') = \sum_{\Omega} SF(\mathbf{r},\Omega) \tag{11}$$

The Laplacian of charge density can be correlated to the local electron energy through the local virial theorem [eq.11] allowing to express the Local Source, $LS(\mathbf{r},\mathbf{r}')$.

$$LS(\mathbf{r},\mathbf{r}') = \frac{4m}{\hbar^2}\frac{2G(\mathbf{r}') + V(\mathbf{r}')}{|\mathbf{r}-\mathbf{r}'|} \tag{12}$$

With $G(\mathbf{r}')$ the kinetic energy, and $V(\mathbf{r}')$ the potential energy. Such $LS(\mathbf{r}_{cp},\mathbf{r}')$ provides the local contribution from $\mathbf{r}'$ characterizing it like a "sink", when $LS(\mathbf{r}_{cp},\mathbf{r}') < 0$, or like a "source", when $LS(\mathbf{r}_{cp},\mathbf{r}') > 0$, to $\mathbf{r}_{cp}$. Others topological tools where developed during the last decades into the framework of Bader's Theory, such as the Espinosa indexes [75], delocalization indexes, $\delta(I,J)$ [76], domain-averaged Fermi hole (DAFH) [59-63], showing the strength of such theory in getting precious insights on chemistry.

4.4 Espinosa Indexes

The Espinosa indexes [75] are topological parameters evaluated at BCP, which allow to classify the type of bond. At the base of classification in three different class so called: shared shell, transition zone and closed shell; there is the ration between the absolute value of potential energy density, $|V(\mathbf{r}_{BCP})|$ and kinetic energy density, $G(\mathbf{r}_{BCP})$. Furthermore, the other topological tools considered are $\nabla^2\rho_e(\mathbf{r}_{BCP})$, the total energy density, $\mathcal{H}(\mathbf{r}_{BCP})$, and the ratio between $\mathcal{H}(\mathbf{r}_{BCP})$and $\rho_e(\mathbf{r}_{BCP})$ defined like the bond degree parameter in case of shared shell or defined like the softness parameter in case of closed shell. Table 1 clarifies how to read these topological parameters at the BCP to classify the type of bond.

Table 1. Classification of type of bond second Espinosa[74] by the topological parameter at the bond critical point (BCP): charge density,$\rho_e(\mathbf{r}_{BCP})$, Laplacian of charge density, $\nabla^2\rho_e(\mathrm{r}_{BCP})$, kinetic energy density, $G(\mathbf{r}_{BCP})$, potential energy density, $V(\mathbf{r}_{BCP})$, and the total energy density, $\mathcal{H}(\mathbf{r}_{BCP})$.

Shared shell	**Transition zone**	**Closed shell**
$\lvert V_{BCP}\rvert > 2G_{BCP}$	$1 \leq \lvert V_{BCP}\rvert / G_{BCP} \leq 2$	$\lvert V_{BCP}\rvert < G_{BCP}$
$\nabla^2\rho_{BCP} < 0$	$\nabla^2\rho_{BCP} > 0$	$\nabla^2\rho_{BCP} > 0$
$H_{BCP} \ll 0$	$H_{BCP} < 0$	$H_{BCP} > 0$
$H_{BCP}/\rho_{BCP} < 0$	-	$H_{BCP}/\rho_{BCP} > 0$

4.5 Delocalization Index

At the Hartree-Fock level the delocalization index, $\delta(I,J)$ [76], has a simple physical interpretation being obtained from the double integration, over the atoms in question *I* and *J*, of the exchange density contributing to the pair density, $\rho_e^{(2)}(\mathbf{r}_1,\sigma_1,\mathbf{r}_2,\sigma_2)$, that describes the exchange of same-spin electrons between the spin orbitals $\phi_\alpha(\mathbf{r})$. Denoting the overlap of a pair of spin orbitals over an atom *I* by $S_{\alpha\beta}(I)$, it is found that:

$$\delta(I,J) = \delta(J,I) = -\sum_\alpha \sum_\beta S_{\alpha\beta}(I) S_{\alpha\beta}(J) \tag{13}$$

Such topological tool was showed to be useful to contribute to chemical bonding description correlating the increasing of sharing of electron pairs with the increasing of covalent bond order. Furthermore, a low sharing of electron pairs was correlated to closed shell interaction typically of interacting ions.

At the delocalization indices are associated the multicentre indexes, which are useful to describe in hypervalent atoms the strength of bonds, which 3-centre-4electron and 3-centre-2electron bonds [59-62].

The 3-centre bond index was heuristically defined as a triatomic term for the closed shell systems with *N*-electrons,

$$I_{ABC} = \sum_{\alpha}^{A}\sum_{\beta}^{B}\sum_{\gamma}^{C}(PS)_{\alpha\beta}(PS)_{\beta\gamma}(PS)_{\gamma\alpha} \tag{14}$$

Resulting from the partitioning of the expression

$$\sum_{\alpha}^{A}\sum_{\beta}^{B}\sum_{\gamma}^{C}(PS)_{\alpha\beta}(PS)_{\beta\gamma}(PS)_{\gamma\alpha} = 2^{2}N \tag{15}$$

With *P* and *S*, which denote the normal first order density matrix and the overlap matrix, respectively. Into mono-, bi-, and triatomic contributions. Analogously, z-center bond indexes [59-62] were then related to the partitioning of the product

$$\sum_{\alpha}\sum_{\beta}\dots\sum_{\omega}(PS)_{\alpha\beta}(PS)_{\beta\gamma}\dots(PS)_{\omega\alpha} = 2^{z-1}N \tag{16}$$

In case of open shell the 3-bond index described by eq.19 is modified into

$$\sum_{\alpha}^{A}\sum_{\beta}^{B}\sum_{\gamma}^{C}\left({(PS)_{\alpha\beta}}^{s(\alpha)}{(PS)_{\beta\gamma}}^{s(\alpha)}{(PS)_{\gamma\alpha}}^{s(\alpha)} + {(PS)_{\alpha\beta}}^{s(\beta)}{(PS)_{\beta\gamma}}^{s(\beta)}{(PS)_{\gamma\alpha}}^{s(\beta)}\right) = N^{s(\alpha)} + N^{s(\beta)} \tag{17}$$

This models can be solved analytically with the limit of solution for 3c4e and 3-centre-2-electron (3c2e) are the same in absolute value equal to 0.185, but different in sign: negative for the first and positive for the latter.

4.6 Domain-Averaged Fermi Hole (DAFH)

The idea of DAFH [59-62] consists in to know the spin of first electron of a pair fixed the second confined in a region of space like Ω. Thus, within atomic basin Ω the probability, $P_{\Omega,\sigma_2}(\mathbf{r}_1,\sigma_1)$, to find one electron at position $\mathbf{r}_1$ with spin state $\sigma_1$conditionedto second electron fixed at position $\mathbf{r}_2$ with spin state σ_2 is given in terms of pair density, $\rho_e^{(2)}(\mathbf{r}_1,\sigma_1,\mathbf{r}_2,\sigma_2)$:

$$P_{\Omega,\sigma_2}(\mathbf{r}_1,\sigma_1) = 2\int_{\Omega} \rho_e^{(2)}(\mathbf{r}_1,\sigma_1,\mathbf{r}_2,\sigma_2)d\mathbf{r}_2 \Big/ \int_{\Omega} \rho_e(\mathbf{r}_2,\sigma_2)d\mathbf{r}_2 \tag{18}$$

Thus, the DAFH is so derived:

$$h_{\mathbf{r}_2,\sigma_2}(\mathbf{r}_1,\sigma_1) = \rho_e(\mathbf{r}_1,\sigma_1) - P_{\Omega,\sigma_2}(\mathbf{r}_1,\sigma_1) \tag{19}$$

Satisfying the normalization condition:

$$\int_{\Omega} h_{\mathbf{r}_2,\sigma_2}(\mathbf{r}_1,\sigma_1) = 1 \tag{20}$$

The atomic basin partition into the framework of QTAIM was showed by Ponec *et al.* (2010) [63] to give substantial different results with respect to Mulliken approximation in presence of heavy atoms where relativistic effects play an important role. Such differences are due to unfeasible description of atomic partition generated by Mulliken approximation respect a Bader's atomic partition seen into the eq.1.

4.7 References

1. Lewis, G. N.; The Atom and the Molecule. *J.Am.Chem.Soc*. **1916**, 38, 762-785.
2. Pauling, L; The Nature of the Chemical Bond. Third Ed. Cornell University Press, Ithaca, New York, **1960**.
3. Gatti, C. (eds.); Macchi, P. (eds.) Modern Charge Density. Springer Dordrecht Heidelberg: London, New York, **2012**.
4. Kolb, B.; Lentz, L. C.; Kolpak, A. M. Discovering charge density functionals and structure-property relationships with PROPhet: A general framework for coupling machine learning and first-principles methods. *Sci Rep.* **2017**, 7, 1192.
5. Cho, D.; Gye, G.; Lee, J.; Lee, S.-H.; Wang, L.; Cheong, S.-W.; Yeom, H. W. Correlated electronic states at domain walls of a Mott-charge-density-wave insulator 1*T*-TaS_2. *Nat Commun*. 2017, 8, 392.
6. Khon, W. (auth.); Gonis, A. (eds.); Kioussis, N. (eds.); Ciftan, M. (eds.) Electron Correlations and Materials Properties. Springer US **1999**.
7. Ahmed, M.; Jelsch, C.; Guillot, B.; Lecomte, C.; Domagała, S. Relationship between Stereochemistry and Charge Density in Hydrogen Bonds with Oxygen Acceptors. *Cryst. Growth Des.*, **2013**, *13* (1), 315–325.
8. Zhou, J.; Wei, J.; Ngai, To; Wang, Li; Zhu, D.; Shen J. Correlation between Dielectric/Electric Properties and Cross-Linking/Charge Density Distributions of Thermally Sensitive Spherical PNIPAM Microgels. *Macromolecules*, **2012**, 45 (15), 6158–6167.
9. Chowdhury, A.; Harindranath, A.; Maiti, J. Correlation and localization properties of topological charge density and the pseudoscalar glueball mass in SU(3) lattice Yang-Mills theory. *Phys. Rev*. **2015**, D 91, 074507.
10. Hurst, M. O.; Fortenberry, R. C. Factors affecting the solubility of ionic compounds. *Computational and Theoretical Chemistry* **2015**, 1069, 132–137.
11. Lyulin, S. V. Correlation between overcharging peculiarities and the solubility of interpolyelectrolyte complexes. *Chemical Physics Letters* **2016**, 667, 296-300.
12. Collins K. D. Charge Density-Dependent Strength of Hydration and Biological Structure. *Biophysical Journal* **1997**, 72, 65-76.
13. Uchikoga, M.; Takahashi, S.-Y.; Ke, R.; Sonoyama, M.; Mitaku, S. Electric charge balance mechanism of extended soluble proteins. *Protein Science* 2005, 14, 74–80.
14. Zangi, R.; Hagen, M.; Berne, B. J. Effect of Ions on the Hydrophobic Interaction between Two Plates. *J. Am. Chem. Soc.* **2017**, 129, 4678-4686.
15. Sakabe, J.; Uchida, H.; Shimoyama, Y. Modeling of drug solubility in supercritical carbon dioxide using equation of state based on hole theory with molecular surface charge density. *Chemical Engineering Research and Design* **2014**, 92 (12), 2970-2976.
16. Kendrew, J. C.; Dickerson, R. E.; Strandberg, B. E.; Hart, R. G.; Davies, D. R.; Phillips, D. C.; Shor V. C. Structure of Myoglobin: A Three-Dimensional Fourier Synthesis at 2A Resolution. *Nature*, **1960**, 185, 422-427.
17. Lee, B.; Richards, F. M. The interpretation of protein structures: Estimation of static accessibility. Journal of Molecular Biology, **1971**, 55 (3),379–400.
18. Hermann, R. B. Theory of hydrophobic bonding. II. Correlation of hydrocarbon solubility in water with solvent cavity surface area. *J. Phys. Chem.* **1972**, 76 (19), 2754–2759.
19. Richards, F. M. Areas, volumes, packing, and protein structure. *Annual Review of Biophysics and Bioengineering* **1977**, 6 (1), 151–176.
20. Chothia, C. Hydrophobic bonding and accessible surface area in proteins. *Nature*, 1974, 248, 338–339.

21. Reynolds, J. A.; Gilbert, D. B.; Tanford, C. Empirical correlation between hydrophobic free energy and aqueous cavity surface area. *Proc. Natl. Acad. Sci. USA*, **1974**, 71 (8), 2925–2927.
22. Eisenberg, D.; Andrew, A. D.; McLachlan, D. Solvation energy in protein folding and binding. *Nature* **1986**, 319, 199–203.
23. Ooi, T.; Oobatake, M.; Nmmethy, G.; Scheraga, H. A. Accessible surface areas as a measure of the thermodynamic parameters of hydration of peptides. *Proc. Natl. Acad. Sci. USA*, 1987, 84 (10), 3086–3090.
24. Sharp, K. A.; Nicholls, A.; Fine, R. F.; Honig, B. Reconciling the magnitude of the microscopic and macroscopic hydrophobic effects. *Science*, 1991, 252 (5002), 106–109.
25. Brooks, B. R.; Brooks, C. L.; Mackerell, A. D.; Nilsson, L.; Petrella, R. J.; Roux, B.; Won, Y.; Archontis, G.; Bartels, C.; Boresch, S.; Caflisch, A.; Caves, L.; Cui, Q.; Dinner, A. R.; Feig, M.; Fischer, S.; Gao, J.; Hodoscek, M.; Im, W.; Kuczera, K.; Lazaridis, T.; Ma, J.; Ovchinnikov, V.; Paci, E.; Pastor, R. W.; Post, C. B.; Pu, J. Z.; Schaefer, M.; Tidor, B.; Venable, R. M.; Woodcock, H. L.; Wu, X.; Yang, W.; York, D. M.; Karplus M. Charmm: The biomolecular simulation program. *Journal of Computational Chemistry* **2009**, 30 (10), 1545–1614.
26. Connolly M. L. The molecular surface package. *Journal of Molecular Graphics* **1993**, 11 (2), 139–141.
27. Sanner, M. F.; Olson, A. J.; Spehner, J. Reduced surface: An efficient way to compute molecular surfaces. *Biopolymers* **1996**, 38 (3), 305–320.
28. Chothia, C. The nature of the accessible and buried surfaces in proteins. *Journal of Molecular Biology* **1976**, 105 (1), 1–12.
29. Ashbaugh, H. S.; Kaler, E. W.; Paulaitis, M. E. A universal surface area correlation for molecular hydrophobic phenomena. *Journal of the American Chemical Society* **1999**, 121 (39), 9243–9244,.
30. Singh, Y. H.; Gromiha, M. M.; Sarai, A.; Ahmad, S. Atom-wise statistics and prediction of solvent accessibility in proteins. *Biophysical Chemistry* **2006**, 124 (2), 145 – 154.
31. Kapcha, L. H.; Rossky, P. J. A simple atomic-level hydrophobicity scale reveals protein interfacial structure. Journal of Molecular Biology **2014**, 426 (2), 484–498.
32. Janin, J. Surface and Inside Volumes in Globular Proteins. *Nature* **1979**, 277, 491–492.
33. Kyte, J.; Doolittle, R. F. A simple method for displaying the hydropathic character of a protein. *Journal of Molecular Biology* **1982**, 157 (1), 105–132.
34. Eisenberg, D.; Weiss, R. M.; Terwilliger, T. C. The hydrophobic moment detects periodicity in protein hydrophobicity. *Proc. Natl. Acad. Sci. USA*, **1984**, 81 (1), 140–144.
35. Engelman, D. M.; Steitz, T. A.; Goldman A. Identifying nonpolar transbilayer helices in amino acid sequences of membrane proteins. *Annual Review of Biophysics and Biophysical Chemistry* **1986**, 15 (1), 321–353.
36. Kauzmann, W. Thermodynamics of unfolding. *Nature* **1987**, 325, 763–764.
37. Dill, K. A. Dominant forces in protein folding. *Biochemistry* **1990**, 29 (31),7133–7155.
38. Baldwin, R. L. Dynamic hydration shell restores kauzmanns 1959 explanation of how the hydrophobic factor drives protein folding. *Proc. Natl. Acad. Sci. USA*, **2014**, 111 (36), 13052–13056.
39. Onsager, L. Electric moments of molecules in liquids. *Journal of the American Chemical Society* **1936**, 58 (8), 1486–1493.
40. Tanford, C.; Kirkwood, J. G. Theory of protein titration curves. i. general equations for impenetrable spheres. *Journal of the American Chemical Society* **1957**, 79 (20), 5333–5339.
41. Warshel, A.; Levitt, M. Theoretical studies of enzymic reactions: Dielectric, electrostatic and steric stabilization of the carbonium ion in the reaction of lysozyme. *Journal of Molecular Biology* **1976**, 103 (2), 227–249.
42. Warshel, A.; Sharma, P. K.; Kato, M.; Parson, W. W. Modeling electrostatic effects in proteins. *Biochimica et Biophysica Acta (BBA) - Proteins and Proteomics* **2006**, 1764 (11), 1647–1676.

43. Marenich, A. V.; Cramer, C. J.; Truhlar, D. G. Universal solvation model based on solute electron density and on a continuum model of the solvent defined by the bulk dielectric constant and atomic surface tensions. *The Journal of Physical Chemistry B* **2009**, 113 (18), 6378–6396.
44. Benkert, P.; Tosatto, S. C. E.; Schomburg, D. Qmean: A comprehensive scoring function for model quality assessment. *Proteins: Structure, Function, and Bioinformatics* **2008**, 71 (1), 261–277.
45. Kota, P.; Ding, F.; Ramachandran, S.; Dokholyan, N. V.; Gaia: automated quality assessment of protein structure models. *Bioinformatics* **2011**, 27 (16), 2209–2215.
46. Perutz, M. F. Electrostatic effects in proteins. *Science* **1978**, 201 (4362), 1187–1191.
47. Mobley, D. L.; Barber II, A. E.; Fennell, C. J.; Dill, K. A. Charge asymmetries in hydration of polar solutes. *The Journal of Physical Chemistry B* **2008**, 112 (8), 2405–2414.
48. Simonson, T.; Perahia, D. Internal and interfacial dielectric properties of cytochrome c from molecular dynamics in aqueous solution. *Proc. Natl. Acad. Sci. USA*, **1995**, 92 (4), 1082–1086.
49. Tanford, C. Interfacial free energy and the hydrophobic effect. *Proc. Natl. Acad. Sci. USA*, **1979**, 76 (9), 4175–4176.
50. Pang, X.; Zhou, H. X. Poisson-Boltzmann calculations: van der Waals or molecular surface? Commun. Comput. Phys. **2013**, 13 (1), 1–12.
51. Harris, R. C.; Pettitt, B. M. Effects of geometry and chemistry on hydrophobic solvation. *Proc. Natl. Acad. Sci. USA*, **2014**, 111 (41), 14681–14686.
52. Rose, G. D.; Geselowitz, A. R.; Lesser, G. J.; Lee, R. H.; Zehfus, M. H. Hydrophobicity of amino acid residues in globular proteins. *Science*, **1985**, 229 (4716), 834–838.
53. Tantardini, C.; Benassi, E Topology vs. thermodynamics in chemical reactions: the instability of PH_5. *Phys. Chem. Chem. Phys.*, **2017**, 19, 27779-27785.
54. Chopra, D.; Zhurov, V. V.; Zhurova, E. A.; Pinkerton A. A. Chemical Bonding and Structure−Reactivity Correlation in Meldrum's Acid: A Combined Experimental and Theoretical Electron Density Study. *J. Org. Chem.*, **2009**, *74* (6), 2389–2395.
55. Wang, Q.; Li, F.; Shen, X.; Shi, W.; Li, X.; Guo, Y.; Xiong, S.; Zhu, Q. Relation between reactivity and electronic structure for α'_L-, β- and γ-dicalcium silicate: A first-principles study. *Cement and Concrete Research* **2014**, 57, 28-32.
56. Vargas, A.; Bürgi, T.; von Arx, M.; Hess, R.; Baiker, A. Relation between Electronic Structure of -Substituted Ketones and Their Reactivity in Racemic and Enantioselective Platinum-Catalyzed Hydrogenation. *Journal of Catalysis* **2002**, 209, 489-500.
57. Pendas, A. M.; Contreras-Garcia, J. Understanding structure and reactivity from topology and beyond. *Comp. Theo. Chem.* **2015**, 1053, 1.
58. Simons, J.; Chapter 6. Electronic Structures. An introduction to theoretical chemistry, Cambridge, UK: Cambridge University Press, **2003**.
59. Ponec, R.; Duben, A. J. Electron pairing and chemical bonds: Bonding in hypervalent molecules from analysis of Fermi holes. J. Comput. Chem. **1999**, 20 (8), 760−771.
60. Ponec, R.; Yuzhakov, G.; Cooper, D. L.; Multicenter bonding and the structure of electron-rich molecules. Model of three-center four-electron bonding reconsidered. Theor. Chem. Acc., **2004**, 112, 419–430.
61. Ponec, R.; Mayer, I; Investigation of Some Properties of Multicenter Bond Indices. *J. Phys. Chem. A*, **1997**, *101* (9), pp 1738–1741.
62. Ponec, R.; Cooper, D. L.; Anatomy of bond formation. Bond length dependence of the extent of electron sharing in chemical bonds from the analysis of domain-averaged Fermi holes. J. Phys. Chem. A, **2007**, 111, 11294–11301.
63. Ponec, R.; Bučinský, L.; Gatti, C.; Relativistic Effects on Metal-Metal Bonding: Comparison of the Performance of ECP and Scalar DKH Description on the Picture of Metal-Metal Bonding in $Re_2Cl_8^{2-}$. *J. Chem. Theory Comput.* **2010,** 6*,* 3113–3121.

64. Popelier, P. L. A.; Intermolecular Forces and Clusters-Quantum Chemical Topology: On Bonds and Potentials; Springer-Verlag: Berlin, Heidelberg, **2005**.
65. Bader, R. F. W.; Atoms in Molecules. A Quantum Theory; Oxford University Press: Oxford, **1990**.
66. Cassam-Chenai, P.; Jayatilaka, D.; Some fundamental problems with zero flux partitioning of electron densities. *Theor. Chem. Acc.*, **2001**, 105, 213-218.
67. Spackman, M. A.; Munshi, P.; Dittrich, B.; Dipole moment enhancement in molecular crystals from X-ray diffraction data. *Chem. Phys. Chem.*, **2007**, 8, 2051-2063.
68. Dunitz, J. D.; Gavezzotti, A.; Molecular recognition in organic crystals: directed intermolecular bonds or nonlocalized bonding? *Angew. Chem. Int. Ed.*, **2005**, 44, 1766–1787.
69. Galvão, T. L. P.; Rocha, I. M.; Riberio da Silva, M. D. M. C.; Riberio da Silva, M. A. V.; From 2-Hydroxypyridine to 4(3H)-Pyrimidinone: Computational Study on the Control of the Tautomeric Equilibrium. *J. Phys. Chem. A*, **2013**, 117, 12668,
70. Kollman, P. A.; Noncovalent interactions. *Acc. Chem. Res.*, **1977**, 10, 365–371.
71. Otero-de-la-Roza, A.; Johnson, E.R.; Contreras-García, J.; Revealing non-covalent interactions in solids: NCI plots revisited. *Phys. Chem. Chem. Phys.*, 2012, 14, 12165.
72. Saleh, G.; Gatti, C.; Lo Presti, L.; Contreras-García, J.; Revealing Non-covalent Interactions in Molecular Crystals through Their Experimental Electron Densities. *Chem. - A Eur. J.*, **2012**, 18, 15523–15536.
73. Contreras-García, J.; Johnson, E.R.; Keinan, S.; Chaudret, R.; Piquemal, J.-P.; Beratan, D.N.; Yang, W.; NCIPLOT: A Program for Plotting Noncovalent Interaction Regions. *J. Chem. Theory Comput.*, **2011**, 7, 625–632.
74. Bader, R. F. W.; Gatti, C. A Green's function for the density. *Chem. Phys. Lett.*, **1998**, 287, 233−238.
75. Espinosa, E.; Alkorta, I.; Elguero, J.; Molins, E.; From weak to strong interactions: A comprehensive analysis of the topological and energetic properties of the electron density distribution involving X–HF–Y systems. *J. Chem. Phys.*, **2002**, 117, 5529–5542.
76. Fradera, X.; Austen, M. A.; Bader, R. F. W.; The Lewis Model and Beyond. J. Phys. Chem. A, 1999, 103, 304–314.

5.0 OVERVIEW

The aim of this work was to answer to following questions:

- Is it possible to define a new equation for real gases overcoming the old concept, which describes the atoms like spheres? (CHAPTER I)
- Is it possible to define an energy border between blurry hydrogen bond and van der Waals interactions? (CHAPTER I)
- Is it possible to define the limit of long range interactions? (CHAPTER I)
- Which are the non-covalent interactions within meloxicam crystal structures and how are they correlated with solubility of crystals? (CHAPTER II)
- Why Tenoxicam respect to other oxicam is seen to crystallize into Zwitterionic form and not into β-keto-enolic form? (CHAPTER II)
- Does topological analysis explain the reactivity and can be used to predict *a priori* the reactivity? (CHAPTER III)
- How the Pauling electronegativity can be used at high-pressure to explain the *chemical bonding*?

CHAPTER I

Development of Quantum Chemical Topology

Summary:

The chapter describes the development of a new equation of state for real gases into the framework of quantum theory of atoms in molecules (QTAIM) overcoming the old concept of spherical atomic partition presented in van der Waals equation. In this work, van der Waals damping parameters were substituted with respect to their usual derivation from mechanical statistics. The ***a*** parameter was obtained by complexation energy consisting in the dissociation energy corrected for the basis set superposition error, D_0^{CC}, taking into account the zero point energy of the dimer, $ZPE_{AB}^{CC}(\mathbf{G})$, and the zero point energy of each monomer:

$$D_0^{CC} = -V_{AB}^{CC}(\mathbf{G}) - ZPE_{AB}^{CC}(\mathbf{G}) + ZPE_A^{CC}(\mathbf{G}) + ZPE_B^{CC}(\mathbf{G})$$

with $V_{AB}^{CC}(\mathbf{G})$ corresponding to the electronic energy of the dimer corrected for the basis set superposition error.

While, the ***b*** parameter was estimated as the average molecular volume for a couple of interacting molecules of gas for atomic partition in the field of QTAIM.

Subsequently the new equation was tested on a series of gases (monoatomic, diatomic, and triatomic). The different atomic partition and the interaction energy obtained through *ab initio* calculation proposed in the new equation showed the best feasibility of the latter equation respect to van der Waals equation creating a bonding between quantum and classical mechanics.

In the last part of the chapter is given a sound reply to an experimental unsolved question, concerning how to distinguish a hydrogen bond (H-bond) from van der Waals (vdW) interaction for an X–H···Y system looking for an "energy border" between H-bond and vdW interaction, and the consequent limit of long range interactions. The IUPAC definition for an H-bond results incomplete not having determined an "energy border" between H-bond and vdW interaction, but said only that the presence of H-bond should be represented by an experimentally observed stretch of X–H bond for a X–H···Y system. The quantification of this stretch to consider it sufficient to identify an H-bond is a source of controversy among the scientific community that had to be clarified. Such "energy border" was found as the limit of long range interactions, which it was never defined since now. Thanks to my computational investigation, based on systematic, state-of-the-art coupled cluster calculations and Bader analyses based on source function (SF), it was possible to solve these two enigmas determining the presence or not of H-bond with correlated "energy border" between H-bond and vdW interaction, and subsequently to find the limit of long range interactions.

Conclusions:

- The new equation of state for real gases represents a connection between quantum and classic mechanic, where the first determinates the latter, overcoming the odd spherical atomic partition. Thus, this equation substitutes the obsolete vdW equation.
- The "energy border" between H-bond and vdW interaction was found at the increasing of bond distance due to the removal of interaction between acceptor (A) and donor (D) electronic clouds. A topological analysis based on SF was able to reveal the "energy

border" between inter-molecular H-bond and vdW interaction thanks to the source contributions of *A*, *D* and *H* atoms measured at the *A…H* BCP.

- The analogous of "energy border" in the case of bending of bonding angle is the "critical angle", which must be defined not simply through geometric criteria previously proposed in literature, but looking for the effective interactions at the *A…H* BCP using SF or looking for the Cohesion Energy of dimer.
- The limit of long range interactions can be found through an analysis of atomic basins volume variation for both A and H Ωs looking for its first value of plateau respect to $R_{A...D}$ increasing.

Contribution:

The project was conceptualized and managed by me other that the Investigation, data curation, formal analysis thanks to the accumulated experience in Bader's Theory.

Theoretical Chemistry Accounts (2018) 137:93
https://doi.org/10.1007/s00214-018-2271-7

REGULAR ARTICLE

A new equation of state for real gases developed into the framework of Bader's Theory

Christian Tantardini[1,2]

Received: 23 March 2018 / Accepted: 4 June 2018
© Springer-Verlag GmbH Germany, part of Springer Nature 2018

Abstract

The van der Waals equation since now represented the unique equation of state for real gases with a spherical atomic partition, which was disproved during the years by different scientists including Bader and co-workers. Thus, through a work into the framework of Bader's Theory a new equation of state for real gases due to the substitution of van der Walls dumping parameters is presented and tested on a series of gas (monoatomic, diatomic, and triatomic). The different atomic partition and the interaction energy obtained through ab initio calculation proposed in the new equation showed the best feasibility of the latter respect to van der Waals equation.

Graphical abstract

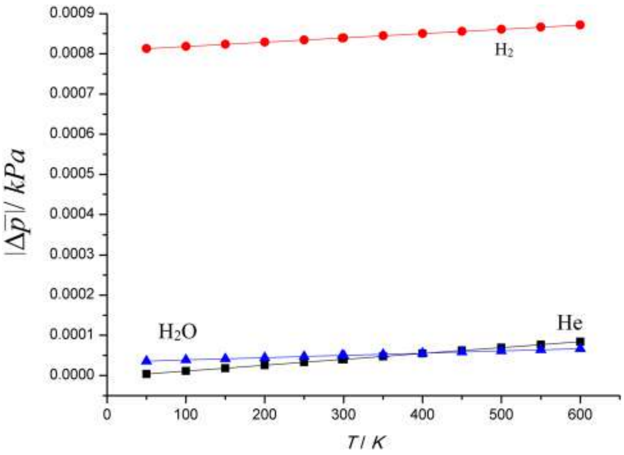

Keywords van der Waals equation · QTAIM · Equation of state · Hydrogen bond

1 Introduction

Since its introduction in the 1873, the van der Waals equation (vdWE) [1] is the basic model used to describe with relative accuracy the behavior of real gases through a series of dumping parameters a and b, respectively, for pressure and volume, introduced into the equation of state for ideal gases ($PV = nRT$). vdWE is so formulated:

$$\left(\bar{p} + \frac{a}{v^2}\right)(v - b) = RT \tag{1}$$

Electronic supplementary material The online version of this article (https://doi.org/10.1007/s00214-018-2271-7) contains supplementary material, which is available to authorized users.

✉ Christian Tantardini
christiantantardini@ymail.com

[1] SkolTech Skolkovo Institute of Science and Technology, ul. Nobelya 3, Moscow, Russian Federation 121205

[2] Novosibirsk State University, ul. Pirogova 2, Novosibirsk, Russian Federation 630090

Published online: 16 June 2018

where $\bar{p}$ is the average pressure, v the molar volume, R the constant of gases, and T the temperature. Such equation during the years was developed and adapted to different problems [2–7] to overcome its weakens consisting in a model, which considers in the first approximation the atoms like spheres with a proper volume defined as

$$V_{\mathrm{vd}W} = \frac{4}{3}\pi \mathbf{r}^3_{\mathrm{vd}W} \tag{2}$$

where $\mathbf{r}_{vdW}$. is the radii of van der Waals defined as the half imaginary distance between hard spheres representing two atoms. Such kind of definition does not take into account that the electron density varies continuously at the periphery of atoms, and therefore totally disagrees with the modern theory of quantum theory atoms in molecules (QTAIM) introduced by Bader in 1990 [8–10]. In support to the unfeasibility of a spherical model of atomic partition, there are different experimental works [11–28] of X-ray diffraction trying to define new more accurately $\mathbf{r}_{vdW}$ and different works into the framework of QTAIM supported by experimental data [28–39]. Bader introduced an atomic partition within molecule considering the atomic basin like the region of space within is enclosed a nucleus and the surface that delimitates the atomic basin is so-called zero-flux surface (ZFS) [8–10]. This surface, S, is defined by all points in space, $\mathbf{r}_S$, for which the product of the gradient of charge density, $\nabla\rho$, and the normal vector, $\hat{\boldsymbol{n}}$, is zero:

$$\nabla\rho(\mathbf{r}) \cdot \hat{\boldsymbol{n}}(\mathbf{r}) = 0, \forall \mathbf{r} \in S\left(\mathbf{r}_S\right) \tag{3}$$

The atomic basin so defined has a shape that is totally different from spherically model proposed by van der Waals with consequence of failing for van der Waals model and the unfeasible description of real gases.

This work wants to reformulate the equation of state for real gases into the framework of Bader's Theory comparing the results obtained from this new equation, with the results obtained from vdWE.

2 Theoretical background

The vdWE is derived from statistical mechanic [40–43] initially considering the partition function of gas (Z) for N independent particles (see Eq. 4), where the energy of a particle is the sum of kinetic $\left(\mathbf{p}^2/2m\right)$ and potential (U) contributions. In the equation the integral in the space is done on all volume that contains the gas (V) and van der Waals noted that there are regions in which $U \to \infty$ for the repulsion of particles with not null proper volume, V_0. Thus, the integral on the space vanishes in the regions where $V_0 < V$. In the other regions the U is seen to vary relatively slowly, so van der Waals replaced it with average potential energy, $\bar{U}$,

$$\begin{aligned} Z &= \frac{1}{N!}\left[\int e^{-\beta\left(p^2/2m+U\right)}\frac{\mathrm{d}r\mathrm{d}p}{h^3}\right]^N \\ &= \frac{1}{N!}\left[\int e^{-\beta\left(p^2/2m\right)}\frac{\mathrm{d}p}{h^3}\int e^{-\beta U}\mathrm{d}r\right]^N \\ &= \frac{1}{N!}\left[\left(\frac{2\pi m}{\beta h^2}\right)^{\frac{3}{2}}\int e^{-\beta U}\mathrm{d}r\right]^N \\ &= \frac{1}{N!}\left[\left(\frac{2\pi m}{\beta h^2}\right)^{\frac{3}{2}}\left(V - V_0\right)e^{-\beta U}\right]^N \end{aligned} \tag{4}$$

The introduced V_0 and $\bar{U}$ were defined by van der Waals starting to consider that the total potential energy for a gas with N particles must be $N\bar{U}$, but there are $(1/2)N(N-1) \simeq (1/2)N^2$ pairs of particles. The consequent average potential energy is

$$\bar{U} = \frac{1}{2}N\bar{u} \tag{5}$$

where $\bar{u}$ is the mean potential energy u between a pair of particles described simple like

$$u(R) = \begin{cases} \infty, & R < R_0 \\ -u_0\left(R_0/R\right)^s, & R > R_0 \end{cases} \tag{6}$$

where R is the distance between the mass center of two particles, $u_0 > 0$, and $s > 0$. The particles are seen to be weakly attracting hard spheres of radius $(1/2)R_0$, the so-called van der Waals radius. So, van der Waals in the first approximation reducing the shape of particle to a sphere defined the probability of the distance lying between R and $R + dR$ equal to $\left(4\pi R^2\mathrm{d}R\right)/V$, and

$$\bar{u} = \frac{1}{V} - \frac{4\pi u_0}{V}\int_{R_0}^{\infty}\left(\frac{R_0}{R}\right)^s R^2\mathrm{d}R \tag{7}$$

Looking how falls $u(R)$, it was noted that for $s > 3$, it falls sufficiently rapidly with the integral that converge properly and the best choice was achieved for $s = 6$. Thus, the equation for the average potential energy is

$$\bar{U} = \frac{1}{2}N\bar{u} = -a'\frac{N}{V} \tag{8}$$

where

$$a' = \frac{2\pi}{3}\left|R_0\right|^3\left(\frac{3}{s-3}\right)u_0 \tag{9}$$

Thus, defining the molar volume like the volume of container divided for the number of moles, $v = V/n$

$$\frac{N}{V} = \frac{nN_A}{V} = \frac{N_A}{v}, \tag{10}$$

while the volume excluded by interactions between particles approximated as hard spheres is

$$V_0 = b'N \tag{11}$$

where

$$b' = \frac{2\pi}{3}\left|R_0\right|^3 = 4\left[\frac{4\pi}{3}\left(\frac{\left|R_0\right|}{2}\right)^3\right] \tag{12}$$

So, deriving Eq. (4) with respect to the volume we obtained the equation of state for real gas

$$\bar{p} = \frac{1}{\beta}\frac{\partial \ln Z}{\partial V} = \frac{1}{\beta}\frac{\partial}{\partial V}\left[N\ln\left(V - b'N\right) + N\beta a'\frac{N}{V}\right] \tag{13}$$

Obtaining

$$\left(\bar{p} + a'\frac{N^2}{V^2}\right)\left(\frac{V}{N} - b'\right) = kT \tag{14}$$

Then

$$\left(\bar{p} + \frac{a}{v^2}\right)(v - b) = RT \tag{15}$$

where $a = -N_A^2 a'$. and $b = N_A b'$.

3 Theoretical development: from van der Waals equation to new equation of state

It is not of worthy before to introduce the substitution of van der Waals parameters into the framework of Bader's Theory that the arbitrary definition of atomic basin doesn't allow to define unambiguously the atomic domains, Ω, because the interatomic surfaces, along with the surfaces found at infinity, are the only closed surfaces of $\mathbb{R}^3$, which satisfy the zero-flux condition [44]. Thus, in the calculus the ZFS is numerically approximated not only in the bound against vacuum, but also between two atomic basins as the region wherein the $\rho(\mathbf{r})$ is less than 10^{-3} e/bohr^3 considering that it tends to 0 when the its distance from nucleus tends to infinite [8–10]. Under this approximation, Bader demonstrated the accuracy of numerical integration to obtain the atomic energy basin using the virial theorem [8–10] with the calculation of kinetic energy within atomic basin through $L(\Omega)$.

$$L(\Omega) = -\left(\frac{\hbar^2}{4m}\right)\int_{\Omega}\nabla^2\rho(\mathbf{r})\mathrm{d}\tau = -\left(\frac{\hbar^2}{4m}\right)\oint \mathrm{d}S(\Omega,\mathbf{r})\nabla\rho(\mathbf{r})\cdot\hat{\boldsymbol{n}}(\mathbf{r}) \tag{16}$$

If $L(\Omega)$ falls in the range 10^{-4}–10^{-5} kJ/mol, the error in the estimation of kinetic energy, necessary to obtain the atomic basin energy through the application of virial theorem, is less than 0.4 kJ/mol [8–10]. Such error is considerable tiny making the ZFS a feasible model of atomic partition. Furthermore, being the energy of atomic basin calculated with the virial theorem the expectation values of kinetic, $\langle\hat{T}\rangle$, and potential, $\langle\hat{U}\rangle$, energies are corrected for a multiplicative factor $(1+\gamma)$ and $(1+1/\gamma)$, respectively, in order to obtain $E = -\langle\hat{T}\rangle = \langle\hat{U}/2\rangle$for equilibrium geometry [8–10].

Now, looking for the two dumping factors proposed by van der Waals a and b, which describe, respectively, the average interactions between a pair of particle and the volume excluded by these interactions, we have now to reformulate in the framework of Bader's Theory. Initially, for the parameter b' we know from Bader's Theory that the molecular volume is given by the sum of each atomic basin volume $\left(V_\Omega\right)$ so we can define

$$b' = \sum_{\Omega=1}^{M} V_\Omega \tag{17}$$

with $\Omega = 1, \ldots, \mathrm{M}$ the atomic basins within molecule.

Thus,

$$b = N_A b' = N_A\sum_{\Omega=1}^{M} V_\Omega. \tag{18}$$

Such V_Ω is substituted in Eq. (9) in order to take the place of volume spherically approximation initially introduced in Eq. (7) to calculate $\bar{u}$. Moreover, the potential energy at the equilibrium multiplied for a dumping parameter in Eq. (9) is substituted by the interaction energy at the equilibrium for a couple of molecules (X and Y) in the vacuum for T equal zero.

$$a' = -V_\Omega^X u_0^{X\ldots Y} \tag{19}$$

Thus, the term a

$$a = N_A^2 a' = -N_A^2 V_\Omega^X \mu_0^{X\ldots Y} \tag{20}$$

So, substituting the term a and b of Eq. (15) with Eqs. (18) and (20), respectively, we obtain the new equation for real gas as

$$\left(\bar{p} + \frac{N_A^2 V_\Omega u_0^{X\ldots Y}}{v^2}\right)\left(v - N_A\sum_{\Omega=1}^{M} V_\Omega\right) = R \tag{21}$$

4 Application of new equation of state

The validity of Eq. (21) must be shown through its applicability to different types of gas. Thus, it was decided to calculate the parameters a and b for He (monoatomic), H_2 (diatomic) and H_2O (triatomic) gases through a computational approach (see E.S.I.1 Computational Details) and compared with those tabulated by vdW.

In a three-dimensional space, there is an infinity of geometrical configurations between two molecules. They can be reduced for symmetry and only once it should be the favorite one due to intermolecular interactions, which are measured through the complexation energy (E_C). Thus, in

Table 1 The values of damping factors a and b for the van der Waals equation (vdWE) and Eq. (21)

Gas	$a\,[(\mathrm{kPa} * \mathrm{m}^6)/\mathrm{mol}^2]$		$b\,(\mathrm{m}^3)$	
	vdWE [47]	Equation (21)	vdWE [47]	Equation (21)
He	3.460×10^{-6}	1.128×10^{-9}	2.380×10^{-5}	6.235×10^{-6}
H_2	2.476×10^{-5}	8.323×10^{-4}	2.661×10^{-5}	1.091×10^{-5}
H_2O	5.536×10^{-5}	8.862×10^{-5}	3.049×10^{-5}	1.704×10^{-5}

the first approximation, $u_0^{X\ldots Y}$ can be associated with the lowest complexation energy (E_C) of a dimer in vacuum at T equal zero, making it the most favorite one.

$$\mu_0^{X\ldots Y} = E_C \tag{22}$$

The accuracy of E_C is due to the theoretical approach used, which must consider the dispersion energy associated and the basis set superposition error to fit in the best way the intermolecular interactions (see E.S.I.1 Computational Details).

The most simple case is represented by monoatomic gas as He, where the E_C for a dimer is characterized by only one degree of freedom: the distance between two atoms ($R_{He\ldots He}$). The calculation of E_C is complicated looking for a diatomic gas as H_2, which can be modelized as a rigid rotor, and the most important geometrical conformations of its dimer are cataloged: H, L, T, X and Z (see E.S.I.2 Picture of H_2-dimers); such geometrical conformations have different E_C (see E.SI.3 Tables of H_2-dimer energies), and the favorite one is the Z with an $E_C = -319.2$ kcal/mol.

Furthermore, the most complicate case is the triatomic gas as H_2O with the molecules constrained in a C_S dimer being known from the literature [45] to be the favorite configuration characterized by the presence of hydrogen bond (H-bond).

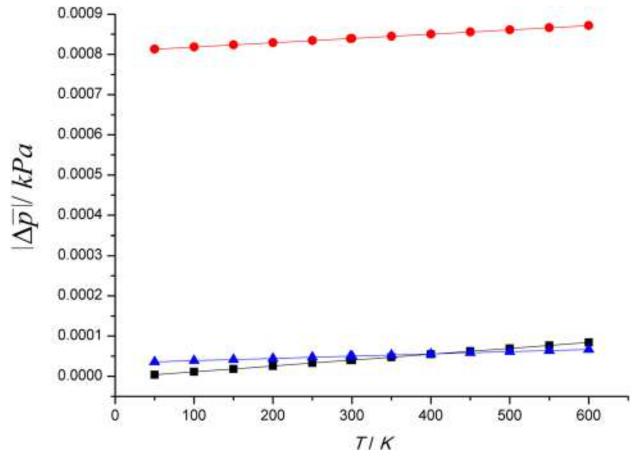

Fig. 1 Graphics of difference in absolute value between $\bar{p}$ calculated with vdWE ($\bar{p}_{vdW}$) and Eq. (21) ($\bar{p}_{new}$) for isochoric with v equal to unitary molar volume (1 m^3/mol) in a range of T from 50 to 600 K. black for He, red for H_2 and blue for H_2O

Therefore, the parameter a will be obtained by the E_C corresponding to $u_0^{X\ldots Y}$ time N_A^2 time the molecular volume obtained through an atomic partition into the framework of QTAIM [8–10]. So, a PROAIM [46] wavefunction associated with each dimer above mentioned was calculated to perform a QTAIM analysis aimed to find the V_Ω within each molecule.

In the most simple case represented by He-dimer, the two Ω are identical for symmetry (i.e., $V_{He} = 1.035 * 10^{-29}\,m^3$), while for the H_2 Z-dimer within each H_2 molecule the Ω are different due to the intermolecular interactions (i.e., $V_{H1}, V_{H4} = 9.058 * 10^{-30}\,m^3$; $V_{H2}, V_{H3} = 9.311 \times 10^{-30}\,m^3$). Thus, the parameter b in case of He is simply due to the V_{He} time N_A, while for H_2 Z-dimer the symmetry guarantees that the molecules have the same molecular volume $\left(V_{H_2}\right)$ albeit different distributed between atoms and the parameter b will be calculated like the V_{H_2} time N_A. The most difficult case is represented by the C_S dimer of water where the two molecular volumes are different due to H-bond which severally modifies the Ω (see E.S.I.4 Table of atomic basins). Thus, the molecular volume of water within C_S dimer can be reasonably approximated as the median of both molecular volume, and the parameter b will be obtained by such median time N_A.

It is possible to see that the difference between vdWE and Eq. (21) associated with parameter b is less than one order of magnitude. Such kind of difference has shown that in the first approximation considering the atom spherically is not wrong at all, while there is a big difference between vdWE and Eq. (21) associated with parameter a (see Table 1). This is due to the total dependence by a fictitious potential for vdWE respect to ab initio calculation for Eq. (21): in vdWE equation the increase of parameter a is correlated with the increase in molecular weight, while for Eq. (21) the $u_0^{X\ldots Y}$ is uniquely main responsible.

Furthermore, provided that known three parameters, then the fourth is calculated through the equation of state, and it was decided to compare the variation of $\bar{p}$ due to T in a range between 50 and 600 K for the isochoric graphs of vdWE and Eq. (21) with v equal to unitary molar volume (1 m^3/mol).

The difference in absolute value between the calculated $\bar{p}$ with vdW and Eq. (21) $\left(|\bar{p}_{new} - \bar{p}_{vdW}|\right)$ shown in Fig. 1 is tiny, and it is marked for the water C_S dimer at low temperature (see E.S.I.5 Table of $\bar{p}$ with vdW and Eq. (21). It is reasonable to think that at low temperature the stretch of O–H…O is close to be frozen with a low H-bond, which does not deform so much the Ω. Thus, the spherical approximation of atomic partition and the fictitious potential for vdWE at low temperature can be considered reasonable.

5 Conclusion

The new equation of state here proposed (Eq. 21) represents a connection between quantum and classic mechanic, where the first determinates the latter. A study of charge density into the framework of QTAIM [8–10] was aimed to overcome the old vision with spherical atomic partition proposed many years ago by vdWE. Such charge density was performed on PROAIM [46] wavefunction obtained through ab initio calculation.

The great difference observed for a parameter is substantially due to $u_0^{X\cdots Y}$, which it was derived by an ab initio calculation for Eq. (21) with respect to fictitious potential with damping factor for vdWE.

For all these reasons Eq. (21) is much more feasible than vdWE filling the gaps of this latter due to its approximations.

Acknowledgements The author would like to express his gratitude to supervisor Prof. Artem R. Oganov for his ongoing support. This work was carried out thanks to the equipment kindly provided by the Siberian Supercomputer Center ICMMG SB RAS and “Supercomputing Center of the Novosibirsk State University” (http://nusc.nsu.ru)

References

1. van der Waals JD (1873) On the Continuity of the Gaseous and Liquid States (doctoral dissertation); Universiteit Leiden
2. Rah K, Eu BC (2001) The generic van der Waals equation of state and self-diffusion coefficients of liquids. J Chem Phys 115:2634–2640
3. Hoover WG, Stell G, Goldmark E, Degani GD (1975) Generalized van der Waals equation of state. J Chem Phys 63:5434–5438
4. Rah K, Eu BC (2002) Generic van der Waals equation of state and theory of diffusion coefficients: binary mixtures of simple liquids. J Chem Phys 116:7967–7976
5. Su G-J, Chang C-H (1946) A generalized van der Waals equation of state for real gases. Ind Eng Chem 38(8):800–802
6. Su G-J, Chang C-H (1946) Generalized equation of state for real gases. Ind Eng Chem 38(8):802–803
7. Metcalf WV (1916) Van der Waals Equation—a supplementary paper. J Phys Chem 20(3):177–187
8. Bader RFW (1990) Atoms in molecules. A quantum theory. Oxford University Press, Oxford
9. Bader RFW (1985) Atoms in molecule. Acc Chem Res 18(1):9–15
10. Bader RFW (1991) A quantum theory of molecular structure and its applications. Chem Rev 91(5):893–928
11. Pauling L (1960) The nature of the chemical bond, 3rd edn. Cornell University, Ithaca
12. Bondi A (1964) Van der Waals volumes and radii. J Phys Chem 68(3):441–451
13. Zefirov YuV, Zorkii PM (1989) Van der Waals radii and their chemical applications. Usp Khim 58(5):713–746
14. Zefirov YuV, Zorkii PM (1995) New chemical applications of the van der Waals radii. Usp Khim 64(5):446–460
15. Filippini G, Gavezzotti A (1993) Empirical intermolecular potentials for organic crystals: the 6-exp approximation revisited. Acta Crystallogr B 49(5):868–880
16. Dunitz JD, Gavezzotti A (1999) Attractions and repulsions in molecular crystals. Acc Chem Res 32(8):677–684
17. Batsanov SS (1998) Van der Waals radii of elements evaluated from the Morse equation. Zh Obshch Khim 68(4):529–534
18. Batsanov SS (1995) Van der Waals radii of elements from structural inorganic chemistry data. Izv Akad Nauk Ser Khim 1:24–29
19. Batsanov SS (2000) Van der Waals radii evaluated from structural parameters of metals. Zh Fiz Khim 74(7):1273–1276
20. Batsanov SS (1999) Calculation of van der Waals radii of atoms from bond distances. J Mol Struct 468:151–159
21. Batsanov SS (2000) Intramolecular contact radii close to the van der Waals radii. Zh Neorg Khim 45(6):992–996
22. Batsanov SS (1994) Van der Waals radii of metals from spectroscopicdata. Izv Akad Nauk Ser Khim 8:1374–1378
23. Batsanov SS (1999) Van der Waals radii of hydrogen in gas-phase and condensed molecules. Struct Chem 10(6):395–400
24. Batsanov SS (2000) Anisotropy of van der Waals atomic radii in the gas-phase and condensed molecules. Struct Chem 11(2/3):177–183
25. Batsanov SS (2001) Anisotropy in the van der Waals area of complex, condensed, and gas-phase molecules. Koord Khim 27:11
26. Wieberg N (1995) Lehrbuch der anorganischen Chemie. Gruyter, Berlin
27. Rowland RS, Taylor R (1996) Intermolecular nonbonded contact distances in organic crystal structures: comparison with distances expected from van der Waals radii. J Phys Chem 100(18):7384–7391
28. Batsanov SS (2001) Van de Waals radii of elements. Inorg Mater 37(9):871–885
29. Grabowski SJ (2011) What Is the covalency of hydrogen bonding? Chem Rev 111(4):2597–2625
30. Grabowski SJ (2012) QTAIM characteristics of halogen bond and related interactions. J Phys Chem A 116(7):1838–1845
31. Parthasarthi R, Subramanian V, Sathyamurthy N (2005) Hydrogen bonding in phenol, water, and phenol-water clusters. J Phys Chem A 109(5):843–850
32. Hathwar VR, Guru Row TN (2011) Charge density analysis of heterohalogen (Cl···F) and Homohalogen (F···F) intermolecular interactions in molecular crystals: importance of the extent of polarizability. Cryst Growth Des 11(4):1338–1346
33. Hirano Y, Takeda K, Miki K (2016) Charge-density analysis of an iron-sulfur protein at an ultra-high resolution of 0.48 Å. Nature 534:281–284
34. Gatti C, Orlando AM, Monza E, Lo Presti L (2016) In applications of topological methods in molecular chemistry. Springer series challenges and advances in computational chemistry and physics, vol 22. Springer, New York, pp 101–129
35. Gatti C, Saleh G, Lo Presti L et al (2012) Sagamore XVII on CSMD. Sapporo, Japan
36. Hey J, Leusser D, Kratzert D, Fliegl H, Dieterich JM, Mata RA, Stalke D (2013) Heteroaromaticity approached by charge density investigations and electronic structure calculations. Phys Chem Chem Phys 15:20600–20610
37. Pal R, Mukherjee S, Chandrasekhar S, Guru Row TN (2014) Exploring cyclopentadienone antiaromaticity: charge density studies of various tetracyclones. J Phys Chem A 118:3479–3489
38. Gatti C, Saleh G, Lo Presti L (2016) Source function applied to experimental densities reveals subtle electron-delocalization effects and appraises their transferability properties in crystals. Acta Crystallogr Sect B Struct Sci Cryst Eng Mater B72:180–193
39. Gatti C, Macchi P (2012) Modern charge-density analysis. Springer, Dordrecht
40. Reif F (1965) Fundamentals of statistical and thermal physics. McGraw-Hill, New York

41. Park D (1992) Introduction to quantum theory, 3rd edn. McGraw-Hil, New York
42. Carter AS (2001) Classical and statistical thermodynamics. Prentice-Hall, Upper Saddle River
43. Hill TL (1948) Derivation of the complete van der Waals' equation from statistical mechanics. J Chem Educ 25(6):347–348
44. Cassam-Chenai P, Jayatilaka D (2001) Some fundamental problems with zero flux partitioning of electron densities. Theor Chem Acc 105:213–218
45. Lane JR (2013) CCSDTQ optimized geometry of water dimer. J Chem Theory Comput 9(1):316–323
46. Gatti C, Fantucci P, Pacchioni G (1987) Charge density topological study of bonding in lithium clusters. Theor Chim Acta 72:433–458
47. Atkins P, De Paula J (2006) Physical Chemistry. Oxford University Press, Oxford

Electronic Supporting Information

for

A new equation of state for real gases into the framework of Bader's Theory

Christian Tantardini[1,2†]

[1]SkolTech Skolkovo Institute of Science and Technology, ul. Nobelya 3, Moscow, Russian Federation, 121205.

[2]Novosibirsk State University, ul. Pirogova 2, Novosibirsk, Russian Federation, 630090.

[†]Corresponding author: christiantantardini@ymail.com.

E.S.I.1 Computational Details

The molecular structures of linear homonuclear dimers of He, H2, and the molecules of water constrained within CS dimer were fully optimized in the gas phase through restricted density functional theory (DFT) with B3LYP[1] exchange-correlation functional with correction of basis set superposition error through counterpoise[2] method. The dispersions were empirically taken into account adding the D3[3] version of Grimme's dispersion with Becke-Johnson[4] damping. The chosen theoretical approach was performed using Dunning triple-z local basis set aug-cc-pVTZ [5,6]. Associated with each optimized dimer molecular structure the PROAIM[7] wavefunction was calculated for the subsequent quantum theory atoms in molecules (QTAIM)[8] analysis.

The full geometry optimization in the gas phase with the associated PROAIM[7] wavefunction were performed using Gaussian G09.D01[9]. The QTAIM[8] analysis was performed using a modified version of PROAIMV[10,11].

E.S.I.2 Picture of H_2-dimers (H, L, T, X and Z) with labels of each atom. In with are the hydrogen atoms.

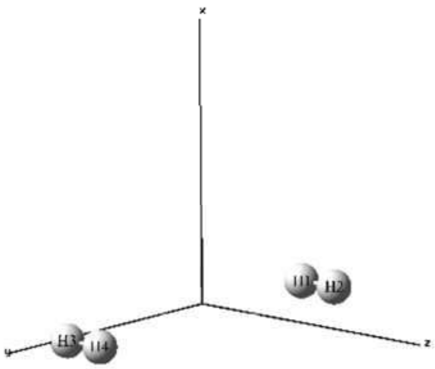

(H)

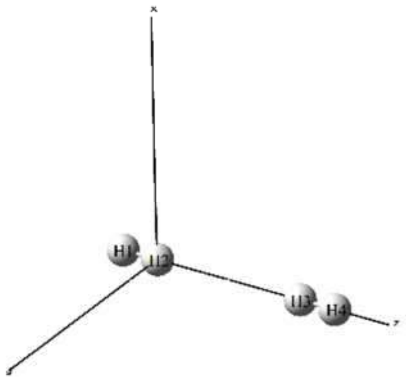

(L)

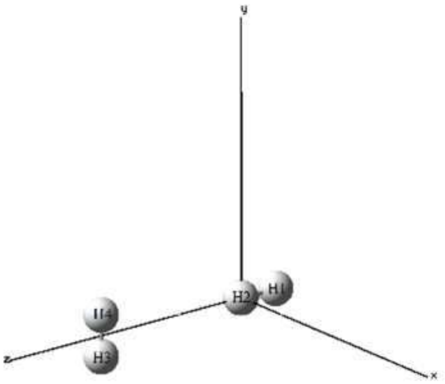

(T)

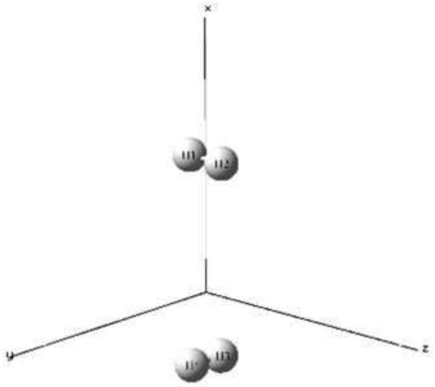

(X)

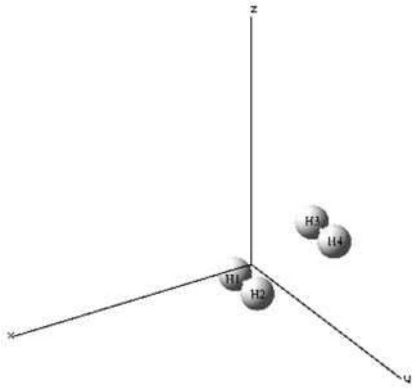

(Z)

E.S.I.3 Table of energy dimer with BSSE corrected through counterpoise method $\left(E_{\mathrm{H_2-H_2}}\right)$, the sum of energies for isolated monomers $\left(E_{\mathrm{H_2}}+E_{\mathrm{H_2}}\right)$, the complexation energy (E_C) associated to each H_2-dimer seen in E.S.I.2.

	H	L	T	X	Z
$E_{\mathrm{H_2-H_2}}$ (*a.u.*)	-2.360312	-2.360331	-2.360419	-2.360329	-2.360378
$E_{\mathrm{H_2}}+E_{\mathrm{H_2}}$ (*a.u.*)	-2.360329	-2.360329	-2.360329	-2.360329	-1.851690
E_{C} (kcal/mol)	$1.058*10^{-2}$	$-1.031*10^{-3}$	$-1.343*10^{-2}$	$2.041*10^{-4}$	$-3.192*10^{2}$

E.S.I.4 Picture (upper) and table (below) of volumes (V_Ω) and energies (E_Ω) of atomic basins for the molecules of water (H_2O^1, H_2O^2) constrained within C_S dimer. The color red is associated to oxygen, with to the hydrogen; the white dashed line represents the hydrogen bond (H-bond) within C_S dimer.

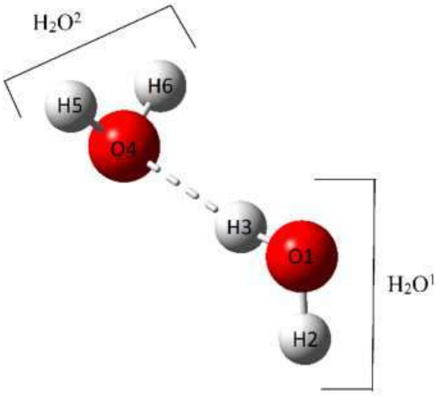

	V_Ω		E_Ω		
	$bohr^3$	m^3	hartree	kJ	kPa $* m^3$
O1	155.506	$2.304*10^{-29}$	-75.737	$-3.302*10^{-19}$	$-3.302*10^{-19}$
H2	23.748	$3.519*10^{-30}$	-0.382	$-1.664*10^{-21}$	$-1.664*10^{-21}$
H3	15.400	$2.282*10^{-30}$	-0.353	$-1.541*10^{-21}$	$-1.541*10^{-21}$
O4	143.012	$2.119*10^{-29}$	-75.746	$-3.302*10^{-19}$	$-3.302*10^{-19}$
H5	22.132	$3.280*10^{-30}$	-0.367	$-1.599*10^{-21}$	$-1.599*10^{-21}$
H6	22.134	$3.280*10^{-30}$	-0.367	$-1.599*10^{-21}$	$-1.599*10^{-21}$
H_2O^1	194.655	$2.885*10^{-29}$	-76.472	$-3.334*10^{-19}$	$-3.334*10^{-19}$
H_2O^2	187.277	$2.775*10^{-29}$	-76.479	$-3.334*10^{-19}$	$-3.334*10^{-19}$
Median (H_2O^1, H_2O^2)	190.966	$2.830*10^{-29}$	-76.476	$-3.334*10^{-19}$	$-3.334*10^{-19}$

E.S.I.5 Graphics (upper) of variation of $\bar{p}$ (kPa) due to T in a range between 50 to 600 K for the isochoric graphs of vdWE and eq.21 (see "I. Theoretical Development" in the main text) with v equal to unitary molar volume (1 m/mol) and table of values (below) for He, H_2 and H_2O.

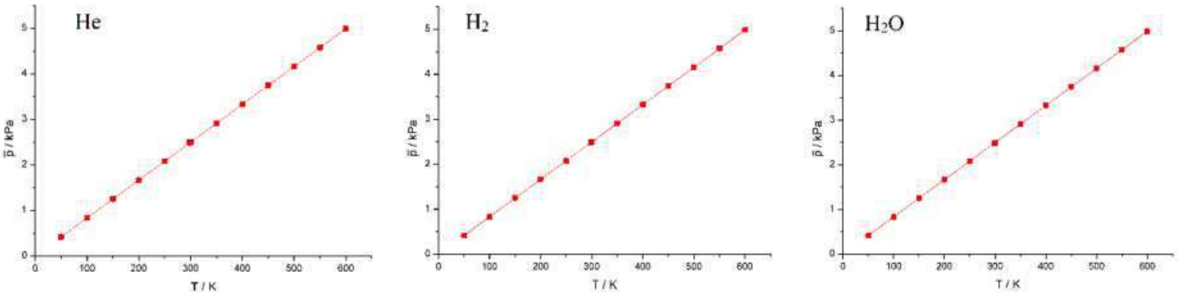

	He			H_2			H_2O		
T / (K)	$\bar{p}_{vdW}$ / (kPa)	$\bar{p}_{eq.21}$ / (kPa)	$\lvert\bar{p}_{vdW} - \bar{p}_{eq.21}\rvert$ / (kPa)	$\bar{p}_{vdW}$ / (kPa)	$\bar{p}_{eq.21}$ / (kPa)	$\lvert\bar{p}_{vdW} - \bar{p}_{eq.21}\rvert$ / (kPa)	$\bar{p}_{vdW}$ / (kPa)	$\bar{p}_{eq.21}$ / (kPa)	$\lvert\bar{p}_{vdW} - \bar{p}_{eq.21}\rvert$ / (kPa)
50.00	0.41571	0.41570	3.843E-06	0.41569	0.41487	8.129E-04	0.41565	0.41562	3.607E-05
100.00	0.83142	0.83141	1.115E-05	0.83140	0.83058	8.182E-04	0.83136	0.83058	3.887E-05
150.00	1.24713	1.24711	1.845E-05	1.24710	1.24628	8.236E-04	1.24707	1.24629	4.168E-05
200.00	1.66284	1.66281	2.575E-05	1.66281	1.66199	8.290E-04	1.66278	1.66200	4.449E-05
250.00	2.07855	2.07851	3.305E-05	2.07852	2.07769	8.343E-04	2.07849	2.07770	4.730E-05
298.15	2.47887	2.47883	4.008E-05	2.47885	2.47801	8.395E-04	2.47882	2.47803	5.001E-05
300.00	2.49426	2.49422	4.035E-05	2.49423	2.49339	8.397E-04	2.49420	2.49341	5.011E-05
350.00	2.90997	2.90992	4.765E-05	2.90994	2.90910	8.450E-04	2.90991	2.90912	5.292E-05
400.00	3.32568	3.32562	5.496E-05	3.32565	3.32480	8.504E-04	3.32562	3.32482	5.573E-05
450.00	3.74139	3.74132	6.226E-05	3.74136	3.74051	8.558E-04	3.74133	3.74053	5.854E-05
500.00	4.15710	4.15703	6.956E-05	4.15707	4.15621	8.611E-04	4.15704	4.15624	6.135E-05
550.00	4.57281	4.57273	7.686E-05	4.57278	4.57192	8.665E-04	4.57275	4.57195	6.416E-05
600.00	4.98852	4.98843	8.416E-05	4.98849	4.98762	8.718E-04	4.98846	4.98765	6.697E-05

References

1. Becke A. D. (1993) Density-functional thermochemistry. III. The role of exact exchange. J. Chem. Phys. 98: 5648-5652.
2. Boys S. B., Bernardi F. (1970) Mol. Phys. 19: 553.
3. Grimme S., Antony J., Ehrlich S., Krieg H. (2010) A consistent and accurate ab initio parameterization of density functional dispersion correction (DFT-D) for the 94 elements H-Pu. J. Chem. Phys. 132, 154104.
4. Grimme S., Ehrlich S., Goerigk L. (2011) Effect of the damping function in dispersion corrected density functional theory. J. Comp. Chem. 32: 1456-1465.
5. Dunning T. H. Jr. (1989) Gaussian basis sets for use in correlated molecular calculations. I. The atoms boron through neon and hydrogen. J. Chem. Phys. 90: 1007-1023.
6. Woon D. E., Dunning T. H. Jr. (1994) Gaussian basis sets for use in correlated molecular calculations. IV. Calculation of static electrical response properties J. Chem. Phys. 100: 2975-2988.
7. Gatti C., Fantucci P., Pacchioni G. (1987) Charge density topological study of bonding in lithium clusters. Theor. Chim. Acta 72: 433−458.
8. Bader R. F. W. (1990) Atoms in molecules. A quantum theory; Oxford University Press: Oxford.
9. Frisch M. J., Trucks G. W., Schlegel H. B., Scuseria G. E., Robb M. A., Cheeseman J. R., Scalmani G., Barone, V., Mennucci B., Petersson G. A., et al. (2009) Gaussian 09; Gaussian, Inc.: Wallingford, CT.
10. AIMPAC download page: http:www.chemistry.mcmaster.ca/aimpac/imagemap/imagemap.htm.
11. Keith T., Bader R. F. W. (1993) Calculation of magnetic response properties using a continuous set of gauge transformations. Chem. Phys. Lett. 210: 223−231.

When Does a Hydrogen Bond Become a van der Waals Interaction? A Topological Answer

Christian Tantardini*

The hydrogen bond (H-bond) is among the most important noncovalent interaction (NCI) for bioorganic compounds. However, no "energy border" has yet been identified to distinguish it from van der Waals (vdW) interaction. Thus, classifying NCIs and interpreting their physical and chemical importance remain open to great subjectivity. In this work, the "energy border" between vdW and H-bonding interactions was identified using a dimer of water, as well as for a series of classical and nonclassical H-bonding systems. Through means of the quantum theory of atoms in molecules and in particular the source function, it was possible to clearly identify the transition from H-bonding to vdW bonding via analysis of the electronic structure. This "energy border" was identified both on elongating the interatomic interaction and by varying the contact angle. Hence, this study also redefines the "critic angle" previously proposed by Galvão et al. (J. Phys. Chem. A 2013, 117, 12668). Consequently, such "energy border" through an analysis of atomic basins volume variation was possible to identify the end of *long-range* interactions. © 2019 Wiley Periodicals, Inc.

DOI:10.1002/jcc.25774

Introduction

The hydrogen bond (H-bond) is of fundamental importance in nature, with particular importance for bioorganic compounds. Despite its importance, the H-bond is not rigorously defined by International Union of Pure and Applied Chemistry, stating simply that "the H-bond is an attractive interaction between a hydrogen atom from a molecule or a molecular fragment X–H in which X is more electronegative than H, and an atom or a group of atoms in the same or a different molecule, in which there is evidence of bond formation."[1] This definition does not necessarily differentiate between H-bonds and the weaker van der Waals (vdW) interaction. Experimentally, the border between them should be only represented by a sufficient stretching of X—H···Y.[2] Actually, the experimental techniques are still working to discriminate between blurry H-bond and vdW interaction. Thus, this ambiguity is an important hole in our current understanding of noncovalent interactions (NCIs). Current literature generally defines H-bonding based on geometric parameters.[3] The research of an efficient way to distinguish between H-bond and vdW is actually of high biological interest that should be investigated by a theoretical approach to get a solution that cannot be obtained experimentally.

The study of chemical bonding via analysis of charge density is now well established within the quantum theory of atoms in molecules (QTAIM).[4,5] Within this theory, the existence of a bond is accompanied with a bond critical point (BCP) defined by label (3, −1): 3 corresponds to the number of eigenvalues of the Hessian of charge density; −1 corresponds to the sum of these eigenvalues.[5] If a BCP is located between two atoms, it is generally accepted that a chemical bond is present between them. However, a BCP is not always present when weak H-bonds are present. Using 1,2-ethanediol as a model system, Lane et al.[6] showed the presence of a blurry intramolecular H-bond, despite the absence of a BCP located between hydrogen (*H*) and acceptor (*A*) atoms. Although such cases exist, the overwhelming majority of H-bonds contain a BCP along the bond path, and the strength of the H-bond can be evaluated based on the contributions of the atoms to the BCP charge density.[7] The atomic contribution to charge density at the BCP as in any other points of the space can be successfully calculated through the topological tool based on QTAIM, the source function (SF).[7–16]

In this work, we aim to identify the transition point between H-bond and vdW interactions. The investigation is focused on bond strength variation as a function of $A\cdots D$ distance ($R_{A\cdots D}$) and $\theta(D-H\cdots A)$ angle within a model systems for classical[7] and nonclassical[17,18] H-bonds characterized by the presence of $A\cdots H$ BCP. The estimation of bond strength will be evaluated by means of the SF.[7] Furthermore, evaluation of atomic basin volume variation will be considered to define the end of long-range interaction in both types of H-bonds.

Theoretical Background

Bader and Gatti[8] showed that in a closed system, the contribution from an atomic basin (Ω) to the charge density, ρ, in a point **r** of the space is due to the integral of Laplacian of charge density, $\nabla^2\rho$, weighted as a function of its distance from the point of interest **r**. This integral is over all points inside Ω, termed $\mathbf{r}'$, each with a respective weighting factor $|\mathbf{r}-\mathbf{r}'|^{-1}$.

$$\rho(\mathbf{r}) = -\frac{1}{4\pi}\int_{\Omega} d\mathbf{r}'\frac{\nabla^2\rho(\mathbf{r}')}{|\mathbf{r}-\mathbf{r}'|} = -\frac{1}{4\pi}\sum_{\Omega}\int_{\Omega} d\mathbf{r}' LS(\mathbf{r},\mathbf{r}') \equiv \sum_{\Omega} SF(\mathbf{r},\Omega) \tag{1}$$

Within QTAIM, the surface that bounds Ω is called the zero flux surface.[5] This surface S is defined by all points in a space,

C. Tantardini
Center for Electrochemical Energy Storage, SkolTech Skolkovo Institute of Science and Technology, ul. Nobelya 3, Moscow 143026, Russian Federation
E-mail: christiantantardini@ymail.com
© 2018 Wiley Periodicals, Inc.

$\mathbf{r}_S$, for which the product of the gradient of charge density, $\nabla\rho$, and the normal vector, $\hat{\mathbf{n}}$, is zero:

$$\nabla\rho(\mathbf{r})\cdot\hat{\mathbf{n}}(\mathbf{r})=0,\ \forall\mathbf{r}\in S(\mathbf{r}_S) \tag{2}$$

It is worth noting that the Laplacian of charge density is correlated to the local electronic energy through the local virial theorem, offering a useful definition of the local source,

$$\mathrm{LS}(\mathbf{r},\mathbf{r}')=\frac{4m}{\hbar^2}\frac{2G(\mathbf{r})+V(\mathbf{r})}{|\mathbf{r}-\mathbf{r}'|} \tag{3}$$

where $G(\mathbf{r})$ corresponds to the kinetic energy with positive contribute, $V(\mathbf{r})$ corresponds to potential energy with negative contribute, and m is the mass of an electron. LS($\mathbf{r}$, $\mathbf{r}'$) can be interpreted as the local contribution of $\mathbf{r}'$ to $\mathbf{r}$. When $\nabla^2\rho(\mathbf{r}') > 0$, then LS($\mathbf{r}$, $\mathbf{r}'$) < 0 and $\mathbf{r}'$ is a "sink" (depleting the charge density at $\mathbf{r}$); when $\nabla^2\rho(\mathbf{r}') < 0$, then LS($\mathbf{r}$, $\mathbf{r}'$) > 0 and $\mathbf{r}'$ is a "source" (enriching the charge density at $\mathbf{r}$).[7–16]

Computational Details

The dimer of water molecules was constructed to have point group C_s. This dimer was fully optimized in vacuo using MP2/6-31G(d,p).[19–24] PROAIM[25] wavefunction and complexation energy (E_C) were calculated at the optimized geometry using couple cluster single and double substitutions,[26–29] CCSD, and basis set aug-cc-pVTZ.[30] The correction of basis set superposition error associated at the E_C was done through counterpoise method.[31] At the same level of theory, a PROAIM[25] wavefunction was performed along a series of $R_{A\ldots D}$ distances 3.00, 3.25, 3.50, 3.75, 4.00, 4.25, 4.50, 4.75, 5.00, 6.00, 7.00, 8.00, 9.00, and 10.00 Å, and the angle $\theta(D-H\cdots A)$ was varied 160°, 150°, 140°, 130°, 120°, 110°, 100°, and 90°, maintaining fixed $R_{A\ldots H}$ at 2.026 Å.

The dimers made by a molecule of water with ethane ($CH_3\cdots OH_2$), ethene ($CH_2\cdots OH_2$), and ethyne ($CH\cdots OH_2$) molecules in a geometrical arrangement characterized by C—H···O long interaction and dimers of water with ammonia ($HOH\cdots NH_3$) and methylenimine ($NH\cdots OH_2$) molecules in a geometrical arrangement characterized, respectively, by O—H···N and N—H···O long interactions were fully optimized using MP2/6-31G (d,p).[19–24]

A PROAIM[25] wavefunction was performed using CCSD/aug-cc-pVTZ[26–30] at the equilibrium and elongated $R_{A\ldots D}$ distances for $CH_3\cdots OH_2$ (4.00, 4.25, 4.50, 4.75, 5.00, 6.00, 7.00, 8.00, 9.00, and 10.00 Å), $CH_2\cdots OH_2$ (3.75, 4.00, 4.25, 4.50, 4.75, 5.00, 6.00, 7.00, 8.00, 9.00, and 10.00 Å), $CH\ldots OH_2$ (3.50, 3.75, 4.00, 4.25, 4.50, 4.75, 5.00, 6.00, 7.00, 8.00, 9.00, and 10.00 Å), $HOH\cdots NH_3$ (3.00, 3.25, 3.50, 3.75, 4.00, 4.25, 4.50, 4.75, 5.00, 6.00, 7.00, 8.00, 9.00, and 10.00 Å), and $NH\cdots OH_2$ (3.25, 3.50, 3.75, 4.00, 4.25, 4.50, 4.75, 5.00, 6.00, 7.00, 8.00, 9.00, 10.00 Å).

The restricted all-electron PROAIM[25] wavefunctions were generated in Gaussian v09 (revision D.01).[32] Location of BCPs and subsequent calculation of SF[7] values were performed using a modified version of the PROAIMV program.[33,34] The SF values quoted in this article are provided in terms of SF%, which offers a more direct numerical comparison.[7] This value is defined as[7]

$$SF(\mathbf{r}_{BCP},\Omega\%)=\frac{SF(\mathbf{r}_{BCP},\Omega)}{\rho(\mathbf{r}_{BCP})}\times 100 \tag{4}$$

where $\mathbf{r}_{BCP}$ is the vector position of BCP being investigated.

The mean error for basin integration calculation using CCSD wavefunction at each geometry was maintained ≤10^{-4}. Furthermore, the final virial ratio of CCSD wavefunction at each geometry is given in E.S.I.1,2,4-9.

Results and Discussion

The water molecules within the linear C_S dimer represents an ideal example of intermolecular H-bonding with a $A\ldots H$ BCP. This therefore offers an excellent system to begin discussion. The $A\cdots H$ BCP was first analyzed based the optimized structure, by varying $R_{A\ldots D}$ and angle $\theta(D-H\cdots A)$. To identify the "energy border" along $R_{A\cdots D}$, the bond distance was elongated to the noninteracting limit, with a BCP being located at each distance. The SF was then used to analyze the BCP composition:

$$SF\%(AHD)=SF\%(A)+SF\%(H)+SF\%(D) \tag{5}$$

The value of SF%(*AHD*) is used to describe the strength of H-bond according to Gatti and coworkers.[7,35–37] A similar procedure was subsequently performed for the $\theta(D-H\cdots A)$ bond angle.

An increase of $R_{A\cdots D}$ in the C_S water dimer is associated with a reduction of charge density at the $A\cdots H$ BCP (ρ_{BCP}), trending to zero as $R_{A\cdots D}\rightarrow 10.00$ Å. Ultimately, the BCP is lost at this limit and is taken to be indicative of the noninteracting limit of this bond.[5] As $R_{A\cdots D}$ is elongated, SF%(*AHD*) decreases and becomes negative (Fig. 1 and Supporting Information Table S1). SF%(*AHD*) changes from 1.26% to −51.73% between 3.50 and 3.75 Å $R_{A\cdots D}$ with ρ_{BCP} changing from 0.006 to 0.004 e/Bohr^3 (see Supporting Information Table S1).

To be sure that the SF changing from positive to negative values does not intrinsically depend by the internuclear distance, but is characteristic of passage from H-bond to VdW, a *gedanken-experiment* was performed on a F_2 gas phase molecule. BCP was again generated along the F···F internuclear axis as the bond was elongated to a limit of 10 Å. The SF was again calculated at each case. However, despite loss of the BCP at the noninteracting limit, the sign of SF%(FF) did not change (see results and computational details for F_2 in Supporting Information Table S2). F_2 was chosen because it is characterized by strong correlation effects which influence the charge density and also taking into account them there is no change in the SF sign.

Thus, such changing in the sign of SF%(*AHD*) can be reasonably associated to the passage from H-bond to vdW interaction. So, a transition between these two interactions appears possible based on the values of SF%(*AHD*). The currently performed topological analysis allowed to overcome the problem associated to the impossibility to predict an "energy border" through consideration of complexation energy (E_C), which simply decreases as $R_{A\cdots D}$ increases (see Supporting Information Table S1).

Moreover, to better explain the causes of SF%(*AHD*) changing from positive to negative, the SF contribution of each atomic basin is considered. In Figure 1, the value of SF%(*A*) remains

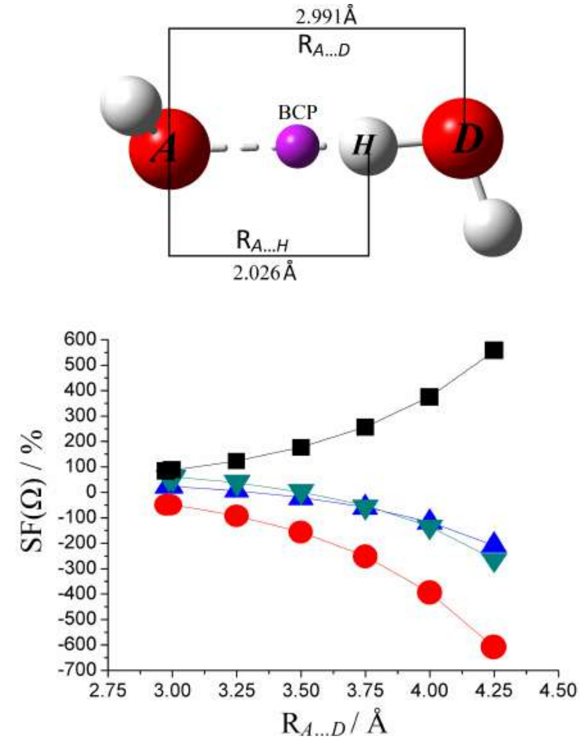

Figure 1. (Top) C_S dimer of water at the equilibrium with $\theta(D - H \ldots A)$ angle equal to 175.99°. Distance is defined between A and D ($R_{A\ldots D}$) and between A and H ($R_{A\ldots H}$). Atoms are colored as H, white, and O, red. BCPs are indicated in violet. (Bottom) Atomic basin SF percentage contributions (SF(Ω)%) at the $A\ldots H$ BCP of linear C_s water dimer at varying values of $R_{A\ldots D}$. SF%(D), black; SF%(A), blue; SF%(H), red; SF%(AHD) water, green.[a]

[a] H, D, and A are, respectively, the hydrogen atom directly involved in the H-bond, the H-donor, and the H-acceptor oxygen atoms. [Color figure can be viewed at wileyonlinelibrary.com]

positive for all internuclear distances within the H-bond regime and becomes negative as the bond is elongated further. This change in the sign of SF% can be associated with the local contribution [eq. (3)] of each atom to the $A\cdots H$ BCP. Hence, at equilibrium, we find SF%(A) and SF%(D) > 0, which act like "source" providing ρ to the $A\cdots H$ BCP, which compensates the depleting of ρ from $A\cdots H$ BCP because of the "sink" effect of SF %(H) < 0. Subsequently, as the $R_{A\cdots D}$ increases, A changes its "source" into "sink" effect passing from SF%(A) > 0 to SF% (A) < 0. When the (negative) contributions of SF%(A) and SF% (H) become larger than the (positive) contribution of SF%(D), there is the passage from H-bond to vdW interaction (see Fig. 1). While SF%(D) is seen to maintain its "source" effect into $A\cdots H$ BCP at the $R_{A\cdots D}$ increasing (see Fig. 1 and Supporting Information Table S1).

The change of A local contribution can be the cause of change of SF%(AHD) from positive to negative, and it can be explained by increase in $R_{A\ldots D}$, as to a certain distance (SF% (A) < 0), A will not be able to share its charge density along the $A\cdots H$ bond path making an H-bond, but it will be attracted with more strength to A nucleus, generating at the same time an electrostatic perturbation in the $A\cdots H$ BCP due to contraposed effects of A (*sink*) and B (*source*) in that point. Such electrostatic perturbation is so accountable for vdW interactions and will decrease up to the end with the increase of $R_{A\cdots D}$.

It is worth noting that SF% values are very large in magnitude, and occasionally exceed 100 (Supporting Information Table S1). The presence of SF% > 100 arises because of the inaccuracies in the reconstruction of ρ, especially for points in which $\rho < 10^{-3}$ e/Bohr^3. The same difficulties were previously identified for the reconstruction of spin density(s) by spin density SF (SDSF).[38] These difficulties were shown to be generated by two factors: (1) a low s, which is close to change its sign from positive to negative; and (2) a low number of points of radial numerical integration within core, because their s has undergone fast variation with major difficulties in its fitting.[38] In common, s and ρ as shown in eq. (1) are rebuilt from their respectively Laplacian, for which for values in the order of 10^{-3} e/Bohr^5 or lesser, the sign is uncertain with an impact on the calculation, respectively, of SDSF[38] and SF.[10]

Thus, an increase in the number of integration points cannot solve the above problem. As such, the calculation of SF can only be interpreted qualitatively at points with $\rho < 10^{-3}$ e/Bohr^3. Importantly, this does not affect the validity of SF in general but does restrict from quantitative to qualitative interpretation of the SF value for interactions composed of low density, including weak H-bond and vdW interactions.[10]

As $R_{A\cdots D}$ increases beyond the H-bond/vdW border, there will be the end of vdW interactions between H and A, or simply the end of *long-range* interactions. Thus, to find such limit, one can consider the variation in volume of the atomic basin, $V(\Omega)$. In the present case, we consider $V(A)$ and $V(H)$. These values are both found to reach a maximum at $R_{A\cdots D} \approx 4.00$ Å, and subsequently decrease to a plateau (Fig. 2 and Supporting Information Table S1).

This initial increase in V results from the continued existence of long-range interactions, and thus distortion of their "ideal" electronic distribution. However, as the strength of the interaction decreases, the perturbation does as well and leads to restoration of the ideal distribution (plateau); thus, the noninteraction regime can be identified in this way.

Thus, for this reason, the initial value of plateau can be associated to the limit of long interactions between H and A Ωs, which in the specific case for C_S dimer of water is registered to 4.50 Å $R_{A\cdots D}$.

Having studied the NCI boarder between H-bond and vdW upon elongation of $R_{A\cdots D}$, it was worth considering the second geometric parameter typically used to define H-bonds: angle $\theta(D - H\cdots A)$, see Supporting Information Figure S3. As already showed by Galvão et al.,[39] closing $\theta(D - H\cdots A)$ to a certain degree, $A\cdots H$ BCP shifts from the straight line between A and H going close to the straight line between A and D. This is due to the strongest interaction between the electronic clouds of more electronegative A and D with respect to direct interaction between A and H when A and D are at sufficient distance. Galvão et al.[39] seen this shifting angle degree $\theta(D - H\cdots A)$ of 120.00 and associated it to the end of H-bond interaction calling it: "critical angle."[39]

As done for $R_{A\cdots D}$, the BCP was identified as a function of $\theta(D - H\cdots A)$ for the C_S water dimer. At θ=130°, that is, 10° larger than defined by Galvão et al.[39] was found the shifting of $A\cdots H$ BCP from straight line between A and H. Thus, within the definition of H-bonding presented in this work, this "critical

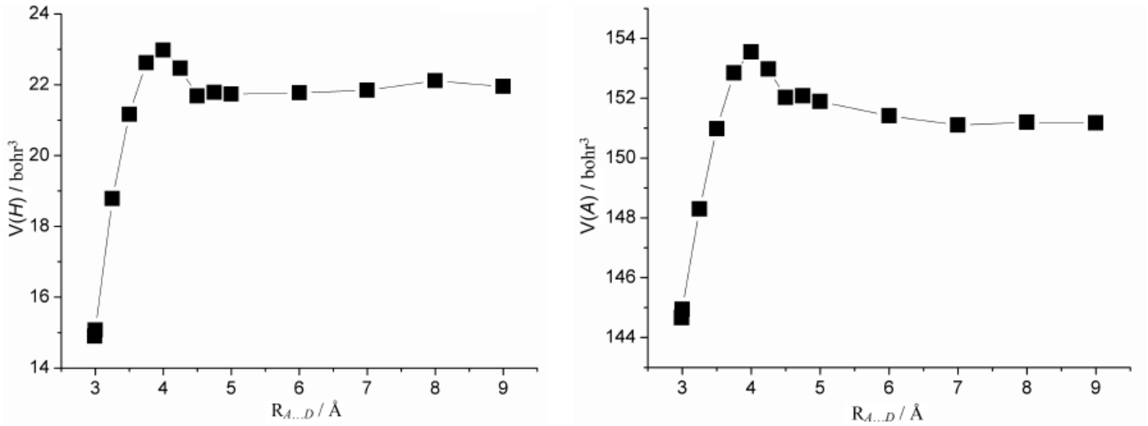

Figure 2. Volume of atomic basin, $V(\Omega)$, of linear C_s water dimer constrained from the equilibrium (2.991 Å) to 9.000 Å of *A*...*D* distance ($R_{A...D}$).[a]
[a]*H* and *A* are, respectively, the hydrogen atom directly involved in the H-bond and the H-acceptor oxygen atom.

angle” develops a new definition. Hence, to define the “critical angle,” it seems more appropriate to evaluate SF%(*AHD*) and the E_C between two dimers. SF%(*AHD*) was found to decreases as $\theta(D - H\cdots A)$ decreased, reaching a minimum of 61.18% at $\theta = 120^o$. Interestingly, SF%(*AHD*) increased as θ was compressed further, reacting 70.37% by $\theta = 90^o$ (Fig. 3 and Supporting Information Table S4). The minimum can be defined as a “critical angle.” Importantly, this technique is applicable to any general system, for which a system-dependent critical angle can be expected. Furthermore, for $\theta > 120^o$, E_C is attractive (i.e., negative), while for $90^o < \theta < 120^o$, E_C is repulsive (i.e., positive), see Supporting Information Table S4. It is not possible to define a “critical angle” like the “energy border” previously defined, because there is not a passage from H-bond to vdW interaction but a passage from H-bond to steric repulsion.

Two additional examples of classical H-bonds were tested: $HOH\cdots NH_3$ and $HOH\cdots NH_3$. These systems contain O—H···N and N—H···O bonds, respectively. For both systems, SF%(*D*) and SF%(*A*) increase with increasing $R_{A\cdots D}$[1]; thus, we see the same behavior independent of the type of atom: SF%(*D*) > 0, and increases with R, with SF%*(A)* changing from positive to negative at some critical value of $R_{A\cdots D}$ (Fig. 4 and Supporting Information Tables S5 and S6). Furthermore, for both systems, SF%(*AHD*) changes in sign (from 19.62% to −19.72% for $HOH\cdots NH_3$; from 25.21% to −11.85% for $NH\cdots OH_2$) between 3.25 and 3.50 Å showing the “energy border” in the same place found for the C_S water dimer. The values of $V(\Omega)$ were again monitored as a function of $R_{A\cdots D}$, with $V(\Omega)_{\text{plateau}}$ corresponding to the end of long-range interactions occurring at 5.00 and 4.75 Å for $HOH\cdots NH_3$ and $NH\cdots OH_2$, respectively (Supporting Information Tables S5 and S6). Thus, this method of interpreting H-bonding appears general for classical H-bonding systems.

To investigate its generality further, nonclassical H-bonds were subsequently investigated. For this study, a dimer was constructed between water and one of ethane ($CH_3\cdots OH_2$), ethene ($CH_2\cdots OH_2$), and ethyne ($CH\cdots OH_2$). In the first instance, this analysis was performed simply to confirm or refute the potential presence of H-bonds in these systems. The loss of saturation for C—C bond is associated with the increase of NCI strength as shown by SF%(*AHD*): vdW interaction for $CH_3\cdots OH_2$ (i.e., −133.86%) and $CH_2\cdots OH_2$ (i.e., −57.94%) and H-bond for $CH\cdots OH_2$ (i.e., 12.32%) (see Fig. 5 and Supporting Information Tables S5 and S6). The presence of *H* between two more electronegative atoms (*A*, *D*) is not sufficient to guarantee the presence of a H-bond, and $CH_3\cdots OH_2$ and $CH_2\cdots OH_2$ are such example. Thus, we stress the inadequacy of defining H-bond simply on geometrical criteria as those provided by Arunan et al.[1]

It is noteworthy that during the $R_{A\cdots D}$ compression for both $CH_3\cdots OH_2$ and $CH_2\cdots OH_2$, SF%(*AHD*) is seen to change from negative (i.e., equilibrium) to positive (i.e., $R_{A\cdots D} = 3.25$ Å) passing from vdW to H-bond (Fig. 1). Going forward with compression for both dimers at $R_{A\cdots D} = 2.75$ Å, SF%(*H*) passes from negative to positive corresponding to change from “sink” into “source” *H* effect (Fig. 1; see Supporting Information Tables S7 and S8). The squeezing of $R_{A\cdots D}$ under equilibrium distance was

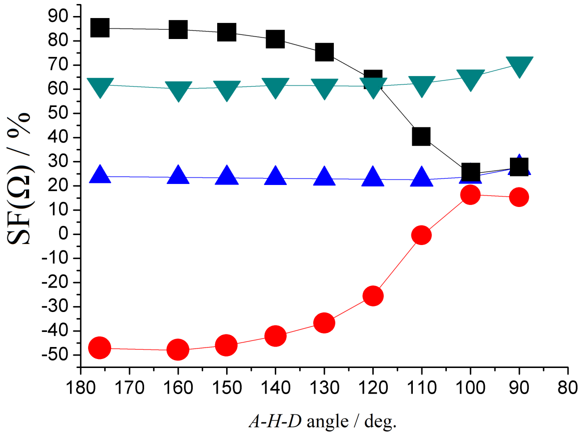

Figure 3. Atomic basin SF percentage contributions (SF(Ω)%) at the *A*...*H* BCP of linear C_s water dimer constrained from $D{-}\hat{H}\cdots A$ equilibrium (175.99°) to 90.00°. Legend: SF%(*D*), black; SF%(*A*), blue; SF%(*H*), red; SF%(*AHD*) water, green.[a]
[a]*H*, *D*, and *A* are, respectively, the hydrogen atom directly involved in the H-bond, the H-donor, and the H-acceptor oxygen atoms. [Color figure can be viewed at wileyonlinelibrary.com]

---

[1] *The SF values were calculated till the disappearance of* A...H *BCP due to the* $R_{A...D}$ *elongation.*

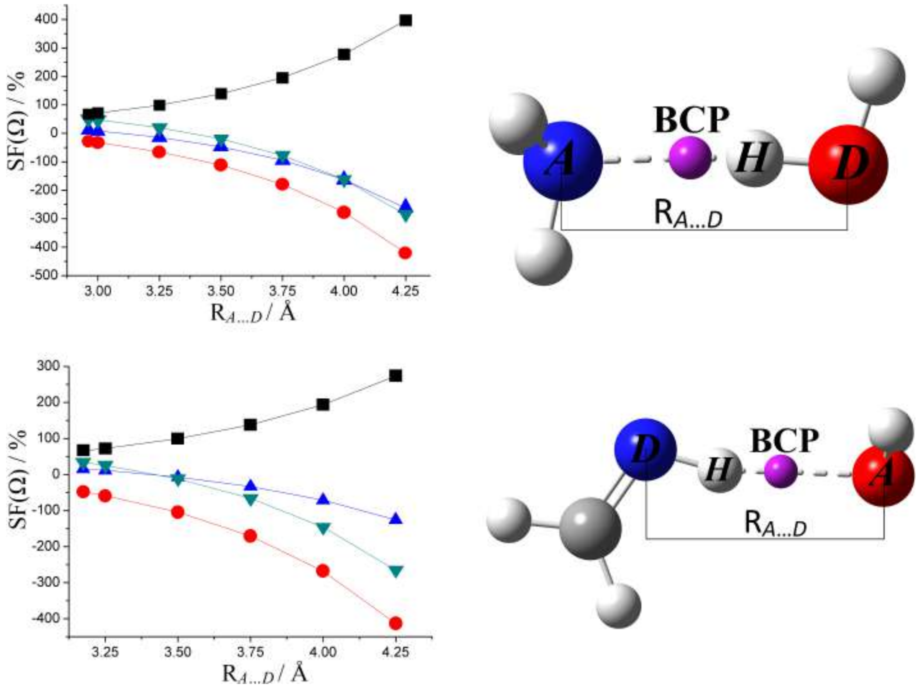

Figure 4. Atomic basin SF percentage contributions (SF(*Ω*)%) at the *A*…*H* BCP of dimers of water paired, respectively, with (top) ammonia (HOH…NH_3) from the equilibrium (2.961 Å) to 4.250 Å *A*…*D* distance ($R_{A\ldots D}$), (bottom) methylenimine (NH…OH_2) from the equilibrium (3.174 Å) to 4.250 Å $R_{A\ldots D}$. Legend of graph: SF%(*D*), black; SF%(*A*), blue; SF%(*H*), red; SF%(*AHD*) water, green.[a] Atoms are colored as H, white; O, red; and N, blue. BCPs are indicated in violet.

[a] *H*, *D*, and *A* are, respectively, the hydrogen atom directly involved in the H-bond, the H-donor oxygen atom for HOH…NH_3 (nitrogen for HOH…NH_3), and the H-acceptor nitrogen for HOH…NH_3 (oxygen for HOH…NH_3). [Color figure can be viewed at wileyonlinelibrary.com]

already tested by Gatti et al.[7] for different intramolecular and intermolecular H-bonds showing the same behavior seen here. Gatti et al.[7] also compared the theoretical $\nabla^2\rho$ evaluated at the $A\cdots H$ BCP with those obtained by experimental charge densities confirming the validity of SF to describe such H-bonds. But at that time, he was not aware of the subsequent works done by Lane et al.[6] and Galvão et al.,[39] which described the failure of Bader's theory associated to research of $A\cdots H$ BCP in intramolecular H-bonds, but equally valid for such systems in term of reduced density gradient.[40–43] Thus, he could not postulate what we can do now about the SF%(*H*) changing for short $R_{A\cdots D}$ into intermolecular H-bonds: the changing of *H* effect from "sink" (SF%(*H*) < 0) to "source" (SF% (*H*) > 0) is the end of H-bond due to the failing of necessary

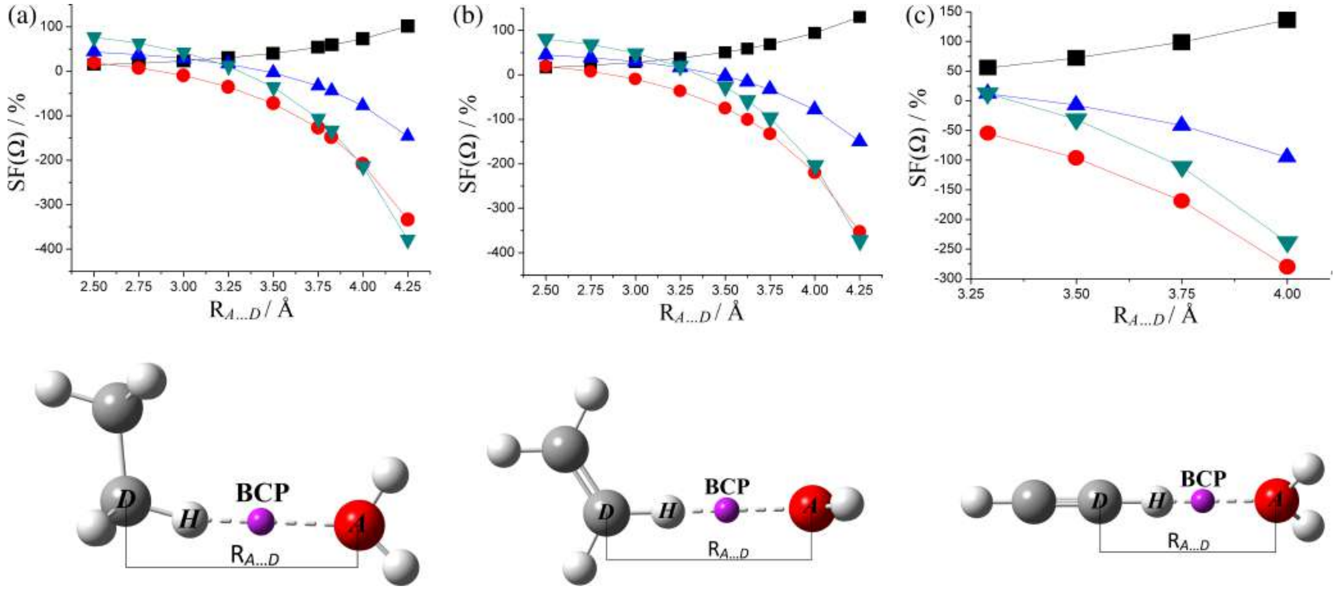

Figure 5. Atomic basin SF percentage contributions (SF(*Ω*)%) at the *A*…*H* BCP of dimers of water paired respectively with a) ethane (CH_3…OH_2) from 2.500 Å (equilibrium equal to 3.826 Å) to 4.250 Å of *A*…*D* distance ($R_{A\ldots D}$), b) ethene (CH_2…OH_2) from 2.500 Å (equilibrium equal to 3.624 Å) to 4.250 Å of *A*…*D* distance ($R_{A\ldots D}$), and c) ethyne (CH…OH_2) from the equilibrium (3.624 Å) to 4.250 Å of *A*…*D* distance ($R_{A\ldots D}$). Legend: SF%(*D*), black; SF%(*A*), blue; SF%(*H*), red; SF%(*AHD*) water, green.[a] Atoms are colored as H, white; O, red; and C, gray. BCPs are indicated in violet.

[a] *H*, *D*, and *A* are, respectively, the hydrogen atom directly involved in the H-bond, the H-donor carbon atom, and the H-acceptor oxygen atom. [Color figure can be viewed at wileyonlinelibrary.com]

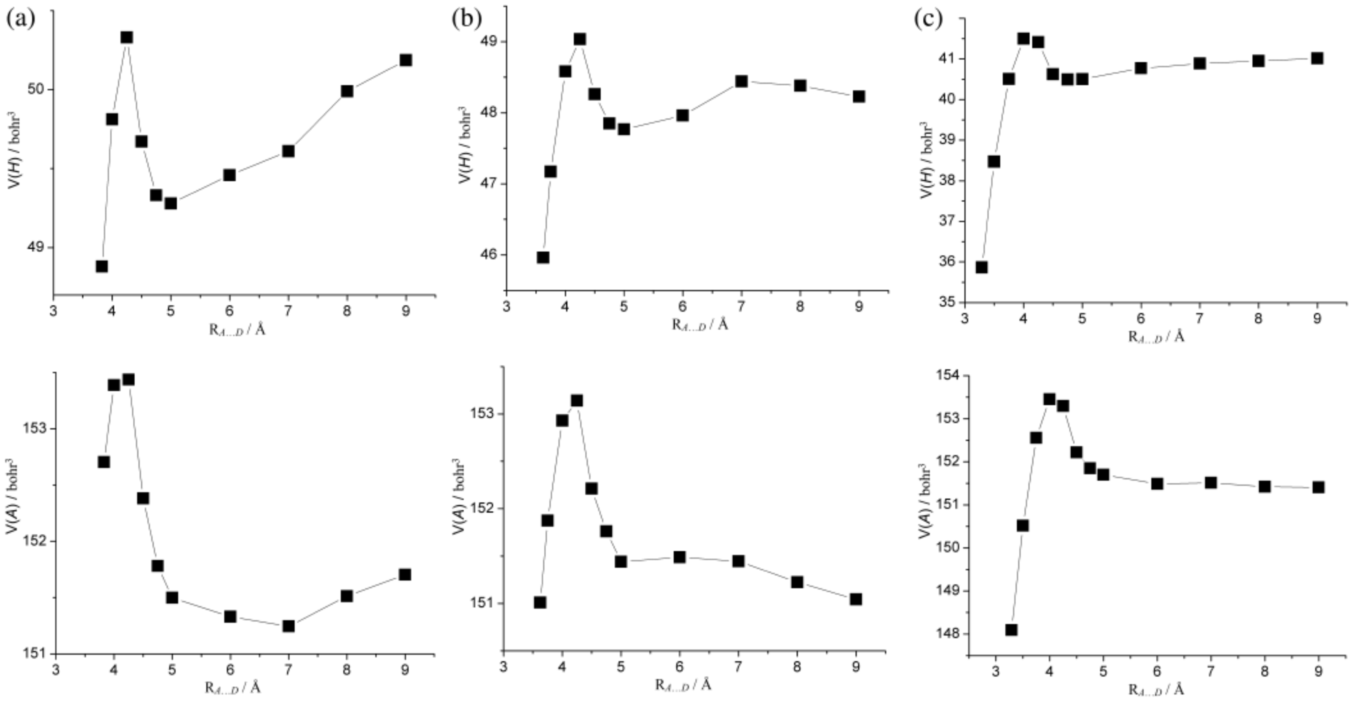

Figure 6. (Top) *V*(*H*) and (down) *V*(*A*) calculated for dimers of water paired respectively with a) ethane ($CH_3...OH_2$) from the equilibrium (3.826 Å) to 9.000 Å of *A*…*D* distance ($R_{A...D}$), b) ethene ($CH_2...OH_2$) from the equilibrium (3.624 Å) to 9.000 Å of *A*…*D* distance ($R_{A...D}$), and c) ethyne ($CH...OH_2$) from the equilibrium (3.624 Å) to 9.000 Å of *A*…*D* distance ($R_{A...D}$).[a]
[a] *H* and *A* are, respectively, the hydrogen atom directly involved in the H-bond and the H-acceptor oxygen atom.

condition consisting into hydrogen atom, which attracts on itself charge density from two closest more electronegative atoms.

The H-bonding boarder in $CH\cdots OH_2$ was found at ca. $R_{A\cdots D}$ = 3.50 Å, identified as SF%(*AHD*) changed from 11.99% to −31.42%, that is, from positive to negative. The noninteracting limit observed in the nonclassical H-bonds exhibited the same behavior as for the classical examples corresponding to V(*A*) and V(*H*) plateau. This limit was identified in $CH\cdots OH_2$ at ca. $R_{A\cdots D}$ = 4.75 Å and in both $CH_2\cdots OH_2$ and $CH_3\cdots OH_2$ at ca. $R_{A\cdots D}$ = 5.00 Å (Fig. 6 and Supporting Information Tables S7–S9).

Thus, it appears that for both classical and nonclassical H-bond systems, the SF is able to determine and reveal the consequences of chemical transferability,[4,5,43–46] confirming again to be a robustness descriptor.

Conclusions

The model systems for classical and nonclassical H-bonds gave results, which can be generalized for the other systems: (1) the "energy border" is fixed to null value of SF%(*AHD*) at the $A\cdots H$ BCP; (2) vdW interaction is characterized by negative value of SF%(*AHD*) at the $A\cdots H$ BCP and the weakness of vdW increases with the magnitude of SF%(*AHD*); (3) a "critical angle" must be defined not simply through geometric criteria proposed by Galvão et al.,[39] but looking for the effective interactions to $A\cdots H$ BCP through SF%(*AHD*) in that critical point or looking for the E_C changing from negative to positive; and (4) the limit of long-range interactions can be found through an analysis of atomic basins volume variation for both *A* and *H* *Ωs* looking for its first value of plateau respect to $R_{A\cdots D}$ increasing.

Acknowledgment

The author would like to thank Dr. Davide Ceresoli for technical assistance with Gaussian calculations and his supervisor Prof. Artem R. Oganov for his ongoing support.

Keywords: H-bond · Van der Waals · quantum theory atoms in molecule · source function

How to cite this article: C. Tantardini. *J. Comput. Chem.* **2019**, *40*, 937–943. DOI: 10.1002/jcc.25774

Additional Supporting Information may be found in the online version of this article.

[1] E. Arunan, G. R. Desiraju, R. A. Klein, J. Sadlej, S. Scheiner, I. Alkorta, D. C. Clary, R. H. Crabtree, J. J. Dannenberg, P. Hobza, H. G. Kjaergaard, A. C. Legon, B. Mennucci, D. J. Nesbitt, *Pure Appl. Chem.* **2011**, *83*, 1637.
[2] R. Parthasarathi, V. Subramanian, N. Sathyamurthy, *J. Phys. Chem. A* **2006**, *110*, 3349.
[3] G. A. Jeffrey, An Introduction to Hydrogen Bonding, Oxford University Press, New York, **1997**.
[4] R. F. W. Bader, H. J. Essen, *J. Chem. Phys.* **1984**, *80*, 1943.
[5] R. F. W. Bader, Atoms in Molecules. A Quantum Theory, Oxford University Press, Oxford, **1990**.
[6] J. R. Lane, J. Contreras-Garcia, J.-P. Piquemal, B. J. Miller, H. G. Kjaergaard, *J. Chem. Theory Comput.* **2013**, *9*, 3263.
[7] C. Gatti, F. Cragnoni, L. Bertini, *J Comput. Chem* **2003**, *24*, 422.
[8] R. F. W. Bader, C. Gatti, *Chem. Phys. Lett.* **1998**, *287*, 233.

[9] C. Gatti, Electron Density and Chemical Bonding II. Structure and Bonding Series, Vol. *147*, Springer, Berlin, Germany, **2012**, p. 193.

[10] C. Gatti, D. Lasi, *Faraday Discuss.* **2007**, *135*, 55.

[11] C. Gatti, *Phys. Scr.* **2013**, *87*, 048102.

[12] E. Monza, C. Gatti, L. Lo Presti, E. Ortoleva, *J. Phys. Chem. A* **2011**, *115*, 12864.

[13] C. Gatti, A. M. Orlando, E. Monza, L. Lo Presti, Applications of Topological Methods in Molecular Chemistry. Springer Series Challenges and Advances in Computational Chemistry and Physics, Vol. *22*, Springer, New York, **2016**, p. 101.

[14] J. Hey, D. Leusser, D. Kratzert, H. Fliegl, J. M. Dieterich, R. A. Mata, D. Stalke, *Phys. Chem. Chem. Phys.* **2013**, *15*, 20600.

[15] C. Gatti, G. Saleh, L. Lo Presti, *Acta Crystallogr. Sect. B: Struct. Sci. Cryst. Eng. Mater.* **2016**, *B72*, 180.

[16] C. Tantardini, E. V. Boldyreva, E. Benassi, *J. Phys. Chem. A* **2016**, *120*, 10289.

[17] C. Gatti, E. May, R. Destro, F. Cragnoni, *J. Phys. Chem. A* **2002**, *105*, 2707.

[18] S. Scheiner, S. J. Grabowski, T. Kar, *J. Phys. Chem. A* **2001**, *105*, 10607.

[19] M. J. Frisch, M. Head-Gordon, J. A. Pople, *Chem. Phys. Lett.* **1990**, *166*, 275.

[20] M. J. Frisch, M. Head-Gordon, J. A. Pople, *Chem. Phys. Lett.* **1990**, *166*, 281.

[21] M. Head-Gordon, J. A. Pople, M. J. Frisch, *Chem. Phys. Lett.* **1988**, *153*, 503.

[22] M. Head-Gordon, T. Head-Gordon, *Chem. Phys. Lett.* **1994**, *220*, 122.

[23] S. Saebø, J. Almlöf, *Chem. Phys. Lett.* **1989**, *154*, 83.

[24] P. C. Hariharan, J. A. Pople, *Theoret. Chim. Acta* **1973**, *28*, 213.

[25] C. Gatti, P. Fantucci, G. Pacchioni, *Theor. Chim. Acta* **1987**, *72*, 433.

[26] J. Cížek, In Advances in Chemical Physics, Vol. *14*; P. C. Hariharan, Ed., Wiley Interscience, New York, **1969**, p. 35.

[27] G. D. III Purvis, R. J. Bartlett, *J. Chem. Phys.* **1982**, *76*, 1910.

[28] G. E. Scuseria, C. L. Janssen, H. F. Schaefer, III., *J. Chem. Phys.* **1988**, *89*, 7382.

[29] G. E. Scuseria, H. F. Schaefer, III., *J. Chem. Phys.* **1989**, *90*, 3700.

[30] T. H. Dunning, Jr., *J. Chem. Phys.* **1989**, *90*, 1007.

[31] S. B. Boys, F. Bernardi, *Mol. Phys.* **1970**, *19*, 553.

[32] M. J. Frisch, G. W. Trucks, H. B. Schlegel, G. E. Scuseria, M. A. Robb, J. R. Cheeseman, G. Scalmani, V. Barone, B. Mennucci, G. A. Petersson, H. Nakatsuji, M. Caricato, X. Li, H. P. Hratchian, A. F. Izmaylov, J. Bloino, G. Zheng, J. L. Sonnenberg, M. Hada, M. Ehara, K. Toyota, R. Fukuda, J. Hasegawa, M. Ishida, T. Nakajima, Y. Honda, O. Kitao, H. Nakai, T. Vreven, J. A. Montgomery, Jr., J. E. Peralta, F. Ogliaro, M. Bearpark, J. J. Heyd, E. Brothers, K. N. Kudin, V. N. Staroverov, R. Kobayashi, J. Normand, K. Raghavachari, A. Rendell, J. C. Burant, S. S. Iyengar, J. Tomasi, M. Cossi, N. Rega, J. M. Millam, M. Klene, J. E. Knox, J. B. Cross, V. Bakken, C. Adamo, J. Jaramillo, R. Gomperts, R. E. Stratmann, O. Yazyev, A. J. Austin, R. Cammi, C. Pomelli, J. W. Ochterski, R. L. Martin, K. Morokuma, V. G. Zakrzewski, G. A. Voth, P. Salvador, J. J. Dannenberg, S. Dapprich, A. D. Daniels, Ö. Farkas, J. B. Foresman, J. V. Ortiz, J. Cioslowski, D. J. Fox, Gaussian 09, Gaussian, Inc., Wallingford, CT, **2009**.

[33] AIMPAC. Download page. http:www.chemistry.mcmaster.ca/aimpac/imagemap/imagemap.htm

[34] T. Keith, R. F. W. Bader, *Chem. Phys. Lett.* **1993**, *210*, 223.

[35] E. Espinosa, C. Lecomte, E. Molins, *Chem. Phys. Lett.* **1999**, *300*, 745.

[36] M. A. Spackman, *Cryst. Growth Des.* **2015**, *15*, 5624.

[37] C. Gatti, G. Macetti, R. J. Boyd, C. F. Matta, *J. Comput. Chem.* **2018**, *39*, 1112.

[38] G. Gatti, A. M. Orlando, L. Lo Presti, *Chem. Sci.* **2015**, *6*, 3845.

[39] T. L. P. Galvão, I. M. Rocha, M. D. M. C. Riberio da Silva, M. A. V. Riberio da Silva, *J. Phys. Chem. A* **2013**, *117*, 12668.

[40] E. R. Johnson, S. Keinan, P. Mori-Sànchez, J. Contreras-Garcia, A. J. Cohen, W. Yang, *J. Am. Chem. Soc.* **2010**, *132*, 6498.

[41] A. Otero-de-la-Roza, E. R. Johnson, J. Contreras-García, *Phys. Chem. Chem. Phys.* **2012**, *14*, 12165.

[42] J. Contreras-García, E. R. Johnson, S. Keinan, R. Chaudret, J.-P. Piquemal, D. N. Beratan, W. Yang, *J. Chem. Theory Comput.* **2011**, *7*, 625.

[43] C. Lefebvre, G. Rubez, H. Khartabil, J.-C. Boisson, J. Contreras-García, E. Hénon, *Phys. Chem. Chem. Phys.* **2017**, *19*, 17928.

[44] C. F. Matta, R. F. W. Bader, *Proteins* **2000**, *40*, 310.

[45] C. F. Matta, N. Castillo, R. J. Boyd, *J. Phys. Chem. B* **2006**, *110*, 563.

[46] C. Gatti, Handbook Electron Density and Chemical Bonding, Springer, Berlin, **2012**, *147*, 193.

Received: 4 November 2018
Revised: 6 December 2018
Accepted: 8 December 2018

Published online in Wiley Online Library

Electronic Supporting Information

for

When does a Hydrogen bond become a Van der Waals interaction? A topological answer.

Christian Tantardini[†a]

[a] *Center for Electrochemical Energy Storage, SkolTech Skolkovo Institute of Science and Technology, ul. Nobelya 3, Moscow, Russian Federation, 143026.*

[†] *Corresponding author email: christiantantardini@ymail.com.*

E.S.I.1 Source Function percentage contributions (SF%), volume of atomic basin, V(Ω), virial ratio, $-V/T$, charge densities (ρ_{BCP}), and complexation energy (E_C) at the *A…H* BCP of linear C_s water dimer (universal proton acceptor and donor) from equilibrium (eq) *A…D* distance ($R_{A…D}$) to 9 Å.[a]

$R_{A…D}$ (Å)	$-V/T$	ρ_{BCP} (e/bohr^3)	SF%(*A*)	SF%(*H*)	SF%(*D*)	SF%(*AHD*)	E_C (kcal/mol)	V(*H*) (bohr^3)	V(*A*) (bohr^3)
2.991$^{(eq)}$	2.001030	1.99711E-02	23.88	-47.16	85.21	61.93	-4.54	14.8981	144.6626
3.000	2.001035	1.95435E-02	23.41	-48.44	86.32	61.29	-4.53	15.0768	144.9388
3.250	2.001116	1.08531E-02	6.28	-92.07	123.37	37.58	-4.03	18.7861	148.3012
3.500	2.001136	6.14801E-03	-19.33	-156.68	177.27	1.26	-3.28	21.1639	150.9800
3.750	2.001132	3.51638E-03	-57.99	-251.06	257.32	-51.73	-2.60	22.6195	152.8448
4.000	2.001121	2.02207E-03	-116.85	-393.99	376.78	-134.05	-2.05	22.9766	153.5425
4.250	2.001110	1.16459E-03	-209.43	-610.32	555.83	-263.91	-1.62	22.4659	152.9745
4.500	2.001100	6.67747E-04	-355.91	-942.65	827.83	-470.73	-1.30	21.6824	152.0268
4.750	2.001092	3.79178E-04	-593.80	-1462.92	1251.55	-805.17	-1.05	21.7856	152.0801
5.000	2.001087	2.14060E-04	-984.68	-2282.93	1911.76	-1355.85	-0.87	21.7395	151.8886
6.000	2.001074	2.56179E-05	-5991.95	-11897.67	9500.97	-8388.65	-0.44	21.7743	151.4103
7.000	2.001069	4.16692E-06	-27058.47	-49506.69	38427.93	-38137.22	-0.26	21.8438	151.1014
8.000	2.001067	7.42468E-07	-113947.15	-203073.23	154776.17	-162244.21	-0.17	22.1140	151.1922
9.000	2.001065	1.07887E-07	-598563.64	-1071684.82	808414.39	-861834.07	-0.11	21.9505	151.1739

[a] *H*, *D*, and *A* are, respectively, the hydrogen atom directly involved in the H-bond, the H-donor, and the H-acceptor oxygen atoms.

E.S.I.2. Source Function percentage contributions (SF%) charge densities (ρ_{BCP}), and virial ratio, -*V*/*T*, at the *A…H* BCP of linear F_2 dimer from the equilibrium (eq) to 10 Å of F…F distance ($R_{F…F}$).[b]

R_{FF} (Å)	-*V*/*T*	ρ_{BCP} (e/bohr^3)	SF%(F1)	SF%(F2)	SF%(FF)
1.058$^{(eq)}$	2.000746	0.29782	49.99	49.99	99.98
2.000	2.001770	1.95435E-02	49.96	49.97	99.93
4.000	2.001886	1.08531E-02	50.00	49.99	99.98
6.000	2.001643	6.14801E-03	49.96	49.98	99.94
8.000	2.001339	3.51638E-03	49.93	49.95	99.88
10.000	2.001092	2.02207E-03	50.07	50.08	100.15

[b] Computational Details: The F_2 dimer was optimized in vacuo using CCSD/aug-cc-pVTZ[1-5] and subsequently it was performed a PROAIM[6] wavefunction at the equilibrium and elongated $R_{A…D}$ distances at the same level of theory.

E.S.I.3. Pictures of water dimer C_S constrained undergone $\theta(D - H \ldots A)$ angle variation from 90 to 175.99 deg. [equilibrium (eq)]. In the picture is seen the distance between *A* and *D* ($R_{A \ldots D}$) and the distance between *A* and *H* ($R_{A \ldots H}$). The hydrogen is withe, oxygen red and the *A*…*H* BCP is violet.[a]

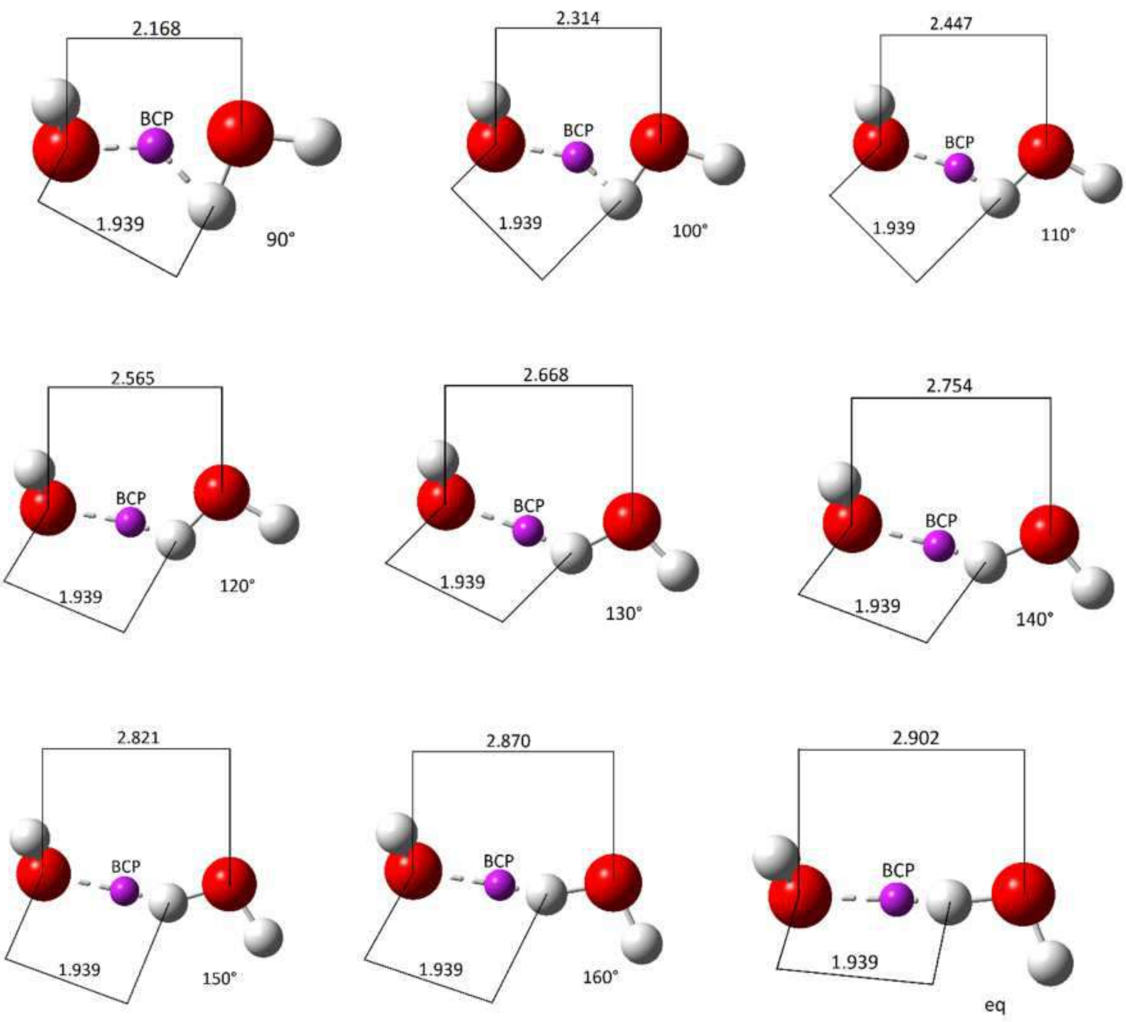

---

[a] *H*, *D*, and *A* are, respectively, the hydrogen atom directly involved in the H-bond, the H-donor, and the H-acceptor oxygen atoms.

E.S.I.4. Source Function percentage contributions (SF%), volume of atomic basin, V(Ω), virial ratio, -*V*/*T*, charge densities (ρ_{BCP}), and complexation energy (E_C) at the *A*…*H* BCP of linear C_s water dimer (universal proton acceptor and donor) evaluated at different bond angle $\theta(D-H\ldots A)$ from the equilibrium (eq) to 90 deg. with fixed *A*…*H* distance at the equilibrium.[a]

$\theta(D-H\ldots A)$ (deg.)	-*V*/*T*	ρ_{BCP} (e/bohr^3)	SF%(*A*)	SF%(*H*)	SF%(*D*)	SF%(*AHD*)	E_C (kcal/mol)
175.994$^{(eq)}$	2.001030	1.99711E-02	23.88	-47.16	85.21	61.93	-4.54
160	2.001015	1.99625E-02	23.50	-48.05	84.73	60.18	-4.40
150	2.000992	2.00887E-02	23.31	-45.98	83.42	60.75	-4.09
140	2.000957	2.03721E-02	23.12	-42.17	80.69	61.64	-3.57
130	2.000902	2.09150E-02	22.99	-36.73	75.18	61.43	-2.77
120	2.000817	2.18896E-02	22.71	-25.54	64.01	61.18	-1.56
110	2.000682	2.36669E-02	22.57	-0.51	40.39	62.45	0.33
100	2.000459	2.73909E-02	23.68	16.44	24.98	65.10	3.42
90	2.000082	3.56930E-02	27.55	15.35	27.47	70.37	8.72

[a] *H*, *D*, and *A* are, respectively, the hydrogen atom directly involved in the H-bond, the H-donor, and the H-acceptor oxygen atoms.

E.S.I.5 Source Function percentage contributions (SF%), volume of atomic basin, V(Ω), virial ratio, *-V/T*, and charge densities (ρ_{BCP}) at the *A…H* BCP dimer of water used like universal proton donor and paired with ammonia (HOH…NH_3) from the equilibrium (eq) to 9 Å of *A…D* distance ($R_{A…D}$).[a]

$R_{A…D}$ (Å)	*-V/T*	ρ_{BCP} (e/bohr^3)	SF%(*A*)	SF%(*H*)	SF%(*D*)	SF%(*AHD*)	V(*H*) (bohr^3)	V(*A*) (bohr^3)
2.961$^{(eq)}$	2.001030	2.74356E-02	11.55	-28.20	67.43	50.79	13.42240	129.51746
3.000	2.001035	2.51576E-02	8.71	-32.21	70.94	47.45	14.11854	130.35740
3.250	2.001116	1.44443E-02	-14.33	-65.04	99.00	19.62	17.93807	135.51912
3.500	2.001136	8.42700E-03	-47.18	-111.47	138.92	-19.72	20.71902	139.39096
3.750	2.001132	4.98275E-03	-94.31	-179.06	196.01	-77.37	22.61936	142.26542
4.000	2.001121	2.97029E-03	-162.52	-277.40	278.03	-161.90	23.55659	143.97894
4.250	2.001110	1.77879E-03	-262.89	-420.79	397.23	-286.45	23.57531	144.59983
4.500	2.001100	1.06557E-03	-413.40	-631.85	571.65	-473.60	22.69093	143.67168
4.750	2.001092	6.35453E-04	-643.03	-948.03	830.24	-760.82	22.06621	142.88900
5.000	2.001087	3.76334E-04	-999.01	-1427.61	1219.47	-1207.15	21.89798	142.43647
6.000	2.001074	4.94019E-05	-5385.05	-6950.07	5618.29	-6716.84	22.05277	142.24181
7.000	2.001069	8.36097E-06	-23100.00	-27928.76	21986.08	-29042.68	22.16695	142.19304
8.000	2.001067	1.68048E-06	-85549.16	-101417.84	78349.76	-108617.25	22.24395	142.03907
9.000	2.001065	2.85682E-07	-383739.65	-454396.72	347189.56	-490946.81	22.27528	142.01707

[a] *H*, *D*, and *A* are, respectively, the hydrogen atom directly involved in the H-bond, the H-donor oxygen atom, and the H-acceptor nitrogen atoms.

E.S.I.6. Source Function percentage contributions (SF%), volume of atomic basin, V(Ω), virial ratio, -*V*/*T*, and charge densities (ρ_{BCP}) at the *A*…*H* BCP dimer of water used like universal proton acceptor and paired with methylenimine (NH…OH_2) from the equilibrium (eq) to 9 Å of *A*…*D* distance ($R_{A…D}$).[a]

$R_{A…D}$ (Å)	-*V*/*T*	ρ_{BCP} (e/bohr^3)	SF%(*A*)	SF%(*H*)	SF%(*D*)	SF%(*AHD*)	V(*H*) (bohr^3)	V(*A*) (bohr^3)
3.174$^{(eq)}$	2.001062	1.63712E-02	16.40	-48.09	65.88	34.19	26.86415	145.10014
3.250	2.001091	1.38584E-02	11.76	-59.04	72.49	25.21	28.06734	146.20832
3.500	2.001142	8.09494E-03	-6.95	-104.46	99.56	-11.85	31.25626	149.44408
3.750	2.001158	4.78413E-03	-33.46	-170.56	137.99	-66.03	33.38887	151.91841
4.000	2.001160	2.84310E-03	-71.38	-268.26	193.61	-146.03	34.42338	153.27492
4.250	2.001157	1.69211E-03	-125.82	-413.70	273.61	-265.91	34.54959	153.57679
4.500	2.001152	1.00362E-03	-206.50	-633.10	390.57	-449.02	33.72858	152.83382
4.750	2.001148	5.89898E-04	-329.88	-969.67	564.84	-734.70	33.29444	152.22313
5.000	2.001144	3.43842E-04	-523.62	-1492.81	827.18	-1189.25	33.28191	152.04093
6.000	2.001134	4.46878E-05	-2720.94	-7464.19	3548.95	-6636.18	33.21997	151.82836
7.000	2.001130	7.50510E-06	-10975.97	-30423.49	12879.26	-28520.21	33.25315	151.64553

[a] *H*, *D*, and *A* are, respectively, the hydrogen atom directly involved in the H-bond, the H-donor oxygen atom, and the H-acceptor nitrogen atom.

E.S.I.7. Source Function percentage contributions (SF%), volume of atomic basin, V(Ω), virial ratio, $-V/T$, and charge densities (ρ_{BCP}) at the $A\ldots H$ BCP of dimer of water used like universal proton acceptor and paired with ethane ($CH_3\ldots OH_2$) constrained from 2.5 Å, passing for the equilibrium (eq), to 9 Å of $A\ldots D$ distance ($R_{A\ldots D}$).[a]

$R_{A\ldots D}$ (Å)	$-V/T$	ρ_{BCP} (e/bohr^3)	SF%(A)	SF%(H)	SF%(D)	SF%(AHD)	V(H) (bohr^3)	V(A) (bohr^3)
2.500	1.998945	8.66887E-02	43.10	19.00	14.35	76.44	22.7540	134.5110
2.750	1.999904	4.76416E-02	37.42	7.79	17.84	63.05	30.4282	139.4922
3.000	2.000378	2.64881E-02	28.98	-9.57	23.21	42.63	36.8462	143.6605
3.250	2.000604	1.50211E-02	15.99	-35.14	30.58	11.43	41.9022	147.1979
3.500	2.000706	8.70481E-03	-3.42	-72.29	40.11	-35.61	45.7163	150.0316
3.750	2.000749	5.10433E-03	-32.86	-127.05	53.87	-106.04	48.3070	152.2154
3.826$^{(eq)}$	2.000755	4.34794E-03	-44.37	-148.42	58.94	-133.86	48.8791	152.7036
4.000	2.000765	3.00643E-03	-77.43	-209.02	72.97	-213.48	49.8119	153.3869
4.250	2.000769	1.76889E-03	-146.26	-333.72	101.52	-378.47	50.3307	153.4352
4.500	2.000769	1.03543E-03	-254.75	-526.43	142.73	-638.45	49.6699	152.3808
4.750	2.000768	6.01766E-04	-427.82	-827.22	205.34	-1049.70	49.3310	151.7815
5.000	2.000767	3.48332E-04	-705.00	-1297.58	295.69	-1706.89	49.2787	151.4977
6.000	2.000763	4.25310E-05	-4458.24	-7115.44	1281.79	-10291.89	49.4584	151.3306
7.000	2.000762	6.16966E-06	-23552.67	-34347.89	5136.91	-52763.66	49.6096	151.2457
8.000	2.000761	9.75617E-07	-114034.65	-164088.14	22815.31	-255307.47	49.9892	151.5129
9.000	2.000761	1.30644E-07	-663217.31	-965881.74	124329.81	-1504769.24	50.1866	151.7029

[a] *H*, *D*, and *A* are, respectively, the hydrogen atom directly involved in the H-bond, the H-donor carbon atom, and the H-acceptor oxygen atom.

E.S.I.8. Source Function percentage contributions (SF%), volume of atomic basin, V(Ω), virial ratio, $-V/T$, and charge densities (ρ_{BCP}) at the $A\ldots H$ BCP of dimer of water used like universal proton acceptor and paired with ethene ($CH_2\ldots OH_2$) constrained from 2.5 Å, passing for the equilibrium (eq), to 9 Å of $A\ldots D$ distance ($R_{A\ldots D}$).[a]

$R_{A\ldots D}$ (Å)	$-V/T$	ρ_{BCP} (e/bohr^3)	SF%(A)	SF%(H)	SF%(D)	SF%(AHD)	V(H) (bohr^3)	V(A) (bohr^3)
2.500	1.999009	9.04694E-02	44.82	18.95	16.58	80.35	21.0162	133.5497
2.750	2.000025	4.91259E-02	38.69	8.17	21.34	68.20	29.2527	138.8243
3.000	2.000521	2.70427E-02	29.96	-9.35	28.17	48.79	35.7532	143.1341
3.250	2.000753	1.51827E-02	16.76	-35.91	37.80	18.66	40.7985	146.8547
3.500	2.000857	8.71336E-03	-2.96	-74.79	50.80	-26.96	44.5520	149.7708
3.624$^{(eq)}$	2.000884	6.64342E-03	-16.29	-100.59	58.95	-57.94	45.9606	151.0083
3.750	2.000900	5.06105E-03	-32.88	-132.46	68.68	-96.65	47.1711	151.8730
4.000	2.000916	2.95393E-03	-78.63	-219.54	94.13	-204.04	48.5830	152.9297
4.250	2.000920	1.72237E-03	-150.04	-353.25	130.20	-373.09	49.0355	153.1393
4.500	2.000919	9.99159E-04	-262.97	-561.62	182.22	-642.36	48.2610	152.2117
4.750	2.000918	5.75561E-04	-444.81	-889.91	258.15	-1076.57	47.8494	151.7608
5.000	2.000916	3.30222E-04	-738.51	-1407.88	367.10	-1779.29	47.7665	151.4400
6.000	2.000912	3.95812E-05	-4747.49	-7872.66	1363.41	-11256.75	47.9618	151.4880
7.000	2.000910	5.82234E-06	-24751.36	-37376.82	4165.28	-57962.90	48.4399	151.4452
8.000	2.000909	9.51694E-07	-116639.49	-171757.66	11447.94	-276949.21	48.3794	151.2230
9.000	2.000909	1.29133E-07	-671336.54	-994015.04	31016.26	-1634335.32	48.2269	151.0422

[a] H, D, and A are, respectively, the hydrogen atom directly involved in the H-bond, the H-donor carbon atom, and the H-acceptor oxygen atom.

E.S.I.9. Source Function percentage contributions (SF%), volume of atomic basin, V(Ω), virial ratio, $-V/T$, and charge densities (ρ_{BCP}) at the $A\ldots H$ BCP of dimer of water used like universal proton acceptor and paired with ethyne (CH…OH$_2$) constrained from the equilibrium (eq) to 9 Å of $A\ldots D$ distance ($R_{A\ldots D}$).[a]

$R_{A\ldots D}$ (Å)	$-V/T$	ρ_{BCP} (e/bohr^3)	SF%(A)	SF%(H)	SF%(D)	SF%(AHD)	V(H) (bohr^3)	V(A) (bohr^3)
3.624$^{(eq)}$	2.001296	1.24582E-02	11.99	-55.22	55.55	12.32	35.8627	148.0937
3.500	2.001361	7.69551E-03	-7.27	-96.51	72.36	-31.42	38.4701	150.5169
3.750	2.001391	4.37974E-03	-41.65	-168.78	99.18	-111.25	40.5029	152.5554
4.000	2.001399	2.50425E-03	-95.07	-279.94	136.59	-238.42	41.4978	153.4505
4.250	2.001398	1.43067E-03	-180.29	-453.17	189.44	-444.02	41.4118	153.2923
4.500	2.001395	8.14002E-04	-316.97	-726.79	264.36	-779.40	40.6206	152.2154
4.750	2.001392	4.59937E-04	-542.59	-1164.37	370.35	-1336.61	40.4921	151.8482
5.000	2.001389	2.57973E-04	-916.38	-1872.35	519.27	-2269.46	40.5011	151.6991
6.000	2.001383	2.71975E-05	-6558.76	-11880.14	1667.17	-16771.73	40.7703	151.4848
7.000	2.001380	3.61298E-06	-37137.31	-63177.98	1753.91	-98561.37	40.8875	151.5105
8.000	2.001379	5.53800E-07	-185057.03	-309834.47	-19996.38	-514887.88	40.9496	151.4201
9.000	2.001379	6.99752E-08	-1146278.66	-1934928.04	-275184.19	-3356390.89	41.0119	151.4043

[a] H, D, and A are, respectively, the hydrogen atom directly involved in the H-bond, the H-donor carbon atom, and the H-acceptor oxygen atom.

References

1. J. Cížek, in *Advances in Chemical Physics*, Ed. P. C. Hariharan, Wiley Interscience, New York, **1969**, 14, 35.
2. G. D. III Purvis, R. J. Bartlett, *J. Chem. Phys.*, **1982**, 76, 1910-1918.
3. G. E. Scuseria, C. L. Janssen, H. F. III Schaefer, *J. Chem. Phys.*, **1988**, 89, 7382-7387.
4. G. E. Scuseria, H. F. III Schaefer, *J. Chem. Phys.*, **1989**, 90, 3700-3703.
5. T. H. Jr. Dunning, *J. Chem. Phys.* **1989**, 90, 1007.
6. C. Gatti, P. Fantucci, G. Pacchioni, *Theor. Chim. Acta* **1987**, 72, 433−458.

CHAPTER II

Application of Quantum Chemical Topology in the study of non-covalent interactions within Oxicams

Summary:

This chapter starts with a description in details of the crystal structure of meloxicam polymorph I, in which different types of non-covalent interactions (NCIs) are present. Two controversial models were previously proposed by Cheney et al. (Supramolecular Architectures of Meloxicam Carboxylic Acid Cocrystals, a Crystal Engineering Case Study, *Cryst. Growth Des.*, 2010, 10, 4401–4413, DOI: 10.1021/cg100514g) and Tumanov et al. (Are meloxicam dimers really the structure-forming units in the 'meloxicam–carboxylic acid' co-crystals family? Relation between crystal structures and dissolution behavior, *CrystEngComm*, 2012, 14, 305–313, DOI: 10.1039/C1CE05902E) for describing the NCIs in this system. They argued about the main structural motifs and the presence of particular types of interactions within the structure but both relied on geometrical parameters only. We resolved the controversial questions addressed in the previous studies and represented a new model of NCIs supported by a number of computational tools, namely Hirshfeld surface analysis, DFT calculations, and reduced density gradient (RDG) analysis. For more precise investigation, the structure of meloxicam polymorph I was initially taken from the experimental X-ray diffraction data, measured at lowered temperature (100 K) as a part of this work, and then fully optimized by solid-state PW-DFT calculations.

A strong point of this work is the combination of different methods which allow seeing the system from all sides. Our study demonstrates how the final model of NCIs can be eventually found from a detailed step-by-step analysis by means of different computational tools. We think that the methodology and results described in the present work will be useful for further studies of not only meloxicam and its co-crystals but also many other compounds with similar structural features.

Subsequently, the chapter describes as a co-crystal was obtained from powder samples of a 1:1 co-crystal of meloxicam [4-hydroxy-2-methyl-N-(5-methyl-1,3-thiazol-2-yl)-1,1-dioxo-2H-1λ^6,2-benzothiazine-3-carboxamide], MXM, with benzoic acid, BZA, via liquid-assisted co-grinding using as fluid additives solvents with different polarity: benzene, toluene, ortho-xylene, meta-xylene, para-xylene, THF and water. Single crystals of this co-crystal were crystallised from a THF solution. Crystal structure was solved, and non-covalent interactions in this structure were analysed.

The low aqueous solubility of this co-crystal is different to the values reported earlier for MXM co-crystals with other co-formers with aromatic molecular fragments. To rationalize this fact, we have analysed the non-covalent interactions in all the MXM co-crystals deposited in the most recent version of the Cambridge Database. The results of this analysis suggest that both the interactions in the initial crystals (weaker binding between MXM molecules in co-crystals, as supposed in Tumanov, N.A., Myz, S.A., Shakhtshneider, T.P. & Boldyreva, E.V. (2012). *CrystEngComm* 14: 305)and the possibility to form molecular clusters between MXM and a co-former in aqueous solution [Cysewski, P. (2018) *J. Mol. Model* 24:112] are important for the solubility of MXM co-crystals in water. In particular, the $\pi \ldots \pi$ interactions between a co-former and MXM molecule in a co-crystal favour the aqueous solubility.

Furthermore, this chapter gives a sound reply to an experimentally unsolved question, concerning the possibility to find tenoxicam (TXM) within crystal structures only in the zwitterionic form with respect to other oxicams, which are typically present in β-keto-enolic form. Oxicams are active pharmaceutical ingredients belonging to a class of nonsteroidal anti-inflammatory drugs amply used in the last years for

the cancer treatment. Due to their limited solubility in aqueous solution there is a demand to increase it by creation of co-solvates with different partners. Among all possible keto-enolic forms, the zwitterionic form has the highest water solubility that makes TXM as a highly promising candidate for medical treatment with respect to other oxicams. Up to now, the causes of this TXM phenomenon were unknown leaving it as an open question of last decades. Investigation performed in this work revealed for the first time the S-bond, a non-covalent interaction between S-atom of thiophen unit and oxygen of carbonyl group, to be the driving force of TXM crystallization. This study further confirms the importance of S-bond in the drug design although nowadays it is still underestimated as stated by Beno et al. [B. R. Beno, K-S Yeung, M. D. Bartberger, L. D. Pennington, N. A. Meanwell, J. Med. Chem, 2015, 58 (11), 4383–4438]. Our findings highlight the importance of S-bond, which could play a key role in other molecular systems. The strong point of this work is the joint use of different experimental approaches in liquid and solid state together with high-level calculations. The latter give results in agreement with experimental data that allows the discrimination of the driving force of TXM crystallization.

Conclusions:

- In the case of MXM co-crystals with non-aromatic carboxylic acids, both
- H-bonds and π…π interactions are similar and the different solubility behavior can be related to the different carbon chain length of the carboxylic acids.
- In the case of the MXM cocrystals with aromatic carboxylic acids, the H-bonds are similar, but π…π interactions are different, and this latter difference can account for the differences in the dissolution behavior.
- In the case of MXM-BZA co-crystals, the weakness of the π…π interactions between the MXM and the BZA molecules prevents the formation of complex made by a MXM molecule and a co-former in solution, and the solubility falls down, almost to the level of pure MXM, because the solubility is higher for those structures, in which there are the π…π interactions between aromatic co-former and MXM, like in most co-crystals with aromatic co-formers at exception of MXM-BZA co-crystal.
- The main motif in the crystal structure of meloxicam polymorph I is a repeating dimeric unit (denoted as fragment ***A*** in this study) formed *via* the medium-strength N–H···O hydrogen bonds. The other molecular pair within the crystal structure (fragment ***B*** in the present study) is linked by two types of weaker van der Waals interactions, namely the S···O and O–H···O contacts, both being present in the structure. This can be useful for further studies of meloxicam co-crystals and analogous compounds.
- The polarity of a solvent modulates the TXM keto-enol equilibrium in solution with the dominance of the BKE form in low polarity solvents and the ZWC form in high polarity solvents.
- Regardless of the starting conformation, the crystallization process always leads to the ZWC form within the crystal structures. This makes the variation of solvent polarity to crystallize TXM in one or another keto-enolic form meaningless.
- The S-bond between the thiophenyl ring and carbonyl oxygen according to the analysis of intra-molecular interactions via the NBO theory shown that S-bond is significantly stronger for the ZWC form as compared to that for the flatten BKE form; this directs the crystallization of TXM only in the ZWC form.

Contribution:

The project was conceptualized and managed by Christian Tantardini other that performed theoretical investigation part. The experimental crystallographic part was performed in the Boldyreva's lab at the Novosibirsk State University by Dr.Sergey G. Arkhipov, Dr. Tatiana N. Drebushchak and at the National Research Center "Kurchatov Institute" in Moscow by Dr. Vladimir A. Lazarenko. At the International Tomographic Center in Novosibirsk experimental absorption and fluorescence spectra were performed by Dr. Petr S. Sherin, while experimental NMR spectra were performed by Dr. Alexey S. Kiryutin. Mr. Alexey Yu. Fedorov assisted in part at the analysis of results and at the writing of manuscript: Alexey Yu. Fedorov, Tatiana N. Drebushchak and **Christian Tantardini*** Seeking the best model for non-covalent interactions within the crystal structure of meloxicam. *Computational and Theoretical Chemistry*, 2019,1157, 47-53; under supervision of Christian Tantardini.

Computational and Theoretical Chemistry 1157 (2019) 47–53

Contents lists available at ScienceDirect

Computational and Theoretical Chemistry

journal homepage: www.elsevier.com/locate/comptc

Seeking the best model for non-covalent interactions within the crystal structure of meloxicam☆

Alexey Yu. Fedorov[a,b], Tatiana N. Drebushchak[a,b], Christian Tantardini[a,c,*]

[a] *Novosibirsk State University, 2 Pirogova st, Novosibirsk 630090, Russia*
[b] *Institute of Solid State Chemistry and Mechanochemistry, 18 Kutateladze st, Novosibirsk 630128, Russia*
[c] *SkolTech Skolkovo Institute of Science and Technology, 3 Nobelya st, Moscow 143026, Russia*

A R T I C L E I N F O

Keywords:
Non-covalent interactions
DFT calculations
Hirshfeld surface
Reduced density gradient

A B S T R A C T

In crystals, molecules are linked by different types of non-covalent interactions (NCIs). Sometimes it can be an intricate task to define without resorting to calculations what type of NCIs is mainly responsible for maintaining the structure. One of such examples is meloxicam in the polymorphic form I, for which two controversial models describing NCIs are known to date. These models proposed by Cheney et al. (2010), and Tumanov et al. (2012), differ in structural motifs and a presence of particular types of interactions therein. However, they both rely on geometrical parameters only and were not confirmed quantitatively. Here we show the final model of NCIs within the crystal structure of meloxicam polymorph I supported by DFT calculations, Hirshfeld surface analysis and reduced density gradient (RDG) investigation. We found that both types of weak van der Waals interactions described in the previously proposed models (namely, S···O and O—H···O contacts) are actually present in the structure and take part in linking the N—H···O-bonded meloxicam dimers with each other. These dimers are formed by medium-strength H-bonds and represent the main building blocks of the structure. Our study demonstrates how a model of NCIs can be unambiguously revealed by means of different computational tools. We hope that the results obtained in the present work will be useful for further studies of meloxicam, its co-crystals and analogous compounds.

1. Introduction

Non-covalent interactions (NCIs) are important for organic, inorganic and biological systems [1–6] but complicated to study at the same time [7,8]. They encompass a large number of interactions of different nature, such as hydrogen bonds, CH–π and π–π interactions, dipole-dipole interactions, steric repulsion, London dispersion and others [9]. The competition between different types of NCIs during a crystallisation process leads to the formation of a particular three-dimensional structure. In spite of a notable advance in the field of crystal structure prediction, it is still impossible to fully govern NCIs in designing new crystal forms [10]. Nevertheless, plenty of tools have been devised to distinguish and analyse them in the already obtained crystal structures [11–15]. Applying a combination of these tools to an object of study, researchers can understand better how their structure is formed and reveal more details in it.

One of the challenging systems for describing NCIs is meloxicam (MXM), 4-hydroxy-2-methyl-*N*-(5-methyl-2-thiazolyl)-2*H*-1,2-benzothiazine-3-carboxamide-1,1-dioxide (Fig. 1), a non-steroidal anti-inflammatory drug of the oxicam family, selectively inhibiting COX-2 enzymes [16,17]. During the last decades, the interest in the investigation of meloxicam was mainly focused on enhancing its poor aqueous solubility [18] and dissolution rate [19] through co-crystallisation with different carboxylic acids [20–28]. In order to rationalise the different dissolution behaviour of meloxicam and its co-crystals, their crystal structures have been comprehensively studied with respect to structure-forming units and intermolecular interactions. As a result, two controversial models were proposed for the structure of meloxicam in the polymorphic form I [26,27]. Cheney et al. [26] claimed that the MXM molecules form infinite chains sustained by N—H···O(═S) hydrogen bonds and S(thiazole)···O(hydroxyl) interactions (Fig. 2a) and selected two potential supramolecular synthons for co-crystal formation (fragments ***A*** and ***B*** in Fig. 2a). Besides that, they reported that the MXM dimers constituting fragment ***B*** in polymorph I serve as structure-forming units in many MXM co-crystals [26]. Subsequently, Tumanov et al. [27] argued that the molecular fragment ***B*** can be hardly considered a dimer and supramolecular synthon for building the structures. In their interpretation (Fig. 2b), it

---

☆ This paper is dedicated to the memory of Professor Alexei P. Chupakhin (1952–2018).

[*] Corresponding author at: SkolTech Skolkovo Institute of Science and Technology, 3 Nobelya st, Moscow 143026, Russia.
E-mail address: christiantantardini@ymail.com (C. Tantardini).

https://doi.org/10.1016/j.comptc.2019.04.012
Received 19 March 2019; Received in revised form 18 April 2019; Accepted 18 April 2019
Available online 20 April 2019
2210-271X/ © 2019 Elsevier B.V. All rights reserved.

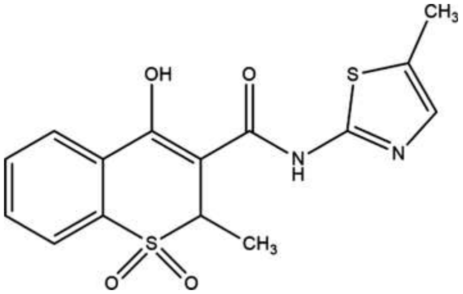

Fig. 1. Molecular structure of meloxicam.

represents a molecular pair sustained by very weak O—H···O(=C) interactions and formed virtually due to steric effects [27]. Thus, for meloxicam polymorph I the authors supposed different structural motifs (infinite chains by Cheney et al. [26]; a repeating dimeric unit by Tumanov et al. [27]) and reported different non-covalent interactions linking the MXM molecules in fragment ***B*** (S···O interactions by Cheney et al. [26] and O—H···O(=C) interactions by Tumanov et al. [27]). However, both proposed models were built based on geometrical consideration only so neither of them can be unambiguously called correct or incorrect without any quantitative analysis.

In this work, we aimed to give the final answer which model best describes the NCIs within the structure of meloxicam polymorph I. The system has been explicitly investigated using an approach that combines an experimental structure analysis and solid-state DFT calculations. Particularly, we have calculated the energies of the above-mentioned fragments ***A*** and ***B*** and analysed Hirshfeld surfaces and reduced density gradient plots to see the strength of NCIs between the MXM molecules. Thus, the final model proposed in the present work has been supported by several tools for consideration of intermolecular interactions at once.

2. Experimental details

Meloxicam was purchased from Sigma-Aldrich Co. Ltd and was recrystallised by slow evaporation from methanol solution in order to obtain a single crystal.

Table 1
Single-crystal X-ray diffraction data collection and refinement details for meloxicam polymorph I at 100 K.

Crystal data	
Chemical formula	$C_{14}\ H_{13}\ N_3\ O_4\ S_2$
M_r	351.39
Crystal system, space group	Triclinic, $P\bar{1}$
Temperature (K)	100(2)
a, b, c (Å)	6.88045(4), 8.06575(4), 13.50833(5)
α, β, γ (°)	86.1717(4), 88.5527(4), 75.4600(5)
V	724.00(1)
Z	2
Radiation type	Mo $K\alpha1$
μ (mm^{-1})	0.39
Crystal size (mm)	0.33 × 0.18 × 0.11
Data collection	
Diffractometer	Xcalibur, Ruby, Gemini Ultra
Absorption correction	Multi-scan *CrysAlis PRO* 1.171.38.43 (Rigaku Oxford Diffraction, 2015)
T_{min}, T_{max}	0.831, 1.000
No. of measured independent and observed [$I > 2\sigma(I)$] reflections	100267, 7194, 6980
R_{int}	0.034
(sin θ/λ)max (Å^{-1})	0.840
Refinement	
$R[F^2 > 2\sigma(F^2)]$, $wR(F^2)$, S	0.023, 0.068, 1.08
No. of reflections	7194
No. of parameters	218
H-atom treatment	H atoms were treated by a mixture of independent and constrained refinement
$\Delta\rho_{max}$, $\Delta\rho_{min}$ (e Å^{-3})	0.57, −0.32

Crystal data, data collection and structure refinement details are summarised in Table 1. The crystal structure of meloxicam polymorph I, previously refined at room temperature (CSD refcode: SEDZOQ) [16], was now determined at 100 K (CSD refcode: 1875635) to minimize the atomic anisotropic displacements.

Single-crystal X-ray diffraction was carried out using an Oxford Diffraction Gemini R Ultra diffractometer with Mo-Kα radiation ($\lambda = 0.71073$ Å), a Ruby CCD 2D detector and a graphite monochromator. A low-temperature Oxford Instruments CryojetHT device was used for varying temperature.

All H atoms were initially located in a difference Fourier map. The H2N and H3O atoms (see Table S1 and Fig. S2 in the Supplementary material) were refined isotropically. The positions of all other H atoms

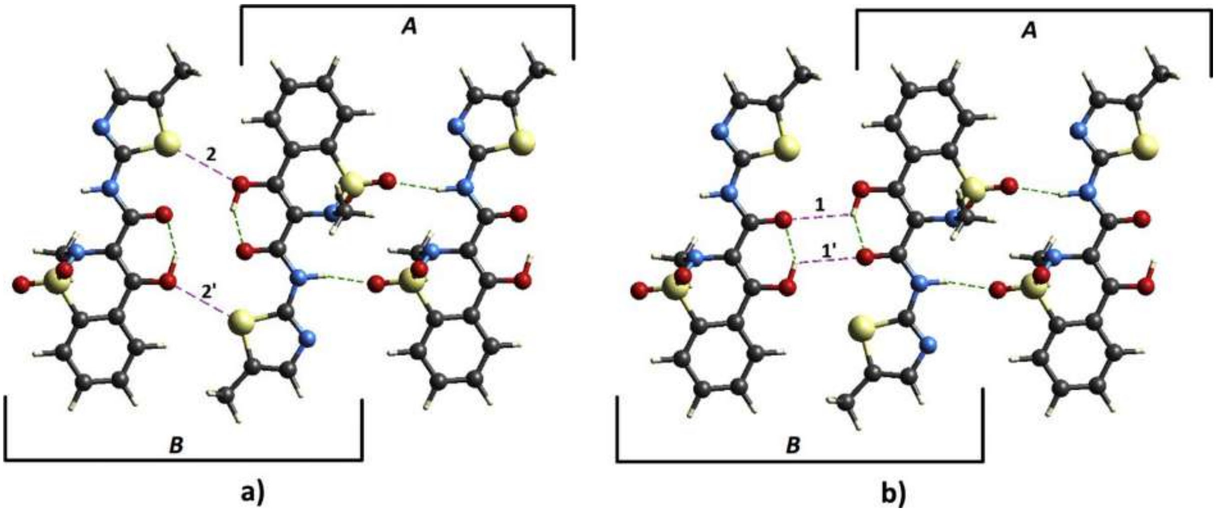

Fig. 2. Two models of non-covalent interactions within the crystal structure of meloxicam polymorph I proposed by Cheney et al. [26] (a) and Tumanov et al. [27] (b). Two potential supramolecular synthons are denoted as fragments ***A*** and ***B***. Different NCIs proposed by the different authors for linking the molecules in fragment ***B*** are labelled with numbers: **1** and **1′** for O—H···O(=C) interactions; **2** and **2′** for S(thiazole)···O(hydroxyl) interactions (the prime symbol denotes the interactions which are identical by symmetry). The colour scheme is as follows: yellow for sulphur, red for oxygen, turquoise for nitrogen, grey for carbon, white for hydrogen; light green dot lines correspond to H-bonds; violet dot lines denote vdW interactions.

Table 2
Geometrical parameters of intermolecular interactions shown in the Fig. 2 (the N—H···O H-bond in fragment ***A***; the O—H···O and S···O contacts in fragment ***B***). The values of parameters correspond to the experimental structure refined at 100 K (*Exp.*) and the fully optimized structure (*Calc.*).

Non-covalent interaction (numeration according to Fig. 2)		$R_{D..A}$[a,b] (Å)		$R_{H..A}$[a,b] (Å)		$R_{D..H}$[a,b] (Å)		∠A–H–D[b,c] (°)	
	N—H···O	*Exp.* 2.9695(7)	*Calc.* 3.010	*Exp.* 2.14(1)	*Calc.* 2.004	*Exp.* 0.85(1)	*Calc.* 1.026	*Exp.* 163(1)	*Calc.* 165.63
1, 1′	O—H···O	3.1872(6)	3.083	2.71(2)	2.631	0.89(1)	1.008	115(1)	107.13
2, 2′	S···O	3.2205(5)	3.274	–	–	–	–	–	–

[a] R is the distance between the two atoms indicated in the subscript.

[b] H, D, and A are the hydrogen directly involved in the interaction, the H-donor, and the H-acceptor atoms, respectively. For the S···O interaction, D and A symbols correspond to the atoms directly involved in the interaction: sulphur and oxygen, respectively.

[c] ∠A–H–D is the angle formed by the hydrogen directly involved in the interaction, the H-donor, and the H-acceptor atoms.

Table 3
The total energies (E_{TOT}) of fragments ***A*** and ***B*** (as indicated in Fig. 2) within the crystal structure of meloxicam subdivided into four contributions: electrostatic (E_{ele}), polarization (E_{pol}), dispersion (E_{disp}) and repulsion (E_{rep}).[a]

Fragment	E_{ele}	E_{pol}	E_{disp}	E_{rep}	E_{TOT}
A	−62.1	−12.6	−41.4	73.3	−42.8
B	−7.7	−2.6	−32.3	34.3	−8.1

[a] All the energy values are expressed in kJ/mol.

were subsequently optimized geometrically and refined using a riding model, with the following assumptions and restraints: C—H = 0.95 Å and $U_{iso}(H) = 1.2U_{eq}(C)$ for all C—H groups, C—H = 0.98 Å and $U_{iso}(H) = 1.5U_{eq}(C)$ for CH_3 groups.

3. Computational details

The experimental structure of meloxicam polymorph I refined at 100 K was fully optimized through plane-wave density functional theory (PW-DFT) using the PW86PBE [29,30] exchange–correlation functional in combination with the exchange-hole dipole moment (XDM) dispersion correction [31,32] with damping parameters ($a_1 = 0.6836$ and $a_2 = 1.5045$). This DFT functional with the XDM correction was reported to give the lowest mean absolute percentage deviation between the calculated and experimental energies (namely, 11.7%), compared with other DFT functionals [31,32]. The wave function energy cut-off and the kinetic energy cut-off were set to 46 Ry and 460 Ry, respectively. The ionic positions were allowed to relax until the force on each atom was less than 10^{-8} Ry/Bohr and the total energy converged to 10^{-8} Ry. In addition, the optimized geometry was confirmed by phonon calculation with a 10^{-14} Ry convergence threshold for self-consistency to represent a genuine minimum on the potential energy surface (PES) as indicated by the absence of any imaginary vibrational frequencies (Table S4 in the Supplementary material). All PW-DFT calculations were performed using Quantum ESPRESSO (version 5.4) [33]. The root-mean-square deviation (RMSD) of the calculated structure from the experimental one was equal to 0.697, indicating a good correspondence between the models. The comparison of all bond lengths from the experimental and the optimized structures with those coming from neutron diffraction studies reported in literature [34] showed the differences not exceeding 2%.

The energies of different molecular pairs within the fully optimized structure of meloxicam were calculated with Tonto program [35] as implemented in CrystalExplorer (Version 17.5) [36]. The calculations were performed using B3LYP functional [37] with the Grimme's empirical dispersion correction D2 [38] and cc-pVTZ local basis set [39]. This level of theory was reported to provide accurate calculations of energies of intermolecular interactions in molecular crystals [40]. Hirshfeld surface analysis [11,41–44] was carried out for the fully optimized structure using Crystal Explorer (Version 17.5) [36].

The investigation of NCIs has been carried out for the fully optimized structure of meloxicam through the plots of the reduced density gradient (RDG, defined as $s = 1/(2(3\pi^2)^{1/3})|\nabla\rho|/\rho^{4/3}$) versus $\mathrm{sign}(\lambda_2)\rho$ (λ_2 is the second electron-density Hessian eigenvalue) and the RDG isosurfaces ($s = 0.05$ a.u.) [12,45–47] were drawn for the fully optimized structure using CRITIC2 program [48,49].

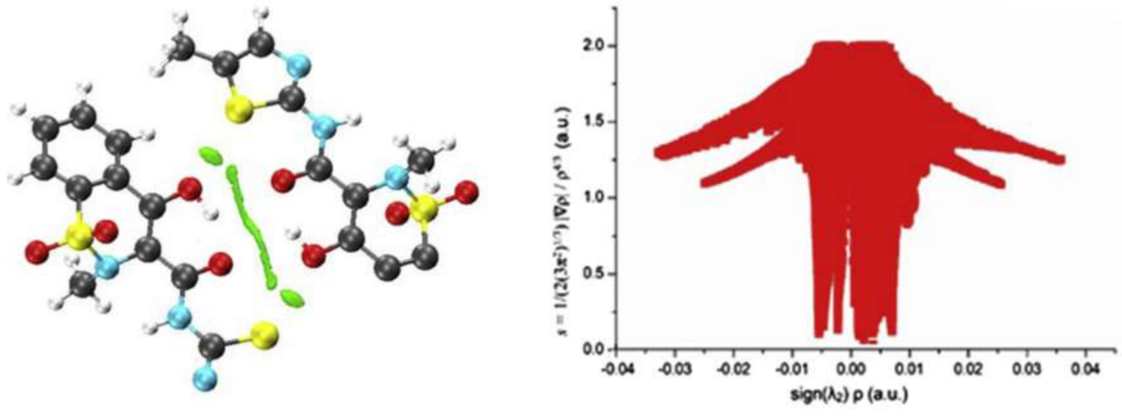

(a) (b)

Fig. 3. Results of the NCI analysis performed for the pair of MXM molecules corresponding to fragment ***B*** (as indicated in Fig. 2): (a) gradient isosurfaces for $s = 0.5$ a.u. and $-0.04 < \mathrm{sign}(\lambda_2)\rho < 0.04$ (colour scale: from blue (strong attractive interactions) through green (moderate vdW interactions) to red (strong non-bonded overlap)) and (b) plot of the reduced density gradient (s) versus the electron density multiplied by the sign of the second Hessian eigenvalue ($\mathrm{sign}(\lambda_2)\rho$). The colour scheme is as follows: yellow for sulphur, red for oxygen, turquoise for nitrogen, grey for carbon, white for hydrogen.

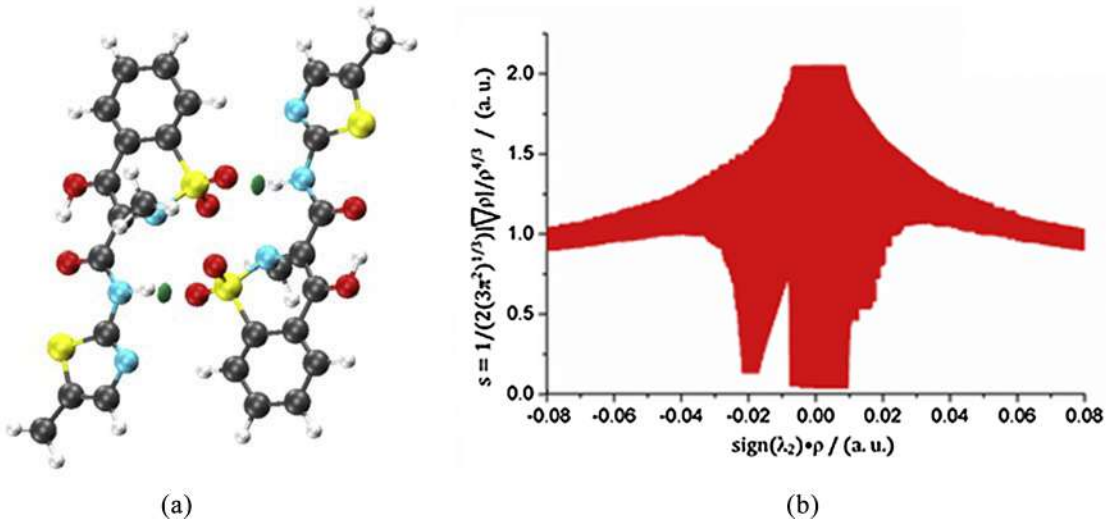

(a) (b)

Fig. 4. Results of the NCI analysis performed for the pair of MXM molecules corresponding to fragment ***A*** (as indicated in Fig. 2): (a) gradient isosurfaces for s = 0.5 a.u. and $-0.08 < \text{sign}(\lambda_2)\rho < 0.08$ (colour scale: from blue (strong attractive interactions) through green (moderate vdW interactions) to red (strong non-bonded overlap)) and (b) plot of the reduced density gradient (*s*) versus the electron density multiplied by the sign of the second Hessian eigenvalue (sign(λ_2)ρ). The colour scheme is as follows: yellow for sulphur, red for oxygen, turquoise for nitrogen, grey for carbon, white for hydrogen.

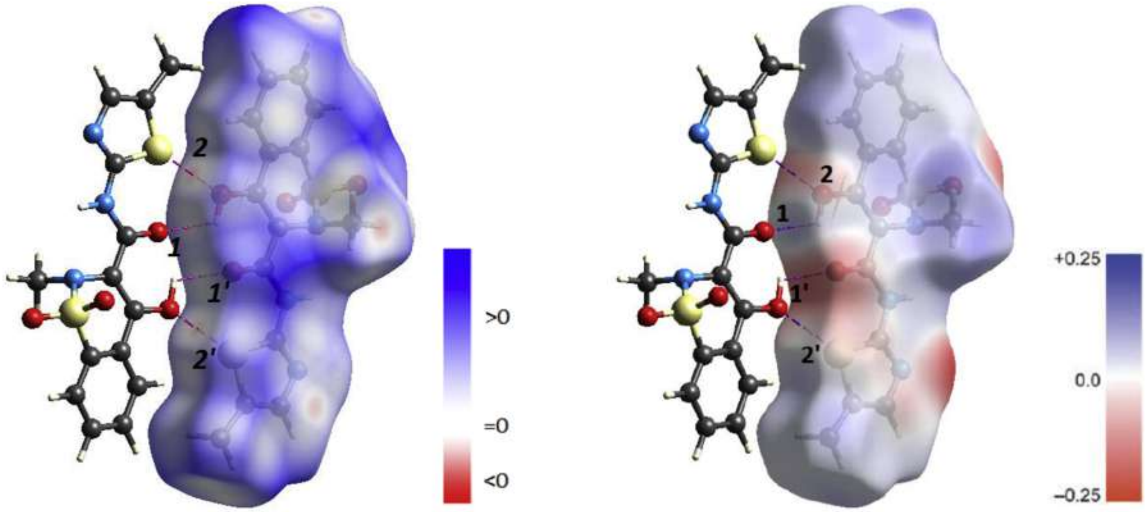

Fig. 5. Hirshfeld surfaces mapped with d_{norm} (a) and electrostatic potential (b) for the MXM molecule within the fragment ***B*** (as indicated in Fig. 2). The non-covalent interactions investigated are shown by violet dot lines and labelled with numbers: **1** and **1′** for O—H···O(=C) interactions; **2** and **2′** for S(thiazole)···O(hydroxyl) interactions (the prime symbol denotes the interactions which are identical by symmetry). The colour scheme is as follows: yellow for sulphur, red for oxygen, turquoise for nitrogen, grey for carbon, white for hydrogen.

4. Results and discussion

4.1. Identifying the main structural motif of meloxicam

To choose the correct model for non-covalent interactions within the MXM crystal structure, two main questions addressed in the previous studies need to be resolved. One of them was an object of controversy between Cheney et al. [26] and Tumanov et al. [27] and consists in whether infinite supramolecular chains or dimers are the main motifs within the crystal structure of meloxicam polymorph I. The structure consists of two types of molecular pairs (fragments ***A*** and ***B*** in Fig. 2) linked by different NCIs (Table 2). Re-phrasing the question, one needs to find out how strongly the MXM molecules are held together in each pair. The previous discussions [26,27] were built on the basis of geometrical parameters only and did not provide any quantitative comparison. The energy calculations of the above-described molecular pairs performed in the present work showed that the total energy (E_{TOT}) of fragment ***A*** is lower than ***B*** by 34.7 kJ/mol. This energy can be subdivided into several contributions: electrostatic, polarisation, dispersion and repulsion (Table 3). The contribution of the electrostatic term (E_{ele}) to the total energy of the two fragments drastically differs (Table 3). As this term gives a measure of the electrostatic attraction between two polar groups, a 54.4 kJ/mol lower E_{ele} of fragment ***A*** with respect to ***B*** should be related to the presence of a relatively strong H-bond in this fragment, unlike in the other one. Indeed, fragment ***A*** is formed *via* the N—H···O hydrogen bonds (Fig. 2). In this case, the hydrogen atom of the amide group covalently bonded with a highly electronegative nitrogen atom is in an electric field created by another closely located highly electronegative atom, namely the oxygen of the sulfonyl group of the neighbouring molecule (Fig. 2). The NCIs in fragment ***B*** apparently have essentially another nature. Based on the energy calculations, one can conclude that they are weaker and more van der Waals-like since the dispersion term has a predominant negative contribution to the total energy of the fragment.

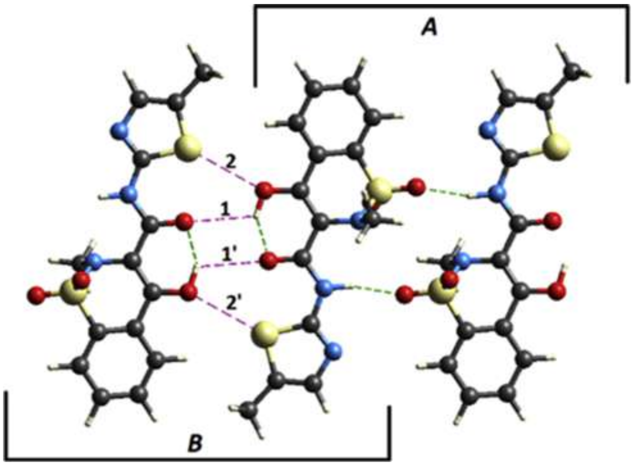

Fig. 6. The final model of non-covalent interactions within the crystal structure of meloxicam polymorph I. Fragment ***A*** is formed via N—H⋯O(=S) hydrogen bonds (shown as light green dot lines). The NCIs responsible for linking the molecules in fragment ***B*** are shown by violet dot lines and labelled with numbers: **1** and **1′** for O—H⋯O(=C) interactions; **2** and **2′** for S(thiazole)⋯O (hydroxyl) interactions (the prime symbol denotes the interactions which are identical by symmetry). The colour scheme is as follows: yellow for sulphur, red for oxygen, turquoise for nitrogen, grey for carbon, white for hydrogen.

It is important to note that a difference in NCIs is clearly reflected in the electron density distribution within the framework of Bader's theory of atoms in molecules (QTAIM) [50]. However, based on QTAIM, one can only identify the presence of intermolecular H-bonds through the investigation of bond critical points [50] along the bond paths between the hydrogen and the H-acceptor atoms [51]. For seeking the weaker intermolecular interactions of different nature, such as van der Waals interactions or steric repulsions, the NCI approach should be used. In the present work, this approach was implemented by a reduced density gradient (RDG) analysis [12,45–47] of the molecular fragments ***A*** and ***B*** within the MXM crystal structure. In the low-density, low-gradient region of the NCI plot associated with fragment ***B*** (Fig. 3a), all the values of reduced density gradient (s) fall very close to zero ($\rho < 0.008$ a.u.), indicating the presence of weak van der Waals interactions only. In case of fragment ***A***, the low-density, low-gradient region includes a spike lying at more negative values of $\text{sign}(\lambda_2)\rho$ (near -0.02 a.u., Fig. 4a) which are related to attractive medium-strength H-bonding. The gradient isosurface ($s = 0.05$ a.u.) plotted for fragment ***A*** (Fig. 4b) clearly visualises that these attractive interactions are located between the amide and sulfonyl groups of the neighbouring meloxicam molecules.

Thus, MXM molecules are bonded significantly stronger in fragment ***A*** and this fragment was correctly supposed by Tumanov et al. [27] to be the main structure-forming unit in the crystals of meloxicam polymorph I.

*4.2. Determination of the interactions responsible for linking the MXM molecules in fragment **B***

Despite the MXM molecules are linked stronger in fragment ***A*** than in ***B***, this fragment is being broken when the co-crystals of meloxicam with carboxylic acids are formed [20–28]. During this process, the H-bonds linking the MXM molecules are being replaced by H-bonds or other interactions with co-formers which are apparently more favourable. In this relation, it is interesting to note that much weaker interactions maintaining fragment ***B*** are present not only in the individual form of meloxicam but also in its co-crystals with a majority of co-formers. Cheney et al. [26] reported the S⋯O contacts to be responsible for linking the MXM molecules in this fragment. Tumanov et al. [27] mentioned that weak O—H⋯O(=C) interactions are present in this case, but the fragment is formed virtually due to steric effects. These contradictory suggestions lead to the second question to be resolved in the present study: which interactions are actually present in fragment ***B***? Both contacts revealed by Cheney et al. [26] and Tumanov et al. [27] are clearly seen on the d_{norm}-mapped Hirshfeld surfaces [11,43] of the MXM molecule (Fig. 5a). These surfaces provide a good visualisation of non-covalent contacts between two neighbouring molecules, combining the distances from a point on the surface to the nearest atoms inside and outside the surface with vdW radii of these atoms. In case of meloxicam, faint red spots in the region of surface associated to S⋯O contacts (Fig. 5a) indicate that the contact distance is slightly shorter than the sum of vdW radii of sulphur and oxygen. The O—H⋯O interactions are characterised by white colour on the surface showing that the contact distance is near the sum of vdW radii of the atoms in this case. However, all contacts are adjusted to a local crystalline environment and the comparison of the distances characterising them with a simple sum of van der Waals radii is not so helpful for a qualitative assessment of their strength and nature.

More specified information on intermolecular interactions can be obtained from Hirshfeld surfaces mapped with electrostatic potential (Fig. 5b) [11,41]. Two electronegative (red) and two electropositive (blue) patches can be observed in the region corresponding to the O—H⋯O (denoted as **1** and **1′** in Fig. 5b) and S⋯O (denoted as **2** and **2′** in Fig. 5b) interactions within the crystal structure of meloxicam. The red patches are associated with donor atoms (the hydroxyl oxygen for the S⋯O contacts and the carbonyl oxygen for the O—H⋯O interactions) while the blue ones are related to acceptors (the sulphur for the S⋯O contacts and the hydrogen of the hydroxyl group for the O—H⋯O interactions). The molecular pair formed *via* these contacts is centrosymmetric, therefore each molecule in it has both donor and acceptor atoms related to these interactions. It is clearly seen for both contacts that electronegative and electropositive regions are complementary so that the principle of electrostatic complementarity [11,41] is completely fulfilled in this case and neither of the contacts can be neglected.

The RDG analysis performed also shows the co-presence of the two interactions under consideration. Fig. 3b displays that the gradient isosurfaces ($s = 0.05$ a.u.) spread in the region related to both S⋯O and O—H⋯O intermolecular interactions. Since the density gradient (s) values lie close to zero value of density (Fig. 3a), these interactions are weakly attractive and van der Waals-like in nature. Thus, the information obtained from Hirshfeld surfaces agrees well with the results of NCI analysis and indicates that both interactions are responsible for linking the molecules within the crystal structure of meloxicam polymorph I. The model of NCIs in this system should definitely include both interactions as it is reflected in Fig. 6.

5. Conclusions

The final model of NCIs within the crystal structure of meloxicam polymorph I has been built on the basis of the results of DFT calculations, Hirshfeld surface analysis and investigation of the reduced density gradient (RDG) plots (Fig. 6). The main motif in the crystal structure is a repeating dimeric unit (denoted as fragment ***A*** in this study) formed *via* the medium-strength N—H⋯O hydrogen bonds. The other molecular pair within the crystal structure (fragment ***B*** in the present study) is linked by two types of weaker van der Waals interactions, namely the S⋯O and O—H⋯O contacts, both being present in the structure. Thus, the resulting model represents meloxicam dimers which are weakly bonded with each other and combines the two models proposed previously [26,27]. This case study of meloxicam in the polymorphic form I shows how applying different computational tools helps to investigate unclear NCIs within the crystal structure and can be useful for further studies of meloxicam co-crystals and analogous compounds.

Acknowledgements

The authors acknowledge the Supercomputing Center of the Novosibirsk State University (http://nusc.nsu.ru) for provided computational resources.

Tatiana N. Drebushchak acknowledges that this work was supported by the state assignment (project No. AAAA-A17-117030310274-5).

Appendix A. Supplementary material

Supplementary data contain the information on single-crystal X-ray diffraction data collection and refinement details, unit-cell parameters and atomic coordinates for the crystal structure of meloxicam refined at 100 K. In addition, they provide a list of frequencies obtained by phonon calculations of the fully optimized structure of meloxicam and the fingerprint of the Hirshfeld surface for meloxicam.

Supplementary data to this article can be found online at https://doi.org/10.1016/j.comptc.2019.04.012.

References

[1] P. Hobza, R. Zahradník, K. Müller-Dethlefs, The world of non-covalent interactions: 2006, Collect. Czechoslov. Chem. Commun. 71 (2006) 443–531, https://doi.org/10.1135/cccc20060443.

[2] P.R. Varadwaj, A. Varadwaj, H.M. Marques, K. Yamashita, Significance of hydrogen bonding and other noncovalent interactions in determining octahedral tilting in the CH 3 NH 3 PbI 3 hybrid organic-inorganic halide perovskite solar cell semiconductor, Sci. Rep. 91 (9) (2019) 50, https://doi.org/10.1038/s41598-018-36218-1.

[3] C. Kashyap, S.S. Ullah, L.J. Mazumder, A. Kanti Guha, Non-covalent interaction in benzene and substituted benzene: a theoretical study, Comput. Theor. Chem. 1130 (2018) 134–139, https://doi.org/10.1016/J.COMPTC.2018.03.023.

[4] J. Fan, W.Y. Sun, T.A. Okamura, Y.Q. Zheng, B. Sui, W.X. Tang, N. Ueyama, Novel metal-organic frameworks with specific topology formed through noncovalent Br⋯Br interactions in the solid state, Cryst. Growth Des. 4 (2004) 579–584, https://doi.org/10.1021/cg034190b.

[5] J. Černý, P. Hobza, Non-covalent interactions in biomacromolecules, Phys. Chem. Chem. Phys. 9 (2007) 5291, https://doi.org/10.1039/b704781a.

[6] W. Wang, O. Donini, C.M. Reyes, P.A. Kollman, Biomolecular simulations: recent developments in force fields, simulations of enzyme catalysis, protein-ligand, protein-protein, and protein-nucleic acid noncovalent interactions, Annu. Rev. Biophys. Biomol. Struct. 30 (2001) 211–243, https://doi.org/10.1146/annurev.biophys.30.1.211.

[7] K. Müller-Dethlefs, P. Hobza, Noncovalent Interactions: a challenge for experiment and theory, Chem. Rev. 100 (2002) 143–168, https://doi.org/10.1021/cr9900331.

[8] C. Dykstra, J. Lisy, Experimental and theoretical challenges in the chemistry of noncovalent intermolecular interaction and clustering, J. Mol. Struct. THEOCHEM. 500 (2000) 375–390, https://doi.org/10.1016/S0166-1280(00)00388-2.

[9] P.A. Kollman, Noncovalent interactions, Acc. Chem. Res. 10 (1977) 365–371, https://doi.org/10.1021/ar50118a003.

[10] A.J. Cruz-Cabeza, Crystal structure prediction: are we there yet? Acta Crystallogr. Sect. B Struct. Sci. Cryst. Eng. Mater. 72 (2016) 437–438, https://doi.org/10.1107/S2052520616011367.

[11] M.A. Spackman, D. Jayatilaka, Hirshfeld surface analysis, CrystEngComm 11 (2009) 19–32, https://doi.org/10.1039/B818330A.

[12] E.R. Johnson, S. Keinan, P. Mori-Sánchez, J. Contreras-García, A.J. Cohen, W. Yang, Revealing noncovalent interactions, J. Am. Chem. Soc. 132 (2010) 6498–6506, https://doi.org/10.1021/ja100936w.

[13] L. Goerigk, H. Kruse, S. Grimme, Benchmarking density functional methods against the S66 and S66x8 datasets for non-covalent interactions, ChemPhysChem 12 (2011) 3421–3433, https://doi.org/10.1002/cphc.201100826.

[14] C. Barberot, J.C. Boisson, S. Gérard, H. Khartabil, E. Thiriot, G. Monard, E. Hénon, AlgoGen: a tool coupling a linear-scaling quantum method with a genetic algorithm for exploring non-covalent interactions, Comput. Theor. Chem. 1028 (2014) 7–18, https://doi.org/10.1016/J.COMPTC.2013.11.020.

[15] A. Kellett, Z. Molphy, C. Slator, V. McKee, N.P. Farrell, Molecular methods for assessment of non-covalent metallodrug–DNA interactions, Chem. Soc. Rev. 48 (2019) 971–988, https://doi.org/10.1039/C8CS00157J.

[16] G.F. Fabiola, V. Pattabhi, S.G. Manjunatha, G.V. Rao, K. Nagarajan, IUCr, 4-hydroxy-2-methyl- *N* -(5-methyl-1,3-thiazol-2-yl)-2 *H* -1,2-benzothiazine-3-carboxamide 1,1-dioxide, Acta Crystallogr Sect. C Cryst. Struct. Commun. 54 (1998) 2001–2003, https://doi.org/10.1107/S0108270198008452.

[17] P. Luger, K. Daneck, W. Engel, G. Trummlitz, K. Wagner, Structure and physicochemical properties of meloxicam, a new NSAID, Eur. J. Pharm. Sci. 4 (1996) 175–187, https://doi.org/10.1016/0928-0987(95)00046-1.

[18] N. Seedher, S. Bhatia, Solubility enhancement of cox-2 inhibitors using various solvent systems, AAPS PharmSciTech 4 (2003) 36–44, https://doi.org/10.1208/pt040333.

[19] N.M. Davies, N.M. Skjodt, Clinical pharmacokinetics of meloxicam, Clin. Pharmacokinet. 36 (1999) 115–126, https://doi.org/10.2165/00003088-199936020-00003.

[20] R.P. Fernandes, A.L.C.S. do Nascimento, A.C.S. Carvalho, J.A. Teixeira, M. Ionashiro, F.J. Caires, Mechanochemical synthesis, characterization, and thermal behavior of meloxicam cocrystals with salicylic acid, fumaric acid, and malic acid, J. Therm. Anal. Calorim. (2019) 1–13, https://doi.org/10.1007/s10973-019-08118-7.

[21] C. Tantardini, S.G. Arkipov, K.A. Cherkashina, A.S. Kil'met'ev, E.V. Boldyreva, Synthesis and crystal structure of a meloxicam co-crystal with benzoic acid, Struct. Chem. 29 (2018) 1867–1874, https://doi.org/10.1007/s11224-018-1166-5.

[22] A.G. Ogienko, S.A. Myz, A.A. Ogienko, A.A. Nefedov, A.S. Stoporev, M.S. Mel'gunov, A.S. Yunoshev, T.P. Shakhtshneider, V.V. Boldyrev, E.V. Boldyreva, Cryosynthesis of Co-crystals of poorly water-soluble pharmaceutical compounds and their solid dispersions with polymers. The "Meloxicam–Succinic Acid" system as a case study, Cryst. Growth Des. 18 (2018) 7401–7409, https://doi.org/10.1021/acs.cgd.8b01070.

[23] C. Tantardini, S.G. Arkhipov, K.A. Cherkashina, A.S. Kil'met'ev, E.V. Boldyreva, IUCr, Crystal structure of a 2:1 co-crystal of meloxicam with acetylendicarboxylic acid, Acta Crystallogr. Sect. E Crystallogr. Commun. 72 (2016) 1856–1859, https://doi.org/10.1107/S2056989016018909.

[24] S.A. Myz, T.P. Shakhtshneider, N.A. Tumanov, E.V. Boldyreva, Preparation and studies of the co-crystals of meloxicam with carboxylic acids, Russ. Chem. Bull. 61 (2012) 1798–1809, https://doi.org/10.1007/s11172-012-0248-6.

[25] D.R. Weyna, M.L. Cheney, N. Shan, M. Hanna, M.J. Zaworotko, V. Sava, S. Song, J.R. Sanchez-Ramos, Improving solubility and pharmacokinetics of meloxicam via multiple-component crystal formation, Mol. Pharm. 9 (2012) 2094–2102, https://doi.org/10.1021/mp300169c.

[26] M.L. Cheney, D.R. Weyna, N. Shan, M. Hanna, L. Wojtas, M.J. Zaworotko, Supramolecular architectures of meloxicam carboxylic acid cocrystals, a crystal engineering case study, Cryst. Growth Des. 10 (2010) 4401–4413, https://doi.org/10.1021/cg100514g.

[27] N.A. Tumanov, S.A. Myz, T.P. Shakhtshneider, E.V. Boldyreva, Are meloxicam dimers really the structure-forming units in the 'meloxicam–carboxylic acid' co-crystals family? Relation between crystal structures and dissolution behaviour, CrystEngComm 14 (2012) 305–313, https://doi.org/10.1039/C1CE05902E.

[28] S.A. Myz, T.P. Shakhtshneider, K. Fucke, A.P. Fedotov, E.V. Boldyreva, V.V. Boldyrev, N.I. Kuleshova, Synthesis of co-crystals of meloxicam with carboxylic acids by grinding, Mendeleev Commun. 19 (2009) 272–274, https://doi.org/10.1016/J.MENCOM.2009.09.014.

[29] J.P. Perdew, W. Yue, Accurate and simple density functional for the electronic exchange energy: generalized gradient approximation, Phys. Rev. B 33 (1986) 8800–8802, https://doi.org/10.1103/PhysRevB.33.8800.

[30] J.P. Perdew, K. Burke, M. Ernzerhof, Generalized gradient approximation made simple, Phys. Rev. Lett. 77 (1996) 3865–3868, https://doi.org/10.1103/PhysRevLett. 77.3865.

[31] A. Otero-de-la-Roza, E.R. Johnson, Van der Waals interactions in solids using the exchange-hole dipole moment model, J. Chem. Phys. 136 (2012) 174109, https://doi.org/10.1063/1.4705760.

[32] A. Otero-de-la-Roza, E.R. Johnson, A benchmark for non-covalent interactions in solids, J. Chem. Phys. 137 (2012) 054103, https://doi.org/10.1063/1.4738961.

[33] P. Giannozzi, S. Baroni, N. Bonini, M. Calandra, R. Car, C. Cavazzoni, D. Ceresoli, G.L. Chiarotti, M. Cococcioni, I. Dabo, A. Dal Corso, S. de Gironcoli, S. Fabris, G. Fratesi, R. Gebauer, U. Gerstmann, C. Gougoussis, A. Kokalj, M. Lazzeri, L. Martin-Samos, N. Marzari, F. Mauri, R. Mazzarello, S. Paolini, A. Pasquarello, L. Paulatto, C. Sbraccia, S. Scandolo, G. Sclauzero, A.P. Seitsonen, A. Smogunov, P. Umari, R.M. Wentzcovitch, QUANTUM ESPRESSO: a modular and open-source software project for quantum simulations of materials, J. Phys. Condens. Matter. 21 (2009) 395502, https://doi.org/10.1088/0953-8984/21/39/395502.

[34] F.H. Allen, I.J. Bruno, IUCr, Bond lengths in organic and metal-organic compounds revisited: *X* —H bond lengths from neutron diffraction data, Acta Crystallogr. Sect. B Struct. Sci. 66 (2010) 380–386, https://doi.org/10.1107/S0108768110012048.

[35] D. Jayatilaka, D.J. Grimwood, Tonto: A Fortran Based Object-Oriented System for Quantum Chemistry and Crystallography, Springer, Berlin, Heidelberg, 2003, pp. 142–151 https://doi.org/10.1007/3-540-44864-0_15.

[36] M.J. Turner, J.J. McKinnon, S.K. Wolff, D.J. Grimwood, P.R. Spackman, D. Jajatilaka, M.A. Spackman, CrystalExplorer17, The University of Western Australia, 2017, http://hirshfeldsurface.net.

[37] A.D. Becke, Density-functional thermochemistry. III. The role of exact exchange, J. Chem. Phys. 98 (1993) 5648–5652, https://doi.org/10.1063/1.464913.

[38] S. Grimme, Semiempirical GGA-type density functional constructed with a long-range dispersion correction, J. Comput. Chem. 27 (2006) 1787–1799, https://doi.org/10.1002/jcc.20495.

[39] T.H. Dunning, Gaussian basis sets for use in correlated molecular calculations. I. The atoms boron through neon and hydrogen, J. Chem. Phys. 90 (1989) 1007–1023, https://doi.org/10.1063/1.456153.

[40] Michael J. Turner, Simon Grabowsky, Dylan Jayatilaka, Mark A. Spackman, J. Phys. Chem. Lett. 5 (2014) 4249–4255, https://doi.org/10.1021/jz502271c.

[41] M.A. Spackman, J.J. McKinnon, D. Jayatilaka, Electrostatic potentials mapped on Hirshfeld surfaces provide direct insight into intermolecular interactions in crystals, CrystEngComm 10 (2008) 377–388, https://doi.org/10.1039/b715227b.

[42] J.J. McKinnon, D. Jayatilaka, M.A. Spackman, Towards quantitative analysis of intermolecular interactions with Hirshfeld surfaces, Chem. Commun. (2007) 3814, https://doi.org/10.1039/b704980c.

[43] J.J. McKinnon, M.A. Spackman, A.S. Mitchell, IUCr, Novel tools for visualizing and exploring intermolecular interactions in molecular crystals, Acta Crystallogr. Sect. B Struct. Sci. 60 (2004) 627–668, https://doi.org/10.1107/S0108768104020300.

[44] M.A. Spackman, J.J. McKinnon, Fingerprinting intermolecular interactions in molecular crystals, CrystEngComm 4 (2002) 378–392, https://doi.org/10.1039/B203191B.

[45] A. Otero-de-la-Roza, E.R. Johnson, J. Contreras-García, Revealing non-covalent interactions in solids: NCI plots revisited, Phys. Chem. Chem. Phys. 14 (2012) 12165, https://doi.org/10.1039/c2cp41395g.

[46] G. Saleh, C. Gatti, L. Lo Presti, J. Contreras-García, Revealing non-covalent interactions in molecular crystals through their experimental electron densities, Chem. - A Eur. J. 18 (2012) 15523–15536, https://doi.org/10.1002/chem.201201290.

[47] J. Contreras-García, E.R. Johnson, S. Keinan, R. Chaudret, J.-P. Piquemal, D.N. Beratan, W. Yang, NCIPLOT: a program for plotting noncovalent interaction regions, J. Chem. Theory Comput. 7 (2011) 625–632, https://doi.org/10.1021/ct100641a.

[48] A. Otero-de-la-Roza, E.R. Johnson, V. Luaña, Critic2: a program for real-space analysis of quantum chemical interactions in solids, Comput. Phys. Commun. 185 (2014) 1007–1018, https://doi.org/10.1016/J.CPC.2013.10.026.

[49] A. Otero-de-la-Roza, M.A. Blanco, A.M. Pendás, V. Luaña, Critic: a new program for the topological analysis of solid-state electron densities, Comput. Phys. Commun. 180 (2009) 157–166, https://doi.org/10.1016/J.CPC.2008.07.018.

[50] R.F.W. Bader, Atoms in Molecules: A Quantum Theory, Clarendon Press, 1990.

[51] C. Tantardini, When does a hydrogen bond become a van der Waals interaction? a topological answer, J. Comput. Chem. 40 (2019) 937–943, https://doi.org/10.1002/jcc.25774.

Structural Chemistry
https://doi.org/10.1007/s11224-018-1166-5

ORIGINAL RESEARCH

Synthesis and crystal structure of a meloxicam co-crystal with benzoic acid

Christian Tantardini[1,2] · Sergey G. Arkipov[2,3] · Kseniya A. Cherkashina[2] · Alexander S. Kil'met'ev[2,4] · Elena V. Boldyreva[2,5]

Received: 18 June 2018 / Accepted: 16 July 2018
© Springer Science+Business Media, LLC, part of Springer Nature 2018

Abstract

Single crystals of a 1:1 co-crystal of meloxicam [4-hydroxy-2-methyl-N-(5-methyl-1,3-thiazol-2-yl)-1,1-dioxo-2H-1λ^6,2-benzothiazine-3-carboxamide], MXM, with benzoic acid, BZA, were crystalized from a THF solution. The same MXM-BZA co-crystal has been obtained as a fine powder by liquid-assisted co-grinding using as fluid additives solvents with different polarity: benzene, toluene, ortho-xylene, meta-xylene, para-xylene, THF, and water. The latter is especially eco-friendly and can be a good candidate for industrial production. The crystal structures of all the MXM co-crystals deposited in the most recent version of the Cambridge Database were compared, in order to correlate the non-covalent interactions in these structures with the conclusions from the theoretical analysis of solubility carried out by Cysewski (J. Mol. Model 24:112, 2018).

Keywords Oxicam · Meloxicam · Solubility · Benzoic acid · Co-crystal · Co-former · Aromatic · Carboxylic acid

Introduction

Meloxicam [4-hydroxy-2-methyl-N-(5-methyl-1,3-thiazol-2-yl)-1,1-dioxo-2H-1λ^6,2-benzothiazine-3-carboxamide], MXM, is an important active pharmaceutical ingredient (API) belonging to oxicam family, which represents a class of nonsteroidal anti-inflammatory drugs (NSAID) that selectively inhibit COX-2 over COX-1 receptors [1, 2]. MXM co-crystallizes with different co-formers (e.g., carboxylic acids) [3–7], as other members of this family (i.e., piroxicam, tenoxicam, and lornoxicam) do [8–10]. Co-crystallization helps to improve the solubility as compared with that of pure MXM [3–6, 11, 12]. Unfortunately, not all the co-formers in these co-crystals are pharmaceutically acceptable and therefore many co-crystals cannot in fact find a real application as drug forms. One of the fortunate exceptions is a MXM co-crystal with benzoic acid (BZA). It could be used for oral administration being not human toxic. A drawback of the MXM-BZA co-crystal is that its solubility is substantially lower, than that of the other MXM co-crystals with aromatic co-formers and is very close to the solubility of MXM pure form [6]. To rationalize the aqueous dissolution behavior of MXM and its co-crystals, it is important to know the crystal structures and non-covalent interactions that hold molecules together [5, 13]. Until this work, the MXM-BZA co-crystal could be obtained only as powder and its crystal structure (and thus even its exact composition) remained unknown [3, 4].

The aim of this work was to solve for the first time the MXM-BZA crystal structure and to compare different non-covalent interactions in this co-crystal with those in pure MXM [11, 12] and its other co-crystals [4, 5, 10, 14], in order to relate the crystal structures with aqueous dissolution behavior.

Electronic supplementary material The online version of this article (https://doi.org/10.1007/s11224-018-1166-5) contains supplementary material, which is available to authorized users.

✉ Christian Tantardini
christiantantardini@ymail.com

✉ Sergey G. Arkipov
arksergey@gmail.com

✉ Elena V. Boldyreva
eboldyreva@yahoo.com

[1] SkolTech Skolkovo Institute of Science and Technology, ul. Nobelya 3, Moscow, Russian Federation 121205

[2] Novosibirsk State University, ul. Pirogova 2, Novosibirsk, Russian Federation 630090

[3] Institute of Solid State Chemistry and Mechanochemistry SB RAS, ul. Kutateladze 18, Novosibirsk, Russian Federation 630128

[4] Novosibirsk Institute of Organic Chemistry SB RAS, Lavrentiev Ave. 9, Novosibirsk, Russian Federation 630090

[5] Boreskov Institute of Catalysis SB RAS, Laverentiev Ave. 5, Novosibirsk, Russian Federation 630090

Published online: 25 July 2018

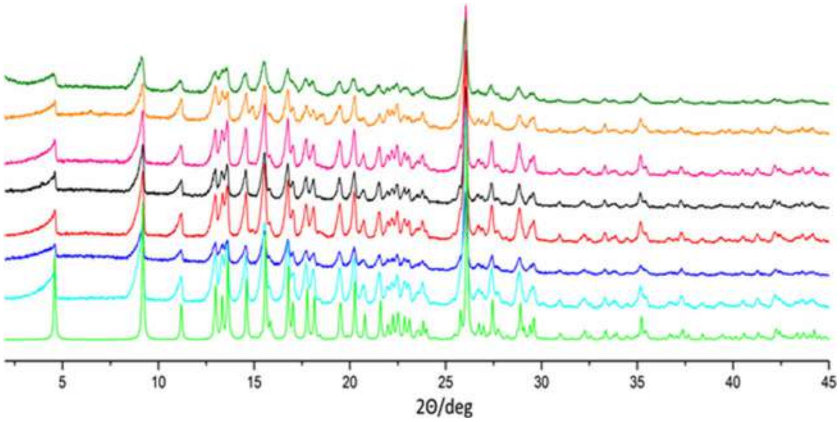

Fig. 1 XRPD patterns of samples prepared by liquid-assisted co-grinding of MXM with BZA; fluids added: water (olive), THF (orange), orto-xylene (purple), metha-xylene (black), para-xylene (red), benzene (blue), and toluene (turquoise); for a comparison—an XRPD pattern calculated from single-crystal X-ray diffraction data (green)

Experimental

Synthesis and characterization

MXM and benzoic acid (purity 99%) were purchased from Sigma-Aldrich. THF, benzene, toluene, o-xylene, m-xylene, and p-xylene were purchased from Reakhim and purified before using: THF was purified by sequential distillation over potassium hydroxide and over sodium, then distilled over sodium under an argon atmosphere; benzene and toluene were washed with concentrated sulfuric acid, then treated with potassium hydroxide, distilled over sodium, then distilled over sodium under an argon atmosphere; orto-xylene, mete-xylene, and para-xylene were distilled over sodium.

Table 1 MXM-BZA (1:1) single-crystal X-ray diffraction data collection and refinement

Crystal data	
Chemical formula	$C_{14} H_{13} N_3 O_4 S_2 \bullet C_7 H_6 O_2$
Mz	473.51
Crystal system space group	Triclinic, $P\overline{1}$
Temperature (K)	293
a, *b*, *c* (Å)	6.9679(4), 8.4287(5), 19.7001(10)
α, β, γ (°)	100.901(4), 92.770(4), 106.665(5)
V	1081.90(10)
Z	2
Radiation type	Mo *K* α1
μ (mm-^{1})	0.29
Crystal size (mm)	0.2 × 0.15 × 0.05
Data collection	
Diffractometer	Xcalibur, Ruby, Gemini ultra
Absorption correction	Multi-scan *CrysAlis PRO* 1.171.38.43 (Rigaku Oxford Diffraction, 2016) empirical absorption correction using spherical harmonics, implemented in SCALE3 ABSPACK scaling algorithm.
*T*min, *T*max	0.910, 1.000
No. of measured independent and observed [$I > 2\sigma(I)$] reflections	15,713, 3804, 2660
*R*int	0.049
(sin θ/λ)max (Å-1)	0.595
Refinement	
R[F2 > 2σ(*F2*)], wR(*F2*), *S*	0.042, 0.102, 1.05
No. of reflections	3804
No. of parameters	365
H-atom treatment	All H-atom parameters refined
Δρmax, Δρmin (e Å-3)	0.21, − 0.23

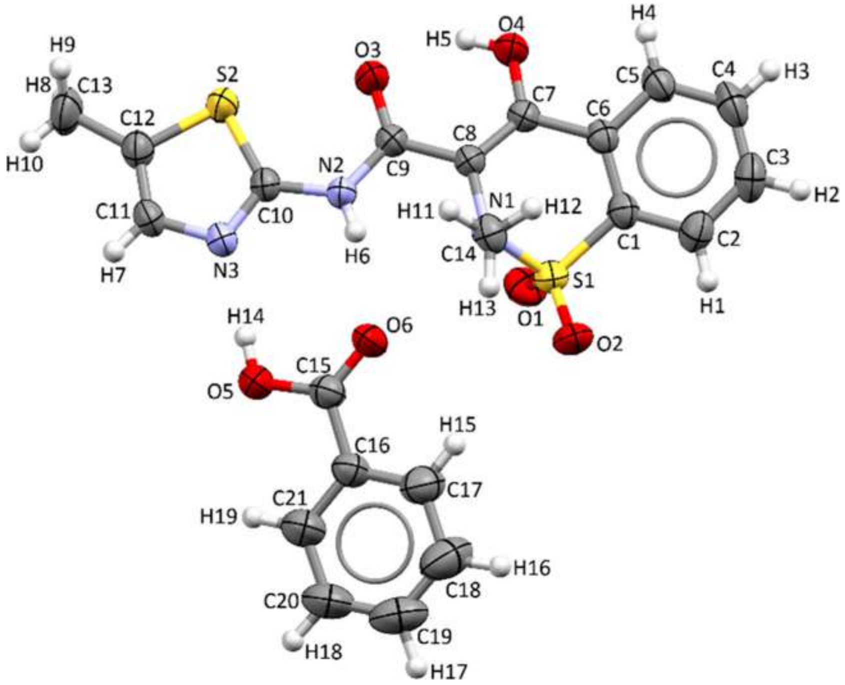

Fig. 2 Asymmetric unit of the 1:1 meloxicam (MXM) co-crystal with benzoic acid (BZA), the atom-numbering scheme is shown. Displacement ellipsoids are drawn at the 50% probability level

Crystals of MXM-BZA suitable for single-crystal X-ray diffraction analysis were obtained from a THF solution by slow evaporation. The equimolar amounts (0.0001 mol of MXM and 0.0001 mol of BZA) were dissolved in 15 ml of THF. The vessel was covered by parafilm in which two small holes were made. Crystallization was carried out at room temperature. The same experiments were made with benzene, toluene, ortho-xylene, meta-xylene, and para-xylene, but no single crystals were obtained.

MXM-BZA powder samples were obtained by liquid-assisted grinding method in a Retsch CryoMill (0.0002 mol of MXM and 0.0002 BZA, room temperature, 30 min, 25 Hz). For these experiments benzene, toluene, ortho-xylene, meta-xylene, para-xylene, THF, and water were used as fluid additives in the quantity of 200 µl for each one. The purity of samples was evaluated through X-ray determination comparing the experimental diffractograms with the theoretical pattern calculated based on single-crystal X-ray diffraction data (see Fig. 1).

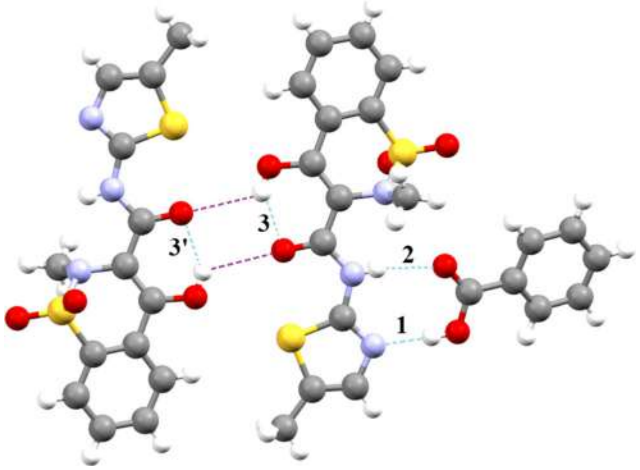

Fig. 3 A fragment of the MXM–BZA 1:1 co-crystal structure showing H-bonds in turquois (**1**, **2**, **3**, and **3′**) and the long O—H…O interactions in violet

X-ray diffraction structure determination

Single-crystal X-ray diffraction data for MXM:BZA (1:1) co-crystal were collected at room temperature (293 K) using an Agilent Xcalibur Ruby Gemini ultra diffractometer with Mo $K_{\alpha 1}$ radiation (λ = 0.71073 Å) and CrysAlis PRO software [15]. The crystal structure was solved using SHELXT [16] and Olex2 [17] as GUI and refined on F_{hkl}^2 with anisotropic displacement parameters for all the non-hydrogen atoms using SHELXL [16]. Hydrogen atoms positions were located from difference Fourier maps and refined freely. Olex2 [17] and

Table 2 Geometrical parameters (Å, °) for the O—H…N (**1**), N—H…O (**2**), O4—H5...O3 (**3**) interactions in the MXM:BZA 1:1 co-crystal (see also Fig. 3)

D—H...A	*D—H*	*H...A*	*D...A*	*D—$\widehat{H}$..A*
O5—H14...N3 (**1**)	0.85(3)	1.85(3)	2.700 (3)	176 (3)
N2—H6...O6 (**2**)	0.77(2)	2.11(3)	2.876 (3)	168 (3)
O4—H5...O3 (**3**)	0.83 (3)	1.91(3)	2.619 (3)	143 (3)

Table 3 Names, stoichiometries of the asymmetric units, space symmetry groups, bi-molecular or tri-molecular clusters and common structural motifs in pure MXM and its co-crystals

Structure	Ref. code/ CSD number	Stoichiometries	Space group	Bi-/tri-/tetra	Common structural motives
Meloxicam (MXM)	SEDZOQ/ 130826 [12] SEDZOQ01/ 107136 [11]	–	$P\bar{1}$	Bi	$R^2_2(14)$
MXM-BZA	1537194, this work	(1:1)	$P\bar{1}$	Bi	$R^2_2(8)$
Meloxicam-salicylic acid (form III)	ENICEK /819113 [4]	(1:1)	$P\,2_1/c$	Bi	$R^2_2(8)$
Meloxicam-1-hydroxy-2-naphthoic acid	ENIBOT/ 819110 [4]	(1:1)	$P\bar{1}$	Bi	$R^2_2(8)$
Meloxicam-acetylsalicylic acid	ARIFOX/ 801314 [23]	(1:1)	$P\,2_1/c$	Bi	$R^2_2(8)$
Meloxicam-succinic acid	ENICOU/ 819115 [4] ENICOU01/ 796926 [4]	(1:0.5)	$P\bar{1}$	Tri	$R^2_2(8) + R^2_2(8)$
Meloxicam-fumaric acid	ENICIO/ 819114 [6]	(1:0.5)	$P\bar{1}$	Tri	$R^2_2(8) + R^2_2(8)$
Meloxicam-acetylendicarboxylic acid	EBOLEP/ 1506179 [24]	(1:0.5)	$P\bar{1}$	Tri	$R^2_2(8) + R^2_2(8)$
Meloxicam-glutaric acid	ENIBUZ/ 819111 [4]	(1:1)	$P\bar{1}$	Tetra	$R^2_2(8) + R^2_2(8) + R^2_2(8)$
Meloxicam-adipic acid	FAKJOS/ 834808 [5]	(1:0.5)	$P\bar{1}$	Tri	$R^2_2(8) + R^2_2(8)$
Meloxicam-terephthalic acid	FAKJUY/ 834809 [5]	(1:0.5)	$P\bar{1}$	Tri	$R^2_2(8) + R^2_2(8)$

Table 4 Comparison of the geometrical parameters of the H-bonds and O…O interactions in meloxicam and its co-crystals

Structure	Ref. code/ CSD number	N—H…O, Å	N—H…O, °	O—H…N, Å	O—H…N, °	O…O, Å	O…O, °
Meloxicam (MXM)	SEDZOQ/ 130826 [12]	3.035(3) O from S-O group	167(3)	–	–	3.236(2)	129(4)
	SEDZOQ01/ 107136 [11]	3.028(2) O from S-O group	166(3)	–	–	3.232(2)	115(3)
MXM-BZA	1537194, this work	2.876(3)	168(3)	2.700(3)	176(3)	3.086(2)	121(3)
Meloxicam-salicylic acid (form III)	ENICEK /819113 [4]	2.968(3)	163.8	2.968(3)	170.4	–	–
Meloxicam-1-hydroxy-2-naphthoic acid	ENIBOT/ 819110 [4]	2.901(3)	166.5	2.563(3)	172.2	3.055(2)	117.9
Meloxicam-acetylsalicylic acid	ARIFOX/ 801314 [23]	2.858(3)	165.5	2.666(3)	174.2	–	–
Meloxicam-succinic acid	ENICOU/ 819115 [4]	2.871(2)	167(2)	2.697(2)	166(2)	2.935(1)	112(2)
	ENICOU01/ 796926 [4]	2.850(4)	164.3	2.683(4)	173.6	2.893(4)	115.2
Meloxicam-fumaric acid	ENICIO/ 819114 [6]	2.857(4)	160(3)	2.658(3)	174.4	2.902(3)	114.7
Meloxicam-acetylendicarboxylic acid	EBOLEP/ 1506179 [24]	2.922(3)	163.7	2.615(3)	174.5	2.943(2)	114.4
Meloxicam-glutaric acid	ENIBUZ/ 819111 [4]	2.839(2)	164.9	2.668(2)	173.96	2.907(2)	115.64
Meloxicam-adipic acid	FAKJOS/ 834808 [5]	2.866(3)	163(2)	2.663(3)	173(4)	–	–
Meloxicam-terephthalic acid-	FAKJUY/ 834809 [5]	2.984(2)	162(2)	2.639(2)	175(3)	–	–

Table 5 Centroid-topocentroid distances (up to 5 Å) and dihedral angels in the meloxicam co-crystals and pure meloxicam

Structure	Ref. code/ CSD number	Type of centroids	Distance between ring centroids, Å	Dihedral angle between planes formed by centroids, °
MXM-BZA	1537194, this work	THY…THY	3.7308(15)	12.06(13)
		AR-BZA AR-BZA	4.207(2)	0.00(18)
		THY…BZR	4.3977(15)	12.06(13)
Meloxicam-salicylic acid (form III)	ENICEK /819113 [4]	THY…AR	3.9539(18)	11.31(16)
		AR…AR	4.424(2)	0.02(17)
Meloxicam-1-hydroxy-2-naphthoic acid	ENIBOT/ 819110 [4]	THY…AR1	3.739(2)	3.07(13)
		BZR…AR2	3.893(2)	17.48(13)
		BZR…AR	4.236(3)	17.48(13)
		THY…AR	4.975(3)	4.93(14)
		THY…AR	4.653(3)	3.07(13)
Meloxicam-acetylsalicylic acid	ARIFOX/ 801314 [23]	THY…AR	3.7399(15)	6.37(12)
		THY…BZR	4.4354(15)	24.04(13)
Meloxicam-succinic acid	ENICOU01/ 796926 [4]	THY...BZR	3.7992(8)	5.53(7)
		THY…THY	4.1287(7)	0.02(7)
	ENICOU/ 819115 [4]	THY...BZR	3.730(2)	4.66(19)
		THY…THY	4.032(2)	0.00(18)
Meloxicam-fumaric acid	ENICIO/ 819114 [6]	THY...BZR	3.785(3)	3.81(14)
		THY…THY	4.104(3)	0.03(14)
Meloxicam-acetylendicarboxylic acid	EBOLEP/ 1506179 [24]	THY...BZR	3.7383(12)	6.68(11)
		THY…THY	4.1139(11)	0.00(10)
Meloxicam-glutaric acid	ENIBUZ/ 819111 [4]	THY...BZR	3.7542(16)	4.47(8)
		THY…THY	4.0222(17)	0.00(8)
Meloxicam-adipic acid	FAKJOS/ 834808 [5]	THY...BZR	4.6829(14)	24.04(11)
		THY…BZR	4.7330(16)	24.04(11)
Meloxicam-terephthalic acid	FAKJUY/ 834809 [5]	THY...BZR	4.5640(11)	20.18(9)
		THY…BZR	4.6658(11)	20.18(9)
Meloxicam	SEDZOQ/ 130826 [12]	THY...BZR	3.7440(16)	11.84(13)
		THY…BZR	4.2123(16)	11.84(13)
	SEDZOQ01/ 107136 [11]	THY...BZR	3.7498(17)	11.70(14)
		THY…BZR	4.2161(18)	11.70(14)

Mercury [18] were used to visualize the structures and to prepare the material for publication. The parameters characterizing data collection and refinement are summarized in Table 1.

All powder samples were characterized by XRPD using a Stoe Stadi-MP diffractometer with Cu Kα1 radiation (λ = 1.54060 Å) at operating potential of 40 kV and electric current of 40 mA, and a Mythen 1 K detector. All data were processed using WinXPOW [19] and Origin programs. XRPD patterns of the co-crystal sample were compared with the patterns of the starting reactants, MXM (CSD Refcode: SEDZOQ [12]), BZA (CSD Refcode: BENZAC02 [20], and powder pattern calculated from MXM-BZA single-crystal X-ray diffraction data (CSD Refcode: 1537194, this work) to prove the formation of the MXM-BZA co-crystal (Fig. 1).

Results and discussion

The asymmetric unit of the MXM-BZA co-crystal is shown in Fig. 2. The structure crystallizes in a triclinic $P\overline{1}$ space symmetry group.

A fragment of molecular structure is shown in Fig. 3, describing the typical NCI which are classified as H-bonds based on the geometrical criteria provided by Arunan et al. [21]. The components of the MXM-BZA structure are linked into a bimolecular cluster via the O—H…N (**1**) and N—H…O (**2**) hydrogen bonds (H-bonds) between MXM and BZA (see Table 2), to form a R_2^2 (8) ring (notations are as in Bernstein et al. [22]). Furthermore, there are long O—H…O interactions formed by the carbonyl and hydroxyl groups of the two MXM molecules, these groups being already involved into the O—H…O (**3**, **3′**) intramolecular H-bond (see Table 2).

Molecular packing and NCI in the MXM-BZA co-crystal can be compared with those in pure MXM and in the other MXM co-crystals (Tables 3, 4, and 5).

The MXM co-crystals can be classified into two groups depending on whether the co-former is a monocarboxylic or a dicarboxylic acid. In both groups, one can find aromatic carboxylic acids among co-formers: salicylic acid; 1-hydroxy-2-naphthoic acid; acetylsalicylic acid; terephthalic acid; benzoic acid (the structure solved in this work for the first time). Four of these co-formers are monocarboxylic acids, while the terephthalic acid is a dicarboxylic one.

The asymmetric units of co-crystals with monocarboxylic acids contain two molecules: MXM and a co-former (Fig. 2). Within this group, co-crystals of MXM with BZA and with 1-hydroxy-2-naphthoic acid have triclinic $P\overline{1}$ space symmetry, while co-crystals of MXM with salicylic acid (form III), and with acetylsalicylic acid, are monoclinic ($P2_1/c$ space symmetry). Structural motifs in MXM-BZA co-crystal are similar to those in the MXM co-crystal with 1-hydroxy-2-naphthoic acid; while MXM co-crystals with acetylsalicylic acid and salicylic acid form bimolecular clusters via O—H…N and N—H…O H-bonds between MXM and co-former, to give R_2^2 (8) rings.

Co-crystals of MXM with dicarboxylic acids contain one MXM molecule and a half of the co-former molecule in the asymmetric unit (Fig. 4). Within such co-crystals the components are linked into tri-molecular clusters via the O—H…N and N—H…O H-bonds between two carboxylic groups belonging to a co-former and two MXM molecules, to form two R_2^2 (8) rings [6].

The only known exception from this general trend is a co-crystal of MXM with glutaric acid (GLU), in which the asymmetric unit has two molecules: a MXM and a co-former. The components are linked into tetra-molecular clusters MXM:GLU:GLU:MXM with O—H…N and N—H…O H-bonds between MXM and GLU, to form R_2^2 (8) rings, and O—H…O H-bonds between two GLU molecules, also to form R_2^2 (8) rings (Fig. 5).

The analysis of different NCIs within pure MXM and its co-crystals shows that monocarboxylic acids form similar O—H…N and N—H…O H-bonds with a MXM molecule. What differentiates pure MXM structure and its co-crystals with monocarboxylic acids are the $\pi…\pi$ interactions. A MXM molecule itself has two aromatic fragments: thiazole (THY) and benzene (BZR) rings. These aromatic fragments can participate in the $\pi…\pi$ interactions both in pure MXM and in its co-crystals. The THY…BZR $\pi…\pi$ interactions are present in pure MXM and its co-crystals with non-aromatic acids, as well as with such aromatic acids as benzoic, acetylsalicylic, and terephthalic acids (Fig. 6e, b, c). The THY…THY $\pi…\pi$ interactions are present in the MXM co-crystals with non-aromatic acids, the co-crystal with the adipic acid being the only known exception.

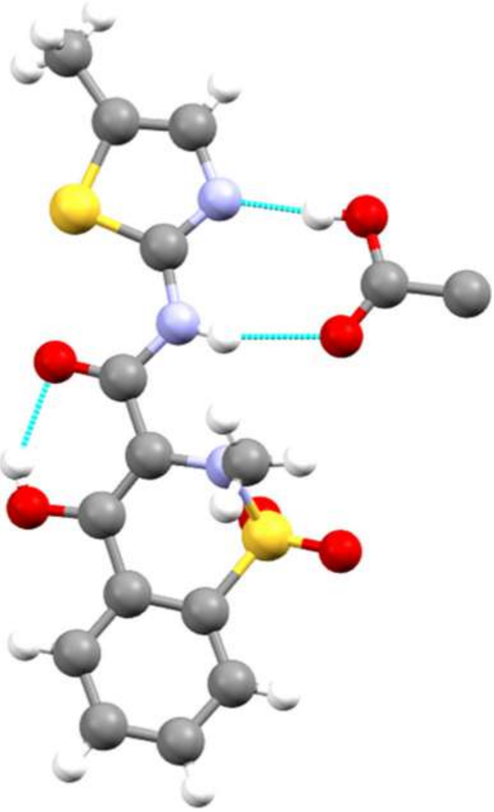

Fig. 4 Asymmetric unit of the 1:0.5 meloxicam (MXM) co-crystal with acetylendicarboxylic acid (ACA), H-bonds are shown turquois

THY and BZR are responsible also for the $\pi…\pi$ interactions with the aromatic ring (AR) belonging to co-former aromatic acids: THY…AR $\pi…\pi$ interaction are present in the MXM co-crystals with salicylic, 1-hydroxy-2-naphthoic, acetylsalicylic, and benzoic acids (Fig. 6a, b, e); BZR…AR $\pi…\pi$ interactions are present in the MXM co-crystals with 1-hydroxy-2-naphthoic acid (Fig. 6a).

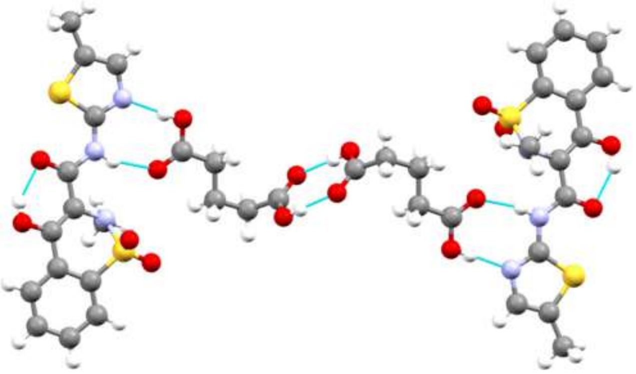

Fig. 5 A tetra-molecular cluster within the meloxicam (MXM) co-crystal with glutaric acid (GLU), H-bonds are shown in turquois

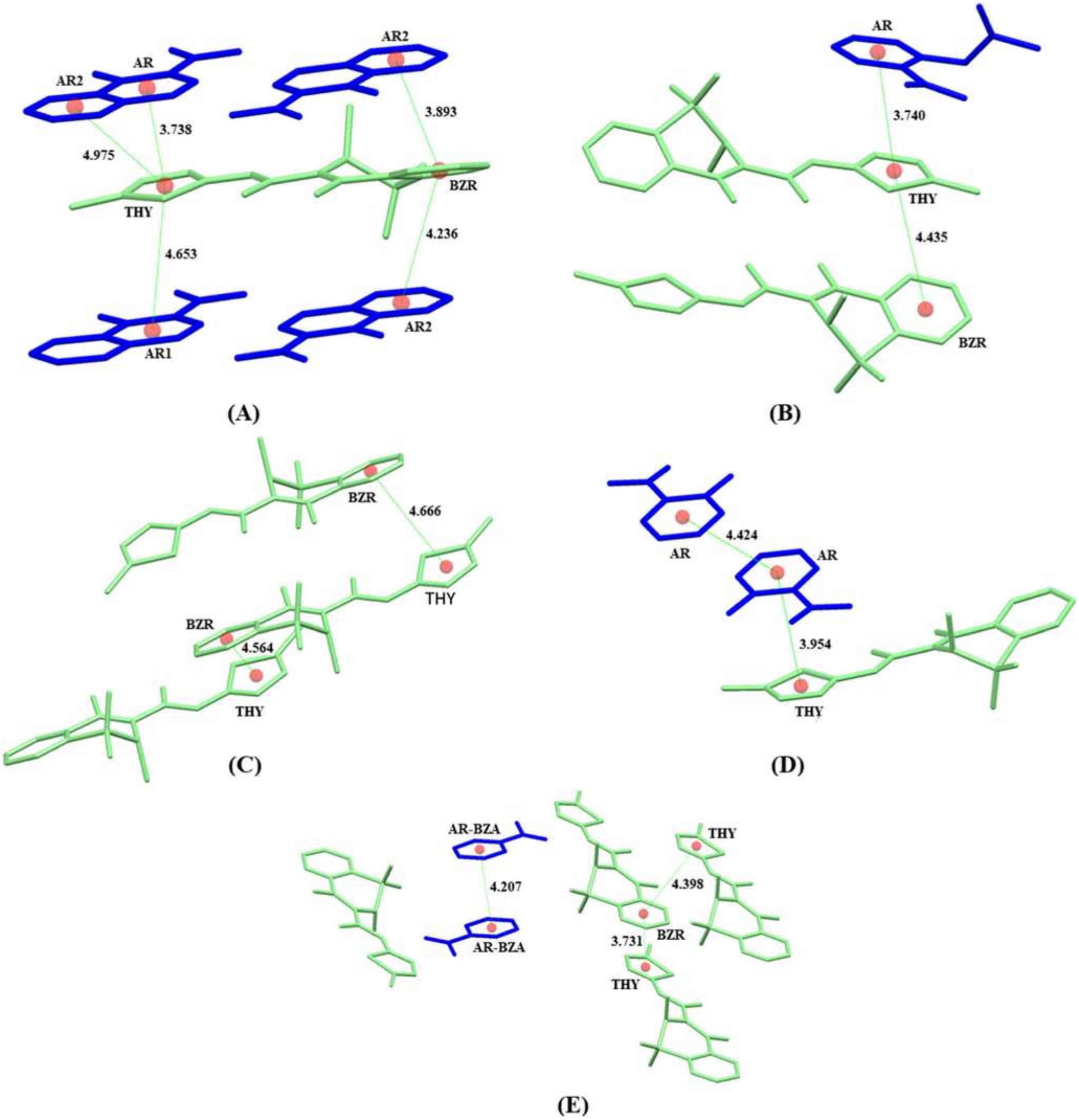

Fig. 6 Centroid/topocentroid (red balls) distances (Å) within MXM co-crystals with **a** 1-hydroxy-2-naphthoic acid [4], **b** acetylsalicylic acid [23], **c** terephthalic acid [5], **d** salicylic acid (form III) [4], and **e** BZA (this work)

These $\pi \ldots \pi$ interactions are not considered for the MXM co-crystal with terephthalic acid, because the distances between centroids (topocentroids[1]) between THY…AR and BZR…AR in this structure exceed 5 Å, that was considered as the upper limit for a possible $\pi \ldots \pi$ interaction. AR…AR $\pi \ldots \pi$ interactions are present also in the MXM co-crystals with salicylic and benzoic acids.

Conclusions

Recently, intermolecular interactions were considered as a direct measure of water solubility advantage of meloxicam cocrystalized with carboxylic acids [1]. It was argued that

---

[1] A topocentroid is a topological index that is calculated for a group of 5-atoms as proposed by Cremer et al. [25] and 6-atoms as proposed by Boeyens et al. [26].

solubility can be quantified by concentration of pairs of molecules formed in water. Extending this approach, one can compare the molecular clusters present in the crystalline state, prior to breaking the NCI as a result of the interaction with the solvent molecules. One can then notice that in the case of MXM co-crystals with non-aromatic carboxylic acids, both H-bonds and $\pi...\pi$ interactions are similar and the different solubility behavior can be related to the different carbon chain length of the carboxylic acids. In the case of the MXM co-crystals with aromatic carboxylic acids, the H-bonds are similar, but $\pi...\pi$ interactions are different, and this latter difference can account for the differences in the dissolution behavior. Both observations agree with the model proposed by Cysewski 2018 [13].

Earlier [5], the increase in the solubility of MXM co-crystals with dicarboxylic acids was supposed to be a consequence of the change in the intermolecular interactions in the solid when the dimers of MXM molecules (present in pure MXM) are broken by dicarboxylic acid molecules and the contact with solvent molecules is facilitated. A theoretical study by Cysewski [13] attempted to correlate aqueous dissolution of MXM co-crystals with the presence of certain molecular clusters in solution. The comparison of the solubilities of the crystalline co-crystals with aromatic and non-aromatic co-formers suggests that aqueous dissolution behavior of MXM co-crystals correlates also with the presence or the absence of the $\pi...\pi$ interactions in the crystal structure. The solubility is higher for those structures, in which there are the $\pi...\pi$ interactions between AR and MXM, like in most co-crystals with aromatic co-formers [4]. In the MXM-BZA co-crystal, these interactions are absent, and the solubility of this co-crystal is almost as low, as that of the pure MXM. This suggests, that for a higher aqueous solubility, it is important not only that the interactions between the MXM molecules in the crystals are weakened, as supposed in [5], but also that a complex formed by a MXM molecule and a co-former is preserved in solution, as modeled in [13]. In the case of MXM-BZA co-crystals, the weakness of the $\pi...\pi$ interactions between the MXM and the BZA molecules prevents the formation of such a complex in solution, and the solubility falls down, almost to the level of pure MXM.

Acknowledgments The authors received funding from the Russian Ministry of Science and Higher Education.

Compliance with ethical standards

Conflict of interest The authors declare that they have no conflict of interest.

References

1. Furst DE (1997). Semin Arthritis Rheum 26:21
2. Schattenkirchner M (1997) Expert. Opin. Investig. Drugs 6:321
3. Myz SA, Shakhtshneider TP, Fucke K, Fedotov AP, Boldyreva EV, Boldyrev VV, Kuleshova NI (2009). Mendeleev Communications 19:272
4. Cheney ML, Weyna DR, Shan N, Hanna M, Wojtas L, Zaworotko MJ (2010). Cryst Growth Des 10:4401
5. Tumanov NA, Myz SA, Shakhtshneider TP, Boldyreva EV (2012). CrystEngComm 14:305–313
6. Weyna DR, Cheney ML, Shan N, Hanna M, Zaworotko MJ, Sava V, Song S, Sanchez-Ramos JR (2012). Mol Pharm 9:2094
7. Myz SA, Shakhtshneider TP, Tumanov NA, Boldyreva EV (2012). Russ Chem Bull 9:1782
8. Fucke K, Myz SA, Shakhtshneider TP, Boldyreva EV, Griesser UJ (2012). New J Chem 36:1969
9. Bolla G, Sanphui P, Nangia A (2013). Cryst Growth Des 13:1988
10. Suresh K, Nangia A (2014). Cryst Growth Des 14:2945
11. Luger P, Daneck K, Engel W, Trummlitz G, Wagner K (1996). Eur J Pharm Sci 4:175
12. Fabiola GF, Pattabhi V, Manjunatha SG, Rao GV, Nagarajan K (1998) Acta Crystallogr. Sect C 54:2001
13. Cysewski P (2018). J Mol Model 24:112
14. Uhlemann T, Seidel S, Müller CW (2017). Phys Chem Chem Phys 19:14625
15. Rigaku OD (2016). *CrysAlis PRO*. Rigaku Oxford diffraction Ltd, Yarnton
16. Sheldrick GM (2015). Acta Cryst. C 71:3
17. Dolomanov OV, Bourhis LJ, Gildea RJ, Howard JAK, Puschmann H (2009). J Appl Crystallogr 42:339
18. Macrae CF, Bruno IJ, Chisholm JA, Edgington PR, McCabe P, Pidcock E, Rodriguez-Monge L, Taylor R, van de Streek J, Wood PA (2008). J Appl Crystallogr 41:466
19. Stoe & Cie (1999) WinXPOW. Stoe & Cie, Darmstadt
20. Feld R, Lehmann MS, Muir KW, Speakman JC (1981). K Zeitschriftfür Kristallographie 157:215
21. Arunan E, Desiraju GR, Klein RA, Sadlej J, Scheiner S, Alkorta I, Clary DC, Crabtree RH, Dannenberg JJ, Hobza P, Kjaergaard HG, Legon AC, Mennucci B, Nesbitt DJ (2011) Pure Appl. Chem 83:1637
22. Bernstein J, Davis RE, Shimoni L, Chang NL (1995). Angew Chem Int Ed Engl 34:1555
23. Cheney ML, Weyna DR, Shan N, Hanna M, Wojtas L, Zaworotko MJ (2011). J Pharm Sci 100:2172
24. Tantardini C, Arkhipov SG, Cherkashina KA, Kil'met'ev AS, Boldyreva EV (2016). Acta Cryst. E 72:1856
25. Cremer D, Pople JA (1975). J Amer Chem Soc 97:1354
26. Boeyens JCA (1978). J Cryst Mol Struct 8:317

Published on 18 July 2019. Downloaded by Bundesanstalt fuer Materialforschung und -pruefung on 8/9/2019 5:03:49 PM.

CrystEngComm

ROYAL SOCIETY OF CHEMISTRY

PAPER

View Article Online
View Journal

Check for updates

Cite this: DOI: 10.1039/c9ce00874h

The role of S-bond in tenoxicam keto–enolic tautomerization†‡

Sergey G. Arkhipov,[abc] Peter S. Sherin,[*ad] Alexey S. Kiryutin,[ad] Vladimir A. Lazarenko[e] and Christian Tantardini§[*f]

A non-steroidal anti-inflammatory drug, 4-hydroxy-2-methyl-*N*-2-pyridyl-2*H*-thieno(2,3-e)-1,2-thiazine-3-carboxamide 1,1-dioxide, called tenoxicam (TXM), with important implications in cancer treatment, has a peculiarity with respect to other molecules from the oxicam family. TXM is predominantly found in the zwitterionic form (ZWC) within the crystal structures of pure compounds and their solvates; however, it can be present in the β-keto–enolic form (BKE) or β-diketone (BDK) form. To understand this phenomenon, the combined effects of environment (solvent) and intra-molecular non-covalent interactions on the TXM keto–enol tautomerization were investigated through a combined experimental and computational study. We found that the polarity of a solvent had a minor influence on the crystallization process; this allowed to us synthesize and solve six new solvates with TXM in the ZWC form. Careful investigation of the non-covalent interactions between the sulphur atom of thiophenyl moiety and oxygen of the carbonyl group (S-bond) through a computational approach with the natural bond orbital (NBO) theory has shown that TXM crystallization is modulated by the S-bond. This study further confirms the importance of the S-bond in the drug design; however, nowadays, it is still underestimated.

Received 5th June 2019,
Accepted 10th July 2019

DOI: 10.1039/c9ce00874h

rsc.li/crystengcomm

Introduction

Oxicams belong to the family of non-steroidal anti-inflammatory drugs, which are widely used in the treatment of osteoarthrosis.[1] In the last decade, oxicams attracted significant attention due to their application in cancer treatment.[2–6] Note that oxicams, as a large part of active pharmaceutical agents, are administrated in solid dosage forms. Thus, the crystalline forms will be dissolved first through the gastrointestinal tract, and then, they will be absorbed. Oxicams are typically characterized by low water solubility with dissolution rate slower than the absorption rate, thus providing high bioavailability of drug after its dissolution.[7–27] Actually, the best way to improve their solubility is their co-crystallization with different co-formers, for instance, organic dicarboxylic acids,[7–21] albeit the oxicam molecular structures are characterised by several protropic groups with the possibility to modulate different keto–enolic forms. *Via* this way, 4-hydroxy-2-methyl-*N*-2-pyridyl-2*H*-thieno(2,3-e)-1,2-thiazine-3-carboxamide 1,1-dioxide, tenoxicam (TXM), shows a peculiarity with respect to other oxicams. TXM has been found in the zwitterionic form (ZWC)[7–22] (within pure, co-crystals and solvate structures), cationic form[7–21] (within salts with strong organic and inorganic acids) and anionic form (within salts with piperazine[3–21]). Moreover, meloxicam, which consists of a thiophenyl group within the backbone, is typically present in the β-keto–enolic form (BKE)[7–21,26,27] (*i.e.*, within pure and co-crystal structures). Albeit, the TXM-ZWC form has the peculiarity to be more water soluble as compared to other oxicams. This increases the dissolution rate, thus significantly reducing the time from its oral administration to real effectiveness in the body. Thus, to modulate the tautomerization of oxicams, it is necessary to understand the reason behind the impossibility to find TXM in the BKE form within crystal structures. To date, these causes are unknown, leaving it an open question of the last few decades.

---

[a] *Novosibirsk State University, Pirogova str. 2, 630090 Novosibirsk, Russian Federation*
[b] *Boreskov Institute of Catalysis SB RAS, Prospekt Akademika Lavrentyeva, 5, 630090 Novosibirsk, Russian Federation*
[c] *Institute of Solid State Chemistry and Mechanochemistry SB RAS, Kutateladze str. 18, 630128 Novosibirsk, Russian Federation*
[d] *International Tomography Center, Institutskaya 3a, 630090 Novosibirsk, Russian Federation. E-mail: sherin@tomo.nsc.ru*
[e] *National Research Center "Kurchatov Institute", Akademika Kurchatova square 1, 123182, Moscow, Russian Federation*
[f] *Center for Energy Science and Technology, Skoltech Skolkovo Institute of Science and Technology, Nobelya str. 3, 143026 Moscow, Russian Federation. E-mail: christiantantardini@ymail.com*

† Dedicated to the memory of Dr. Alexey P. Chupakhin (1952–2018).

‡ Electronic supplementary information (ESI) available: UV-vis and NMR spectra, crystallographic information. CCDC 1538111, 1538134, 1890995, 1904022, 1904023 and 1904101. For ESI and crystallographic data in CIF or other electronic format see DOI: 10.1039/c9ce00874h

§ CT is responsible for the work conception and administration.

Published on 18 July 2019. Downloaded by Bundesanstalt fuer Materialforschung und -pruefung on 8/9/2019 5:03:49 PM.

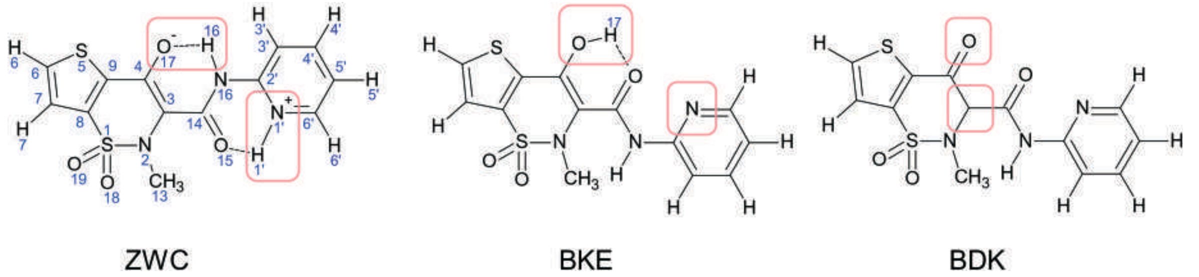

Fig. 1 TXM molecular structures of three different forms: zwitterionic (ZWC), left; β-keto–enolic (BKE), center; and β-diketone (BDK), right. Structural differences between forms are highlighted by red.

TXM keto–enol tautomerization can be correlated with different positions of aromatic rings within the molecular structure: the proximity of the sulphur atom of the thiophenyl ring to the protropic group leads to its involvement in the keto–enol tautomerization. The sulphur atom within the thiophenyl moiety is present in the bivalent form, ensuring the presence of low energy σ* orbitals belonging to the C–S bonds. This provides ground for the non-covalent interactions (NCIs) of the sulphur atom with electron donors including oxygen O17 (see Fig. 1 for atom numeration), which is largely involved in the TXM tautomerization. This NCI, called as the sulphur bond (S-bond), is isosteric with the hydrogen bond (H-bond).[28] Although the S-bond has been found to modulate the molecular conformation in the context of drug design and organic synthesis, it is rather under-estimated.[28] Furthermore, as TXM keto–enolic equilibrium can be modulated by solvent polarity, it can be modulated in solvent assistant crystallization techniques.[28] Thus, the co-presence of all the abovementioned factors creates a fascinating mix, which should be decoded not only to provide an answer to the open question about TXM, but also to obtain information on how to modulate the keto–enol tautomerization. This is important for many other active pharmaceutical ingredients, in particular, anticancer drugs containing sulphur groups within the molecular structures.

Herein, we carried out a combined experimental and computational study on the TXM keto–enol tautomerization. In the beginning, the effect of solvent polarity on the TXM conformation was studied by optical (absorption, fluorescence) and NMR spectroscopies. Next, we tried to use different solvents to obtain the BKE form of TXM within the crystals obtained from a liquid environment; the solvent-assisted crystallization led to the formation of five new solvates (CSD refcode: 1890995, 1904023, 1904022, 1538111, 1538134, 1904101), whose structures were solved through X-ray single-crystal diffraction. Furthermore, the purity of some synthesized substances was confirmed by X-ray powder diffraction method. Finally, the effect of the S-bond on the keto–enol tautomerization was computationally investigated by the examination of the S-bond strength within each TXM form *in vacuo* and subsequent comparison with the TXM conformations extracted from the crystal structures. This analysis has shown a direct correlation between keto–enol tautomerization and the formation of the S-bond within the TXM structure.

Results and discussion

To study the influence of solvent polarity on the TXM keto–enolic equilibrium in solution, we looked the experimental absorption and fluorescence spectra at room temperature in the presence of various solvents and absorption spectra at different temperatures for some of these solvents.

In low polarity solvents, TXM exhibits absorption and fluorescence bands with maxima at 345 and 500 nm, respectively (Fig. 2A), the positions of which are weakly dependent on the solvent polarity (Fig. 2B and Table S1 of ESI‡). The experimental optical data show the presence of one strongly predominant form, initially called ***A*** that has been confirmed by the complete coincidence of the fluorescence excitation spectra with the absorption spectrum (see Fig. 2A for chloroform and S2 in ESI‡ for cyclohexane, dioxane and toluene). The large Stokes shift of around 9×10^3 cm^{-1} indicated significant reorganization of the TXM electron density in the excited state due to charge transfer from amino to carbonyl and sulfonic groups. The excited state of this form was characterized by weak emission with the quantum yield (Φ_F) of around 2×10^{-3} (see Table S1 in ESI‡ for details) and very short fluorescence lifetime <20 ps (Fig. S3 in ESI‡).

In polar solvents, the experimental absorption spectra showed a shoulder at $\lambda > 400$ nm, whose contribution increased with the increasing solvent polarity (Fig. 2B). This band should be assigned to another form of TXM, initially called ***B***, present in polar solvents. The fluorescence emission and excitation spectra showed only the signal from the ***A*** form (Fig. 2C) and no measurable signal for the ***B*** form with excitation at $\lambda > 400$ nm. This indicated very low emission from the ***B*** form with the Φ_F value $< 10^{-4}$. Hence, the absorption and fluorescence data are in favour of the domination of the form ***A*** in low polarity solvents and the co-presence of the ***A*** and ***B*** forms in solvents with high polarity.

Speculating that the keto–enolic equilibrium between the ***A*** and ***B*** forms in polar solvents could be shifted by temperature, we obtained the TXM absorption spectra in acetone and acetonitrile under different ambient conditions (Fig. 2D and S4 in ESI,‡ respectively). For both solvents, a contribution from a long absorbing shoulder significantly increased with the lowering of temperature. This showed an increasing presence of the ***B*** form with respect to that of the ***A*** form at low temperatures and *vice versa* at high

Published on 18 July 2019. Downloaded by Bundesanstalt fuer Materialforschung und -pruefung on 8/9/2019 5:03:49 PM.

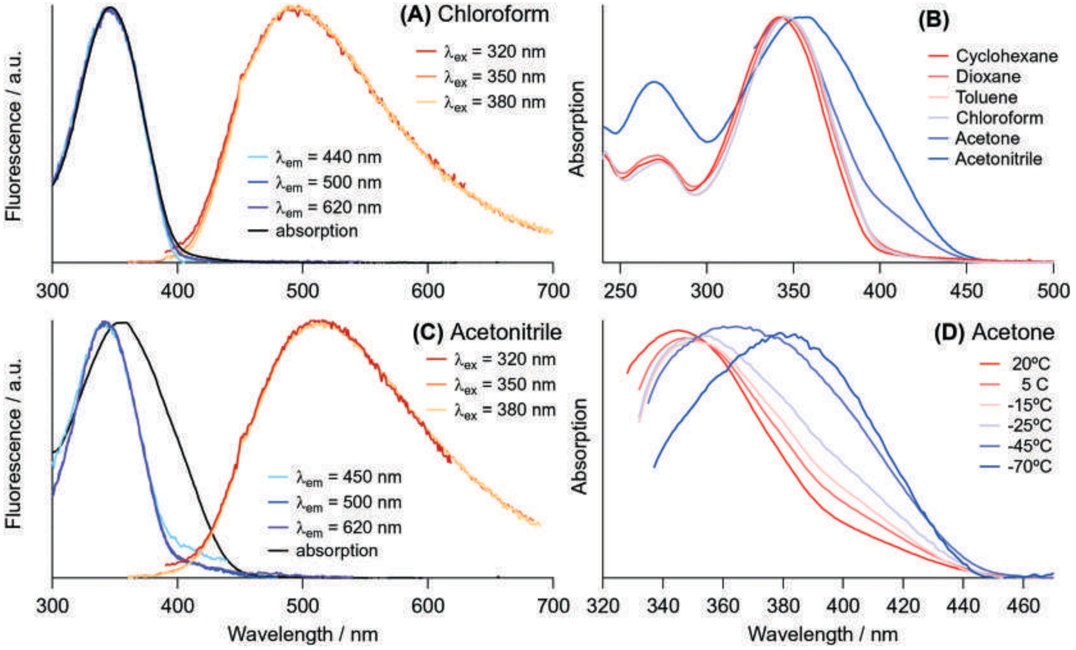

Fig. 2 Absorption and fluorescence emission and excitation spectra obtained for TXM in (A) chloroform and (C) acetonitrile at different excitation and emission wavelengths. (B) TXM absorption spectra in various solvents at room temperature. (D) TXM absorption spectra in acetone at different temperatures.

temperatures. Additional temperature experiments for TXM in low polar chloroform showed a minor variation in the absorption band shape (Fig. S4 in ESI‡) in the studied temperature range. This could be interpreted as a minor contribution of the form ***B*** in chloroform or high similarity between the absorption spectra of the ***A*** and ***B*** forms in low polarity solvents.

To assign which of the TXM keto–enol forms (see Fig. 1 for structures) belongs to the ***A*** and ***B*** forms observed in a liquid environment, we performed a set of NMR measurements using various 1D- and 2D-techniques (see Fig. S5–S19 in ESI‡). The ^{1}H NMR spectrum of TXM in chloroform showed a broadening of peaks corresponding to highly labile protons (O–H and N–H groups), suggesting a high proton exchange between the TXM molecule and residual water. This indicates a solvent-assisted inter-molecular proton transfer between TXM and solvent molecules that makes it difficult to assign the observed peaks to one or another TXM form. To slow down the exchange between the TXM forms and residual water, we obtained the NMR spectra of TXM in chloroform at various temperatures (Fig. 3). The lowering of temperature led to the appearance of new peaks in the ^{1}H NMR spectrum, which became dominating at the lowest possible temperature of −55 °C. This is followed by almost complete vanishing of the peaks observed at +25 °C (Fig. 3). At the intermediate temperature of −25 °C in the 2D NOESY (EXSY) spectrum (Fig. S16 of ESI‡) strong cross-peaks between two sets of peaks were observed that indicated a slow exchange between the two forms of the TXM molecule. For labile protons, additional cross-peaks between residual water (~1.6 ppm) were found. This leads to a solvent-assisted inter-molecular proton transfer between TXM and chloroform to some extent with consequent keto–enol tautomerization between the two forms ***A*** and ***B***.

To fully assign all signals, a set of 1D and 2D NMR spectra were obtained at temperatures 25 °C and −25 °C. The appearance of two additional cross-peaks in the ^{15}N-HSQC at low temperatures (Fig. S17 in ESI‡) undoubtedly proves the existence of the ZWC form, whereas at 25 °C, the ^{15}N-HSQC spectrum contains only one cross-peak (Fig. S9 in ESI‡). The cross-peaks in the ^{15}N-HSQC spectra indicate the presence of N–H covalent bonds in the TXM molecule. Therefore, the NMR spectra proved the presence of both the BKE and ZWC form in chloroform with the former as the predominant form at 25 °C and the latter as the predominant form at −55 °C. Analogous NMR data obtained for TXM in acetone and acetonitrile (Fig. S18 and S19 of ESI‡) have shown the co-presence of the ZWC and BKE forms at room temperature and the dominance of the ZWC form at low temperatures. This unambiguously assigns the form ***A*** observed by optical methods to the BKE form and the form ***B*** to the ZWC form. Note that in chloroform, acetonitrile and acetone, the BDK form is not present. Indeed, the BDK form has a –CH fragment at the position 3 (see Fig. 1), which should provide a signal at the chemical shift of around 4.5 ppm in the NMR spectra. However, no lines in the region 3.5–6.5 ppm for all used solvents (see Fig. S5, S7–S9 of ESI‡) clearly confirmed the absence of this form of TXM in the solution.

Subsequently, the effects of solvent on the TXM crystallization were examined by the growth of solvates, which were characterized by the presence of solvent molecules within the unit cell together with TXM.

Previously, experiments have been reported about the formation of TXM solvates with the following solvents:

Published on 18 July 2019. Downloaded by Bundesanstalt fuer Materialforschung und -pruefung on 8/9/2019 5:03:49 PM.

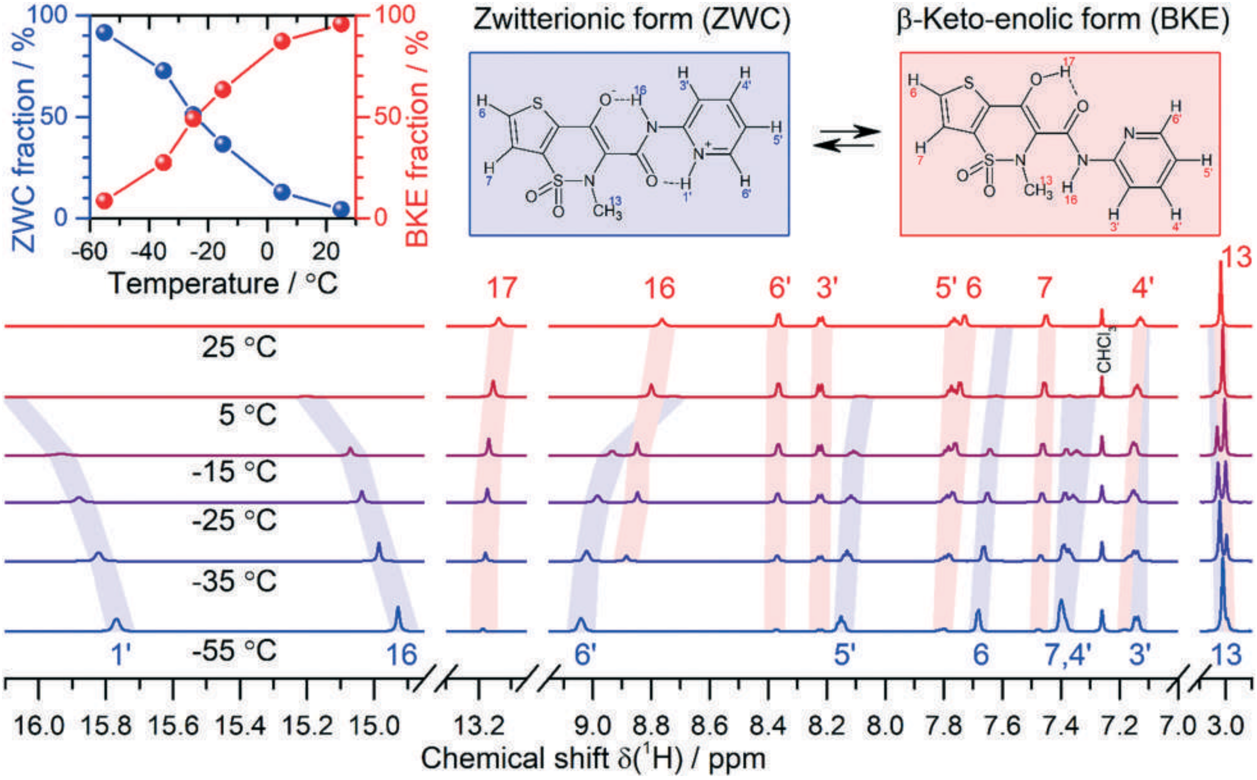

Fig. 3 700 MHz ^{1}H NMR spectra of tenoxicam in $CDCl_3$ detected at various temperatures in the range from −55 to 25 °C. All protons of both ZWC and BKE forms are assigned. The measured fractions of the ZWC and BKE forms are shown in the inset (top-left). The ZWC form is predominant at low temperatures, whereas at high temperatures, the BKE form is favorable. High values of the chemical shifts of the protons 16, 1′ and 17 prove that these atoms participate in hydrogen bonding, forming geometrically stable six-atom rings.

acetonitrile,[22,24] dioxane, *N*,*N*-dimethylformamide (DMF), ethyl acetate, acetone, isopropyl alcohol,[23] chloroform (only one solvate),[15] formic acid, acetic acid, propionic acid and nitromethane.[16] This literature data clearly shows that TXM forms solvates easily with polar solvents than with low and non-polar solvents.

Considering the optical and NMR data about the dominance of the BKE form in low polarity solvents at room temperature, we tried to obtain solvates containing TXM in the BKE form by its crystallization from cyclohexane, toluene, dioxane and chloroform. These experiments showed no crystal phase from cyclohexane and the powder of the TXM polymorph I from dioxane and toluene. Crystallization from chloroform provided single crystals of three different solvates: TXM-$CHCl_3$-I, TXM-$CHCl_3$-II and TXM-$CHCl_3$-III (Tables S20 and S21 in ESI‡ and XRPD patterns S22 and S23 in ESI‡). In all these solvates, TXM is present in the ZWC form. The same ZWC form was found within the single crystals obtained from more polar solvents: acetone (TXM-ACE), *N*,*N*-dimethylformamide (TXM-DMF) and acetonitrile (TXM-ACY),¶ see Table S20 and S21 in ESI‡ and the XRPD patterns S22 and S23 in ESI.‡ Additional details about the crystal structures could be found in the subsection "Crystal structure determination" of the Experimental section at the end of this manuscript.

The comparison between the structures of solvates obtained in this study and those already reported in literature has shown that two TXM-ZWC molecules are interconnected through the N^+–H···O hydrogen bond between the pyridyl and keto groups in the $R^2_2(4)$ $S^1_1(6)$ motif of the TXM molecules. On each side of this dimer, one or two solvent molecules are connected *via* the O–H···O^- hydrogen bond,[16] C–H···O,[16] C–H···N (ref. 22) and C–H···Cl interactions. Total 4 or 6 solvent molecules lie almost in the same plane (Fig. 4a). These units, consisting of two TXM and solvent molecules, are mutually oriented at different angles depending on the structure considered (Fig. 4a). A distinctive feature of the TXM-$CHCl_3$-I structure is the absence of this unit (Fig. 4b). Thus, the spatial organization of molecules in the analyzed structures can be sufficiently different despite insignificant differences in the ZWC conformations within the crystal structures. Moreover, we compared ZWC geometries within all crystal structures through the root-mean square deviation (RMSD) of the backbone atomic positions, without hydrogen atoms (see Table S24 in ESI‡). This analysis has confirmed high coincidence of the ZWC conformations within crystals that indicates a very rigid conformation of the TXM molecule, which is literally unchanged under different intermolecular interactions.

Thus, to understand the nature of TXM crystallization in ZWC form independently from the ratio between different

---

¶ The crystal structure was obtained from the literature.[22]

This journal is © The Royal Society of Chemistry 2019

Published on 18 July 2019. Downloaded by Bundesanstalt fuer Materialforschung und -pruefung on 8/9/2019 5:03:49 PM.

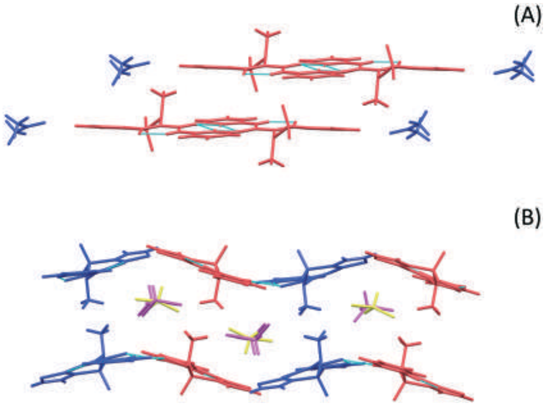

Fig. 4 Fragments of TXM solvates with (A) acetone (TXM-ACA) where TXM and solvent have mutual arrangement in space of two ACA-TXM-TXM-ACA tetramers, and (B) chloroform (TXM-CHCl3-I) where TXM layers are separated by the insertion of solvent. The turquoise dash lines represent the intra- and intermolecular H-bonds.

keto–enolic forms present in solution we examined the structures of all TXM keto–enol forms through a computational approach. The geometries of all three TXM forms were optimized *in vacuo* using density functional theory (DFT), and the thermodynamic parameters were subsequently calculated at 298.15 K for each form. In the first step, we found that the BKE form was the most thermodynamically stable form followed by ZWC and BDK (ΔG between BKE and these two forms was 2.20 kcal mol^{-1} and 12.49 kcal mol^{-1}, see Table S25 in ESI‡). It is important to emphasize that the BKE form is characterized by a large twist between the 2-pyridyl ring and the TXM backbone with respect to the almost flat ZWC form. This difference between BKE and ZWC could be quantified by the dihedral angle 1′–2′–16–14 (see Fig. 1 for atom numeration), which was 42.72° and −1.31° for the former and the latter, respectively, with a total difference between them being *ca.* 45°. Thus, BKE has been found to have the most steric hindrance with respect to ZWC. Therefore, BKE will have to undergo torsion to minimize its steric hindrance to compete with ZWC during crystallization.

To quantify the $\Delta G_{\text{BKE}\rightarrow\text{ZWC}}$ variation for the BKE ground state with respect to flattened BKE, we performed a scan of the BKE dihedral angle 1′–2′–16–14 *in vacuo* from the equilibrium angle (*i.e.*, 42.72°) to 0° (*i.e.*, 180°) with the step of 10°. The torsion increases the BKE electronic molecular energy, see Fig. 5, reducing the $\Delta G_{\text{BKE}\rightarrow\text{ZWC}}$ at 298.15 K from 2.20 kcal mol^{-1} for the BKE ground state to 0.15 kcal mol^{-1} for flattened BKE (*i.e.*, dihedral angle equal to 0°). This small ΔG value shows that BKE and ZWC are similar in energy for the flattened BKE conformation. Thus, the steric hindrance cannot be the driving force of crystallization, which must be investigated in different ways.

Note that all oxicams are characterized by their molecular structure with intra-molecular H-bonds N16–H16···O17$^-$ for ZWC and O17–H17···O15 for BKE (Fig. 1). Although the negative charge-assisted H-bond observed within the ZWC form is considered as the strongest H-bond present in nature,|| not all oxicams are present in the ZWC form within crystals. Oxicams containing a thiophenyl ring at different places of their structures demonstrate different keto–enol tautomerization within the crystal phase: for example, meloxicam, which possesses a thiophenyl ring far away from the protropic group, is found in the BKE form; on the other hand, lornoxicam, which has a thiophenyl ring close to the protropic group, is found in the ZWC form. Thus, H-bonds could not be responsible for the TXM crystallization in ZWC, and another NCI should modulate this process.

This NCI could be the S-bond due to the presence of the sulphur atom close to protropic groups involved in the keto–enol tautomerization.[7–27] The S-bond is an interaction between empty σ* orbitals of C–S bonds, which are low in energy, and the lone pair of oxygen belonging to the protropic groups involved in the keto–enol tautomerization. Thus, this oxygen atom is the so called S-acceptor. As reported by Beno *et al.*,[28] although S-bond plays an important role in the crystallization process, to date, it remains underestimated, especially for a large amount of pharmaceutical compounds containing sulphur.

The presence of the S-bond could be estimated by the natural bond orbital (NBO) theory[29–34] through an interaction between the lone pair of S-acceptor, oxygen atom involved in the keto–enol tautomerization of TXM, and C–S σ* orbitals.[28] NBO allows to explain molecular properties in terms of a Lewis structure depiction of the wave function with direct correspondence to the elementary Lewis dot diagram of freshman chemistry. One-center (lone pair) and two-center bond pair of a Lewis diagram are associated to complete the orthonormal set of NBOs, whereas the remaining ‘non-Lewis’-type NBOs describe the residual resonance delocalization effects (variation from idealized Lewis representation). This combination between the Lewis and the ‘non-Lewis’ structures represents the connection between the modern wave function technology and the elementary valency and bonding concepts.

At the beginning, we calculated the NBOs for all three TXM forms previously optimized *in vacuo*, and the presence of the S-bond was observed only for the ZWC and BKE forms. The interaction energy between the lone pair of S-acceptor and C–S σ* orbitals was estimated through the perturbation theory,[35] which showed the strongest S-bond for ZWC (*i.e.*, 12.71 kcal mol^{-1}) with respect to that for BKE (*i.e.*, 0.80 kcal mol^{-1}). Subsequently, the NBO analysis has shown that the flattening of the BKE form *via* the planarization of the dihedral angle 1′–2′–16–14 reduces the energy of interaction associated with the S-bond down to zero for the planar configuration. The latter could be explained by the mechanism of S-bond formation suggested by Glusker:[36] the S-bond could be formed either *via* electrophilic attack perpendicularly to the C–S–C plane or *via* the nucleophilic attack along one of the C–S bond directions. In the case of the ZWC form, the

---

|| This has been confirmed by subsequent NBO analysis with strongest interaction energy for ZWC with respect to that for planar BKE (Table S26 in ESI‡).

Published on 18 July 2019. Downloaded by Bundesanstalt fuer Materialforschung und -pruefung on 8/9/2019 5:03:49 PM.

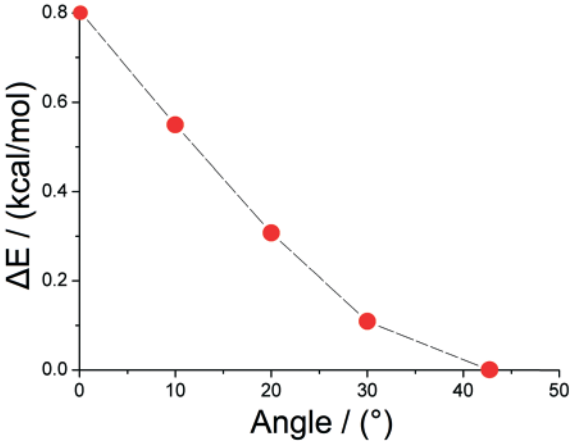

Fig. 5 Delta of electron energy (Δ*E*) for TXM-BKE *in vacuo* with variation of the dihedral angle 1′–2′–16–14, see Fig. 1 for atom numeration.

S-bond is formed with a nucleophile anion oxygen (O^-), whereas in the case of the BKE form, the S-bond is formed with oxygen belonging to the electrophilic hydroxyl group (O–H). Thus, the flattening of the dihedral angle in BKE breaks down the perpendicular orientation of O–H with respect to that of C–S–C plane, leading to the rupture of the S-bond.

Based on the obtained results, we can draw the following picture of the TXM crystallization. In the first step, the steric hindrance of the BKE form should be reduced through the torsion of the dihedral angle 1′–2′–16–14. This equilibrates the energies of the BKE to the ZWC forms with consequent disappearance of the S-bond in BKE. From this point, the strongest S-bond will modulate the TXM crystallization only in the ZWC form. Thus, one or another keto–enol form with respect to the intra-molecular H-bond is modulated by the S-bond; this is in agreement with the experimental results.

This could be generalized for other members of the oxicam family. If the S-bond is formed with the S-acceptor in proximity to the protropic group, crystallization will proceed *via* ZWC form. However, if the S-acceptor is far from the protropic group, we will have BKE like in the case of meloxicam. Therefore, the influence of the S-bond could be extended to all oxicams.

Conclusions

The polarity of a solvent modulates the TXM keto–enol equilibrium in solution with the dominance of the BKE form in low polarity solvents and the ZWC form in high polarity solvents. Regardless of the starting conformation, the crystallization process always leads to the ZWC form within the crystal structures. This makes the variation of solvent polarity to crystallize TXM in one or another keto–enolic form meaningless. The DFT calculations conducted *in vacuo* show that the most thermodynamically stable TXM tautomer is the BKE form with a characteristic feature as the twist between the 2-pyridyl ring and the TXM backbone, whereas the WC form has an almost planar structure. The planarization of the BKE form diminishes the energy difference between the flatten BKE and ZWC forms to almost 0.15 kcal mol^{-1}, which indicates the presence of another weak interaction within the TXM molecule predisposing it to crystallization in the ZWC form. This weak interaction was shown to be the S-bond between the thiophenyl ring and carbonyl oxygen according to the analysis of intramolecular interactions *via* the NBO theory.[29–34] This S-bond is significantly stronger for the ZWC form as compared to that for the flatten BKE form; this directs the crystallization of TXM only in the ZWC form.

Computational

The geometries of the electronic ground state for three keto–enolic TXM forms, *i.e.* zwitterionic (ZWC), β-keto–enol (BKE), and β-diketone (BDK), were optimized in the vacuum gas phase using the restricted density functional theory (DFT) with the B3LYP[37] and 6-311++G(2d,2p) basis set.[38,39] All minimum potential energy surfaces were confirmed by frequency analysis using harmonic approximation without scaling factor, being absent in literature. Subsequently, for all previously optimized TXM forms, the NBO[29–34] analysis was performed. Furthermore, for BKE, previously optimized *in vacuo*, a scan of the dihedral angle 1′–2′–16–14 (Fig. 1) was executed from an equilibrium angle (*i.e.*, 42.72°) to 0° (*i.e.*, 180°) with the step of 10°, and for the flat BKE, the NBO[29–34] analysis was performed.

All calculations were performed using Gaussian v.16 (Revision A.03).[40]

Experimental

UV-vis absorption and fluorescence

The UV-vis absorption spectra were obtained using the Agilent HP 8453 (Agilent, USA) spectrophotometer. The fluorescence excitation and emission spectra were obtained using the FLSP920 spectrofluorometer (Edinburgh Instruments, UK). All fluorescence spectra were corrected for the wavelength-dependent sensitivity of the detection. The fluorescence quantum yields were determined with respect to kynurenine in a neutral aqueous solution ($\Phi_F = 8.2 \times 10^{-3}$ (ref. 41)). The fluorescence dynamics was determined using a time-correlated single-photon counting (TCSPC) unit of the FLSP920 spectrofluorometer. The time profiles were determined at the maximum of emission bands after excitation at 375 nm (diode laser EPL-375, full width at the half maximum ≈ 80 ps).

NMR

All the NMR spectra were obtained using the Bruker AVANCE III HD spectrometer at 16.4 T (700 MHz proton frequency) using a 5 mm TXI z-gradient probe. For the NMR spectra, we used a solution of 2–3 mg tenoxicam in deuterated chloroform, acetone-d_6 and in CD_3CN (saturated solution). One-

This journal is © The Royal Society of Chemistry 2019

Published on 18 July 2019. Downloaded by Bundesanstalt fuer Materialforschung und -pruefung on 8/9/2019 5:03:49 PM.

dimensional ^{1}H and $^{13}C\{^{1}H\}$ and two dimensional NOESY, ^{13}C-HSQC, ^{13}C-HMBC, ^{15}N-HSQC were used to unambiguously assign all signals in $CDCl_3$. The chemical shifts of ^{1}H and ^{13}C nuclei were related to the resonance of chloroform-d_1.[42] The ^{15}N chemical shift has not been adjusted and used as it is from the TOPSPIN software, which uses indirect referencing. Temperature variation was achieved using cold nitrogen gas from the liquid nitrogen evaporator (standard Bruker equipment). A complete assignment of the ^{1}H, ^{13}C and ^{15}N nuclei is presented in Table 1 for the two forms of TXM in chloroform-d_1.

In all three solvents, by lowering temperature, we detected the formation of the ZWC form of tenoxicam. At low temperatures, we observed two signals at about 15–16 ppm. These high chemical shifts are unusual and appear only when the proton is connected to an electronegative atom, such as N or O, and also participates in hydrogen bonding with the second electronegative atom. Similar chemical shifts of protons can be found in the double-stranded DNA duplex, where the imino protons of guanine and thymine located between two N atoms form a Watson–Crick pair.[43] Note that at intermediate temperatures (−25 °C in chloroform), two forms are in exchange with each other; this is confirmed by strong cross-peaks in the 2D EXSY spectrum, as shown in the ESI.‡ The ratio between ZWC and BKE is determined by the temperature (Fig. 5 NMR).

Synthesis and investigation of the TXM solvates

Herein, three sets of crystallization experiments were performed in chloroform: at room temperature, at −18 °C in Novosibirsk city and at −18 °C at the "Kurchatov Institute" in the Center for Synchrotron Radiation and Nanotechnology (Moscow). In every experiment, approximately 0.125 g of TXM was dissolved under slow heating in 7 ml of chloroform. Crystallization at room temperature provided a powder containing two single crystals. Single crystal X-ray diffraction experiment was performed for one of these crystals, and the structure of TXM-$CHCl_3$-I was solved. The calculated powder diffraction of this structure was identical to the experimental powder diffraction determined for the TXM-$CHCl_3$ solvate obtained in the literature[18] (see S22 in ESI‡). X-ray powder diffraction study of the remaining powder showed that this powder of TXM I was a polymorph modification. Crystallization at −18 °C provided needle-shaped crystals, which were very long and thin. We tried to obtain the single crystal X-ray data from these crystals using a laboratory diffractometer in the Department of Solid State Chemistry at the Novosibirsk State University; however, the intensity of the reflections was not enough for structure solution, and only cell parameters were identified. The cell parameters do not match with the cell parameters of TXM-$CHCl_3$-I or with the cell parameters of the known structure of the third polymorphic modification

Table 1 Chemical shifts and assignments of two forms of tenoxicam in chloroform-d_1. Numbering is shown on Fig. 1[a]

Nuclei number	Chemical shift of **ZWC** form (ppm)			Chemical shift of **BKE** form (ppm)			Difference of chemical shifts
Proton	Experimental at −55 °C	Experimental at −25 °C	Predicted by Mnova	Experimental at 25 °C	Experimental at −25 °C	Predicted by Mnova	"ZWC-BKE" at 25 °C (ppm)
H3′	**7.17**	**7.17**	7.45	**8.22**	**8.25**	7.12	−1.08
H4′	**8.17**	**8.14**	8.01	**7.77**	**7.82**	7.72	0.32
H5′	**7.41**	**7.38**	7.80	**7.13**	**7.18**	6.69	0.2
H6′	**9.07**	**9.00**	7.97	**8.37**	**8.39**	8.30	0.61
H1′ (NH)	**15.79**	**15.91**	14.21	**NA**	**NA**	NA	—
H17 (OH)	**NA**	**NA**	NA	**13.14**	**13.20**	11.19	—
H16 (NH)	**14.96**	**15.06**	9.23	**8.77**	**8.88**	9.41	6.18
H13 (CH_3)	**3.04**	**3.05**	3.09	**3.02**	**3.03**	2.86	0.02
H6	**7.71**	**7.66**	7.56	**7.73**	**7.79**	7.47	−0.13
H7	**7.42**	**7.40**	7.44	**7.45**	**7.49**	7.42	−0.09
Carbon							
C2′	**149.69**	**149.88**	147.1	**150.70**	**149.91**	150.6	−0.03
C3′	**115.59**	**115.56**	119.7	**114.44**	**114.41**	115.0	1.15
C4′	**145.72**	**145.48**	143.1	**138.45**	**138.94**	138.1	6.54
C5′	**118.24**	**117.99**	125.5	**120.85**	**121.03**	119.5	−3.04
C6′	**138.48**	**138.06**	142.0	**148.46**	**148.41**	149.1	−10.35
C3	**108.16**	**108.15**	106.0	**111.23**	**110.34**	127.6	−2.19
C4	**167.13**	**NM**	146.6	**156.80**	**156.23**	154.5	10.33[b]
C6	**131.99**	**131.74**	121.2	**132.52**	**132.98**	124.1	−1.24
C7	**123.74**	**123.58**	123.9	**124.07**	**124.07**	124.7	−0.49
C8	**136.39**	**137.36**	138.1	**138.67**	**137.65**	140.1	−0.29
C9	**144.67**	**144.30**	133.8	**135.66**	**135.04**	126.7	9.26
C13	**40.48**	**40.24**	36.1	**40.28**	**40.34**	375	−0.1
C14	**168.55**	**NM**	165.3	**167.14**	**NM**	166.3	1.41[b]
Nitrogen							
N1′	**NM**	**164**	412.7	**NM**	**NM**	275.1	—
N16	**NM**	**118**	121.6	**135**	**148**	126.9	−30

[a] NA - not available, NM – not measured. [b] Calculated for different temperatures, chemical shift prediction was done in Mnova software version 12.

Published on 18 July 2019. Downloaded by Bundesanstalt fuer Materialforschung und -pruefung on 8/9/2019 5:03:49 PM.

of tenoxicam. We suggest that it is the second polymorph modification of the TXM chloroform solvate and call this phase TXM-$CHCl_3$-II. The FTIR spectrum was obtained for this substance. XRPD shows that the TXM-$CHCl_3$-II phase is not the TXM I polymorph modification or TXM-$CHCl_3$-I, and after heating to a temperature of 160 °C degrees and keeping for 1.5 hours at this temperature, the TXM-$CHCl_3$-II phase transforms to the TXM I polymorph modification (see S23 in ESI‡). For the determination of the TXM-$CHCl_3$-II structure, we repeatedly grew the TXM-$CHCl_3$-II crystals at −18 °C at the "Kurchatov Institute" in the Center for Synchrotron Radiation and Nanotechnology (Moscow). To our surprise, except for the crystals of TXM-$CHCl_3$-II, we found new block-shaped crystals. The cell parameters of this phase did not match with the cell parameters of the TXM-$CHCl_3$-I solvate and TXM-$CHCl_3$-II solvate. We called this phase TXM-$CHCl_3$-III.

The crystals of the TXM-ACE solvate were synthesized by dissolving 20 mg of TXM in 10 ml acetone and crystallization under room conditions. The crystals of the TXM-DMFA solvate were synthesized by dissolution of 33.7 mg of TXM in 2 ml of *N*,*N*-dimethylformamide and crystallization at 4 °C. The crystals of TXM-ACE and TXM-DMFA were obtained and characterized only through XRPD early in Cantera *et al.* (2002);[23] however, the crystal structures were not previously solved.

Experiments with cyclohexane (20 mg of TXM/50 ml cyclohexane), toluene (14 mg of TXM/17 ml toluene) and dioxane (20 mg of TXM/10 ml dioxane) were also carried out. No crystal phase was obtained in the case with cyclohexane, and the powder of the TXM polymorph I was found by the XRPD method in the toluene and dioxane cases.

XRPD

All powder samples were characterized by XRPD using the Stoe & Stadi-MP diffractometer with Cu Kα radiation (λ = 1.54060 Å) at the operating potential of 40 kV and the electric current of 40 mA and the Mythen 1 K detector.

FTIR spectroscopy

The powder of TXM-$CHCl_3$-II was extracted from chloroform on filter paper just before obtaining the spectra. The FTIR ATR spectra were obtained using DigiLab Excalibur 3100, Varian spectrometer equipped with a MIRacle ATR accessory in the range 600–4000 cm^{-1} with the resolution of 2 cm^{-1} without any sample preparation.

Crystal structure determination

Suitable-quality crystals of TXM-$CHCl_3$-I, TXM-ACE, TXM-DMFA solvates were selected using polarized light *via* a microscope and mounted by means of MiTeGen MicroMounts using MiTiGen LV Cryo Oil (LVCO-1) onto the Xcalibur (Ruby, Gemini Ultra; ω-scan mode) diffractometer. Suitable-quality crystals of TXM-$CHCl_3$-II andTXM-$CHCl_3$-III were investigated using the "Belok" beamline (λ = 0.7937 Å, direct (θ = 0°) geometry, φ-scan mode) at Kurchatov Synchrotron Radiation Source (National Research Center 'Kurchatov Institute' in Moscow). The diffraction data were obtained at 293(2) K for TXM-$CHCl_3$-I, TXM-ACE, and TXM-DMFA crystals and at 100(2) K for TXM-$CHCl_3$-II and TXM-$CHCl_3$-III crystals. All structures were solved using Olex2 as GUI[44] by the ShelXT solution program[45] and refined with the ShelXL[46] refinement package using least squares minimization. TXM-$CHCl_3$-I and TXM-$CHCl_3$-III were crystallized in the monoclinic $P2_1/c$ space group with two molecules TXM-ZWC and two chloroform molecules in the asymmetric unit of TXM-$CHCl_3$-I structure and one molecule TXM-ZWC and one chloroform molecule in the asymmetric unit of TXM-$CHCl_3$-III. TXM-$CHCl_3$-II crystallizes in the orthorhombic $P2_12_12_1$ space group with two molecules TXM-ZWC and four chloroform molecules in the asymmetric unit. TXM-ACE and TXM-DMF crystallized in the triclinic $P\bar{1}$ space with one TXM-ZWC and one solvent molecule in the asymmetric unit. We checked all the available TXM-$CHCl_3$-I crystals, and the best dataset had R_{int} = 24.7% and I/sigma = 7.5 at 0.84 Å resolution. We speculated that it was connected with particular decomposition of the crystal before or during the X-ray experiment. However, this dataset allowed us to solve and refine this structure (*R*1 of the final model is 11.6%) and reliably determine that tenoxicam was in the zwitterionic state in the TXM-$CHCl_3$-I structure. Solvent molecules in described structures (except for the TXM-$CHCl_3$-III structure) were particularly or completely disordered: in the TXM-$CHCl_3$-I structure, the one chloroform molecule was completely disordered (atom occupancy ratio was 0.545(13)/0.455(13)), and all atoms except carbon were disordered in the second chloroform molecule (atom occupancy ratio was 0.64(4)/0.36(4)); moreover, in the TXM-$CHCl_3$-II structure, carbon of one chloroform molecule was disordered (atom occupancy ratio was 0.5/0.5); however, in the TXM-ACE solvate structure, the methyl group of acetone was disordered (atom occupancy ratio was 0.58(6)/0.42(6)), and in the TXM-DMFA solvate structure, the O and H atoms connected with carbon in the DMFA molecule were disordered (the ratio of atom occupancy was 0.654(18)/ 0.346(18)).

All non-H atoms were anisotropically refined except for the fully disordered chloroform molecule of the TXM-$CHCl_3$-I structure. The C–Cl distances of this molecule were constrained with d = 1.78(2) Å. All H atoms except the H atoms connected with disordered carbon of the acetone molecule in the TXM-ACE structure were refined free. The H atoms in the TXM-$CHCl_3$-I, TXM-$CHCl_3$-II, TXM-$CHCl_3$-III and TXM-DMFA structures were refined using a riding model, with the following assumptions and restraints: N–H = 0.86 Å; C–H (aromatic rings and in DMFA molecule) = 0.93 Å; C–H (methyl groups of TXM, DMFA and acetone) = 0.96 Å and C–H (chloroform molecule) = 0.98 Å and $U_{\text{iso}}(H) = 1.5\ U_{\text{eq}}(C)$ for the $-CH_3$ groups, and 1.2 U_{eq}(C and N) for other groups.

Computer programs: *CrysAlis PRO* 1.171.39.46,[46] *SHELXT*,[45] *SHELXL*,[45] Olex2,[44] Mercury,[47] WinXPOW,[48] and OriginPro v.8.[49] Crystal structure of the TXM solvate with acetonitrile has been already solved by Caira *et al.* (1995);[22] however, for more accuracy in atom coordinate positions, in this

Published on 18 July 2019. Downloaded by Bundesanstalt fuer Materialforschung und -pruefung on 8/9/2019 5:03:49 PM.

study, we obtained the data from this solvate and resolved the structure again.

Conflicts of interest

There are no conflicts to declare.

Acknowledgements

The authors would like to thank Dr. Anatoly A. Politov for useful discussion. SGA would like to thank Prof. Dr. Elena V. Boldyreva for her ongoing support. CT would like to thank his former supervisor Prof. Dr. Elena V. Boldyreva and his present supervisor Prof. Dr. Artem R. Oganov for their ongoing support. SGA is indebted to Ministry of Science and Higher Education of the Russian Federation (project AAAA-A19-119020890025-3). PSS and ASK thank Ministry of Science and Higher Education of the Russian Federation for access to optical and NMR equipment (AAAA-A16-116121510087-5).

Notes and references

1 K. T. Olkkola, A. V. Bruneto and M. J. Mattila, *Clin. Pharmacokinet.*, 1994, **26**, 107.

2 G. Tamasi, M. Casolaro, A. Magnani, A. Sega, L. Chiasserini, L. Messori, C. Gabbiani, S. M. Valiahdi, M. A. Jakupec, B. K. Keppler, M. B. Hursthouse and R. Cini, *J. Inorg. Biochem.*, 2010, **104**, 799–814.

3 S. Roy, R. Banerjee and M. Sarkar, *J. Inorg. Biochem.*, 2006, **100**, 1320–1331.

4 M. Casolaro, R. Cini, B. Del Bello, M. Ferrali and E. Maellaro, *Biomacromolecules*, 2009, **10**(4), 944–949.

5 A. Ashraf, F. Aman, S. Movassaghi, A. Zafar, M. Kubanik, W. A. Siddiqui, J. Reynisson, T. Söhnel, S. M. F. Jamieson, M. Hanif and C. G. Hartinger, *Organometallics*, 2019, **38**(2), 361–374.

6 K. Środa-Pomianek, K. Michalak, A. Palko-Labuz, A. Uryga, B. Szczęśniak-Sięga and O. Wesolowska, *Anticancer Res.*, 2019, **39**(2), 727–734.

7 R. P. Fernandes, A. L. C. S. do Nascimento, A. C. S. Carvalho, J. A. Teixeira, M. Ionashiro and F. J. Caires, *J. Therm. Anal. Calorim.*, 2019, 1–13.

8 C. Tantardini, S. G. Arkipov, K. A. Cherkashina, A. S. Kil'met'ev and E. V. Boldyreva, *Struct. Chem.*, 2018, **29**, 1867–1874.

9 A. G. Ogienko, S. A. Myz, A. A. Ogienko, A. A. Nefedov, A. S. Stoporev, M. S. Mel'gunov, A. S. Yunoshev, T. P. Shakhtshneider, V. V. Boldyrev and E. V. Boldyreva, *Cryst. Growth Des.*, 2018, **18**, 7401–7409.

10 C. Tantardini, S. G. Arkhipov, K. A. Cherkashina, A. S. Kil'met'ev and E. V. Boldyreva, *Acta Crystallogr., Sect. E: Crystallogr. Commun.*, 2016, **72**, 1856–1859.

11 S. A. Myz, T. P. Shakhtshneider, N. A. Tumanov and E. V. Boldyreva, *Russ. Chem. Bull.*, 2012, **61**, 1798–1809.

12 D. R. Weyna, M. L. Cheney, N. Shan, M. Hanna, M. J. Zaworotko, V. Sava, S. Song and J. R. Sanchez-Ramos, *Mol. Pharmaceutics*, 2012, **9**, 2094–2102.

13 M. L. Cheney, D. R. Weyna, N. Shan, M. Hanna, L. Wojtas and M. J. Zaworotko, *Cryst. Growth Des.*, 2010, **10**, 4401–4413.

14 S. A. Myz, T. P. Shakhtshneider, K. Fucke, A. P. Fedotov, E. V. Boldyreva, V. V. Boldyrev and N. I. Kuleshova, *Mendeleev Commun.*, 2009, **19**, 272–274.

15 K. Fucke, S. A. Myz, T. P. Shakhtshneider, E. V. Boldyreva and U. J. Griesser, *New J. Chem.*, 2012, **36**, 1969.

16 G. Bolla, P. Sanphui and A. Nangia, *Cryst. Growth Des.*, 2013, **13**, 1988–2003.

17 K. Suresh and A. Nangia, *Cryst. Growth Des.*, 2014, **14**, 2945–2953.

18 J. R. Patel, R. A. Carlton, T. E. Needham, C. O. Chichester and F. G. Vogt, *Int. J. Pharm.*, 2012, **436**, 685–706.

19 S. Emami, K. Adibkia, M. Barzegar-Jalali and M. Siahi-Shadbad, *Pharm. Dev. Technol.*, 2019, **24**(2), 199–210.

20 M. Nyström, J. Roine, R. M. Murtomaa, R. M. Sankaran, H. A. Santos and J. Salonen, *Eur. J. Pharm. Biopharm.*, 2015, **89**, 182–189.

21 S. L. Childs and K. I. Hardcastle, *Cryst. Growth Des.*, 2007, **7**(7), 1291–1304.

22 M. C. Caira, L. R. Nassimbeni and M. Timme, *J. Pharm. Sci.*, 1995, **84**(7), 884–888.

23 R. G. Cantera, M. G. Leza and C. M. Bachiller, *J. Pharm. Sci.*, 2002, **91**(10), 2240–2251.

24 L. Nabulsi, L. Owais, T. A. Arafat, H. Al-Kaysi, M. Salem, M. Sheikh and A. A. Badwan, *Congr. Int. Technol. Pharm., 6th*, 1992, **1**, 203–212.

25 A. Yu. Fedorov, T. N. Drebushchak and C. Tantardini, *Comput. Theor. Chem.*, 2019, **1157**(1), 47–53.

26 G. F. Fabiola, V. Pattabhi, S. G. Manjuhatha, G. V. Rao and K. Nagarajan, *Acta Crystallogr., Sect. C: Cryst. Struct. Commun.*, 1998, **54**, 2001–2003.

27 B. Kojić -Prodić and Ž. Ružić-Toroš, *Acta Crystallogr., Sect. B: Struct. Crystallogr. Cryst. Chem.*, 1982, **32**, 2948–2951.

28 B. R. Beno, K.-S. Yeung, M. D. Bartberger, L. D. Pennington and N. A. Meanwell, *J. Med. Chem.*, 2015, **58**(11), 4383–4438.

29 J. P. Foster and F. Weinhold, *J. Am. Chem. Soc.*, 1980, **102**, 7211–7218.

30 A. E. Reed, R. B. Weinstock and F. Weinhold, *J. Chem. Phys.*, 1985, **83**, 735–746.

31 A. E. Reed and F. Weinhold, *J. Chem. Phys.*, 1985, **83**, 1736–1740.

32 J. E. Carpenter and F. Weinhold, *J. Mol. Struct.: THEOCHEM*, 1988, **169**, 41–62.

33 A. E. Reed, L. A. Curtiss and F. Weinhold, *Chem. Rev.*, 1988, **88**(6), 899–926.

34 F. Weinhold and J. E. Carpenter, in *The Structure of Small Molecules and Ions*, ed. R. Naaman and Z. Vager, Plenum, 1988.

35 P. Atkins and R. Friedmann, *Molecular Quantum Mechanics*, Oxford University Press, 2005.

36 J. P. Glusker, "*Directional Aspects of Intermolecular Interactions*" *in Topics in Current Chemistry*, vol. 198, Springer Verlag, Berlin, Heidelberg, 1998.

37 A. D. Becke, *J. Chem. Phys.*, 1993, **98**, 5648–5652.

38 R. Krishan, J. S. Binkley, R. Seeger and J. A. Pople, *J. Chem. Phys.*, 1980, **72**, 650.

Published on 18 July 2019. Downloaded by Bundesanstalt fuer Materialforschung und -pruefung on 8/9/2019 5:03:49 PM.

39 A. D. McLean and G. S. Chandler, *J. Chem. Phys.*, 1980, **72**, 5639.

40 M. J. Frisch, G. W. Trucks, H. B. Schlegel, G. E. Scuseria, M. A. Robb, J. R. Cheeseman, G. Scalmani, V. Barone, G. A. Petersson, H. Nakatsuji, X. Li, M. Caricato, A. V. Marenich, J. Bloino, B. G. Janesko, R. Gomperts, B. Mennucci, H. P. Hratchian, J. V. Ortiz, A. F. Izmaylov, J. L. Sonnenberg, D. Williams-Young, F. Ding, F. Lipparini, F. Egidi, J. Goings, B. Peng, A. Petrone, T. Henderson, D. Ranasinghe, V. G. Zakrzewski, J. Gao, N. Rega, G. Zheng, W. Liang, M. Hada, M. Ehara, K. Toyota, R. Fukuda, J. Hasegawa, M. Ishida, T. Nakajima, Y. Honda, O. Kitao, H. Nakai, T. Vreven, K. Throssell, J. A. Montgomery, Jr., J. E. Peralta, F. Ogliaro, M. J. Bearpark, J. J. Heyd, E. N. Brothers, K. N. Kudin, V. N. Staroverov, T. A. Keith, R. Kobayashi, J. Normand, K. Raghavachari, A. P. Rendell, J. C. Burant, S. S. Iyengar, J. Tomasi, M. Cossi, J. M. Millam, M. Klene, C. Adamo, R. Cammi, J. W. Ochterski, R. L. Martin, K. Morokuma, O. Farkas, J. B. Foresman and D. J. Fox, Gaussian, Inc., Wallingford CT, 2016.

41 P. S. Sherin, J. Grilj, Y. P. Tsentalovich and E. Vauthey, *J. Phys. Chem. B*, 2009, **113**, 4953–4962.

42 H. E. Gottlieb, V. Kotlyar and A. Nudelman, *J. Org. Chem.*, 1997, **62**, 7512–7515.

43 G. Otting, R. Grutter, W. Leupin, C. Minganti, K. N. Ganesh, B. S. Sproat, M. J. Gait and K. Wuthrich, *Eur. J. Biochem.*, 1987, **166**, 215–220.

44 O. V. Dolomanov, L. J. Bourhis, R. J. Gildea, J. A. K. Howard and H. Puschmann, *J. Appl. Crystallogr.*, 2009, **42**, 339.

45 G. M. Sheldrick, *Acta Crystallogr., Sect. C: Struct. Chem.*, 2015, **71**, 3.

46 O. D. Rigaku, *CrysAlis PRO*, Rigaku Oxford diffraction Ltd, Yarnton, 2016.

47 C. F. Macrae, I. J. Bruno, J. A. Chisholm, P. R. Edgington, P. McCabe, E. Pidcock, L. Rodriguez-Monge, R. Taylor, J. van de Streek and P. A. Wood, *J. Appl. Crystallogr.*, 2008, **41**, 466.

48 Stoe & Cie, *WinXPOW*, Darmstadt, 1999.

49 http://www.OriginLab.com.

This journal is © The Royal Society of Chemistry 2019

Electronic Supplementary Material (ESI) for CrystEngComm.
This journal is © The Royal Society of Chemistry 2019

Electronic Supporting Information

for

The Role of S-bond in Tenoxicam Keto-Enolic Tautomerization†

Sergey G. Arkhipov[a,b,c], Peter S. Sherin*[a,d], Alexey S. Kiryutin[a,d], Vladimir A. Lazarenko[e] and Christian Tantardini*[f]

---

[a] *Novosibirsk State University, Pirogova str. 2, 630090 Novosibirsk (Russian Federation).*
[b] *Boreskov Institute of Catalysis SB RAS Prospekt Akademika Lavrentyeva, 5, 630090 Novosibirsk (Russian Federation).*
[c] *Institute of Solid State Chemistry and Mechanochemistry SB RAS Kutateladze str. 18, 630128 Novosibirsk (Russian Federation).*
[d] *International Tomography Center Institutskaya 3a, 630090 Novosibirsk (Russian Federation).*
[e] *National Research Center “Kurchatov Institute” Akademika Kurchatova square 1, 123182, Moscow (Russian Federation).*
[f] *Center for Energy Science and Technology, Skoltech Skolkovo Institute of Science and Technology, Nobelya str. 3, 143026 Moscow (Russian Federation).*
*Corresponding to sherin@tomo.nsc.ru (Peter S. Sherin) and christiantantardini@ymail.com (Christian Tantardini).

† Dedicated to the memory of Dr. Alexey P. Chupakhin (1952-2018)

S1. Table of positions of maxima of absorption and fluorescence emission bands in wavelengths (λ_{max}^{abs}, λ_{max}^{flr}) and wavenumbers (v_{max}^{abs}, v_{max}^{flr}), Stokes shifts (Δv) and fluorescence quantum yields (Φ_F) of TXM in various solvents; dielectric constant of used solvents (ε) [1]. [a]

Solvent	ε	λ_{max}^{abs}/nm	λ_{max}^{flr}/nm	v_{max}^{abs} $/10^3 cm^{-1}$	v_{max}^{flr} $/10^3 cm^{-1}$	$\Delta v/10^3 cm^{-1}$	$\Phi_F/10^{-3}$
Cyclohexane	2.02	342	494	29.2	20.2	9.0	2.3
Dioxane	2.21	343	512	29.2	19.5	9.6	2.8
Toluene	2.38	346	500	28.9	20.0	8.9	2.2
Chloroform	4.89	345	492	29.0	20.3	8.7	2.1
THF	7.58	344	503	29.1	19.9	9.2	–*
Acetone	20.6	346	515	28.9	19.4	9.5	1.2
ACN	35.9	354	515	28.3	19.4	8.8	0.9
DMSO	46.4	386	540	25.9	18.5	7.4	–*

* not determined due to large contribution from impurity

[a] The Φ_F values were determinted with respect to kynurenine in aqueous solution, Φ_F (KN) = 8.2×10^{-3} [2].

S2. Picture of Absorption and fluorescence emission and excitation spectra recorded with TXM in cyclohexane, dioxane, toluene and acetone at different excitation and emission wavelengths.

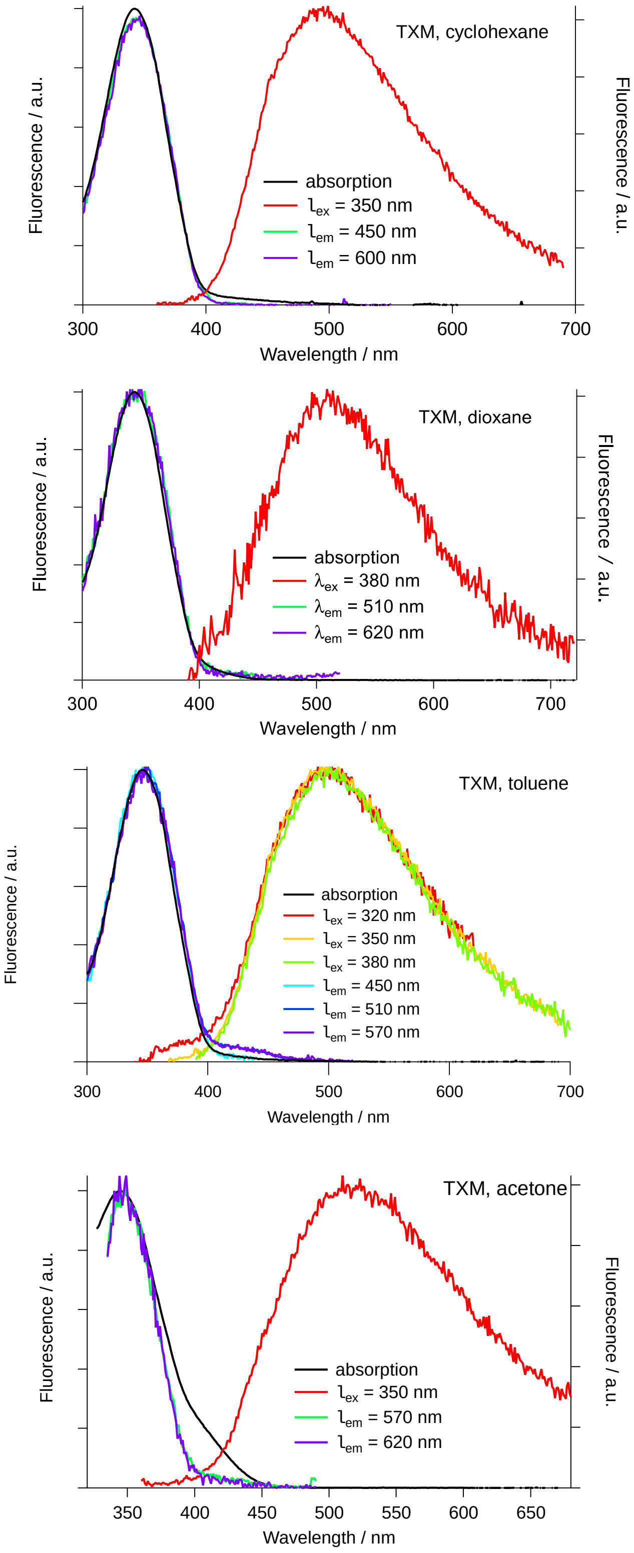

S3. Picture of fluorescence time profiles recorded with TXM in low polar solvents at 500 nm after the excitation at 375 nm.

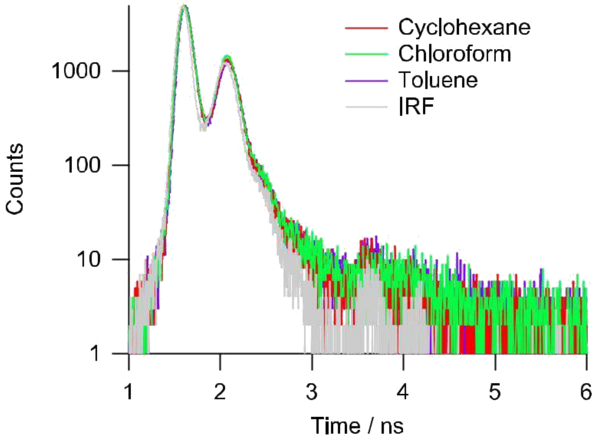

S4 Temperature influence on TXM absorption spectra in Acetonitrile and Chloroform.

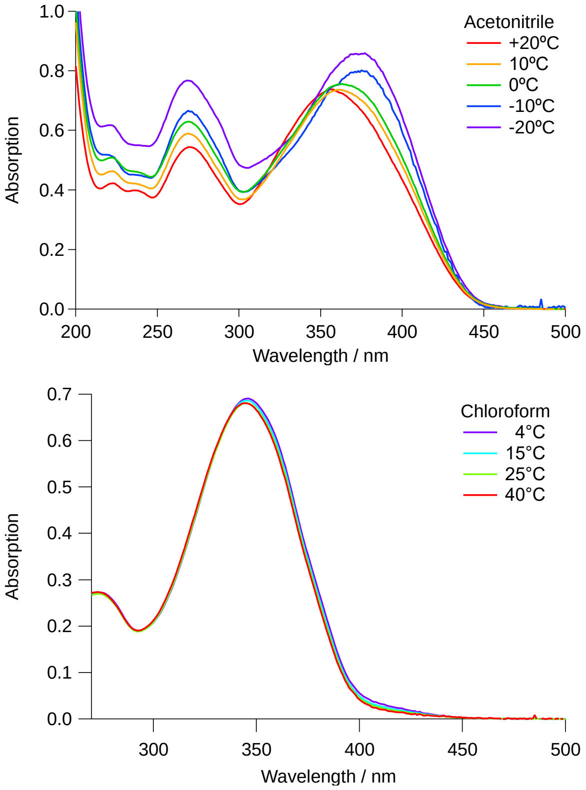

S5. Figure 700 MHz ^{1}H NMR spectrum of TXM in CDCl$_3$ at 25 °C. BKE form of TXM is predominant at high temperature. Assignments of all protons are shown on the spectrum.

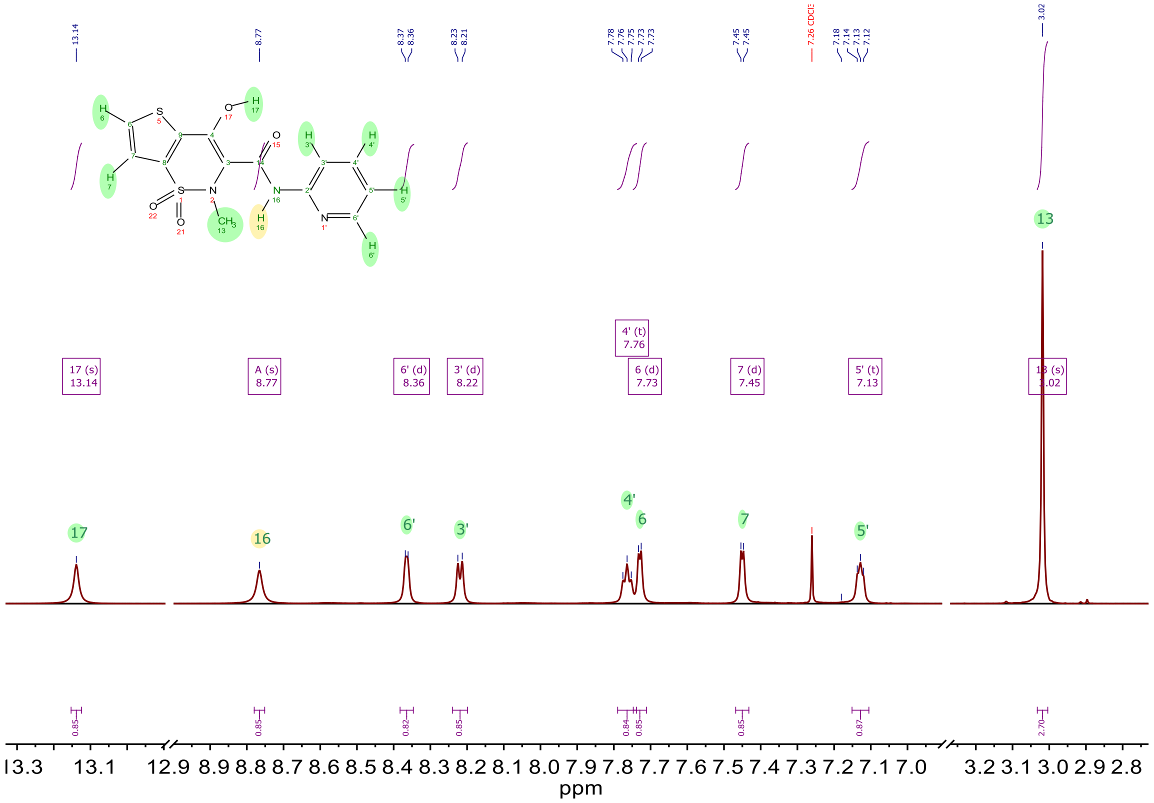

S6. Figure 176.1 MHz ^{13}C{1H} NMR spectrum of TXM in CDCl$_3$ at 25 °C. BKE form of TXM is predominant at high temperature. Assignments of all carbons are shown on the spectrum. To suppress all ^{13}C-^{1}H scalar couplings a broadband decoupling on proton channel was applied during acquisition.

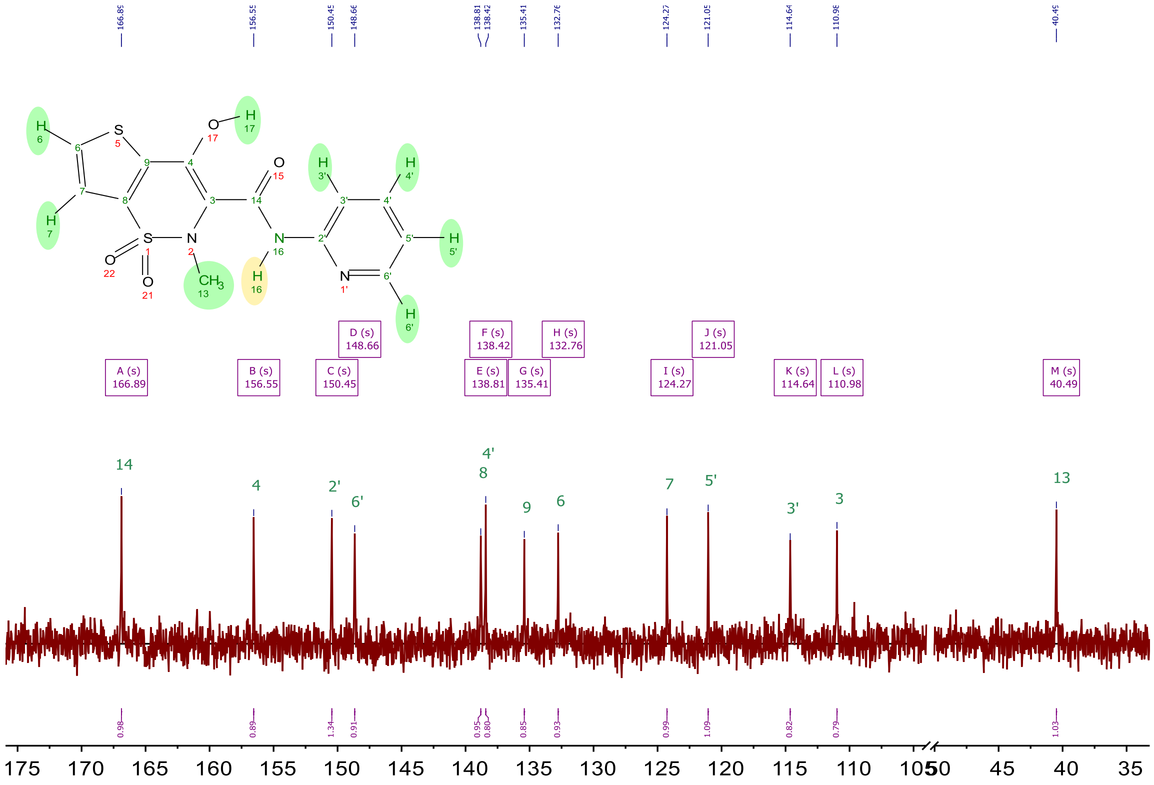

S7. Figure ^{1}H-^{13}C HSQC NMR spectrum of TXM in $CDCl_3$ at 25 °C. BKE form of TXM is predominant at high temperature. Cross-peaks in HSQC spectrum indicate correlation between directly bonded protons and carbons (C-H bonds).

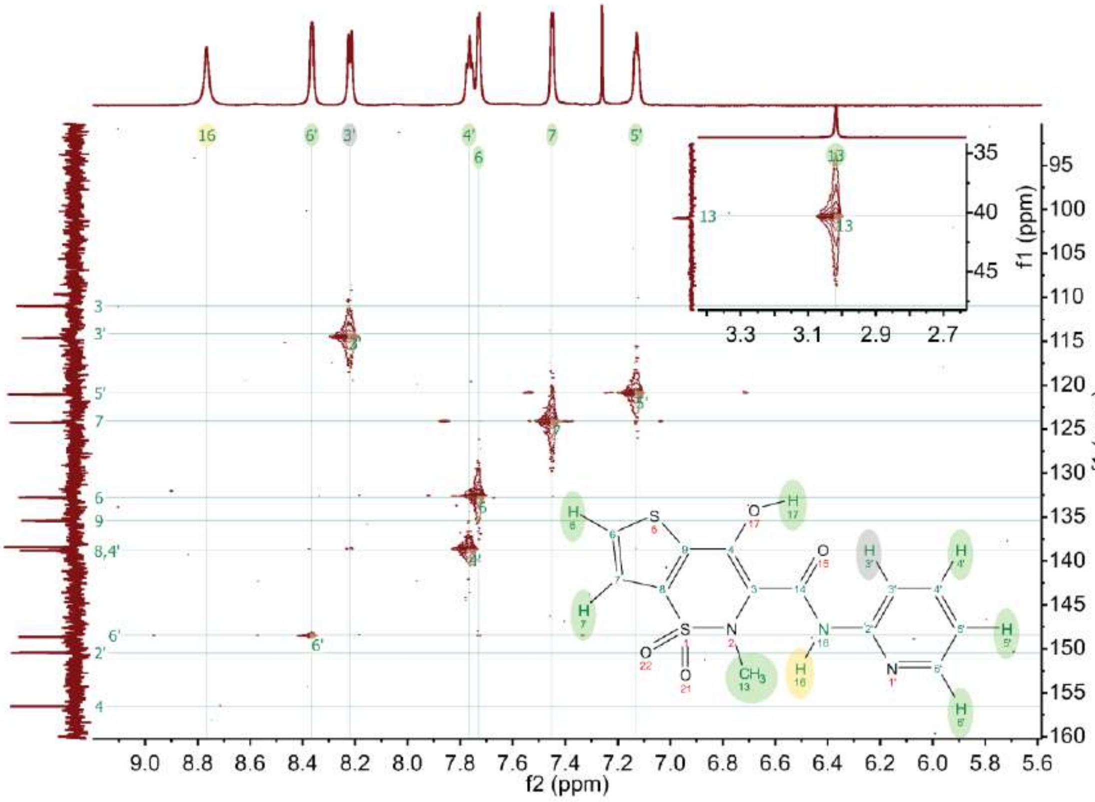

S8. Figure ^{1}H-^{13}C HMBC NMR spectrum of TXM in $CDCl_3$ at 25 °C. BKE form of TXM is predominant at high temperature. Cross-peaks in HMBC spectrum indicate correlation between protons and carbons separated by 2-4 covalent bonds, while direct correlation of single-bonded protons and carbons are suppressed. HMBC allows to assign quaternary carbons and carbonyl fragments.

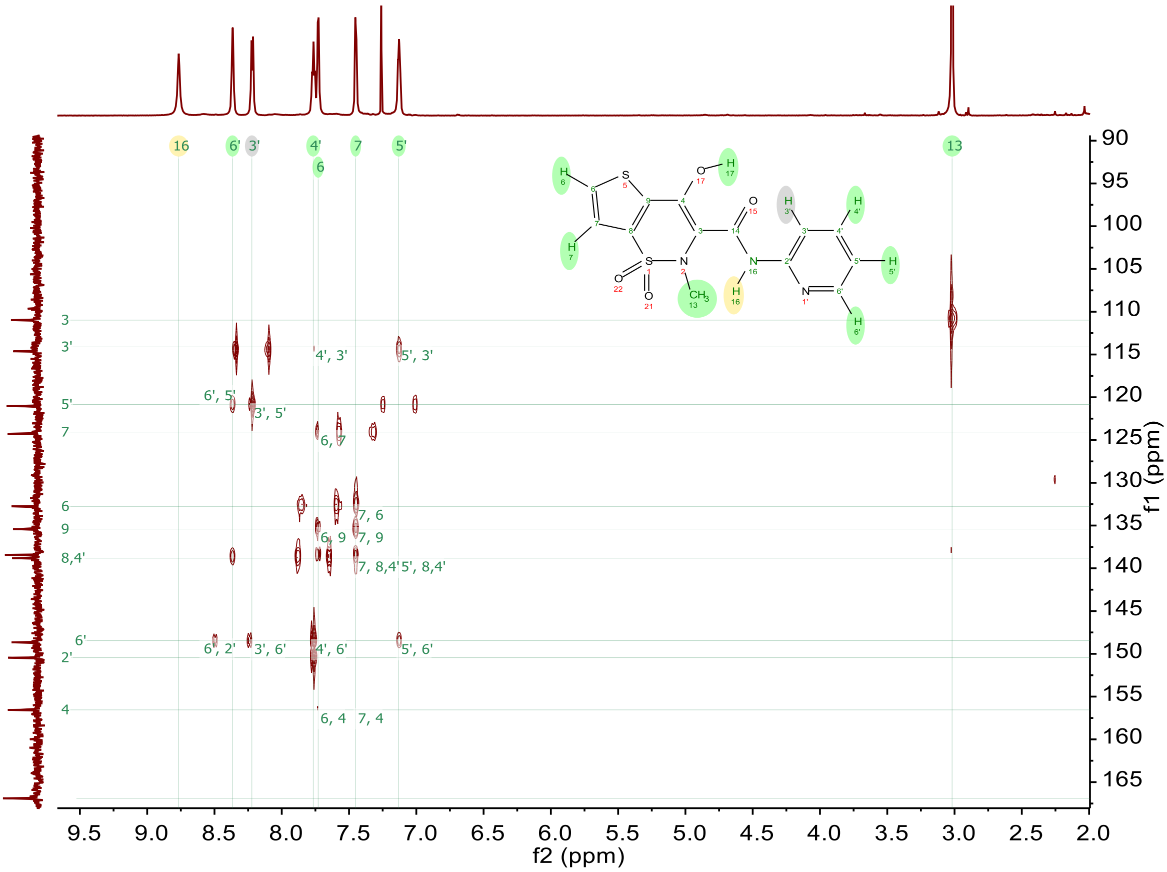

S9. Figure ^{1}H-^{15}N HSQC NMR spectrum of TXM in $CDCl_3$ at 25 °C. BKE form of TXM is predominant at high temperature. Cross-peaks in ^{1}H-^{15}N HSQC spectrum indicate correlation between directly bonded protons and nitrogens (N-H bonds). In BKE form we see only one cross-peaks assigned to H_{16} and N_{16}.

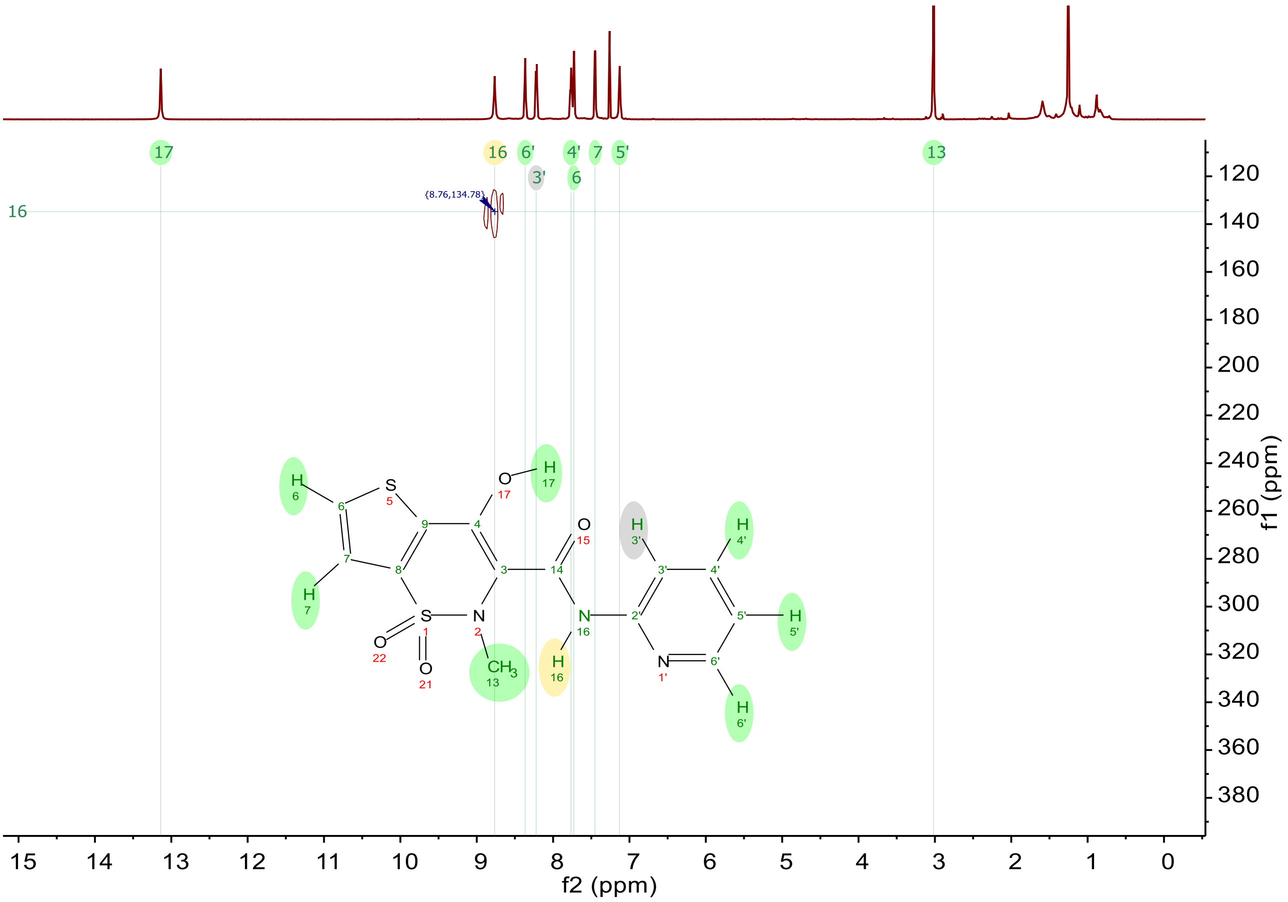

S10. Figure 700 MHz ^{1}H NMR spectrum of TXM in $CDCl_3$ at -55 °C. ZWC form of TXM is predominant at low temperature. Assignments of all protons are shown on the spectrum. Small, not assigned peaks stand for the BKE form.

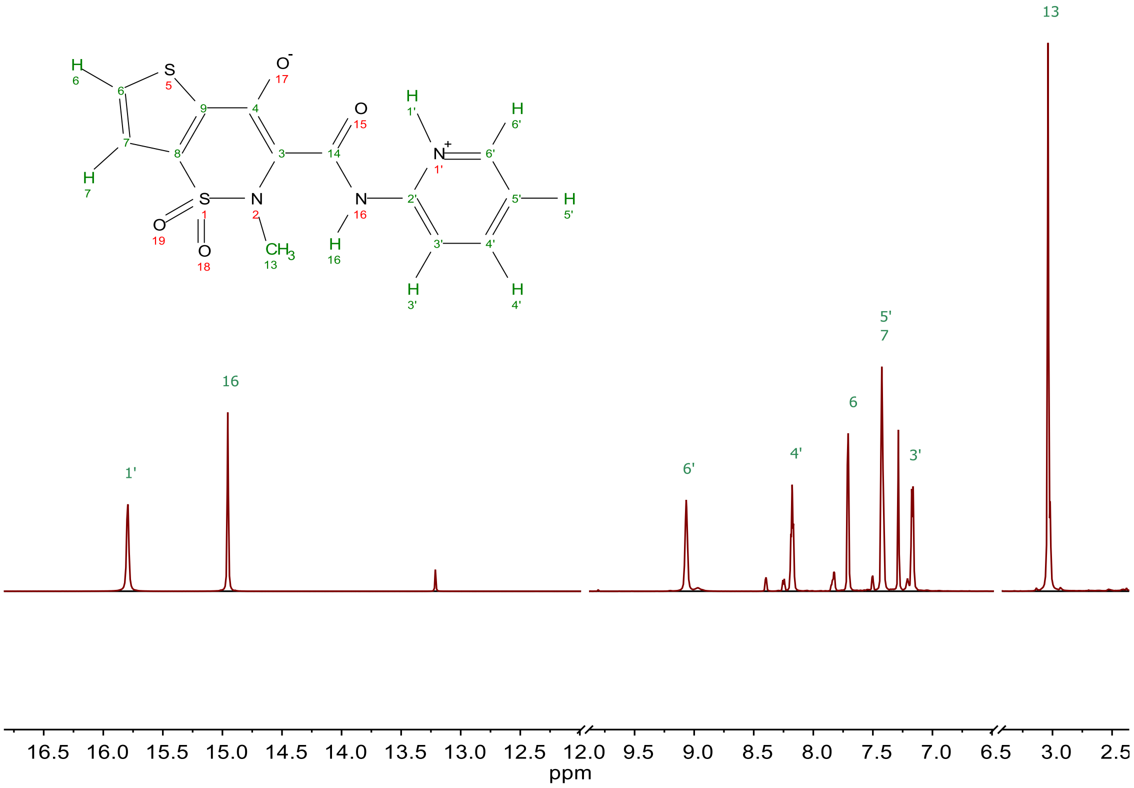

S11. Figure 176.1 MHz ^{13}C{1H} NMR spectrum of TXM in $CDCl_3$ at 25 °C. ZWC form of TXM is predominant at low temperature. Assignments of all carbons are shown on the spectrum. To suppress all ^{13}C-^{1}H scalar couplings a broadband decoupling on proton channel was applied during acquisition.

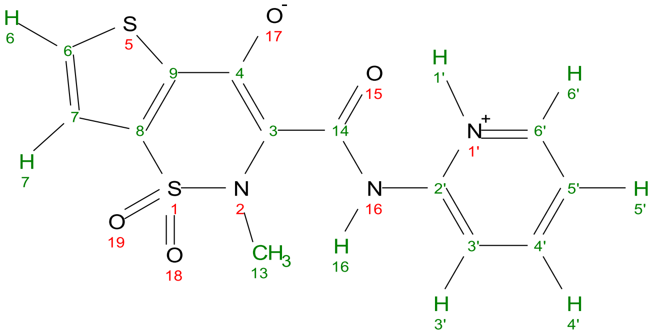

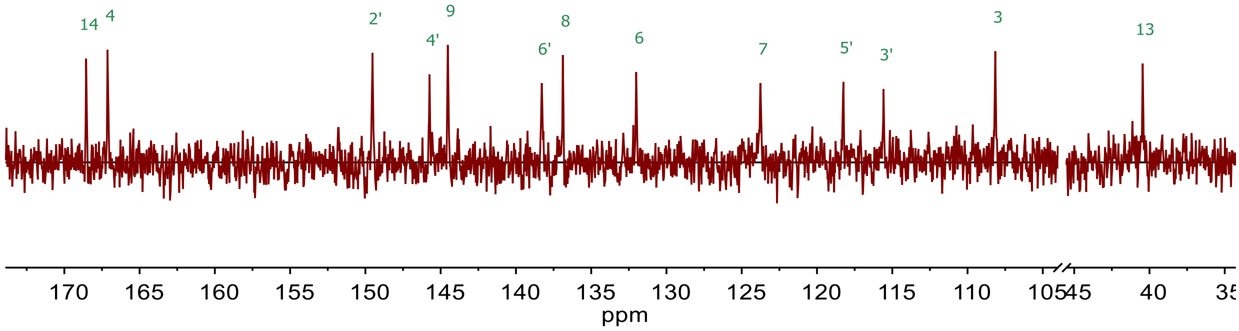

S12. Figure ^{1}H-^{13}C HSQC NMR spectrum of TXM in $CDCl_3$ at 25 °C. ZWC form of TXM is predominant at hlow temperature. Cross-peaks in HSQC spectrum indicate correlation between directly bonded protons and carbons (C-H bonds).

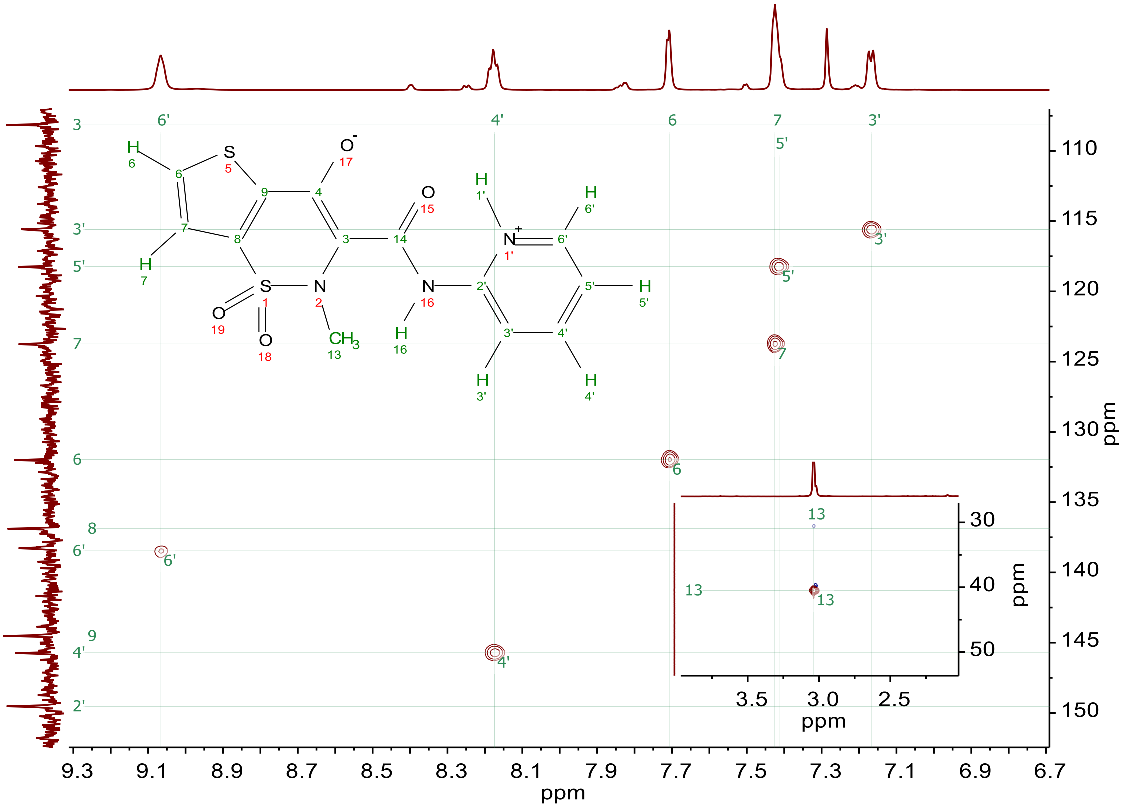

S13. Figure ^{1}H-^{13}C HMBC NMR spectrum of TXM in $CDCl_3$ at 25 °C. ZWC form of TXM is predominant at low temperature. Cross-peaks in HMBC spectrum indicate correlation between protons and carbons separated by 2-4 covalent bonds, while direct correlation of single-bonded protons and carbons are suppressed. HMBC allows to assign quaternary carbons and carbonyl fragments.

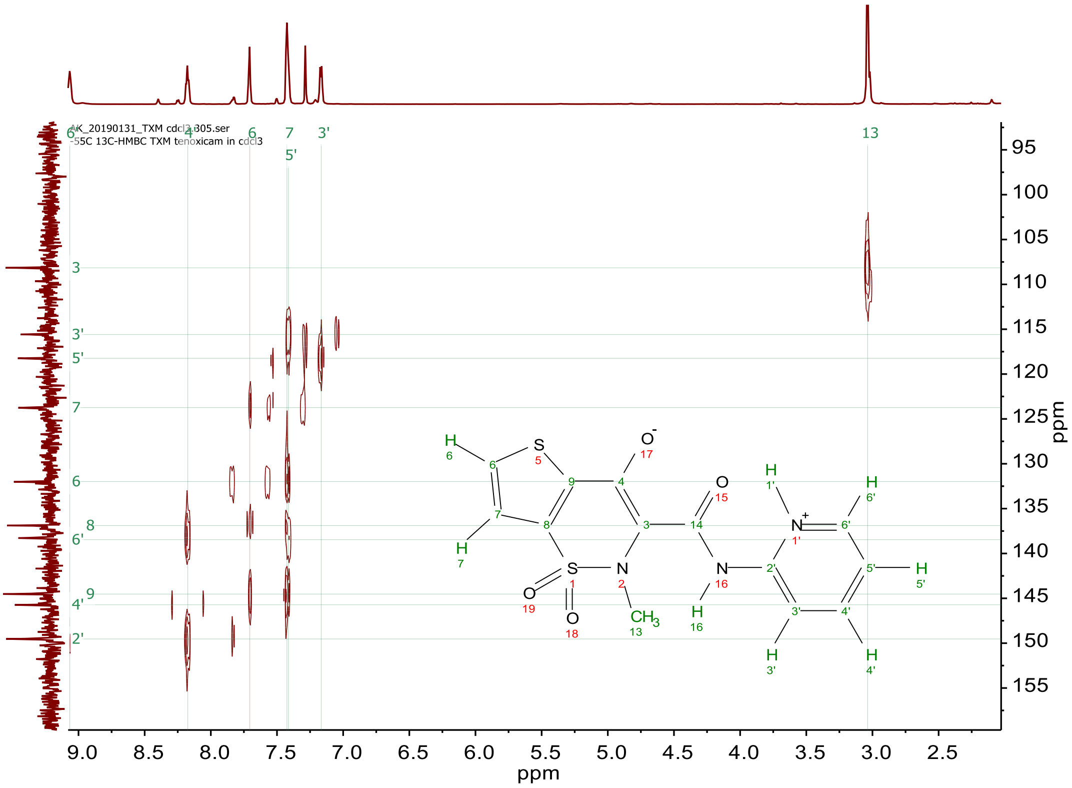

S14. Figure 700 MHz ^{1}H NMR spectrum of TXM in $CDCl_3$ at -25 °C. Both forms (ZWC and BKE) of TXM are present. Assignments of all protons are shown on the spectrum. Here “z” after nuclei number indicates ZWC, while “b” indicates BKE form.

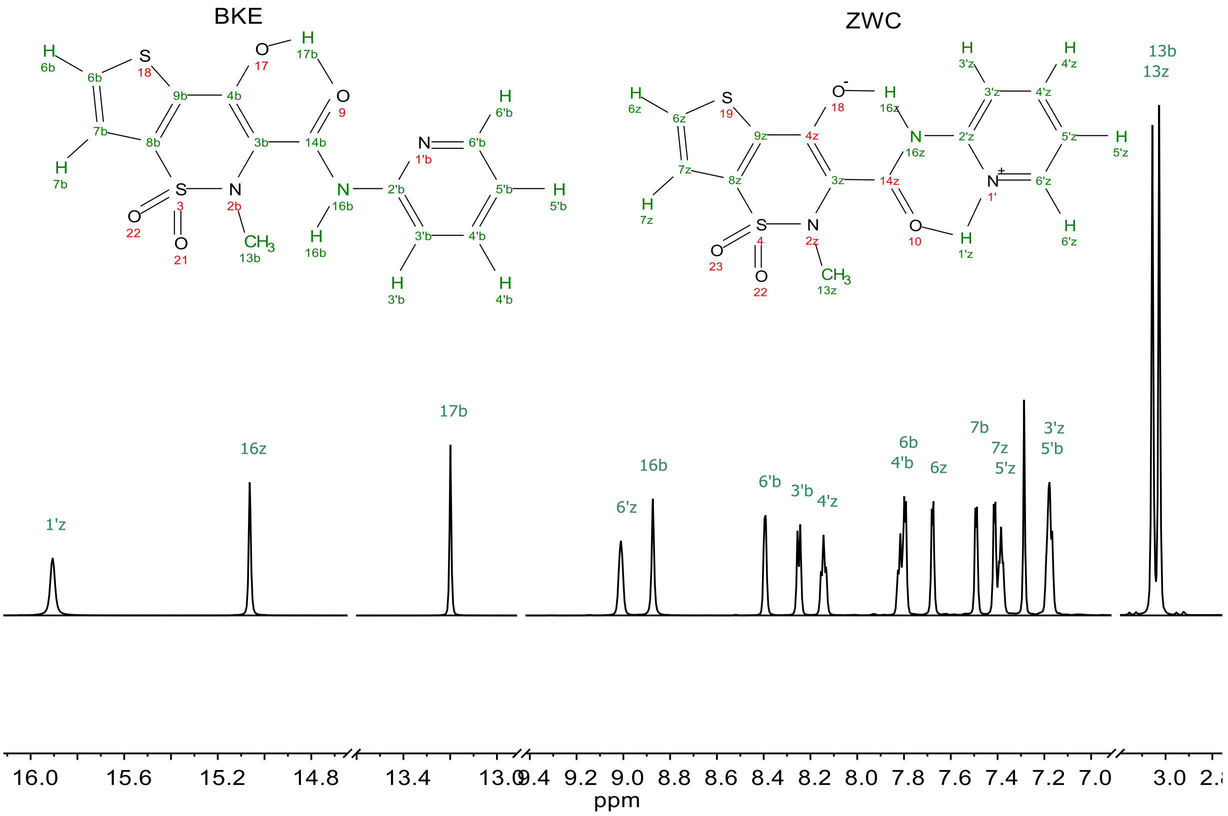

S15. Figure ^1H-^{13}C HSQC NMR spectrum of TXM in $CDCl_3$ at -25 °C. Both forms (ZWC and BKE) of TXM are present. Cross-peaks in HSQC spectrum indicate correlation between directly bonded protons and carbons (C-H bonds). Here “z” after nuclei number indicates ZWC, while “b” indicates BKE form.

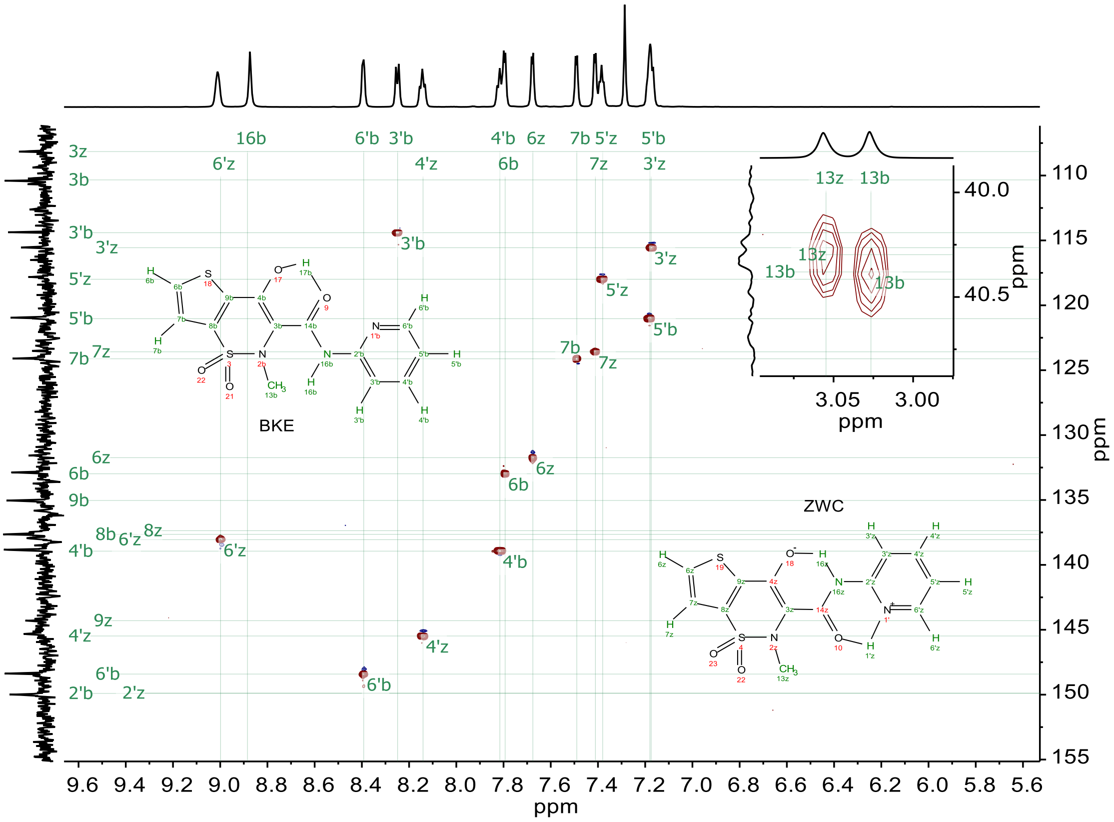

S16. Figure 700 MHz ^{1}H NMR NOESY (EXSY) spectrum of TXM in $CDCl_3$ at -25 °C. Cross-peaks in EXSY spectrum shows exchanging nuclei on a time scale of a mixing time (0.5s). Here “z” after nuclei number indicates ZWC, while “b” indicates BKE form. Labile protons 17b, 16b, 1'z are also in exchange with residual water (not shown here).

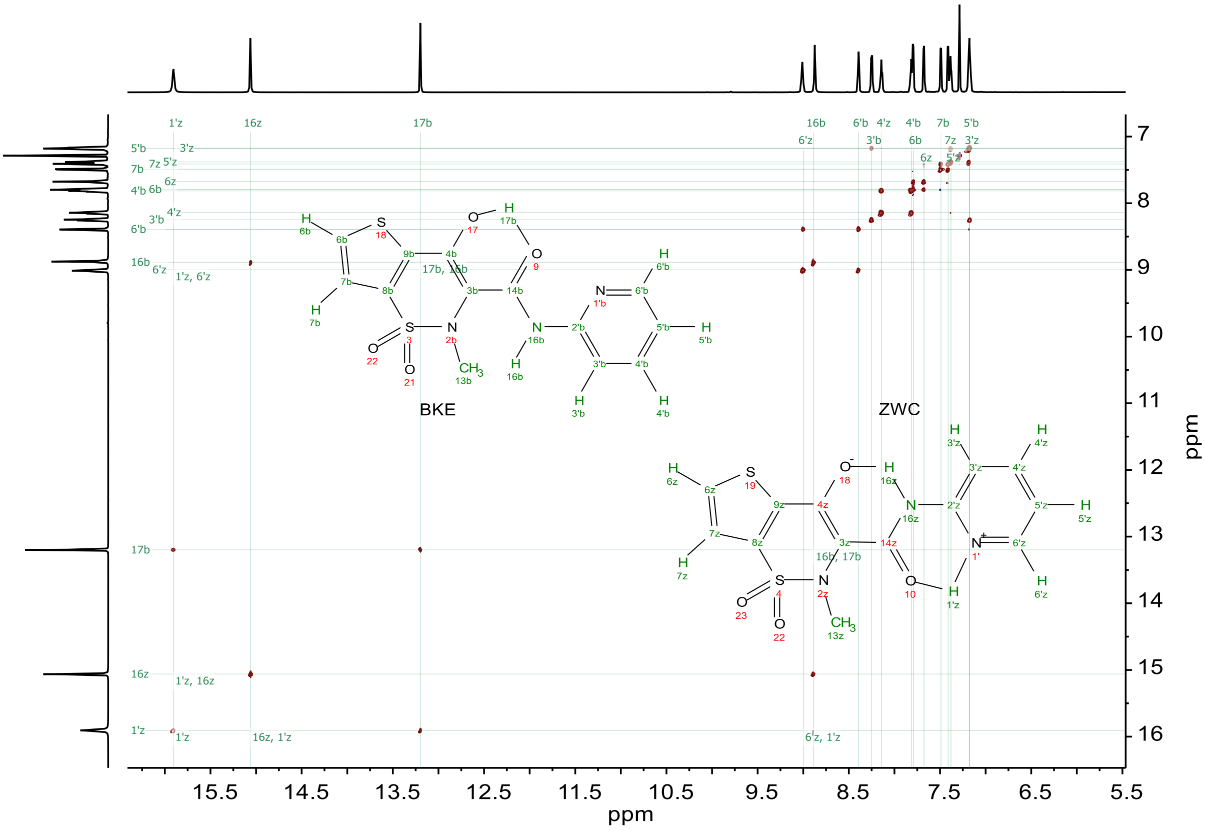

S17. Figure ^{1}H-^{15}N HSQC NMR spectrum of TXM in $CDCl_3$ at -25 °C. Both forms (ZWC and BKE) of TXM are present. Cross-peaks in ^{1}H-^{15}N HSQC spectrum indicate correlation between directly bonded protons and nitrogens (N-H bonds). In BKE form we see only one cross-peaks assigned while in ZWC form we see two cross-peaks, indeed, confirming that H17 proton moved to position H1'.

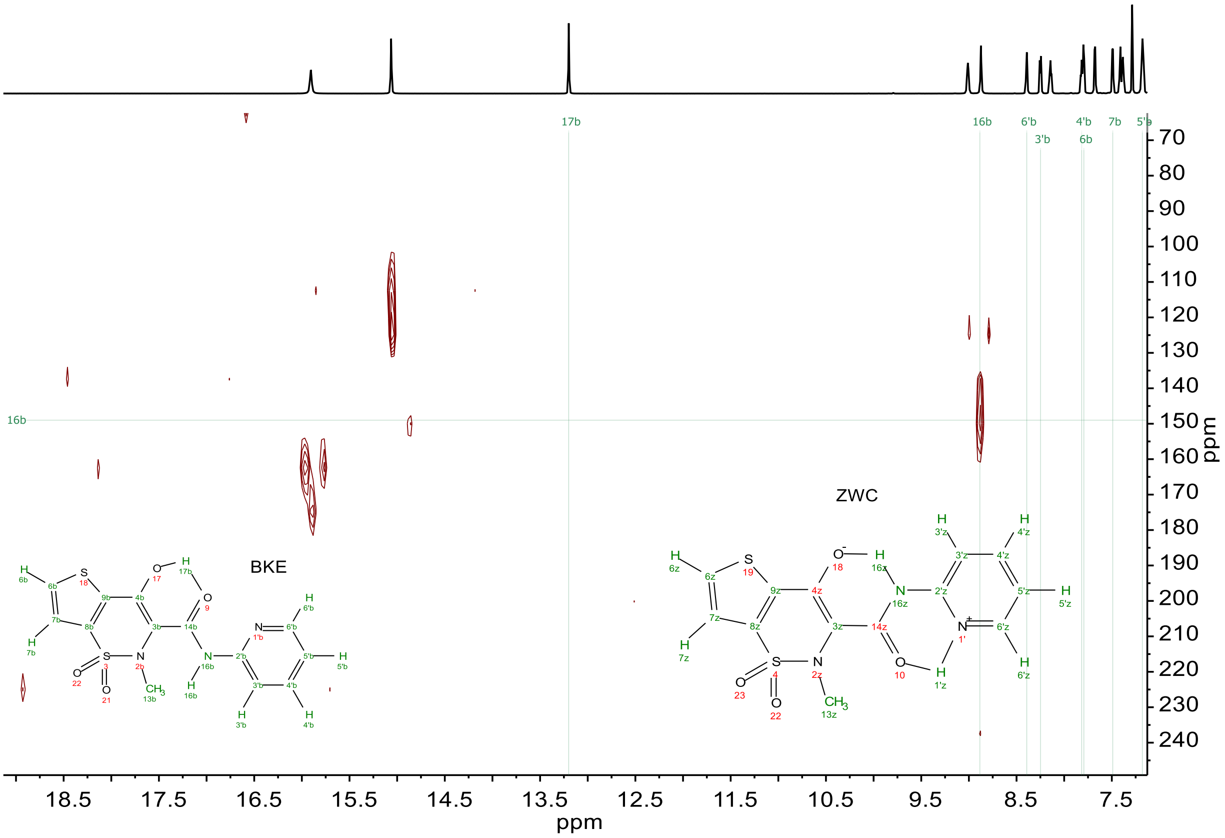

S18. Figure 700 MHz 1H NMR spectra of TXM in deuterated acetone, measured at various temperatures from -85 °C to 25 °C. Similar to spectra in chloroform (see main text) by lowering temperature two new peaks in high chemical shift region (15-16 ppm). This is an indication of hydrogen bond formation in the molecule, so ZWC form. At high temperature BKE form is dominant. At temperature -35 °C we observe broad peaks, this and indication that two forms exchange between each other.

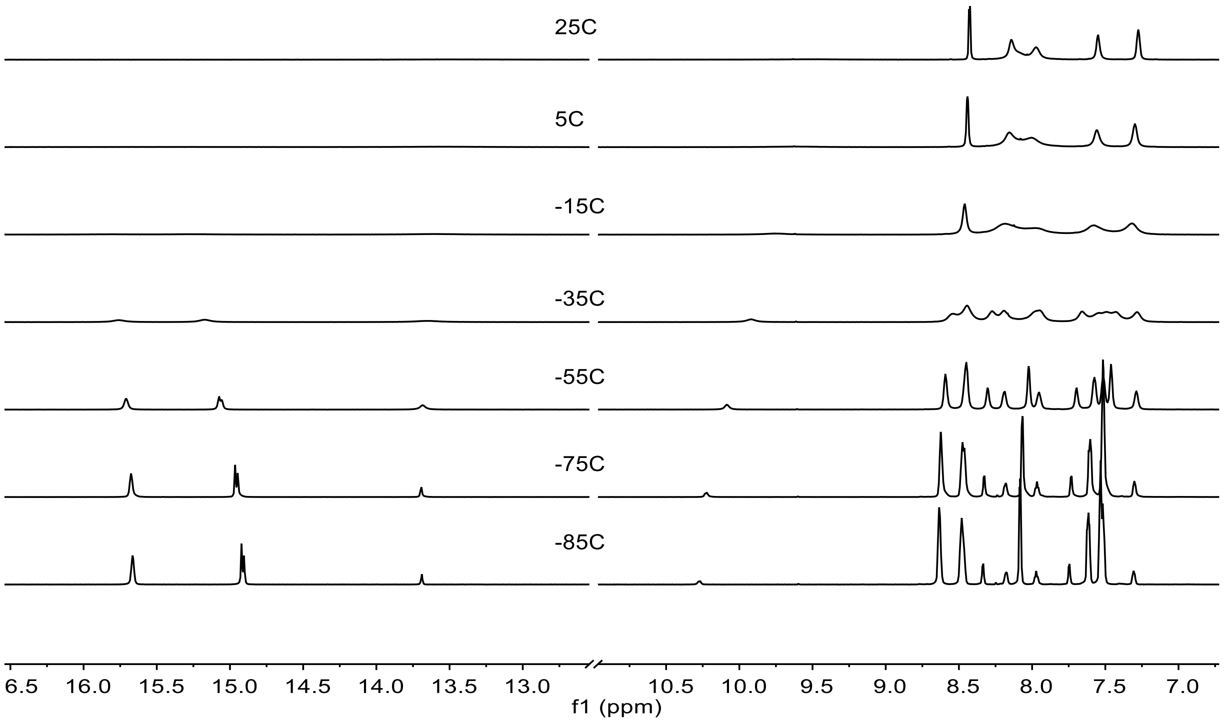

S19. Figure 700 MHz 1H NMR spectra of TXM in deuterated acetonitrile (CD_3CN), measured at various temperatures from -25 °C to 25 °C. Similar to spectra in chloroform (see main text) and in acetone by lowering temperature two new peaks in high chemical shift region (15-15.5 ppm). This is an indication of hydrogen bond formation in the molecule, so ZWC form. At high temperature BKE form is dominant. At temperature -15 °C we observe broad peaks, this and indication that two forms exchange between each other.

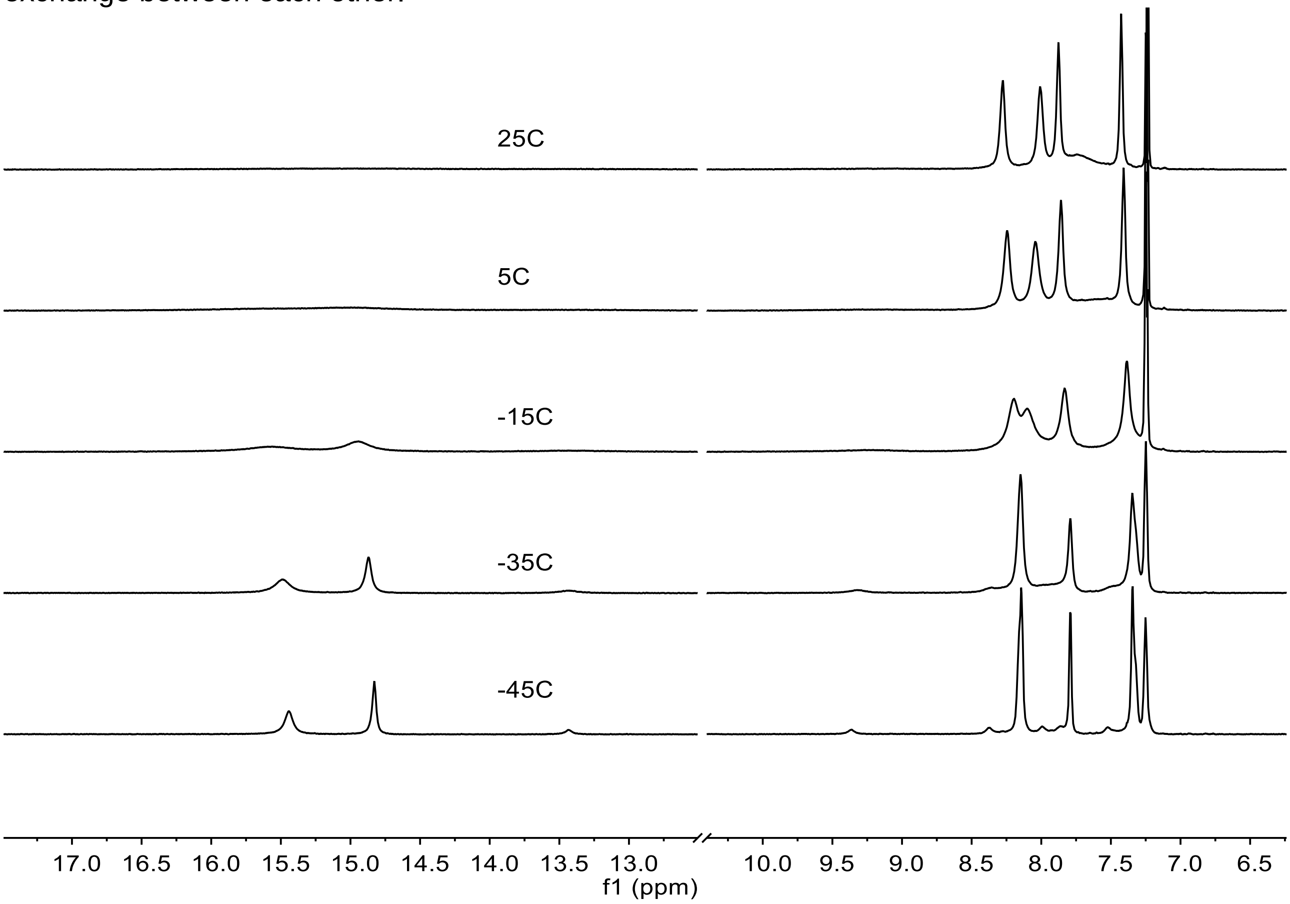

S20. Table of Crystallographic information about TXM solvates with chloroform (TXM-$CHCl_3$-I, TXM-$CHCl_3$-II, TXM-$CHCl_3$-III), acetone (TXM-ACE), N,N-dimetilformamide (TXM-DMFA) and acetonitrile (TXM-ACY); which were synthetized and solved.

	TXM-$CHCl_3$-I	**TXM-$CHCl_3$-II**	**TXM-$CHCl_3$-III**
CCDC number	1890995	1904023	1904022
Crystal data			
Chemical formula	$C_{13}H_{11}N_3O_4S_2\cdot CHCl_3$	$C_{13}H_{11}N_3O_4S_2\cdot 2(CHCl_3)$	$C_{13}H_{11}N_3O_4S_2\cdot CHCl_3$
M_r	456.74	576.10	456.74
Crystal system, space group	Monoclinic, $P2_1/c$	Orthorhombic, $P2_12_12_1$	Monoclinic, $P2_1/c$
Temperature (K)	293(2)	100(2)	100(2)
a, b, c (Å)	10.6019 (12), 12.781 (1), 28.841 (2)	9.5960 (19), 16.740 (3), 28.301 (6)	13.579 (3), 10.135 (2), 14.880 (3)
α, β, γ (°)	90, 92.076 (10), 90	90, 90, 90	90, 116.58 (3), 90
V ($Å^3$)	3905.5 (6)	4546.2 (16)	1831.3 (8)
Z	8	8	4
Radiation type	Mo $K\alpha$	Synchrotron, λ = 0.7937 Å	Synchrotron, λ = 0.7937 Å
μ (mm^{-1})	0.71	1.33	1.04
Crystal size (mm)	0.3 × 0.25 × 0.13	0.1 × 0.03 × 0.03	0.1 × 0.1 × 0.08
Data collection			
Diffractometer	Xcalibur, Ruby, Gemini ultra (Rigaku Oxford Diffraction, 2018)	“Belok” beamline NRC “Kurchatov Institute”	“Belok” beamline NRC “Kurchatov Institute”
Absorption correction	Multi-scan *CrysAlis PRO*	Empirical XDS (Kabsch, 2010)	Empirical XDS (Kabsch, 2010)
T_{min}, T_{max}	0.643, 1.000	0.759, 1	0.911, 1
No. of measured, independent and observed [$I > 2\sigma(I)$] reflections	54415, 6880, 2586	38347, 10006, 7832	17905, 4021, 3593
R_{int}	0.247	0.064	0.037
$(\sin \theta/\lambda)_{max}$ ($Å^{-1}$)	0.595	0.649	0.649
Refinement			
$R[F^2 > 2\sigma(F^2)]$, $wR(F^2)$, S	0.116, 0.396, 1.03	0.064, 0.178, 1.03	0.042, 0.112, 1.06
No. of reflections	6880	10006	4021
No. of parameters	496	552	236
H-atom treatment	H-atom parameters constrained	H-atom parameters constrained	H-atom parameters constrained
$\Delta\rangle_{max}$, $\Delta\rangle_{min}$ (e $Å^{-3}$)	0.76, -0.59	1.22, -0.89	0.34, -0.56
No. of restraints	6	0	0
	TXM-ACE	**TXM-DMFA**	**TXM-ACY**
CCDC number	1538111	1538134	1904101
Crystal data			
Chemical formula	$C_{13}H_{11}N_3O_4S_2\cdot C_3H_6O$	$C_{13}H_{11}N_3O_4S_2\cdot C_3H_7NO$	$C_{13}H_{11}N_3O_4S_2\cdot C_2H_3N$
M_r	395.44	410.46	378.42
Crystal system, space	Triclinic, $P\bar{1}$	Triclinic, $P\bar{1}$	Monoclinic, $P2_1/n$

group			
Temperature (K)	293(2)	293(2)	293(2)
a, *b*, *c* (Å)	8.9341 (4), 8.9659 (5), 11.9315 (6)	9.1060 (4), 9.4381 (4), 11.6586 (6)	9.1718 (3), 8.9965 (3), 21.1092 (8)
α, β, γ (°)	75.325 (4), 81.348 (4), 89.620 (4)	74.530 (4), 77.500 (4), 85.545 (3)	98.591 (4)
V ($Å^3$)	913.55 (8)	942.56 (8)	1722.26 (11)
Z	2	2	4
Radiation type	Mo $K\alpha$	Mo $K\alpha$	Mo $K\alpha$
μ (mm^{-1})	0.32	0.32	0.34
Crystal size (mm)	0.5 × 0.45 × 0.2	0.45 × 0.24 × 0.14	0.13 × 0.07 × 0.01
Data collection			
Diffractometer	Xcalibur, Ruby, Gemini ultra	Xcalibur, Ruby, Gemini ultra	Xcalibur, Ruby, Gemini ultra
Absorption correction	Multi-scan *CrysAlis PRO*	Multi-scan *CrysAlis PRO*	Multi-scan *CrysAlis PRO*
T_{min}, T_{max}	0.907, 1.000	0.827, 1.000	0.823, 1.000
No. of measured, independent and observed [$I > 2\sigma(I)$] reflections	15092, 4269, 3370	11967, 3857, 2958	26375, 3527, 2809
R_{int}	0.028	0.034	0.060
$(\sin \theta/\lambda)_{max}$ ($Å^{-1}$)	0.658	0.625	0.625
Refinement			
$R[F^2 > 2\sigma(F^2)]$, $wR(F^2)$, S	0.038, 0.108, 1.05	0.043, 0.123, 1.04	0.043, 0.101, 1.06
No. of reflections	4269	3857	3527
No. of parameters	289	257	228
H-atom treatment	H atoms treated by a mixture of independent and constrained refinement	H-atom parameters constrained	H-atom parameters constrained
$\Delta\rangle_{max}$, $\Delta\rangle_{min}$ (e $Å^{-3}$)	0.28, -0.34	0.25, -0.30	0.043, 0.101, 1.06

S21. Hydrogen-bond geometry for described structures. Numeration as reported within crystal structures.*

D—H···*A*	*D*—H (Å)	H···*A* (Å)	*D*···*A* (Å)	*D*—H···*A* (°)
TXM-CHCl$_3$-I				
N1A—H1A···O1A	0.86	2.03	2.655 (10)	129.3
N1A—H1A···O1B	0.86	2.20	2.905 (11)	138.7
N1B—H1B···O1A	0.86	2.19	2.872 (11)	136.3
N1B—H1B···O1B	0.86	2.00	2.645 (10)	130.9
N2A—H2A···O2A	0.86	1.87	2.608 (10)	142.3
N2B—H2B···O2B	0.86	1.88	2.606 (11)	141.4
TXM-CHCl$_3$-II				
N2B—H2B···O2B	0.88	1.84	2.584 (9)	140.6
N2A—H2A···O2A	0.88	1.88	2.591 (9)	136.6
N1B—H1B···O1A^{i}	0.88	2.15	2.830 (10)	133.5
N1B—H1B···O1B	0.88	1.96	2.634 (8)	132.5
N1A—H1A···O1A	0.88	1.98	2.645 (8)	131.2
N1A—H1A···O1B^{ii}	0.88	2.12	2.797 (10)	133.5
C14B—H14B···O2B	1.00	2.07	2.963 (11)	146.8
C14A—H14A···O2A^{iii}	1.00	2.12	2.962 (12)	140.7
TXM-CHCl$_3$-III				
N2—H2···O2	0.88	1.85	2.595 (3)	141.4
N1—H1···O1^{iv}	0.88	2.21	2.893 (2)	134.5
N1—H1···O1	0.88	1.96	2.634 (2)	132.1
TXM-ACE				
N2—H2···O2	0.87 (2)	1.86 (2)	2.6098 (19)	143.0 (18)
N1—H1···O1	0.86 (2)	1.97 (2)	2.6155 (18)	130.9 (17)
N1—H1···O1^{v}	0.86 (2)	2.18 (2)	2.8767 (18)	138.2 (17)
TXM-DMFA				
N2—H2···O2	0.86	1.88	2.602 (2)	141.2
N1—H1···O1^{vi}	0.86	2.17	2.871 (2)	137.9
N1—H1···O1	0.86	1.97	2.620 (2)	131.8
TXM-ACY				
N1—H1···O1	0.86	2.00	2.641 (2)	131.1
N1—H1···O1^{vii}	0.86	2.20	2.898 (2)	138.2
N2—H2···O2	0.86	1.90	2.624 (2)	141.3

Symmetry code(s): (i) *x*-1, *y*, *z*; (ii) *x*+1, *y*, *z*; (iii) -*x*+2, *y*-1/2, -*z*+3/2; (iv) -*x*+1, -*y*+1, -*z*+2; (v) -*x*+2, -*y*+2, -*z*+1; (vi) -*x*, -*y*+1, -*z*+1; (vii) -*x*+1, -*y*+1, -*z*+1.

*Look file '*cif*' with CSD Refcode: 1890995, 1904023, 1904022, 1538111, 1538134, 1904101.

S22. Sulphur-bond geometry for described structures.

D—S···*A*	*D*—S (Å)	S···*A* (Å)	*D*···*A* (Å)
TXM-ZWC	1.27	3.03	2.81
TXM-BKE	1.33	3.06	2.82
TXM-BKE-0	1.33	3.06	2.82

S23. Comparison of experimental powder pattern of TXM chloroform solvate publicized in Patel *et. al.*[3] (1) and calculated powder pattern from solved in this work TXM-$CHCl_3$-I structure. This comparison shows that it is similar phases. Blue stars indicate picks from impurity phase in (1) sample. Experimental pattern (1) slightly shifted to the left relative to the calculated diffraction pattern (2).

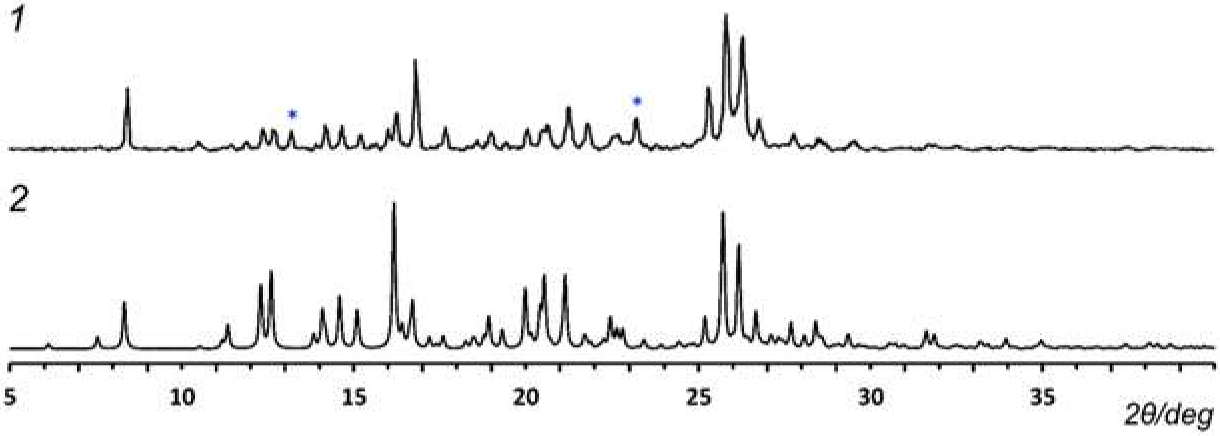

S24. Comparison of theoretical powder diffraction pattern calculated from TXM-$CHCl_3$-I structure (1) with experimental powder pattern from the phase which we call TXM-$CHCl_3$-II (2). Powder pattern (3) was recorded from the sample of TXM-$CHCl_3$-II which was warmed up at a temperature of 160 °C degrees for 1.5 hours. Powder pattern (4) belongs to the polymorph modification 1 of TXM and was taken from Patel *et al.*[3]. This picture shows that TXM-$CHCl_3$-I and TXM-$CHCl_3$-II are different phases and TXM-$CHCl_3$-II passes into the polymorph modification 1 of TXM as a result of desolvation.

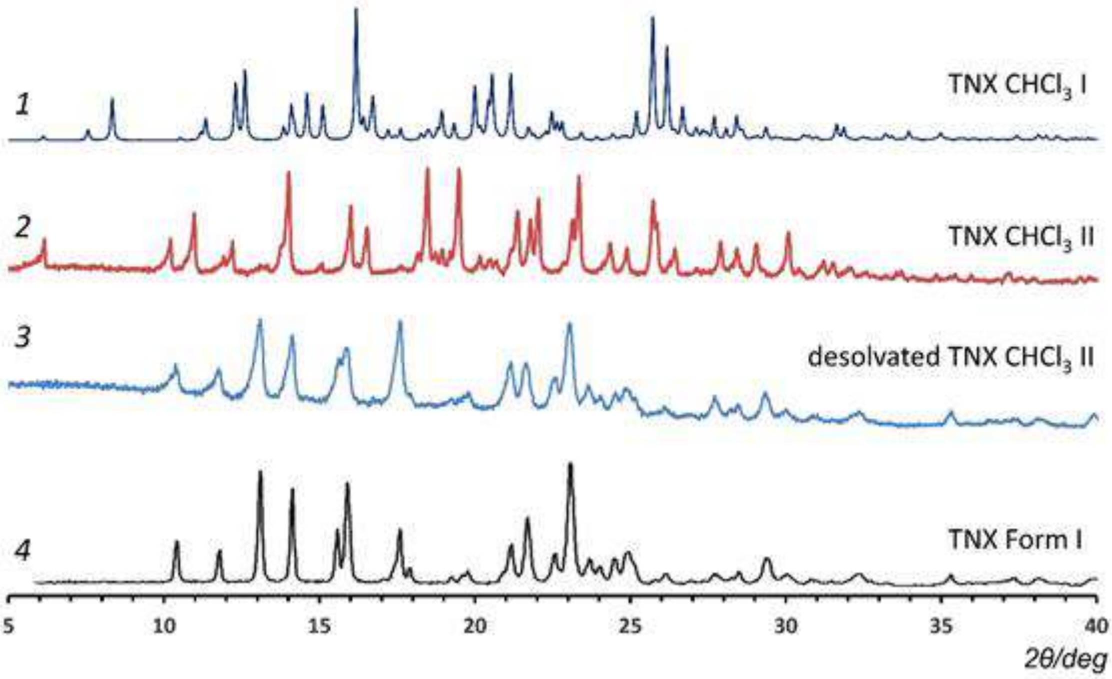

S25. Table of root-mean square deviation (RMSD) of backbone atomic position (without hydrogen atoms) in Angstrom (Å) for the tenoxicam zwitterionic form (TXM-ZWC) within solvents respect its pure form. Highlighted in green are the crystal structures solved in this article.

COFORMER/SOLVENT	RMSD (Å)
-	0
chloroform (form I)	0.091
acetonitrile	0.121
acetone	0.126
salicylic acid	0.130
N,N-dimetilformamide	0.149
benzoic acid	0.154
nitromethane	0.155
chloroform (form III)	0.171
propinoic acid	0.174
catechol	0.194
resorcinol	0.201
acetic acid	0.227
pyrogallol	0.234
chloroform (form II)	0.237
formic acid	0.245

S26. Table of Free energy (G) calculated at 298.15 K for the three full-optimized in vacuo TXM keto-enolic forms: zwitterionic (ZWC), β-keto-enolic (BKE), β-diketone.

TXM keto-enolic form	G / (kcal/mol)
ZWC	-1106709.663952
BKE	-1106711.861490
BDK	-1106699.375304

S27. Table of interaction energy calculated with perturbation theory[4] between the lone pair of H-acceptor and N—H σ* orbitals for ZWC and O—H σ* orbitals for BKE.

TXM keto-enolic form	E (kcal/mol)
ZWC	30.73
BKE	0
BKE0*	19.63

*BKE form with planar dihedral angle 1'—2'—16—14

S28. IR spectra obtained for the TXM solvate with chloroform second form (TXM-$CHCl_3$-**II**) without any sample preparation from 600 to 4000 cm^{-1} with the resolution of 2 cm^{-1}.

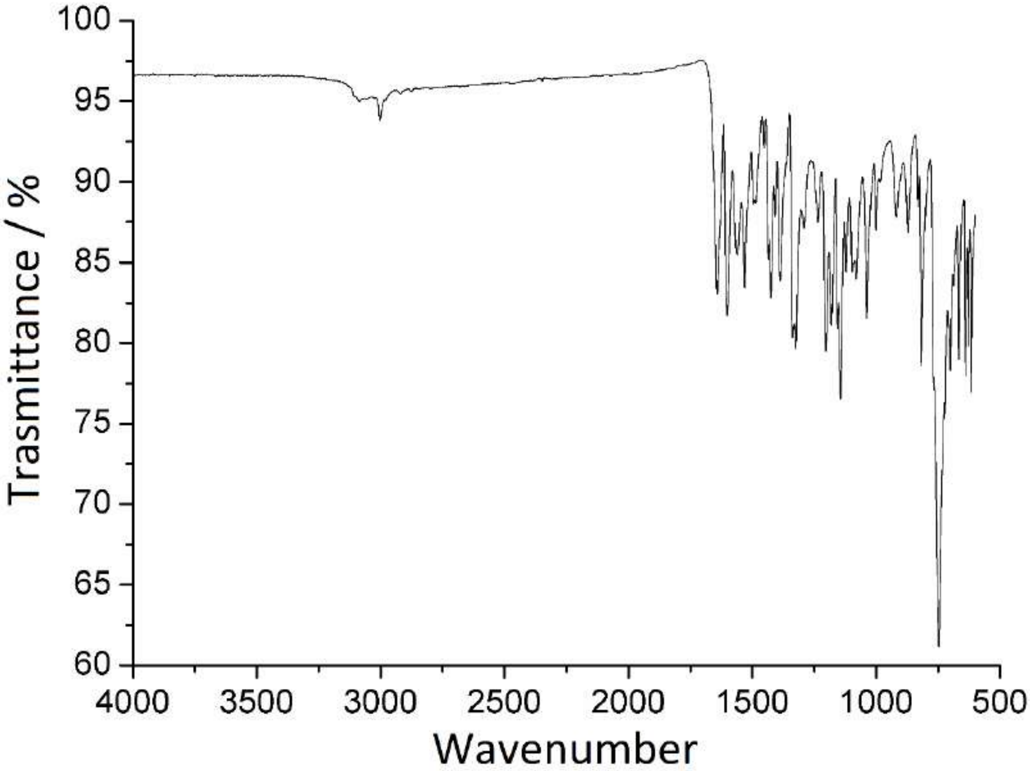

References

1. Y. Marcus, The Properties of Solvents, Jons Wiley and Sons, 1999.
2. P.S. Sherin, J. Grilj, Yu.P. Tsentalovich, E. Vauthey. *J. Phys. Chem. B.* 2009, **113**, 4953-4962.
3. J. R. Patel, R. A. Carlton, T. E. Needham, C. O. Chichester, F. G. Vogt, *Int. J. Pharm.*, 2012, 436, 685–706.
4. P. Atkins, R. Friedmann, Molecular Quantum Mechanics, Eds. Oxford University Press, 2005.

CHAPTER III

Quantum Chemical Topology applied to Catalysis

Summary:

The chapter describes use of a range of advanced computational methodologies to investigate the reactivity of a popular and industrially-important catalytic molecule as Dess-Martin Periodinane (DMP), which is amongst the most popular catalysts for oxidation of simple alcohols. However, despite myriad publications on its experimental applications, very little remains understood about its reactivity. In the present contribution, we explore the reactivity of the DMP molecule by a series of quantum chemical topological tools. It is found that the iodine atom in the DMP molecule, a λ^5-iodane catalyst, is hypervalent due to the presence of two very weak three-centre-four-electron interactions. A combination of the Source Function and Espinosa's topological indices indicates preferential dissociation of only a subset of the iodine-ligand bonds and therefore sheds new light on the favourable reactivity of the molecule. Further, the inability to modify the reactivity of the iodine centre by ligand substitution indicates non-trivial reactivity of the DMP molecule. This is of great interest for experimental development of novel DMP-based catalysts.

The present study makes use of quantum chemical topological tools. These techniques have proven highly successful in the description of molecular reactivity. Despite their success, however, many computational chemists continue to overlook these tools for the investigation of molecular reactivity. The present work not only offers new insight into the reactivity of the DMP molecule, but further highlights the strength of these tools in understanding the reactivity of complex molecules.

Conclusions:

- The Dess-Martin periodinane molecular structure was investigated by a combination of topological analysis and DAFH methods. By combination of these techniques, it was found that the reactivity of the DMP molecule, which is central to its catalytic activity, results from the presence of two labile 3c-4e bonds. Further, in DMP the presence of two 3c-4e bonds confirms a mechanism for the hypervalency of this λ5-iodane center.
- The variation of ED at the aromatic ligand did not result in any notable change in the apparent reactivity of the DMP molecule. Thus, it appears that the main contribution of the aromatic ligand may simply be to modify the sterics of the reactive center. The work presented here offers unique insight into the catalytic reactivity of the DMP molecule, and highlights the power of topological analysis and DAFH methods for such studies.

Contribution:

The project was managed by me other that the Investigation, data curation, formal analysis, While the conceptualization of results was done in in equal part with Dr. Adam A. L. Michalchuk.

Received: 21 June 2018 | Revised: 4 September 2018 | Accepted: 22 October 2018

DOI: 10.1002/qua.25838

WILEY International Journal of QUANTUM CHEMISTRY

FULL PAPER

Dess-Martin periodinane: The reactivity of a λ^5-iodane catalyst explained by topological analysis

Christian Tantardini[1,2] | **Adam A. L. Michalchuk**[2,3,4]

[1]Center for Electrochemical Energy Storage, SkolTech Skolkovo Institute of Science and Technology, Street Nobelya 3, Moscow, Russian Federation

[2]Chair of Solid State Chemistry, Novosibirsk State University, Street Nobelya 3, Novosibirsk, Russian Federation

[3]EaStCHEM School of Chemistry, University of Edinburgh, King's Buildings, West Mains Road, Edinburgh, United Kingdom

[4]EPSRC Center for Continuous Manufacturing and Crystallisation (CMAC), CMAC Future Manufacturing Research Hub, University of Strathclyde, Technology and Innovation Center, Level 6, 99 George Street, Glasgow, United Kingdom

Correspondence
Christian Tantardini, Center for Electrochemical Energy Storage, SkolTech Skolkovo Institute of Science and Technology, Street Nobelya 3, Moscow 121205, Russian Federation.
Email: christiantantardini@ymail.com

Funding information
Russian Ministry of Science and Education; EPSRC, Grant/Award Number: CMAC EP/I033459/1; Edinburgh Global Research Scholarship

Abstract

Dess-Martin periodinane (DMP) and its derivatives are popular organic catalysts. DMP is extremely reactive in the presence of alcohols, catalyzing their oxidative conversion into ketones. However, despite their widespread use, this reactivity has not yet been explained. In the present work, a quantum chemical topological approach is taken to study the electronic structure of DMP. Topological analysis revealed two of the iodine…ligand interactions to be notably weaker than the two others. Combined with study of the domain-averaged Fermi hole (DAFH), it was confirmed that the iodine center is λ^5-hypervalent, forming two 3-center-4-electron and two 3-center-2-electrons bonds. The weakness of these multicenter bonds is ascribed to the high reactivity displayed by DMP. The ability to tune the ligand-iodine interactions is investigated by altering the electronic structure of the ligands. It is demonstrated that DAFH analysis offers powerful insight into the understanding of molecular reactivity.

KEYWORDS

dess-martinperiodinane (DMP), domain-averaged-Fermi-hole (DAFH), Espinosa-indexes, quantum-theory-atom-inmolecules (QTAIM), source function (SF)

1 | INTRODUCTION

Hypervalent iodine compounds are popular organo-catalysts. To date, compounds based on hypervalent iodine have found application across a broad spectrum of syntheses of both academic and industrial interest. Of particular note is the use of these compounds in the production of pharmaceuticals and polymers.[1–9] Among these iodine organo-catalysts, Dess-Martin periodinane (DMP) has found particular popularity as a high yielding and chemo-selective reagent for the oxidation of alcohols.[10,11] The iodine center within this molecule is formally I(V), known as a λ^5-iodane.

The molecular structure of DMP is similar to *o*-iodoxybenzoic acid (IBX),[12] another λ^5-iodane hypervalent catalyst. While IBX is more easily prepared than DMP, it is explosive and thus not usable on an industrial scale. Further, the selectivity and yields of oxidation reactions obtained with IBX are much lower than those catalyzed by DMP.[12] With its beneficial properties and widespread use, DMP is largely regarded as a reference point for the development of novel λ^5-iodane catalysts.[13–15]

A putative mechanism for the reactivity of DMP has been proposed, Scheme 1.[11,12] The alcohol first coordinates to the DMP iodine center, which leads to expulsion of an acetate ligand. Proton transfer occurs from the alcohol to a neighboring acetate ligand, with associated loss of both ligands. Numerous experimental studies have lent support to this mechanism,[16–20] with limited theoretical investigations available.[21] While the available literature has developed this generic reaction scheme, a thorough understanding of its details and driving force remains unknown.

© 2018 Wiley Periodicals, Inc.

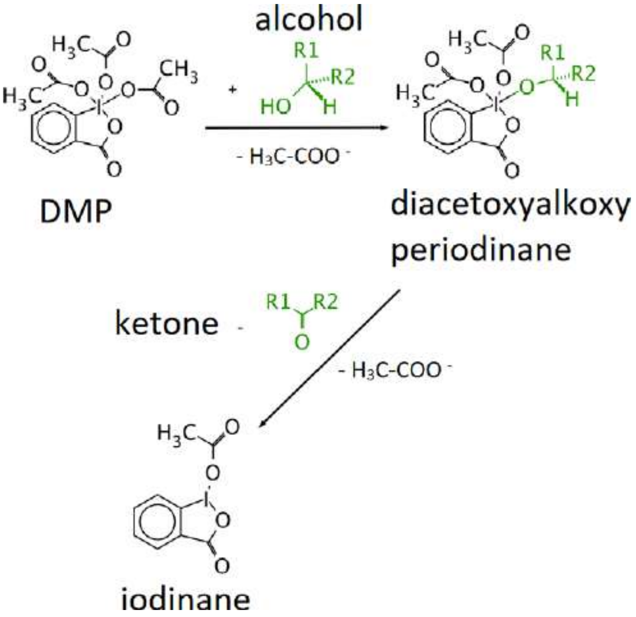

SCHEME 1 Reaction scheme for DMP-catalyzed alcohol oxidation

A recent theoretical investigation of the related λ^3-iodanes[22] has revealed novel insight into iodine-based catalysis. It was found that the driving force for their catalytic activity rests in a pseudo-Jahn-Teller (PJT) process. That is, that a geometric distortion about the central iodine atom was required to introduce formation of the stabilizing 3c4e bond. This therefore poses the question as to whether a similar mechanism is responsible for the popular λ^5-iodane catalyst, DMP. Such information is crucial for the selective design of novel catalytic compounds.

The present work aims to use a novel approach to the study of DMP and its reactivity, namely, via quantum chemical topological analysis. This is done by application of the quantum theory of atoms in molecules (QTAIM)[23] and the study of the domain-averaged Fermi hole (DAFH).[24–27] These methods, based on the direct study of the electron density, have proven to be powerful in order to correlate chemical bonding with molecular reactivity.[22,28–30] This work seeks to better understand the intrinsic electronic factors that drive the reactivity of the DMP molecule. In this process, we aim to offer insight into the mechanisms of a broader class of λ^5-iodane catalyst toward targeted design of new catalytic molecules.

2 | THEORETICAL BACKGROUND

The Fermi hole[31–33] relates to the probability of locating one electron at position $\mathbf{r}_1$with spin state σ_1, if a second is fixed at position $\mathbf{r}_2$ with spin state σ_2. This probability, $P_{\mathbf{r}_2,\sigma_2}(\mathbf{r}_1,\sigma_1)$, is given in terms of pair density $\rho_2(\mathbf{r}_1, \sigma_1, \mathbf{r}_2, \sigma_2)$[31–33]

$$\rho_2(\mathbf{r}_1,\sigma_1,\mathbf{r}_2,\sigma_2)=\binom{N}{2}\int_{(\mathbb{R}^3)^{N-2}}\sum_{\sigma_1,\ldots,\sigma_N\in\mathbb{Z}_2}|\Psi(\mathbf{r}_1,\sigma_1,\mathbf{r}_2,\sigma_2,\ldots,\mathbf{r}_N,\sigma_N)|^2 d\mathbf{r}_3\ldots d\mathbf{r}_N \tag{1}$$

Here, $(\mathbf{r}_i, \sigma_i)\in\mathbb{R}^3\times\mathbb{Z}_2$ are spin-space coordinates for the ith electron. $P_{\mathbf{r}_2,\sigma_2}(\mathbf{r}_1,\sigma_1)$ can therefore be defined as the conditional probability[31–33]

$$P_{\mathbf{r}_2,\sigma_2}(\mathbf{r}_1,\sigma_1)=2\rho_2(\mathbf{r}_1,\sigma_1,\mathbf{r}_2,\sigma_2)/\rho(\mathbf{r}_2,\sigma_2) \tag{2}$$

with,

$$\rho(\mathbf{r}_2,\sigma_2)=\binom{N}{1}\int_{(\mathbb{R}^3)^{N-1}}\sum_{\sigma_1,\ldots,\sigma_N\in\mathbb{Z}_2}|\Psi(\mathbf{r}_1,\sigma_1,\mathbf{r}_2,\sigma_2,\ldots,\mathbf{r}_N,\sigma_N)|^2 d\mathbf{r}_1,d\mathbf{r}_3\ldots d\mathbf{r}_N. \tag{3}$$

The antisymmetry of the electron spin wave function imposes two cases. When electronic spins are parallel, the probability of locating the second electron in the proximity of the first is minimal. Instead, when electronic spins are anti-parallel, there is an increased probability of locating the second electron in the proximity of the first. This probability is defined according to[31–33]

$$h_{\mathbf{r}_2,\sigma_2}(\mathbf{r}_1,\sigma_1)=\rho(\mathbf{r}_1,\sigma_1)-P_{\mathbf{r}_2,\sigma_2}(\mathbf{r}_1,\sigma_1), \tag{4}$$

where $h_{\mathbf{r}_2,\sigma_2}(\mathbf{r}_1,\sigma_1)>0$ signifies a Fermi heap and $h_{\mathbf{r}_2,\sigma_2}(\mathbf{r}_1,\sigma_1)<0$ is indicative of a Fermi hole. The concept of the density averaged Fermi hole (DAFH) follows closely from this concept.[24–27] In DAFH, depending on its spin wavefunction relative to the first electron, the second electron is thought to be confined to a volume space, analogous to an atomic basin Ω. Equation (2) thus becomes[24–27]

$$P_{\Omega,\sigma_2}(\mathbf{r}_1,\sigma_1) = 2\int_\Omega \rho_2(\mathbf{r}_1,\sigma_1,\mathbf{r}_2,\sigma_2)d\mathbf{r}_2 / \int_\Omega \rho(\mathbf{r}_2,\sigma_2)d\mathbf{r}_2. \tag{5}$$

It follows that, the DAFH can be defined as[24–27]

$$h_{\mathbf{r}_2,\sigma_2}(\mathbf{r}_1,\sigma_1) = \rho(\mathbf{r}_1,\sigma_1) - P_{\Omega,\sigma_2}(\mathbf{r}_1,\sigma_1), \tag{6}$$

Equation (6) must satisfying the normalization condition

$$\int_\Omega h_{\mathbf{r}_2,\sigma_2}(\mathbf{r}_1,\sigma_1)dr\,d\sigma = 1. \tag{7}$$

To ensure correct calculation of the DAFH, careful choice of the atomic basin partitioning scheme is required. For heavy atoms with considerable relativistic effects, such as iodine, previous works have shown a Bader partitioning is required. The common Mulliken partitioning scheme leads to unreliable results.[34]

Within the framework of DAFH, one can define multicenter indices. These indices are indicative of multi-electron, multicenter bonds, such as the 3-center-4-electron (3c4e) and 3-center-2-electron (3c2e) interactions. As such, the multicenter indices are useful for the study of hypervalent atoms.[35,36]

For the triatomic system composed of atoms A, B, and C, the 3-center bond index, I_{ABC}, was heuristically defined for a closed shell system according to[35,36]

$$I_{ABC} = \sum_\alpha^A \sum_\beta^B \sum_\gamma^C (PS)_{\alpha\beta}(PS)_{\beta\gamma}(PS)_{\gamma\alpha}, \tag{8}$$

where the summation is over atom triplet permutations, with atom indices α, β, and γ. Equation (8) results from partitioning of the expression[35,36]

$$\sum_\alpha^A \sum_\beta^B \sum_\gamma^C (PS)_{\alpha\beta}(PS)_{\beta\gamma}(PS)_{\gamma\alpha} = 2^2 N. \tag{9}$$

In the above, P and S denote the normal first-order density matrix and the overlap matrix, respectively. More generally, a bond center of order z can be described according[35,36]

$$\sum_\alpha \sum_\beta \cdots \sum_\omega (PS)_{\alpha\beta}(PS)_{\beta\gamma}(PS)_{\omega\alpha} = 2^{z-1} N. \tag{10}$$

This model can be solved analytically with a theoretical limit for 3c4e and 3c2e bonds of −0.185 and +0.185, respectively. Indices near these limits are therefore indicative of the bonding structure of the molecule.

2.1 | Computational details

2.1.1 | Structure optimization

An ansatz structure for Dess-Martin periodinane (DMP) was taken from the experimental crystal structure (CCDC REF:ZAZJOB).[37] Atomic positions were optimized through plane wave density functional theory (PW-DFT) using the B86b[38] exchange and PBE[39,40] correlation functionals in combination with PAW PBE pseudopotentials. For iodine, a relativistic PAW PBE pseudo-potential was used. The PW-DFT was performed in combination with the exchange-hole dipole moment (XDM) dispersion correction,[41–43] with damping parameter (a_1 = 0.6512, a_2 = 1.4633) as reported in literature.[41–43] Atomic positions were relaxed until forces $<10^{-6}$ were achieved and the total SCF energy converged to $<10^{-8}$. A kinetic energy cut-off of 46 Ry was used, and the electronic structure was sampled on a Monkhorst-Pack grid of 2 × 2 × 2, giving a total of 8 k-points in the irreducible Brillouin zone.[44] All PW-DFT calculations were performed using Quantum Espresso v6.0.[45]

2.1.2 | QTAIM analysis

The optimized DMP structure was extracted from the unit cell. A restricted all-electron PROAIM wave function[46] was generated in Gaussian v09 revD.01.[47] A dgdzvp[48,49] basis set was used for the iodine atom and the aug-cc-pVTZ[50,51] basis set for all other atoms. The PBE0[52] DFT functional was used with Douglas-Kroll-Hess second-order scalar relativistic effects (DKH2),[53–57] treating the cores as finite elements. QTAIM analysis was performed using a modified version of the PROAIMV program.[58,59] High quality PROAIM wavefunctions[46] were produced by setting Acc2E = 12 to ensure accuracy of the 2-electron integrals, and Grid = −96 032 to ensure a high-quality integration grid.

2.1.3 | DAFH analysis

The same optimized molecular structure was used, as above. Due to the compatibility of the WinBader program[78] used for DAFH analysis and population analysis, PROAIM wave functions[46] were generated for the DMP molecule using Gaussian03.C02 (G03)[77]. This was done using three different LBS for the noniodine atoms: 3-21G,[60–65] 6-31G,[66–75] and 6-311G[76]. The dgdzvp basis set was used for iodine in all cases. The SCF energy was converged to $<10^{-8}$.

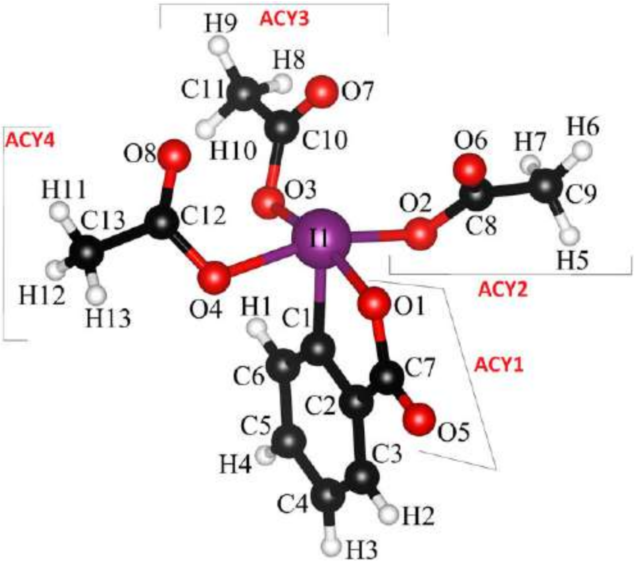

FIGURE 1 Molecular structure of DMP, with associated atomic and ligand labelling. Atoms are given as C (black), H (white), O (red), and I (purple)

2.1.4 | Gedanken experiment

The optimized DMP molecule was used as input structure. Substitution for-NO_2, -NH_2, and -CH_3 groups was performed. The geometry of the substituted ligand was optimized (using G09) using the PBE0 DFT functional, along with the aug-cc-pVTZ-PP[79] basis set for iodine and aug-cc-pVTZ[50,51] for all other atoms. The remainder of the molecule was held frozen. The PROAIM wave function[46] for each substitution was generated within G09 using a dgdzvp basis set[48,49] for iodine and 3-21G,[60–65] 6-31G,[66–75] and 6-311G[76] basis set for the other atoms. The PBE0[68] DFT functional was used with DKH2 relativistic core correction on iodine.[53–57] SCF energy converged to $<10^{-8}$.

3 | RESULTS AND DISCUSSION

The DMP molecule is based around a central iodine atom, Figure 1. The three monodentate acetate ligands and one bidentate benzoic acid ligand form a distorted square-based pyramidal geometry. Four of the five coordinating atoms are oxygen (ie, there are four I…O bonds) with the fifth being carbon (I…C). Due to the flexibility of the ligands, the potential energy surface of the molecule is shallow. As an ansatz structure, the DMP atomic positions were therefore optimized within the crystal structure to limit rotational freedom of the ligands. Our optimized geometry agrees well with the minimum energy gas phase structure reported by Fusaro et al.[21] (see Supporting Information Figure E.S.I.1). For clarity, the following discussion will use atomic labels according to Figure 1. The first step in the DMP-catalyzed oxidation reaction, Scheme 1, is the exchange of an acetate ligand for the alcohol molecule. This suggests that at least one of the acetate ligands must be labile. To examine this lability within the framework of QTAIM, bond critical points (BCP) were identified along the iodine-ligand axes.[23] As expected, topological analysis of the electron density revealed five BCPs: I1-O1, I1-O2, I1-O3, I1-O4, and I1-C1, Figure 1. The electron kinetic (G_{BCP}) and virial (V_{BCP}) energy densities at the BCP are indicative of the nature of the associated interaction, in accordance with Espinosa's classifications (Supporting Information Figure E.S. I.2).[80] The ratio of $|V_{BCP}/G_{BCP}|$ for each of the I…O BCPs fall between 1.5 and 1.6, Table 1, placing them within the so-called transition zone. These types of bonds are characterized by a mixture of covalent and ionic character, and are typical of metal-metal and hydrogen bonding interactions.[80–83] In contrast to the I…O interactions, the $|V_{BCP}/G_{BCP}|$ for the I1…C1 B.P. Table 1, suggests this bond to be a shared shell (purely covalent) interaction. It therefore appears that the iodine center contains five bond paths, characterized by two unique types of interactions.

The formation of five covalent interactions is in clear violation of the well-established octet rule. It was therefore prudent to examine the nature of these interactions in more depth by analysis of the Domain Averaged Fermi Hole (DAFH).[24–27] Diagonalization of the Fermi hole associated with iodine atom revealed 29 nonzero eigenvalues (Supporting Information E.S.I.3). Of these, 24 were equal to 2, and correspond to filled inner shells on the iodine atom. Only a single eigenvalue is near unity, indicating the existence of only one non-polarized "broken-valence" single bond. The corresponding eigenvector, Figure 2, is a σ-type interaction along the I1-C1 bond vector. This is consistent with the closed-shell interaction identified by Espinosa's index for the corresponding BCP. Two additional eigenvalues of approximately 0.7 are found along the I1-O2 and I1-O3 bonds, that is, to two *cis* ligands. The final two nonzero eigenvalues were found along the I1-O1 and I1-O4 bonds, with eigenvalues of approximately 0.12. These eigenvalues <1 are consistent with highly polarized interactions, and further support the transition zone character of the I-O interactions. It is interesting to find that the sum of *trans* I-O interactions leads to eigenvalues near unity in both cases and indicates the potential existence of three-center interactions.

In fact, two 3c4e bonds were identified at the iodine center in DMP: O1-I1-O3 and O2-I1-O4. The three-center indices, Supporting Information E.S.I.4, for these interactions were found to be −0.069 and −0.073, respectively. These 3-center indices deviate significantly from the theoretical

TABLE 1 Topological parameter calculated at the BCP

Bond	ρ_{BCP} (a.u.)	$\nabla^2\rho_{BCP}$ (e.bohr^{-3})	G_{BCP} (a.u.)	V_{BCP} (a.u.)	$\lvert V_{BCP}\rvert/G_{BCP}$	H_{BCP} (a.u.)
I1- C1	0.1438	−0.1499	0.05	−0.13	2.82	−0.08
I1- O1	0.1131	0.1660	0.10	−0.15	1.57	−0.06
I1- O2	0.1183	0.1652	0.10	−0.16	1.60	−0.06
I1- O3	0.1185	0.1620	0.10	−0.16	1.60	−0.06
I1- O4	0.1076	0.1568	0.09	−0.14	1.56	−0.05
RMS(I...O)	0.1144	0.1625	0.09	−0.16	1.58	−0.06

Values calculated according to Espinosa[85]: Charge density, $\rho_{BCP}\rho$BCP, Laplacian of charge density, $\nabla^2\rho_{BCP}$, kinetic energy, G_{BCP}, virial energy, V_{BCP}, and the Hamiltonian, H_{BCP}. The root mean square (RMS) of all I…O bonds for each topological parameter.

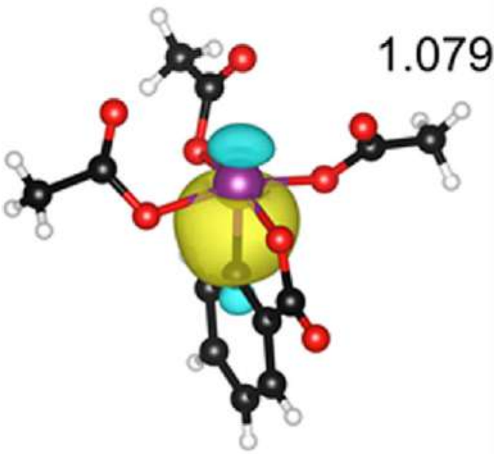

FIGURE 2 Eigenvectors (isovalue = 0.08) of Fermi hole decomposition for the iodine atom of DMP along C1-I1 σ-bond. The Fermi hold phases are shown in blue (negative) and yellow (positive), along with the associated eigenvalue calculated using a 6-311G basis set. Other basis sets in Supporting Information E.S.I.2. Atoms are given as C (black), H (white), O (red), and I (purple)

maximum (ie, strongest 3c4e bond) of −0.185.[36] This confirms the existence of weak multicenter interactions and provides a mechanism for the apparent hypervalency of the λ^5 DMP molecule. Two additional three-center interactions were identified: O2I1C1 and O4I1C1. These interactions were found to correspond to 3c2e bonds, with three-center indices of 0.014 and 0.011, respectively. Again, with magnitudes deviating largely from the theoretical maximum, these are both very weakly bonding interactions. Given the participation of the O2-I1 and O4-I1 interactions in two weak three-center interactions, it follows that the O2-I1 and O4-I1 bonds are the weakest of the four acetate ligand interactions.

The existence of three-center interactions suggests that the BCP corresponding to individual I-O interactions should contain notable contribution from the other members of the three-center bond. We consider first the 3c4e interaction O1-I1-O3. At the I1-O1 BCP, decomposition of the density into atomic basin contributions via the Source Function (SF)[84,85], Supporting Information E.S.I.5, reveals that at least 75.29% of the bond density results from donation of the I1 and O1 atoms. In addition, there is a relatively large donating contribution of O2 to this BCP (1.97%), which is reflected in the eigenvector plots of the associated Fermi hole, Figure 3A. The donating contribution of the O3 atom to this BCP, however, is only approximately 1.2%, Figure 3A. This contribution is no more than that of the other O atom, which does not form part of the three-center interaction. The same situation exists when considering the I1-O3 interaction. The negligible donating contribution of the *trans* atoms to bonding in the three-center interaction strongly suggests that these I-O interactions are very weak and thus labile to exchange. No other major contributions (ie, SF% > 1% exists for either BCP).

It is interesting next to consider the second 3c4e interaction: O2-I1-O4. Both I-O interactions in this case are also involved in the 3c2e interactions O-I1-C1. Analysis of the SF decomposition of the O2-I1 BCP in fact shows the smallest donating contribution to bonding from O4, as compared to the other coordinating oxygen atoms, Figure 3. The same is seen for the O4-I1 BCP. Again, this strongly suggests that the accompanying three-center interaction is very weak. In contrast to the O1-I1 and O3-I1 interactions, there is a contribution to the O2-I1 and O4-I1 BCPs from the C1 atom. In both cases, the C1 atom acts as a sink of electron density at the I-O BCPs. That is to say that it withdraws electron density from the O2-I1 and O4-I1 bonding interactions. While this contribution is small, it does indicate added weakening of the O2-I1 and O4-I1 interactions through the 3c2e interactions.

The involvement of the C1 atom as an electron density sink in only two of the four I1-O1 suggests that modification of the electron density on the benzoic acid ligand may offer a means to tune the interactions within the DMP molecule. To this end, a series of substitutions (-NO_2, -NH_2, and -CH_3) were made on the benzoic acid ring, Supporting Information E.S.I.6, *para* to the iodine coordination site (ie, on the C4 site of

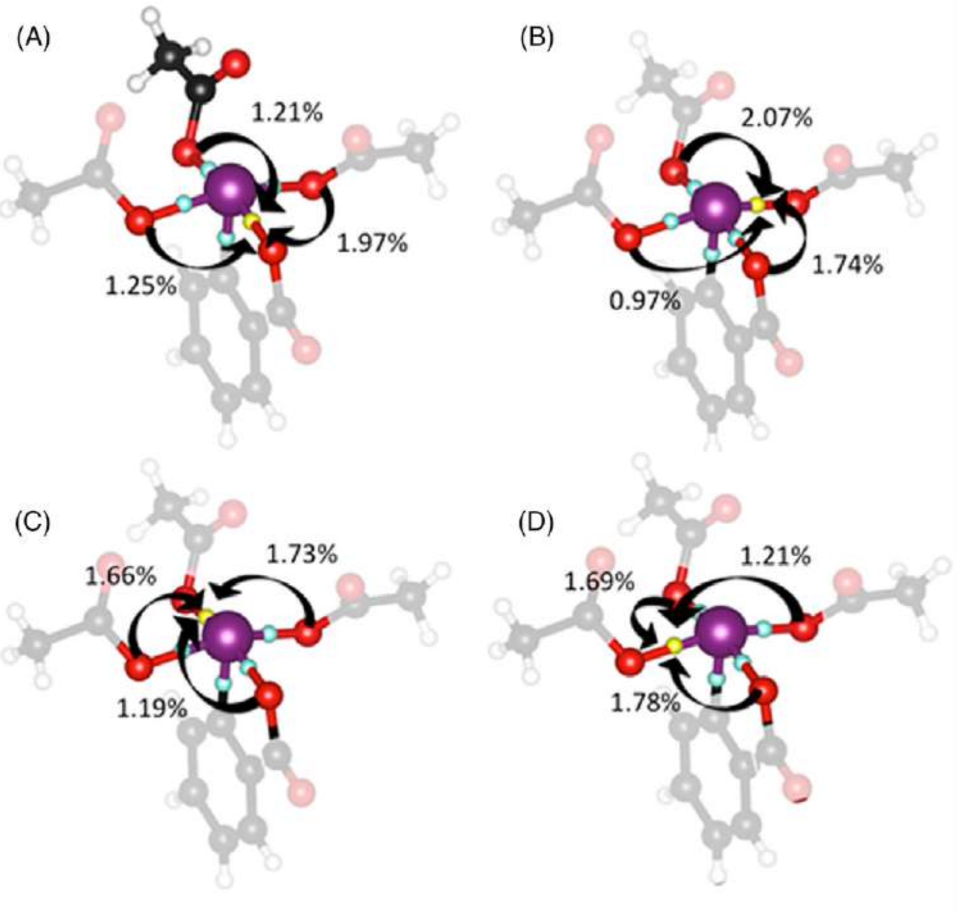

FIGURE 3 Source function decomposition of the oxygen atom contributions to the (A) O1-I1 BCP, (B) O2-I1 BCP, (C) O3-I1 BCP, and (D) O4-I1 BCP. Atoms are given as C (black), H (white), O (red), and I (purple)

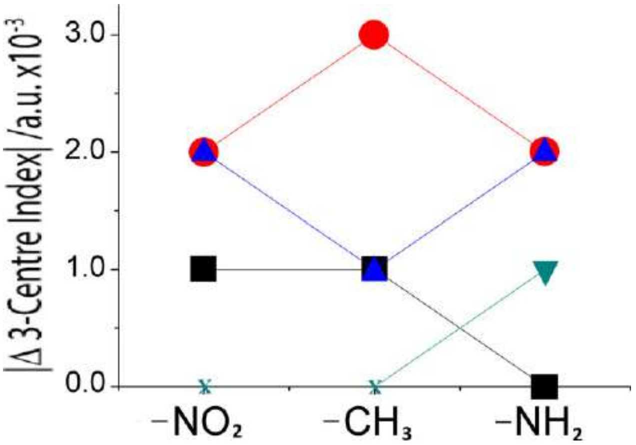

FIGURE 4 Changes in the value of the 3-centre index as a result of aromatic electrophilic substitution at the C4 site (Figure 1) of DMP molecule. Relative changes are shown as a Δ from the original DMP values for 3c4e bonds (black) O1-I1-O3 and (red) O2-I1-O4, as well as the 3c2e bonds (blue) O2-I1-C1 and (green) O4-I1-C1. Where the substitution led to a loss of the 3c4e interaction it was not possible to calculate the 3-centre index. Hence, these points are marked as X

Figure 1). Substitution of the aromatic ring did lead to some changes in the relative stabilities of the three-center indices, Figure 4. However, in the cases tested here, it was seen that the absolute magnitude of these changes is on the order of 10^{-3}. These changes are very small and are not significant within the remit of topological analysis. Previous attempts at modifying the reactivity of DMP and related catalyzes have focused on changes in the oxygen-based ligands. It appears that these attempts are most appropriate, as changes to the C1-coordinated aromatic substituent leads to no notable change in the reactivity of the iodine center.

4 | CONCLUSION

The Dess-Martin periodinane molecular structure was investigated by a combination of topological analysis and DAFH methods. By combination of these techniques, it was found that the reactivity of the DMP molecule, which is central to its catalytic activity, results from the presence of two labile 3c-4e bonds: O1–I1–O3, O2–I1–O4. The ligands in the iodine coordination sphere are correspondingly found to be only weakly bound, and thus labile to exchange. This is supported by DAFH analysis and calculation of BCP source function contributions. Further, the presence of these 3c-4e bonds confirms a mechanism for the hypervalency of this λ^5-iodane center.

The presence of multicenter interactions further suggests that it may be possible to modify reactivity of a catalytic center by modification of ligand electronic properties. In particular, due to the low source-function contribution of the C1 atom in the DMP molecule, it was proposed that modification of the electron density within this region of the molecule could be sufficient to induce changes in the reactivity. Surprisingly, however, variation of the electron density of this ligand did not result in any notable change in the apparent reactivity of the DMP molecule. Thus, it appears that the main contribution of the C1 ligand may simply be to modify the sterics of the reactive center. The work presented here offers unique insight into the catalytic reactivity of the DMP molecule, and highlights the power of topological analysis and DAFH methods for such studies.

ACKNOWLEDGMENTS

This work was carried out thanks to the equipment kindly provided by the Siberian Supercomputer Center ICMMG SB RAS, the "Supercomputing Center of Novosibirsk State University" (http://nusc.nsu.ru) and the Slovak University of Technology in Bratislava, Slovakia. The authors thank Carlo Gatti, Lukáš Bučinský, and Robert Ponec for useful discussion and technical assistance with calculations. Funding is gratefully acknowledged from an Edinburgh Global Research Scholarship (AM), EPSRC CMAC EP/I033459/1 (AM), and the Russian Ministry of Science and Education (CT/AM). CT thanks his supervisor Artem R. Oganov for ongoing support. AM thanks E. V. Boldyreva and C. R. Pulham for ongoing support.

CONFLICT OF INTEREST

The authors declare no conflict of interest.

AUTHOR CONTRIBUTIONS

Contribution role: Tantardini, Michalchuk
Conceptualization: Tantardini, Michalchuk
Investigation, data curation, formal analysis: Tantardini
Project administration: Tantardini
Visualization: Tantardini, Michalchuk
Writing - original draft preparation: Tantardini, Michalchuk
Writing - review & editing: Tantardini, Michalchuk

ORCID

Christian Tantardini https://orcid.org/0000-0002-2412-9859

REFERENCES AND NOTES

[1] *T. Wirth, Hypervalent Iodine Chemistry: Modern Developments in Organic Synthesis in Topics in Current Chemistry*; Springer: New York, vol. 224, **2003**.
[2] V. V. Zhdankin, P. J. Stang, *Chem. Rev.* **2008**, *108*, 5299.
[3] X. Q. Wang, T. Yang, X. L. Cheng, Q. L. Shen, *Angew. Chem. Int. Ed.* **2013**, *52*, 12860.
[4] T. Dohi, A. Maruyama, N. Takenaga, K. Senami, Y. Minamitsuji, H. Fujioka, S. B. Caemmerer, Y. Kita, *Angew. Chem. Int. Ed.* **2008**, *47*, 3787.
[5] T. Dohi, N. Takenaga, T. Nakae, Y. Toyoda, Y. Yamasaki, M. Shiro, H. Fujioka, A. Maruyama, Y. Kita, *J. Am. Chem. Soc.* **2013**, *135*, 4558.
[6] S. M. Altermann, S. Schäfer, T. Wirth, *Tetrahedron* **2010**, *66*, 5902.
[7] M. S. Yusubova, V. V. Zhdankin, *Resource-Efficient Technol.* **2015**, *1*, 49.
[8] M. S. Yusubov, P. S. Postnikov, R. Ya. Yusubova, A. Yoshimura, G. Jürjens, A. Kirschning, V. V. Zhdankin, *Adv. Syn. Cataly.*, **2017**, *359* (18), 3207–3216.
[9] R. Sanichar, C. Carroll, R. Kimmis, B. Reiza, J. C. Vederas, *Org. Biomol. Chem.* **2018**, *16*, 593.
[10] D. B. Dess, J. C. Martin, *J. Org. Chem.* **1983**, *48*, 4155.
[11] D. B. Dess, J. C. Martin, *JACS* **1991**, *113*, 7277.
[12] K. C. Nicolaou, T. Montagnon, P. S. Baran, Y.-L. Zhong, *J. Am. Chem. Soc* **2002**, *124*, 2245.
[13] K. C. Nicolau, P. S. Baran, Y.-L. Zhong, K. Sugita, *J. Am. Chem. Soc.* **2002**, *124*, 2212.
[14] K. C. Nicolau, K. Sugita, P. S. Baran, Y.-L. Zhong, *J. Am. Chem. Soc.* **2002**, *124*, 2221.
[15] K. C. Nicolau, P. S. Baran, Y.-L. Zhong, S. Barluenga, K. W. Hunt, R. Kranich, J. A. Vega, *J. Am. Chem. Soc.* **2002**, *124*, 2233.
[16] S. De Munari, M. Frigerio, M. Santagostino, *J. Org. Chem.* **1996**, *61*, 9272.

[17] J. J. Li, Dess–Martin periodinane oxidation. in *Name Reactions*, Springer, Berlin, Heidelberg **2009**.
[18] H. Tohma, Y. Kita, *Adv. Synth. Catal.* **2004**, *346*, 111.
[19] S. D. Meyer, S. L. Schreiber, *J. Org. Chem.* **1994**, *59*, 7549.
[20] J. S. Yadav, B. V. S. Reddy, A. K. Basak, A. V. Narsaiah, *Tetrahedron* **2004**, *60*, 2131.
[21] L. Fusaro, M. Luhmer, G. Cerioni, F. Mocci, *J. Org. Chem.* **2009**, *74*, 8818.
[22] H. P. Magalhães, H. P. Lüthi, P. Bultinck, *Phys. Chem. Chem. Phys.* **2016**, *18*, 846.
[23] R. F. W. Bader, *Atoms in Molecules: A Quantum Theory*, Oxford University Press: Ontario, Canada **1994**.
[24] R. Ponec, D. L. Cooper, *J. Phys. Chem. A* **2007**, *111*, 11294.
[25] R. Ponec, F. Feixas, *J. Phys. Chem. A* **2009**, *113*, 5773.
[26] A. I. Baranov, R. Ponec, M. Kohout, *J. Chem. Phys.* **2012**, *137*, 214109.
[27] E. Francisco, A. Martín Pendás, M. A. Blanco, *J. Chem. Phys.* **2009**, *131*, 124125.
[28] R. Ponec, D. L. Cooper, *J. Phys. Chem. A* **2007**, *111*, 11294.
[29] R. Ponec, G. Yuzhakov, X. Gironés, G. Frenking, *Organometallics* **2004**, *23*, 1790.
[30] C. Tantardini, E. Benassi, *Phys. Chem. Chem. Phys.* **2017**, *19*, 27779.
[31] R. J. Boyd, C. A. Coulson, *J. Phys. B: Atom. Mol. Phys.* **1974**, *7*, 1805.
[32] C. A. Coulson, A. H. Neilson, *Proc. Phys. Soc.* **1961**, *78*, 831.
[33] R. J. Boyd, C. A. Coulson, *J. Phys. B: Atom. Mol. Phys.* **1973**, *6*, 782.
[34] R. Ponec, L. Bučinský, C. Gatti, *J. Chem. Theory Comput.* **2010**, *6*, 3113.
[35] R. Ponec, D. L. Cooper, *Struct. Chem.* **2017**, *28*, 1033.
[36] R. Ponec, I. Mayer, *J. Phys. Chem. A* **1997**, *101*, 1738.
[37] A. Schröckeneder, D. Stichnoth, P. Mayer, D. Trauner, J. Beilstein, *Org. Chem.* **2012**, *8*, 1523.
[38] A. D. Becke, *J. Chem. Phys.* **1986**, *85*, 7184.
[39] J. P. Perdew, K. Burke, M. Ernzerhof, *Phys. Rev. Lett.* **1996**, *77*, 3865.
[40] J. P. Perdew, K. Burke, M. Ernzerhof, *Phys. Rev. Lett.* **1997**, *78*, 1396.
[41] A. Otero-de-la-Roza, E. R. Johnson, *J. Chem. Phys.* **2012**, *136*, 174109.
[42] A. Otero-de-la Roza, E. R. Johnson, *J. Chem. Phys.* **2012**, *137*, 054103.
[43] E. R. Johnson, A. Otero-de-la-Roza, *J. Chem. Theory Comput.* **2012**, *8*, 5124.
[44] P. Wisesa, K. A. McGill, T. Mueller, *Phys. Rev. B* **2016**, *93*, 155109.
[45] P. Giannozzi, S. Baroni, N. Bonini, M. Calandra, R. Car, C. Cavazzoni, D. Ceresoli, G. L. Chiarotti, M. Cococcioni, I. Dabo, et al., *J. Phys.: Condens. Matter* **2009**, *21*, 395502.
[46] C. Gatti, P. Fantucci, G. Pacchioni, *Theor. Chim. Acta* **1987**, *72*, 433.
[47] M. J. Frisch, G. W. Trucks, H. B. Schlegel, G. E. Scuseria, M. A. Robb, J. R. Cheeseman, G. Scalmani, V. Barone, B. Mennucci, G. A. Petersson, et al., *Gaussian 09*, Gaussian, Inc., Wallingford, CT **2009**.
[48] K. A. Peterson, B. C. Shepler, D. Figgen, H. Stoll, *J. Phys. Chem. A* **2006**, *110*, 13877.
[49] R. A. Kendall, T. H. Dunning Jr. , R. J. Harrison, *J. Chem. Phys.* **1992**, *96*, 6796.
[50] D. E. Woon, T. H. Dunning Jr. , *J. Chem. Phys.* **1993**, *98*, 1358.
[51] N. Godbout, D. R. Salahub, J. Andzelm, E. Wimmer, *Can. J. Chem.* **1992**, *70*, 560.
[52] C. Sosa, J. Andzelm, B. C. Elkin, E. Wimmer, K. D. Dobbs, D. A. Dixon, *J. Phys. Chem.* **1992**, *96*, 6630.
[53] C. Adamo, V. Barone, *J. Chem. Phys.* **1999**, *110*, 6158.
[54] M. Douglas, N. M. Kroll, *Ann. Phys. (NY)* **1974**, *82*, 89.
[55] B. A. Hess, *Phys. Rev. A* **1985**, *32*, 756.
[56] B. A. Hess, *Phys. Rev. A* **1986**, *33*, 3742.
[57] G. Jansen, B. A. Hess, *Phys. Rev. A* **1989**, *39*, 6016.
[58] AIMPAC. Available at: http:www.chemistry.mcmaster.ca/aimpac/imagemap/imagemap.htm
[59] T. Keith, R. F. W. Bader, *Chem. Phys. Lett.* **1993**, *210*, 223.
[60] J. S. Binkley, J. A. Pople, W. J. Hehre, *J. Am. Chem. Soc.* **1980**, *102*, 939.
[61] M. S. Gordon, J. S. Binkley, J. A. Pople, W. J. Pietro, W. J. Hehre, *J. Am. Chem. Soc.* **1982**, *104*, 2797.
[62] W. J. Pietro, M. M. Francl, W. J. Hehre, D. J. Defrees, J. A. Pople, J. S. Binkley, *J. Am. Chem. Soc.* **1982**, *104*, 5039.
[63] K. D. Dobbs, W. J. Hehre, *J. Comp. Chem.* **1986**, *7*, 359.
[64] K. D. Dobbs, W. J. Hehre, *J. Comp. Chem.* **1987**, *8*, 861.
[65] K. D. Dobbs, W. J. Hehre, *J. Comp. Chem.* **1987**, *8*, 880.
[66] R. Ditchfield, W. J. Hehre, J. A. Pople, *J. Chem. Phys.* **1971**, *54*, 724.
[67] W. J. Hehre, R. Ditchfield, J. A. Pople, *J. Chem. Phys.* **1972**, *56*, 2257.
[68] P. C. Hariharan, J. A. Pople, *Theor. Chem. Acc.* **1973**, *28*, 213.
[69] P. C. Hariharan, J. A. Pople, *Mol. Phys.* **1974**, *27*, 209.
[70] M. S. Gordon, *Chem. Phys. Lett.* **1980**, *76*, 163.
[71] M. M. Francl, W. J. Pietro, W. J. Hehre, J. S. Binkley, D. J. DeFrees, J. A. Pople, M. S. Gordon, *J. Chem. Phys.* **1982**, *77*, 3654.
[72] R. C. Binning Jr. , L. A. Curtiss, *J. Comp. Chem.* **1990**, *11*, 1206.
[73] J.-P. Blaudeau, M. P. McGrath, L. A. Curtiss, L. Radom, *J. Chem. Phys.* **1997**, *107*, 5016.
[74] V. A. Rassolov, J. A. Pople, M. A. Ratner, T. L. Windus, *J. Chem. Phys.* **1998**, *109*, 1223.
[75] V. A. Rassolov, M. A. Ratner, J. A. Pople, P. C. Redfern, L. A. Curtiss, *J. Comp. Chem.* **2001**, *22*, 976.
[76] K. Raghavachari, J. S. Binkley, R. Seeger, J. A. Pople, *J. Chem. Phys.* **1980**, *72*, 650.
[77] M. J. Frisch, G. W. Trucks, H. B. Schlegel, G. E. Scuseria, M. A. Robb, J. R. Cheeseman, J. A. Montgomery Jr.. , T. Vreven, K. N. Kudin, J. C. Burant, J. M. Millam, S. S. Iyengar, J. Tomasi, V. Barone, B. Mennucci, M. Cossi, G. Scalmani, N. Rega, G. A. Petersson, H. Nakatsuji, M. Hada, M. Ehara, K. Toyota, R. Fukuda, J. Hasegawa, M. Ishida, T. Nakajima, Y. Honda, O. Kitao, H. Nakai, M. Klene, X. Li, J. E. Knox, H. P. Hratchian, J. B. Cross, V. Bakken, C. Adamo, J. Jaramillo, R. Gomperts, R. E. Stratmann, O. Yazyev, A. J. Austin, R. Cammi, C. Pomelli, J. W. Ochterski, P. Y. Ayala, K. Morokuma, G. A. Voth, P. Salvador, J. J. Dannenberg, V. G. Zakrzewski, S. Dapprich, A. D. Daniels, M. C. Strain, O. Farkas, D. K. Malick, A. D. Rabuck, K. Raghavachari, J. B. Foresman, J. V. Ortiz, Q. Cui, A. G. Baboul, S. Clifford, J. Cioslowski, B. B. Stefanov, G. Liu, A. Liashenko, P. Piskorz, I. Komaromi, R. L. Martin, D. J. Fox, T. Keith, M. A. Al-Laham, C. Y. Peng, A. Nanayakkara, M. Challacombe, P. M. W. Gill, B. Johnson, W. Chen, M. W. Wong, C. Gonzalez, J. A. Pople, *Gaussian 03*, *Revision C.02*, Gaussian, Inc., Wallingford, CT **2004**.

[78] F. Feixas, X. Girones, R. Ponec and J. Roithova, WinBader, v1.0, ICPF, AS CR, Prague, Czech Republic, **2003**, available upon request, contact: ponec@icpf.cas.cz.
[79] K. A. Peterson, B. C. Shepler, D. Figgen, H. Stoll, *J. Phys. Chem. A* **2006**, *110*, 13877.
[80] E. Espinosa, I. Alkorta, J. Elguero, E. Molins, *J. Chem. Phys.* **2002**, *117*, 5529.
[81] X. Fradera, M. A. Austen, R. F. W. Bader, *J. Phys. Chem. A* **1999**, *103*, 304.
[82] C. L. Firme, O. A. C. Antunes, P. M. Esteves, *Chem. Phys. Lett.* **2009**, *468*, 129.
[83] C. Gatti, D. Lasi, *Faraday Discuss.* **2007**, *135*, 55.
[84] R. F. W. Bader, C. Gatti, *Chem. Phys. Lett.* **1998**, *287*, 233.
[85] C. Gatti, *The Source Function Descriptor as a Tool to Extract Chemical Information from Theoretical and Experimental Electron Densities. In Electron Density and Chemical Bonding II; Structure and Bonding Series*, Vol. 147, Springer, Berlin, Germany **2012**, p. 193.

SUPPORTING INFORMATION

Additional Supporting Information may be found online in the supporting information tab for this article.

How to cite this article: Tantardini C, Michalchuk AAL. Dess-Martin periodinane: The reactivity of a λ^5-iodane catalyst explained by topological analysis. *Int J Quantum Chem*. 2018;e25838. https://doi.org/10.1002/qua.25838

Electronic Supporting Information
for

Dess-Martin periodinane: the reactivity of a λ^5-iodane catalyst explained by topological analysis

Christian Tantardini, [1, 2]* Adam A. L. Michalchuk, [2, 3, 4]

[1]*C. Tantardini*
SkolTech Skolkovo Institute of Science and Technology, st. Nobelya 3, Moscow, Russian Federation, 121205.
[2]*C. Tantardini, A. A. L. Michalchuk*
Novosibirsk State University, st. Pirogova 2, Novosibirsk, Russian Federation, 630090.
[3]*A. A. L. Michalchuk*
EaStCHEM School of Chemistry, University of Edinburgh, King's Buildings, West Mains Rd., Edinburgh, UK.
[4]*A. A. L. Michalchuk*
EPSRC Centre for Continuous Manufacturing and Crystallisation (CMAC).
*Correspondence to: Christian Tantardini (christiantantardini@ymail.com)

E.S.I.1 Picture of compared DMP molecular structures from optimization with Plane Waves as reported in the Computational Details and the Fusaro et al.[1] optimized structure (blue).

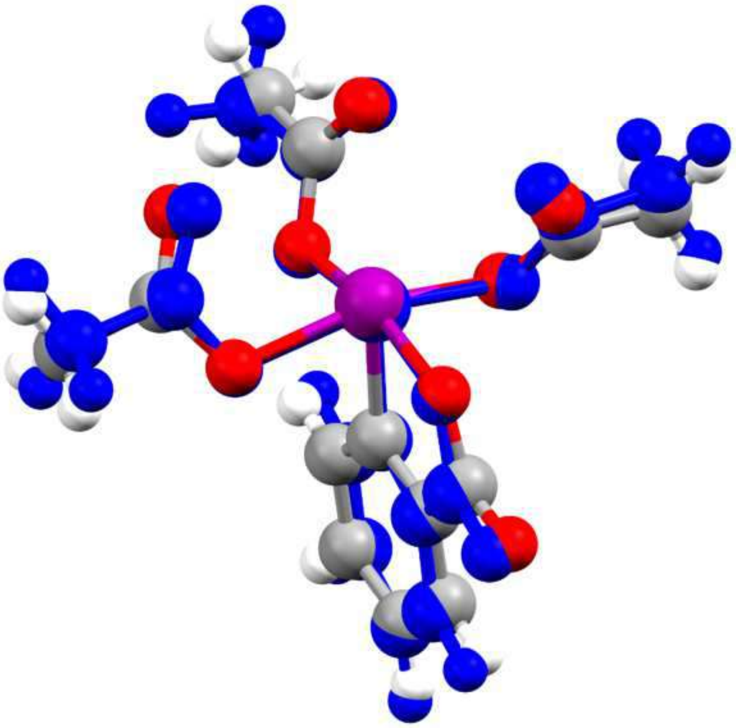

E.S.I.2 Classification of type of bond second Espinosa[2] by the topological parameter at the bond critical point (BCP): charge density,ρ_{BCP} , Laplacian of charge density, $\nabla^2\rho_{BCP}$, kinetic energy, G_{BCP}, virial energy, V_{BCP}, and the Hamiltonian, H_{BCP}

Shared shell	Transition zone	Closed shell
$\nabla^2\rho_{BCP} < 0$	$\nabla^2\rho_{BCP} > 0$	$\nabla^2\rho_{BCP} > 0$
$\|V_{BCP}\|>2G_b$	$1\leq\|V_{BCP}\|/G_{BCP}\leq 2$	$\|V_{BCP}\|<G_b$
$H_{BCP}\ll 0$	$H_{BCP}<0$	$H_{BCP}>0$
$H_{BCP}/\rho_{BCP} < 0$	-	$H_{BCP}/\rho_{BCP} > 0$

E.S.I.3 Eigenvalues of domain-averaged Fermi hole(DAFH) for iodine within DMP, generated from restricted PBE0 with different basis set using Bader-like[3] approach.

I1	Bader-like	
basis set	Degeneracy	Eigenvalues
3-21G/DGDZVP	18	2.000
	3	1.999
	1	1.998
	1	1.996
	1	1.871
	1	1.053
	1	0.720
	1	0.681
	1	0.123
	1	0.120
	1	0.066
	1	0.054
	1	0.046
	1	0.023
	1	0.016
	1	0.015
	2	0.010
	1	0.008
	1	0.007
	1	0.005
	3	0.004
	2	0.003
	1	0.002
	1	0.001
6-31G/DGDZVP	18	2.000
	3	1.999
	1	1.998
	1	1.996
	1	1.876
	1	1.079
	1	0.736
	1	0.698
	1	0.127
	1	0.121
	1	0.073
	1	0.059
	1	0.051
	1	0.026
	1	0.017
	1	0.016
	1	0.012
	1	0.010
	2	0.009
	1	0.006

	3	0.004
	2	0.003
	1	0.020
	2	0.001
6-311G/DGDZVP	18	2.000
	3	1.999
	1	1.998
	1	1.996
	1	1.876
	1	1.079
	1	0.736
	1	0.698
	1	0.127
	1	0.121
	1	0.073
	1	0.059
	1	0.051
	1	0.026
	1	0.017
	1	0.016
	1	0.012
	1	0.010
	2	0.009
	1	0.006
	2	0.004
	2	0.003
	1	0.002
	1	0.001

E.S.I.4 3-indexes bond performed for DMP using restricted PBE0 full electron basis set (3-21G, 6-31G, 6-311G) with Bader-like[3] approach of analysis of population.

	Bader-like		
3 center	3-21g	6-31g	6-311g
O1 O2 I1	-	-	-
O1 O3 I1	-0.065	-0.069	-0.069
O1 O4 I1	-	-	-
O1 I1 C1	-	-	-
O2 O3 I1	-	-	-
O2 O4 I1	-0.070	-0.073	-0.073
O2 I1 C1	0.016	0.014	0.014
O3 O4 I1	-	-	-
O3 I1 C1	-	-	-
O4 I1 C1	0.013	0.011	0.011

E.S.I.5 Table of charge density and SF% values into the bond critical point connected to the bond path of iodine atom in DMP

bond	ρ_b (e/bohr^3)	SF%(I1)	SF%(C1)	SF%(O1)	SF%(O2)	SF%(O3)	SF%(O4)	SF%(TOT)
I1—C1	0.1438	39.36	31.48	2.25	1.35	1.17	1.11	81.21
I1—O1	0.1131	37.20	0.70	38.09	1.97	1.21	1.25	85.60
I1—O2	0.1183	37.50	-0.15	1.74	37.93	2.07	0.91	86.14
I1—O3	0.1185	37.40	-0.02	1.19	1.73	37.94	1.66	86.11
I1—O4	0.1076	36.56	-0.27	1.78	1.21	1.69	37.47	82.08

E.S.I.6 Substituted DMP molecules with (A) –NH_2, (B) –$CH_3$and (C) –NO_2.

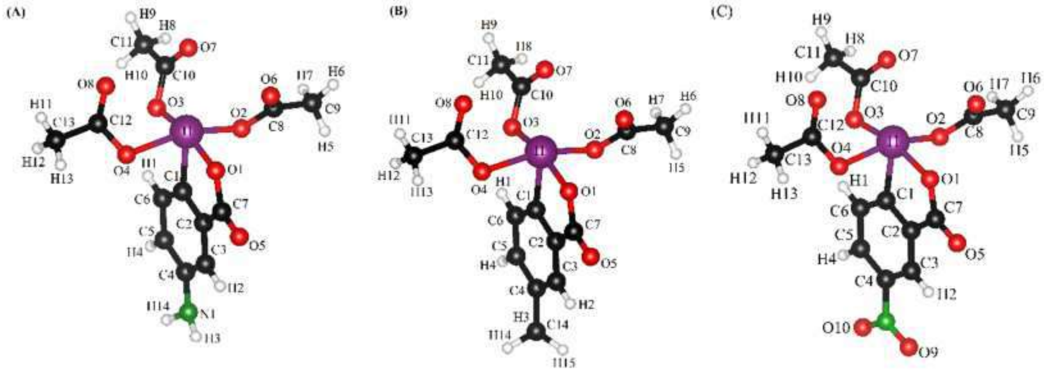

E.S.I.7 Eigenvalues of domain-averaged Fermi hole (DAFH) for iodine within DMP with substitution at the benzene ring with -NH_2 group, generated from restricted PBE0 with different basis set using Bader-like[3] approach

I1	Bader-like	
basis set	Degeneracy	Eigenvalues
3-21G/DGDZVP	17	2.000
	3	1.999
	1	1.998
	1	1.997
	1	1.996
	1	1.860
	1	1.060
	1	0.715
	1	0.677
	1	0.119
	1	0.116
	1	0.064
	1	0.054
	1	0.045
	1	0.023
	1	0.015
	1	0.014
	1	0.010
	1	0.009
	2	0.007
	2	0.004
	4	0.003
	1	0.002
	2	0.001
	1	-0.001
	1	-0.002
	1	-0.003
	1	-0.004
	1	-0.005
	1	-0.013
6-31G/DGDZVP	17	2.000
	3	1.999
	2	1.998
	1	1.995
	1	1.867
	1	1.087
	1	0.730
	1	0.693
	1	0.123
	1	0.118
	1	0.071
	1	0.058
	1	0.050
	1	0.025

	1	0.016
	1	0.015
	1	0.012
	1	0.010
	2	0.009
	1	0.005
	1	0.004
	4	0.003
	2	0.002
	2	0.001
	1	-0.001
	2	-0.002
	1	-0.003
	1	-0.007
	1	-0.012
6-311G/DGDZVP	17	2.000
	3	1.999
	2	1.998
	1	1.995
	1	1.864
	1	1.089
	1	0.724
	1	0.687
	1	0.121
	1	0.118
	1	0.070
	1	0.058
	1	0.050
	1	0.025
	1	0.016
	1	0.015
	1	0.012
	1	0.010
	2	0.009
	1	0.005
	1	0.004
	4	0.003
	2	0.002
	2	0.001
	2	-0.001
	2	-0.002
	1	-0.003
	1	-0.007
	1	-0.012

E.S.I.8 Eigenvalues of domain-averaged Fermi hole (DAFH) for iodine within DMP with substitution at the benzene ring with -CH_3 group, generated from restricted PBE0 with different basis set using Bader-like[3] approach.

I1	Bader-like	
basis set	Degeneracy	Eigenvalues
3-21G/DGDZVP	17	2.000
	3	1.999
	2	1.998
	1	1.996
	1	1.855
	1	1.055
	1	0.712
	1	0.679
	1	0.120
	1	0.118
	1	0.064
	1	0.054
	1	0.046
	1	0.023
	2	0.014
	1	0.010
	1	0.009
	1	0.008
	1	0.007
	1	0.005
	2	0.004
	3	0.003
	1	0.002
	4	0.001
	2	-0.002
	1	-0.003
	1	-0.007
	1	-0.010
6-31G/DGDZVP	17	2.000
	3	1.999
	2	1.998
	1	1.995
	1	1.863
	1	1.082
	1	0.724
	1	0.696
	1	0.125
	1	0.119
	1	0.070
	1	0.058
	1	0.050
	1	0.025
	1	0.016
	1	0.015

	1	0.011
	1	0.010
	1	0.009
	1	0.008
	1	0.006
	1	0.004
	3	0.003
	2	0.002
	2	0.001
	2	-0.001
	1	-0.002
	1	-0.003
	1	-0.007
	1	-0.011
6-311G/DGDZVP	17	2.000
	3	1.999
	2	1.998
	1	1.995
	1	1.861
	1	1.084
	1	0.718
	1	0.690
	1	0.123
	1	0.119
	1	0.069
	1	0.058
	1	0.050
	1	0.025
	1	0.016
	1	0.015
	1	0.011
	1	0.010
	2	0.009
	1	0.006
	1	0.004
	3	0.003
	2	0.002
	2	0.001
	2	-0.001
	1	-0.002
	1	-0.003
	1	-0.006
	1	-0.010

E.S.I.9 Eigenvalues of domain-averaged Fermi hole (DAFH) for iodine within DMP with substitution at the benzene ring with -NO_2 group, generated from restricted PBE0 with different basis set using Bader-like[3] approach.

I1	Bader-like	
basis set	Degeneracy	Eigenvalues
3-21G/DGDZVP	17	2.000
	3	1.999
	1	1.998
	1	1.997
	1	1.996
	1	1.859
	1	1.031
	1	0.722
	1	0.681
	1	0.119
	1	0.116
	1	0.064
	1	0.053
	1	0.046
	1	0.022
	2	0.014
	1	0.010
	1	0.009
	2	0.007
	1	0.005
	2	0.004
	3	0.003
	1	0.002
	2	0.001
	2	-0.001
	1	-0.002
	2	-0.003
	1	-0.005
	1	-0.011
6-31G/DGDZVP	17	2.000
	3	1.999
	2	1.998
	1	1.995
	1	1.865
	1	1.054
	1	0.736
	1	0.699
	1	0.124
	1	0.118
	1	0.071
	1	0.056
	1	0.050
	1	0.025

	1	0.016
	1	0.014
	1	0.011
	1	0.010
	1	0.009
	1	0.008
	1	0.005
	1	0.004
	4	0.003
	1	0.002
	3	0.001
	1	-0.001
	1	-0.002
	1	-0.003
	1	-0.004
	1	-0.006
	1	-0.010
6-311G/DGDZVP	17	2.000
	3	1.999
	2	1.998
	1	1.995
	1	1.862
	1	1.057
	1	0.730
	1	0.693
	1	0.122
	1	0.118
	1	0.070
	1	0.056
	1	0.050
	1	0.025
	1	0.016
	1	0.014
	1	0.011
	1	0.010
	1	0.009
	1	0.008
	1	0.005
	1	0.004
	4	0.003
	1	0.002
	3	0.001
	1	-0.001
	1	-0.002
	1	-0.004
	1	-0.006
	1	-0.009

E.S.I.10 3-indexes bond performed for DMP with substitution at the benzene ring with -NH_2 group using restricted PBE0 full electron basis set (3-21G, 6-31G, 6-311G) with Bader-like[3] approach of analysis of population.

	Bader-like		
3 center	3-21g	6-31g	6-311g
O1 O2 I1	-	-	-
O1 O3 I1	-0.066	-0.069	-0.069
O1 O4 I1	-	-	-
O1 I1 C1	-	-	-
O2 O3 I1	-	-	-
O2 O4 I1	-0.070	-0.072	-0.071
O2 I1 C1	0.014	0.012	0.012
O3 O4 I1	-	-	-
O3 I1 C1	-	-	-
O4 I1 C1	0.013	0.010	0.010

E.S.I.11 3-indexes bond performed for DMP with substitution at the benzene ring with -CH_3 group using restricted PBE0 full electron basis set (3-21G, 6-31G, 6-311G) with Bader-like[3] approach of analysis of population.

	Bader-like		
3 center	3-21g	6-31g	6-311g
O1 O2 I1	-	-	-
O1 O3 I1	-0.065	-0.069	-0.068
O1 O4 I1	-	-	-
O1 I1 C1	-	-	-
O2 O3 I1	-	-	-
O2 O4 I1	-0.070	-0.072	-0.070
O2 I1 C1	0.015	0.013	0.013
O3 O4 I1	-	-	-
O3 I1 C1	-	-	-
O4 I1 C1	0.012	-	-

E.S.I.12 3-indexes bond performed for DMP with substitution at the benzene ring with -NO_2 group using restricted PBE0 full electron basis set (3-21G, 6-31G, 6-311G) with Bader-like[3] approach of analysis of population.

	Bader-like		
3 center	3-21g	6-31g	6-311g
O1 O2 I1	-	-	-
O1 O3 I1	-0.065	-0.068	-0.068
O1 O4 I1	-	-	-
O1 I1 C1	-	-	-
O2 O3 I1	-	-	-
O2 O4 I1	-0.070	-0.072	-0.071
O2 I1 C1	0.014	0.012	0.012
O3 O4 I1	-	-	-
O3 I1 C1	-	-	-
O4 I1 C1	0.012	-	-

References

1. E. L. Fusaro, M. Luhmer, G. Cerioni, F. Mocci, *J. Org. Chem*., **2009**, 74, 8818.
2. E. Espinosa, I. Alkorta, J. Elguero, E. Molins, J. Chem. Phys., **2002**, 117, 5529.
3. R. Ponec, L. Bučinský, C. Gatti, *J. Chem. Theory Comput.*, **2010**, 6, 3113.

CHAPTER IV

Atomic Electronegativities at High Pressure

Introduction:

Democritus was the first Greek philosopher who defined the atom as the indivisible particle constituting matter [1]. If nowadays this concept has been overcome by the knowledge of subatomic particles, the atom continues to be considered as the constituent unity of matter through the concept of the *chemical bond*: the forces acting between two or a group of atoms are such, to lead to the formation of an aggregate with sufficient stability to make it convenient for the chemist to consider it as an independent molecular species [2]. Albeit such definition was introduced by Lewis in 1916 and it was adopted by IUPAC, being still in use, it left a certain freedom to the subjective interpretation with obvious misunderstandings. Such misunderstandings were largely dispelled in 1932, thanks to the work of Pauling on the nature of the *chemical bond* [3], where some properties such as electron affinity, ionization energy and electronegativity were defined to describe the chemical behavior of elements. The electronegativity defined by Pauling [3] (Figure 1) is related to the ionic contribution added to the expected covalent part of the energy of the bond

$$|\chi_A - \chi_B| = \sqrt[2]{E_d(AB) - \frac{E_d(AA) + E_d(BB)}{2}} \qquad (1)$$

Pauling generated a relative scale of electronegativity (where electronegativities of all elements were defined relatively to fluorine, whose electronegativity was set equal to 4 and later revised to 3.98).

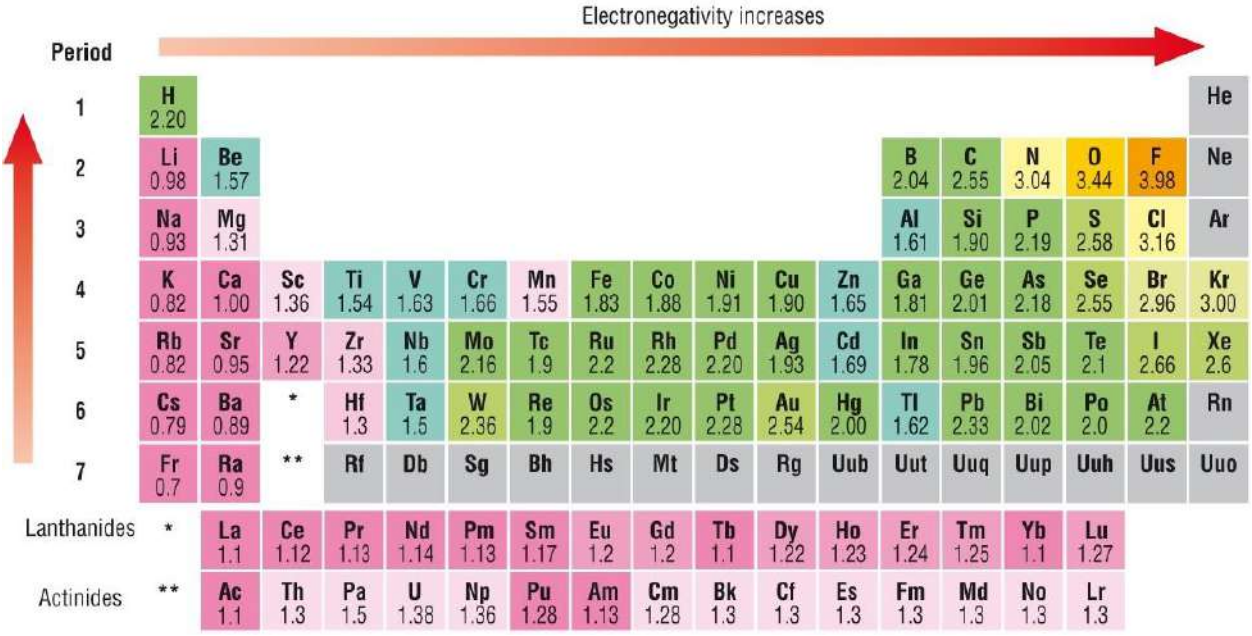

Period																		
1	H 2.20																	He
2	Li 0.98	Be 1.57											B 2.04	C 2.55	N 3.04	O 3.44	F 3.98	Ne
3	Na 0.93	Mg 1.31											Al 1.61	Si 1.90	P 2.19	S 2.58	Cl 3.16	Ar
4	K 0.82	Ca 1.00	Sc 1.36	Ti 1.54	V 1.63	Cr 1.66	Mn 1.55	Fe 1.83	Co 1.88	Ni 1.91	Cu 1.90	Zn 1.65	Ga 1.81	Ge 2.01	As 2.18	Se 2.55	Br 2.96	Kr 3.00
5	Rb 0.82	Sr 0.95	Y 1.22	Zr 1.33	Nb 1.6	Mo 2.16	Tc 1.9	Ru 2.2	Rh 2.28	Pd 2.20	Ag 1.93	Cd 1.69	In 1.78	Sn 1.96	Sb 2.05	Te 2.1	I 2.66	Xe 2.6
6	Cs 0.79	Ba 0.89	*	Hf 1.3	Ta 1.5	W 2.36	Re 1.9	Os 2.2	Ir 2.20	Pt 2.28	Au 2.54	Hg 2.00	Tl 1.62	Pb 2.33	Bi 2.02	Po 2.0	At 2.2	Rn
7	Fr 0.7	Ra 0.9	**	Rf	Db	Sg	Bh	Hs	Mt	Ds	Rg	Uub	Uut	Uuq	Uup	Uuh	Uus	Uuo
Lanthanides	*	La 1.1	Ce 1.12	Pr 1.13	Nd 1.14	Pm 1.13	Sm 1.17	Eu 1.2	Gd 1.2	Tb 1.1	Dy 1.22	Ho 1.23	Er 1.24	Tm 1.25	Yb 1.1	Lu 1.27		
Actinides	**	Ac 1.1	Th 1.3	Pa 1.5	U 1.38	Np 1.36	Pu 1.28	Am 1.13	Cm 1.28	Bk 1.3	Cf 1.3	Es 1.3	Fm 1.3	Md 1.3	No 1.3	Lr 1.3		

Figure 1. Periodic table of electronegativity using the Pauling scale.

Such definition of electronegativity is seen to be a good index to define the *chemical bond* between two atoms, when they are bonded in vacuo, but actually cannot be used to explain the *chemical bond* at high pressure where we know the chemical behavior of the elements to be very different from their behavior at room pressure. It is seen in literature that the application of high pressure (hundreds gigapascals) to materials, besides modifying their properties dramatically changes their reactivity. An example of these new phenomena are the reactivity of noble gases, metal-to-insulator transition and participation of inner electronic shells in chemical bonding. Consequently, new compounds are formed, which violate the chemical paradigms known to date. In fact, it was recently discovered that sodium subchlorides (Na_xCl, x>1) and superchlorides (NaClx, x>1) become stable at high pressures [4,5] and physical explanation about how pressure acts in stabilizing these odd compounds is still lacking. Across the years, different scales of electronegativity have appeared, including Mulliken's scale, which is an absolute scale calculated where the electronegativity is defined as the arithmetic mean of electron affinity and ionization energy, Allen's scale which is the average energy of valence electrons in a free atom. However, it is Pauling's electronegativity that is directly defined on the *chemical bond*. Furthermore, especially for Allen's scale, it is not easy to correctly compute electronegativities under pressure: the *pV* term is completely neglected; and the ambiguity of choosing valence electronic configuration for different atoms: transition metals, and not only they, can have different valence electronic configuration due to different environment. In a 2015 preprint, Dong et al. [7] computed Mulliken's electronegativity of ~60 elements as a function of pressure. Electronegativity of most elements was seen to rise with pressure initially, and then decrease; the maximum was typically reached at ~ 20 GPa or below. More recently, Rahm *et al.* [6] (2019) have published a work where they have computed the electronegativity at high pressure for 90 atoms using Allen's definition. While they obtained reasonable electronegativities for isolated atoms, the electronegativity values at non-zero pressures are incorrect as they neglect the *pV* term. Here we wish to define and compute thermochemical (Pauling's and related to Pauling's) electronegativities of the elements at high pressure, in the hope to obtain a powerful instrument to understand and anticipate unusual chemical phenomena now widely known to occur at high pressure. We present Pauling's electronegativity for 91 elements of Periodic Table till to 300 GPa fixing the fluorine electronegativity equal to 4.00 at all pressures.

Computational Details:

A model fcc structure of He was fully optimized at hydrostatic pressures equal to 0, 50, 100, 200 and 300 GPa. Based on this relaxed structure, we created, at each pressure, a 3x3x3 supercell (i.e. the final supercell contained 108 helium atoms), and then replacing two nearest-neighbor helium atoms by different atoms, re-relaxed to find optimal geometries of μ—F and μ—μ dimers at each given pressure. The helium matrix acted as an inert pressure-transmitting medium.

The calculations were carried out with norm-conserving (NC) Vanderbilt [8] pseudopotentials for all elements except for lanthanoids and actinoids using Quantum Espresso code [9,10]. The calculations for the latters were carried out with projector-augmented wave [11] (PAW) potentials using the VASP code [12-16].

All calculations were performed using density functional theory with PBE [17] exchange-correlation functional and Monkhorst-Pack [18] *k*-points grid for He unit cell equal to 8 x 8 x 8, while for supercells it was equal to 1 x 1 x 1. The plane wave kinetic energy cut-off for NC pseudopotentials was chosen equal to 160 Ry, which gave excellent convergence, and calculations proceeded until self-consistency with energy and force convergence thresholds equal to 10^{-8} Ry. The large kinetic energy cut-off used can be considered enough to achieve the converged solution as reported in literature [19]. The kinetic energy cut-off for PAW calculations was chosen equal to 1000 eV, and with energy and force convergence thresholds were equal to 10^{-8}.

For comparison, we also computed Pauling's electronegativities for Li and Cs using Li—F, Cs—F, Li—Li, Cs—Cs and F—F dimers in an empty box with dimensions 10 x 10 x 10 Å.

Results:

Pauling's electronegativity was calculated from eq.1 using the enthalpies of fully optimized helium matrix made of 106 helium atoms and 2 atoms of dimers μ—F and μ—μ, with μ corresponding to the 91 chosen atoms of Periodic Table, instead of dissociation energies as in eq.1.

In primis, we have compared our results on electronegativity in *vacuo* with those tabulated by Pauling to see how much our results are aligned with his scale. At the first glance our values agree with Pauling values (Figure 2), except a very large discrepancy for the 1st and 2nd group: Pauling's scale shows very low values and the trend of the electronegativity is to decrease when going down the Periodic Table, but this is not what we see. Then we decided to make a test, where we extracted the electronegativities for Li and Cs from the enthalpies of their dimers with fluorine (i.e., Li—F and Cs—F) within empty box to confirm that the quality of our results are absolutely unaffected by the helium matrix. Pauling's scale reported 0.98 $eV^{-1/2}$ for Li and 0.79 $eV^{-1/2}$ for Cs, but they disagree with our computed results: 1.94 $eV^{-1/2}$ for Li and 1.97 $eV^{-1/2}$ for Cs. To evaluate if our inversed electronegativity trend respect that proposed by Pauing's scale was due to helium matrix we have calculated the electronegativity of Li and Cs from their energy dimers in *vacuo* (within empty box, see "Computational Details" section) obtaining 1.98 $eV^{-1/2}$ for Li and 2.05 $eV^{-1/2}$ for Cs. Indeed, if we directly apply Pauling's definition, eq.(1), to our results (both in helium matrix and *in vacuo)* and to experimental dissociation energies at 298K [20], we find, to our surprise, that the resulting values come out to be very far from Pauling's values and very close to our values. This showed that the presence of the helium matrix does not distort the results to any significant extent. Unfortunately, Pauling died many years ago and we cannot know how exactly he generated his scale of electronegativity. Thus, if we are unable to reproduce such results we cannot use his scale as *vademecum* for all chemists, but it is necessary to recalculate all electronegativity values giving values that are truly aligned with experimental dissociation energies.

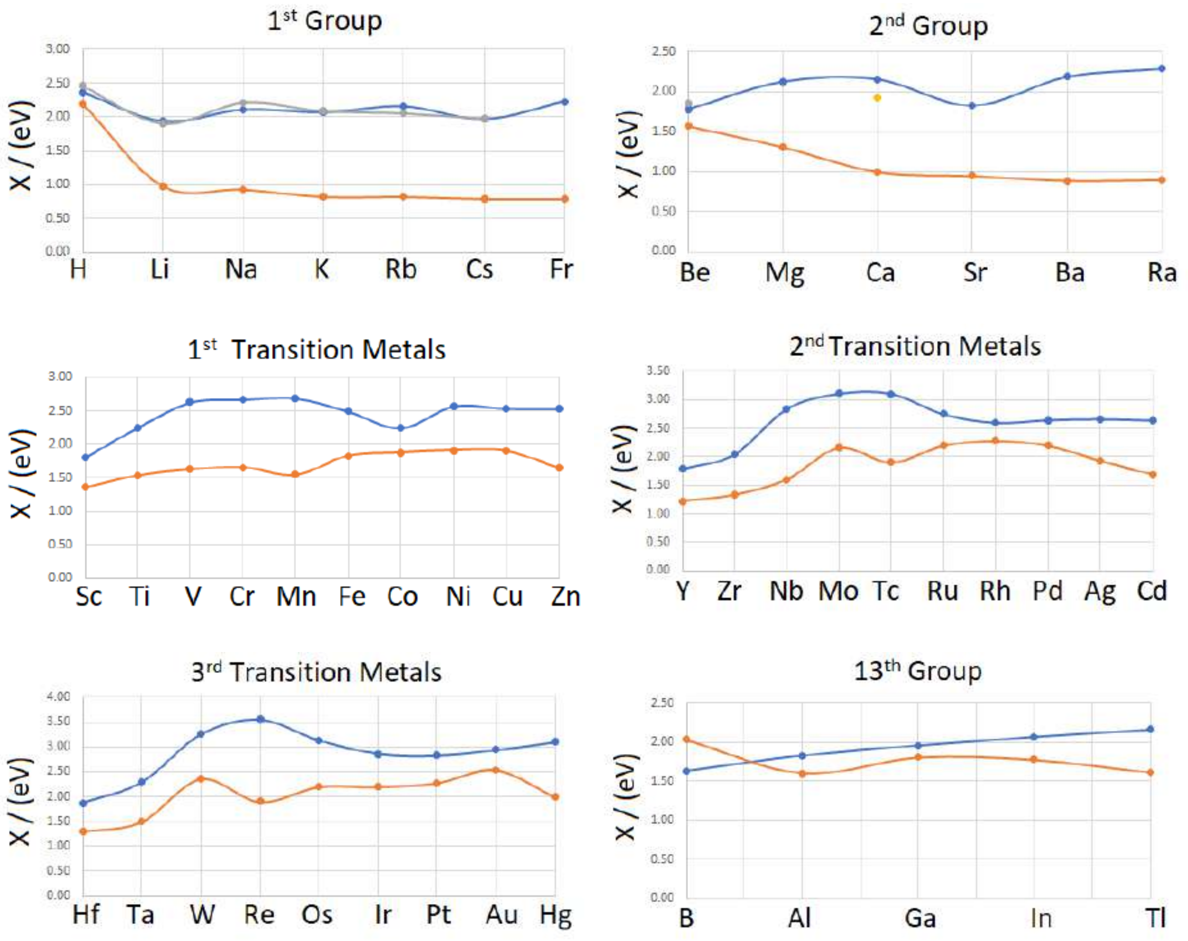

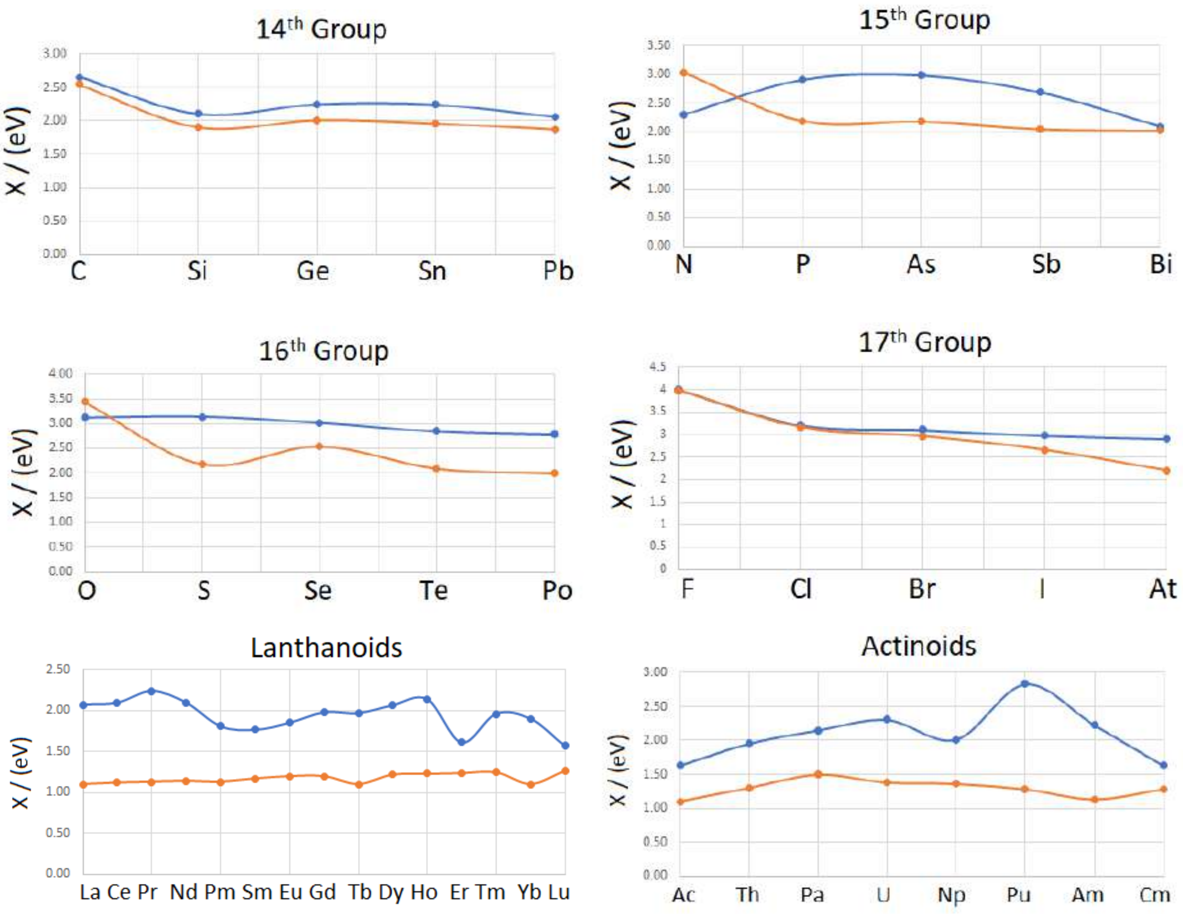

Figure 2. Electronegativity values tabulated by Pauling (orange), computed by helium matrix method here (blue) and calculated by us from experimental dissociation energies (grey, yellow) for 91 different elements.

Thus, we have computed the electronegativity values, as showed in the Figure 3, at pressures up to 300 GPa. For very heavy atoms relativistic effects become important and we see that for s-elements they increase electronegativity and for *d*- and *f*-elements decrease. For lanthanoids and actinoids pseudopotentials available in VASP and Quantum Espresso, reliability (in particular, under pressure) and convergence are less straightforward than for the other elements. Thus, it was decided to study them using tested *f*-electron-free pseudopotentials only up to 100 GPa. All of computed electronegativities for lanthanoids and actinoids are seen to decrease with pressure (Figure 3).

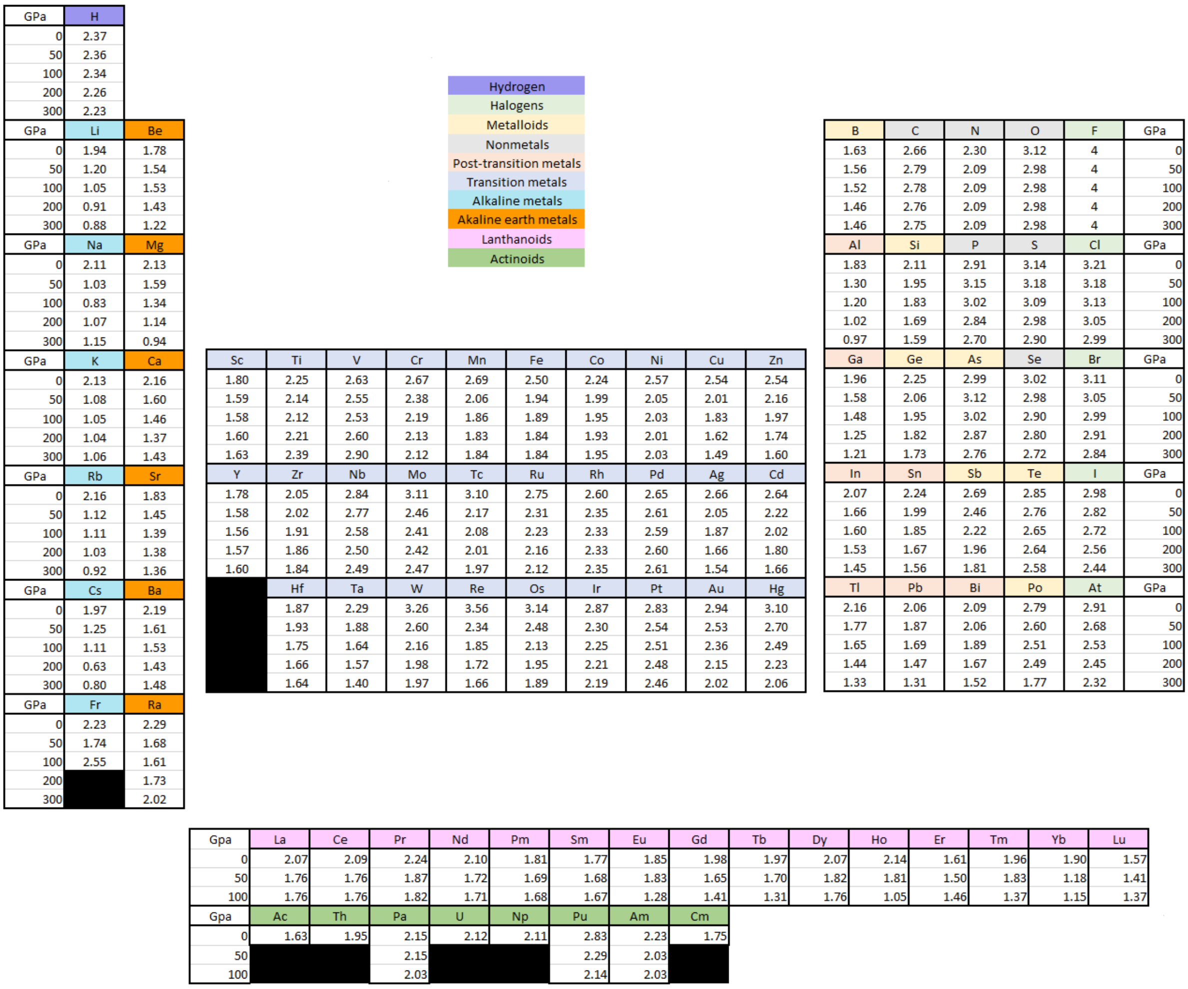

Hydrogen
Halogens
Metalloids
Nonmetals
Post-transition metals
Transition metals
Alkaline metals
Akaline earth metals
Lanthanoids
Actinoids

GPa	H
0	2.37
50	2.36
100	2.34
200	2.26
300	2.23

GPa	Li	Be	B	C	N	O	F
0	1.94	1.78	1.63	2.66	2.30	3.12	4
50	1.20	1.54	1.56	2.79	2.09	2.98	4
100	1.05	1.53	1.52	2.78	2.09	2.98	4
200	0.91	1.43	1.46	2.76	2.09	2.98	4
300	0.88	1.22	1.46	2.75	2.09	2.98	4

GPa	Na	Mg	Al	Si	P	S	Cl
0	2.11	2.13	1.83	2.11	2.91	3.14	3.21
50	1.03	1.59	1.30	1.95	3.15	3.18	3.18
100	0.83	1.34	1.20	1.83	3.02	3.09	3.13
200	1.07	1.14	1.02	1.69	2.84	2.98	3.05
300	1.15	0.94	0.97	1.59	2.70	2.90	2.99

GPa	K	Ca	Sc	Ti	V	Cr	Mn	Fe	Co	Ni	Cu	Zn	Ga	Ge	As	Se	Br
0	2.13	2.16	1.80	2.25	2.63	2.67	2.69	2.50	2.24	2.57	2.54	2.54	1.96	2.25	2.99	3.02	3.11
50	1.08	1.60	1.59	2.14	2.55	2.38	2.06	1.94	1.99	2.05	2.01	2.16	1.58	2.06	3.12	2.98	3.05
100	1.05	1.46	1.58	2.12	2.53	2.19	1.86	1.89	1.95	2.03	1.83	1.97	1.48	1.95	3.02	2.90	2.99
200	1.04	1.37	1.60	2.21	2.60	2.13	1.83	1.84	1.93	2.01	1.62	1.74	1.25	1.82	2.87	2.80	2.91
300	1.06	1.43	1.63	2.39	2.90	2.12	1.84	1.84	1.95	2.03	1.49	1.60	1.21	1.73	2.76	2.72	2.84

GPa	Rb	Sr	Y	Zr	Nb	Mo	Tc	Ru	Rh	Pd	Ag	Cd	In	Sn	Sb	Te	I
0	2.16	1.83	1.78	2.05	2.84	3.11	3.10	2.75	2.60	2.65	2.66	2.64	2.07	2.24	2.69	2.85	2.98
50	1.12	1.45	1.58	2.02	2.77	2.46	2.17	2.31	2.35	2.61	2.05	2.22	1.66	1.99	2.46	2.76	2.82
100	1.11	1.39	1.56	1.91	2.58	2.41	2.08	2.23	2.33	2.59	1.87	2.02	1.60	1.85	2.22	2.65	2.72
200	1.03	1.38	1.57	1.86	2.50	2.42	2.01	2.16	2.33	2.60	1.66	1.80	1.53	1.67	1.96	2.64	2.56
300	0.92	1.36	1.60	1.84	2.49	2.47	1.97	2.12	2.35	2.61	1.54	1.66	1.45	1.56	1.81	2.58	2.44

GPa	Cs	Ba		Hf	Ta	W	Re	Os	Ir	Pt	Au	Hg	Tl	Pb	Bi	Po	At
0	1.97	2.19		1.87	2.29	3.26	3.56	3.14	2.87	2.83	2.94	3.10	2.16	2.06	2.09	2.79	2.91
50	1.25	1.61		1.93	1.88	2.60	2.34	2.48	2.30	2.54	2.53	2.70	1.77	1.87	2.06	2.60	2.68
100	1.11	1.53		1.75	1.64	2.16	1.85	2.13	2.25	2.51	2.36	2.49	1.65	1.69	1.89	2.51	2.53
200	0.63	1.43		1.66	1.57	1.98	1.72	1.95	2.21	2.48	2.15	2.23	1.44	1.47	1.67	2.49	2.45
300	0.80	1.48		1.64	1.40	1.97	1.66	1.89	2.19	2.46	2.02	2.06	1.33	1.31	1.52	1.77	2.32

GPa	Fr	Ra
0	2.23	2.29
50	1.74	1.68
100	2.55	1.61
200		1.73
300		2.02

Gpa	La	Ce	Pr	Nd	Pm	Sm	Eu	Gd	Tb	Dy	Ho	Er	Tm	Yb	Lu
0	2.07	2.09	2.24	2.10	1.81	1.77	1.85	1.98	1.97	2.07	2.14	1.61	1.96	1.90	1.57
50	1.76	1.76	1.87	1.72	1.69	1.68	1.83	1.65	1.70	1.82	1.81	1.50	1.83	1.18	1.41
100	1.76	1.76	1.82	1.71	1.68	1.67	1.28	1.41	1.31	1.76	1.05	1.46	1.37	1.15	1.37

Gpa	Ac	Th	Pa	U	Np	Pu	Am	Cm
0	1.63	1.95	2.15	2.12	2.11	2.83	2.23	1.75
50			2.15			2.29	2.03	
100			2.03			2.14	2.03	

Figure 3. Periodic Table of Pauling's electronegativity: the values were computed from 0 to 300 GPa. To obtain absolute electronegativities, we fixed the electronegativity of F at 4.00.

The obtained results gave us the idea to formulate a new scale of electronegativity based on a different formula

$$E_d(AB) = E_{COV}(AB) \cdot (1 + \Delta\chi^2) \quad , \tag{2}$$

where $E_{COV}(AB)$ is the covalent energy evaluated in two different ways

$$E_{COV}(AB) = \frac{E_d(AA) + E_d(BB)}{2} \tag{3}$$

$$E_{COV}(AB) = \sqrt{E_d(AA) \cdot E_d(BB)} \tag{4}$$

In this way we obtain a new thermochemical scale of electronegativities (Pauling's scale is also thermochemical), but this time electronegativities are dimensionless and the difference of electronegativities quantifies the relative enhancement of bond energy. We have tested the new formula calculating the electronegativity values from experimental dissociation energies fixing the fluorine electronegativity equal to 4.00. Oxygen and chlorine atoms presented a negative value of $\Delta\chi^2$ due to their too close electronegativity to fluorine one. Thus, we have calculated the electronegativity of oxygen and chlorine atoms from the obtained energies of H—O (within H_2O) and H—Cl bonds (see Figure 4). The electronegativity of bismuth is expected to be less than those of atoms of the lower period, but from our data is not like that. Thus, we have tried to recalculate it from Bi—H and Bi—Cl bonds obtaining from the first a Bi electronegativity of 2.76 calculated only for covalent energy expressed in the eq.4: $\Delta\chi^2$ calculated from the covalent energy expressed in the eq.3 showed a negative value; while, for the latter a Bi electronegativity of 3.07 for both covalent energies. It is noteworthy that there is a quite difference between the electronegativity values calculated from different atoms

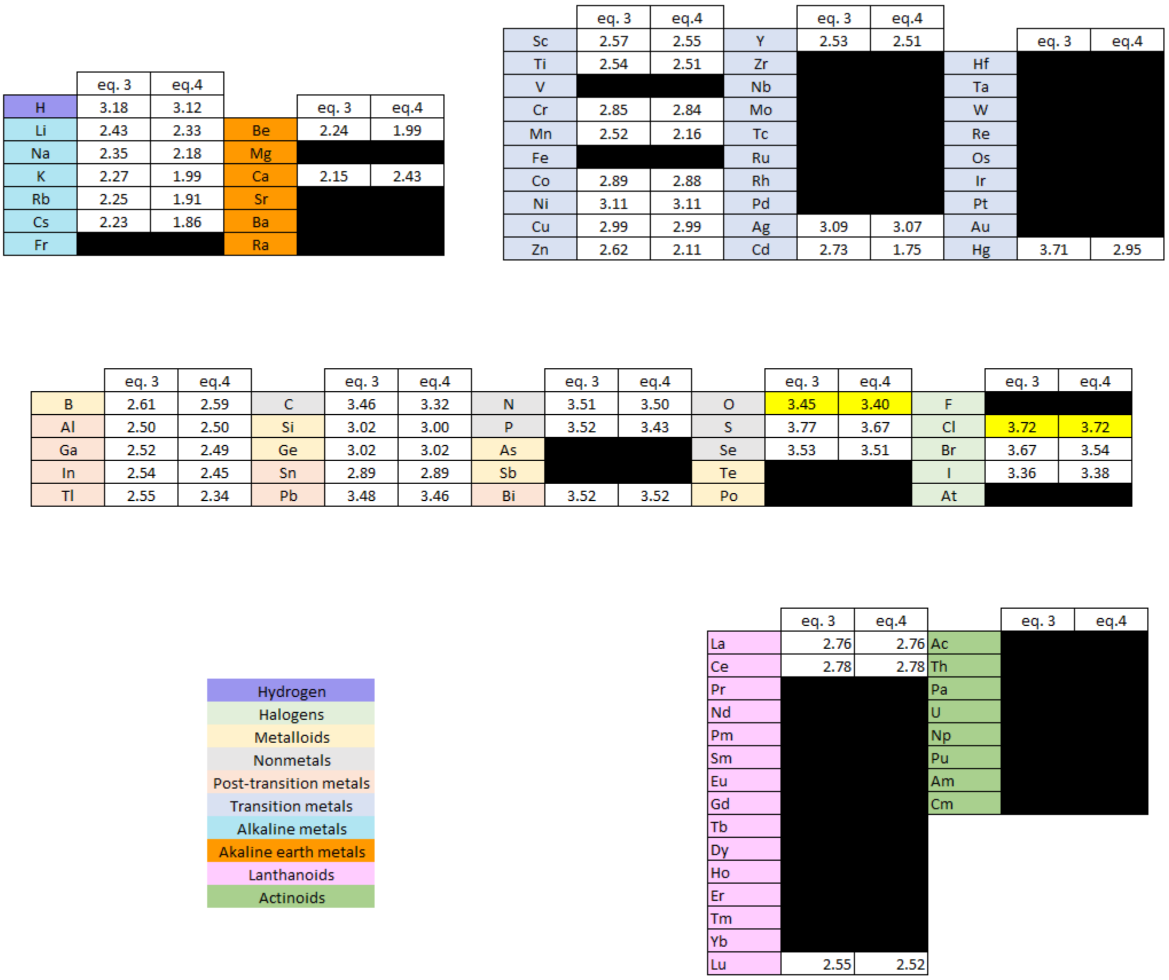

	eq. 3	eq.4
H	3.18	3.12
Li	2.43	2.33
Na	2.35	2.18
K	2.27	1.99
Rb	2.25	1.91
Cs	2.23	1.86
Fr		

	eq. 3	eq.4
Be	2.24	1.99
Mg		
Ca	2.15	2.43
Sr		
Ba		
Ra		

	eq. 3	eq.4		eq. 3	eq.4		eq. 3	eq.4
Sc	2.57	2.55	Y	2.53	2.51			
Ti	2.54	2.51	Zr			Hf		
V			Nb			Ta		
Cr	2.85	2.84	Mo			W		
Mn	2.52	2.16	Tc			Re		
Fe			Ru			Os		
Co	2.89	2.88	Rh			Ir		
Ni	3.11	3.11	Pd			Pt		
Cu	2.99	2.99	Ag	3.09	3.07	Au		
Zn	2.62	2.11	Cd	2.73	1.75	Hg	3.71	2.95

	eq. 3	eq.4		eq. 3	eq.4		eq. 3	eq.4		eq. 3	eq.4		eq. 3	eq.4
B	2.61	2.59	C	3.46	3.32	N	3.51	3.50	O	3.45	3.40	F		
Al	2.50	2.50	Si	3.02	3.00	P	3.52	3.43	S	3.77	3.67	Cl	3.72	3.72
Ga	2.52	2.49	Ge	3.02	3.02	As			Se	3.53	3.51	Br	3.67	3.54
In	2.54	2.45	Sn	2.89	2.89	Sb			Te			I	3.36	3.38
Tl	2.55	2.34	Pb	3.48	3.46	Bi	3.52	3.52	Po			At		

Hydrogen
Halogens
Metalloids
Nonmetals
Post-transition metals
Transition metals
Alkaline metals
Akaline earth metals
Lanthanoids
Actinoids

	eq. 3	eq.4		eq. 3	eq.4
La	2.76	2.76	Ac		
Ce	2.78	2.78	Th		
Pr			Pa		
Nd			U		
Pm			Np		
Sm			Pu		
Eu			Am		
Gd			Cm		
Tb					
Dy					
Ho					
Er					
Tm					
Yb					
Lu	2.55	2.52			

Figure 4. Electronegativity scale obtained using the new formulas and experimental dissociation energies.

Conclusions:

We have computed, as a function of pressure, Pauling's electronegativities, and defined a new scale of dimensionless thermochemical electronegativities. Electronegativities at high pressure should provide a useful frame for understanding chemical bonding in newly discovered exotic compounds. To complete the "high-pressure Periodic Table" in the future, the covalent and ionic radii of each element at different pressure will be calculated. The new electronegativity scale presented here gave interesting preliminary results that require a further investigation to consider them All this information will represent a sort of *vademecum* for scientists who want to understand matter at high pressure allowing them to know a *priori* the possible *chemical bonds* and bond distances — fundamental information for understanding and even anticipating interesting phenomena under pressure before difficult experiments or computationally heavy crystal structure predictions, e.g. using the evolutionary algorithm USPEX [19-21], are utilized. Furthermore, the new scale proposed by us will hopefully prove useful in this regard.

Contribution:

The project was performed by Christian Tantardini under supervision of Prof. Artem R. Oganov.

References

1. Pullman, B; The Atom in the History of Human Thought. Oxford, England: Oxford University Press. **1998**, pp. 31–33.
2. Lewis, G. N.; The Atom and the Molecule. *J.Am.Chem.Soc*. **1916**, 38, 762-785.
3. Pauling, L.; The Nature of the Chemical Bond. Third Ed. Cornell University Press, Ithaca, New York, **1960**.
4. Zhang, W.; Oganov, A. R.; Goncharov, A. F.; Zhu, Q.; Boulfelfel, S. E.; Lyakhov, A. O.; Stavrou, E.; Somayazulu, M.; Prakapenka, V. B.; Konopkova, Z.; Unexpected stable stoichiometries of sodium chlorides. *Science*, **2013**, 342, 1502–1505.
5. Saleh, G.; Oganov, A. R.; Alkali subhalides: high-pressure stability and interplay between metallic and ionic bonds. *Phys. Chem. Chem. Phys.*, **2016**, 18, 2840-2849.
6. Rahm, M.; Cammi, R.; Ashcroft, N. W.; Hofmann, R.; Squeezing All Elements in the Periodic Table: Electron Configuration and Electronegativity of the Atoms under Compression. *J. Am. Chem. Soc.*, **2019**, 141, 10253-10271.
7. Dong, X.; Oganov, A. R.; Qian, G.; Zhou, X.-F.; Zhu, Q.; Wang, H.-T.; How do chemical properties of the atoms change under pressure. arXiv:1503.00230 [cond-mat.mtrl-sci], **2015**.
8. Hamann, D. R.; Optimized norm-conserving Vanderbilt pseudopotentials. *Phys. Rev. B*, **2013**, 88, 085117.
9. Giannozzi, P.; *et al.*; QUANTUM ESPRESSO: a modular and open-source software project for quantum simulations of materials. *J. Phys.: Condens. Matter*, **2009**, 21, 395502.
10. Giannozzi, P.; *et al.*; Advanced capabilities for materials modelling with Quantum ESPRESSO. *J. Phys.: Condens. Matter*, **2017**, 29, 465901.
11. Blöchl, P. E.; Projector augmented-wave method. *Phys. Rev. B*, **1994**, 50, 17953.
12. Kresse, G.; Hafner, J.; Ab initio molecular dynamics for liquid metals. *Phys. Rev. B*, **1993**, 47 , 558.
13. Kresse, G.; Hafner, J.; Ab initio molecular-dynamics simulation of the liquid-metal–amorphous-semiconductor transition in germanium. *Phys. Rev. B*, **1994**, 49, 14251.
14. Kresse, G.; Furthmüller, J.; Efficiency of ab-initio total energy calculations for metals and semiconductors using a plane-wave basis set. *Comput. Mat. Sci.*, **1996**, 6 , 15.
15. Kresse, G.; J. Furthmüller, J.; Efficient iterative schemes for ab initio total-energy calculations using a plane-wave basis set. *Phys. Rev. B*, **1996**, 54 , 11169.
16. Kresse, G.; Joubert, D.; From ultrasoft pseudopotentials to the projector augmented-wave method. *Phys. Rev.*, **1999**, 59 , 1758.
17. Perdew, J. P.; Yue, W.; Density-functional approximation for the correlation energy of the inhomogeneous electron gas. *Phys. Rev. B*, **1986**, B33, 8800.
18. Monkhorst, H. J.; Pack, J. D.; Special points for Brillouin-zone integrations. *Phys. Rev. B*, **1976**, 13, 5188.
19. Shlipf, M.; Gygi, F.; Optimization algorithm for the generation of ONCV pseudopotentials. *Comp. Phys. Comm.*, **2015**, 196, 36-44.
20. Somayajulu, G. R.; Dissociation Energies of Diatomic Molecules. *J. Chem. Phys.*, **1960**, 33, 1541.
21. Oganov, A. R; Glass, C. W.; Crystal structure prediction using ab initio evolutionary techniques: Principles and applications. J. Chem. Phys., **2006**, 124, 244704.
22. Oganov, A. R.; Lyakhov, A. O.; Valle, M.; *Acc. Chem. Res.*, **2011**, 44 (3), 227-237.
23. Lyakhov, A. O., Oganov, A. R., Stokes, H. T. & Zhu, Q. New developments in evolutionary structure prediction algorithm uspex. *Computer Physics Communications*, **2013**, 184, 1172-1182.

6.0 CONCLUSION AND FUTURE PROSPECTIVES

The human mind gets information from experiences, and collection of those can be described by the same abstracted model in the same group. In case an experience cannot be connected by anyone to an already present model, then the human mind will create a new model. The human mind is constantly looking for an explanation of the surrounding environment and this is achieved through abstracted models to catalogue the information.

Scientists, more than everyone, are driven by this ancestral need and, through continuous research and the creation of new definitions, want to describe the physical phenomena. In fact, even if the definitions change over time, they change or become obsolete thanks to continuous research. It is remarkable that for a period have allowed us to describe the physical reality for which they were created.

So, looking the IUPAC definition for an H-bond, a lacuna was found about the “energy border” between H-bond and vdW interaction. It seems a simple concept, because the presence of H-bond should be represented by a sufficient stretch of X–H···Y observed under the given experimental conditions, but the quantification of this stretch is not defined. In the present work, the “energy border” between H-bond and vdW interaction as the limit of long range interactions was defined through the topological descriptor source function [1-2], that was shown earlier to stem from the description of the electron density in the field of quantum theory of atoms in molecule [3] (QTAIM). This approach depends only on the method used to describe the charge density, which can be density functional theory [4-7] (DFT), Møller−Plesset perturbation theory [8-20] (MP) and coupled cluster [21-26] (CC). CC calculations are time demanding albeit they give back results that agree with experimental ones. For big systems DFT exchange/correlation functionals with different semiempirical corrections as DFT-D [27,28], Tkatchenko-Scheffler [29,30] or exchange-hole dipole moment [31-36] (XDM) dispersion model are able to estimate with a certain accuracy the dispersion energies generated by non-covalent interactions and the intermolecular charge density. Thus, the proposal to discriminate between a blurry H-bond and vdW interaction can fail, making this definition useless if there is not a very accurate description of charge density. This becomes easier with the increase of system size and should always be kept in mind during the study of non-covalent interactions. Albeit the defined “energy border” through a topological approach is characterized by obstacles that limit its applications, actually the present work is the first endeavor to estimate it. Such definition could be used in crystal structure prediction of molecular crystals in order to evaluate in presence of X–H···Y interactions if they are H-bonds or vdW interactions with the consequence that a larger presence of the first ones determine a better stability of the structure. This concept expressed by “energy border” for molecular crystal is similar to the concept expressed by crystal orbital Hamilton population [37] (COHP) for metal crystal structures, for which if such indicator is further away from the Fermi energy then the crystal structure is more stable.

Another improvement of theory with possible future perspective is the new proposal of an equation of state for real gases. It represents an advance in theory of gases in that atoms are no more considered like spheres, but as asymmetric atomic units in agreement with QTAIM. The spherical approximation can be feasible for monoatomic gas (i.e., He) due to the only presence of nuclear spin that generates a slight ellipsoidal distortion of atoms. However, the spherical approximation fails for diatomic and triatomic gases, being characterized by interatomic and inter-molecular interactions, which affect considerably the shape of the atoms. Specially for strong conditions (i.e., high pressure and high temperature) such interactions are extremely modified, with consequent impact on the shape of atoms, that cannot be neglected. The classical physics is seen to arise from quantum physics through an equation of state for real gases that considers the deformation of atoms induced by interatomic and inter-molecular interactions. The atomic partition made in the field of QTAIM can be considered a right choice due to previous theoretical and experimental works [38-41]. In the next future it will be necessary to compare the Van der Waals coefficients ***a*** and ***b*** calculated in the field of QTAIM with semiempirical coefficients extrapolated for *P* and T equal to 0 by potential curves built from experimental data of infra-red (IR) spectroscopy for several gases. This will allow us to finally validate the new equation of state for real gases with subsequently possible applications. For example, ***a*** and ***b*** coefficients calculated for a certain pressure, temperature and volume from the new equation of state for real gases will correspond to the interaction energy and average molecular/atomic volume at such conditions. Such calculated coefficients will be compared with those extrapolated through the Dunham's rules[42] by Tang-Tonnies [43] potential curve specific for Van der Waals (vdW) interactions and Lippincot–Schroeder [44] potential curve specific for hydrogen bonds (H-bonds). This will allow us to understand what kind of inter-molecular/atomic interaction exists within particles of a gas by ***a*** and ***b*** coefficients and what dimension associated to such particles. This information can give us the possibility to identify possible molecular compounds with specific functional groups that can interact with the particles of a gas for at specific conditions using one or another type of non-covalent interactions. Furthermore, different crystal structures with enough empty space could be considered as host for the particles of gas at predetermined conditions with relevant consequences in the crystal structure prediction of storage materials.

The crystal structure prediction of molecular crystals is strongly affected by the non-covalent interactions as said before, and a deep study of such interactions within very well-known compounds as oxicams allowed us to better understand the mechanism of synthon formations. Such synthons as seen for oxicams are affected not only by H-bonds, but sulphur bonds (S-bonds) and π…π interactions between aromatic fragments, and affects the presence of one or another conformer generating a one or another polymorph during the crystallization. Thus, for the future prospective in the field of crystal structure prediction, it is necessary to consider them especially when we are interested to obtain new co-crystals structures. First, the molecular structures with different functional groups that allow them to make non-covalent interactions should be searched as well as the molecular structure with aromatic fragments should be searched with the possibility to make between them π…π interactions. All possible dimeric combinations should be optimized in *vacuo* and subsequently used by USPEX [45-47] evolutionary algorithm to generate the first population. USPEX [45-47] evolutionary algorithm will create different periodical structures from the most stable molecular dimers in *vacuo* to consider the non-covalent interactions during the generation of subsequently populations until a certain number of structures stable under predetermined conditions are obtained. Thus, the tuning of non-covalent interaction should be reflected on the crystal structure prediction allowing us to obtain one or another polymorph of the considered molecular crystal.

Also in the field of crystal structure prediction the study of chemical bond through the investigation of electronegativity at high pressure gave important information for future prediction of new structures knowing *a priori* the type of bond and consequent oxidation number. This will allow us to reduce the number of possible structures that characterize the populations generated by USPEX [45-47] evolution algorithm other that the possibility to tune the entire process of crystal structure prediction focusing on a desired specific bond between two atoms to obtain different physical, chemical and mechanical proprieties. Everything correlated with the explanation of chemical bonding can be traced to the properties of a molecule and subsequently to the properties of its periodical structure as explained by QTAIM [3].

Furthermore, in order to explain a specific chemical propriety as the reactivity of a molecule a catalyst as Dess-Martin periodinane [48,49] (DMP) was investigated. DMP is very important in organic chemistry for the oxidation of alcohols into ketones [48,49]. As DMP, many other organic compounds are used by industry as catalysts without knowing the causes of their high reactivity. The possibility of a topological study with different tools allowed to investigate the causes and also the possibility of tuning of reactivity. The tuning of reactivity plays an important role into the design of new catalysts. In the optic of future prospective the *a priori* knowledge of the intrinsic causes within molecular structure that affect the reactivity will allow to go ahead in investigating how the reactivity is affected by environment (i.e., solvents). All these information will allow one to develop an new genetic algorithm within USPEX [45-47] code to predict new crystal structures of catalysts with high reactivity for predetermined environments.

The study of chemical bonding within this work can be considered a first step for the subsequent crystal structure prediction of new materials with different properties.

6.1 References

1. Bader, R. F. W.; Gatti, C. A Green's function for the density. *Chem. Phys. Lett.*, **1998**, 287, 233.
2. Gatti, C.; The Source Function Descriptor as a Tool to Extract Chemical Information from Theoretical and Experimental Electron Densities. In Electron Density and Chemical Bonding II; Structure and Bonding Series, Vol. 147, Springer, Berlin, Germany **2012**, p. 193
3. Bader, R. F. W.; Atoms in Molecules. A Quantum Theory; Oxford University Press: Oxford, **1990**
4. Hohenberg, P.; Kohn, W.; Inhomogeneous Electron Gas. *Phys. Rev.*, **1964**, 136, B864-B871.
5. Kohn, W.; Sham, L. J.; Self-Consistent Equations Including Exchange and Correlation Effects. *Phys. Rev.*, **1965**, 140, A1133-A1138.
6. Parr, R. G.; Yang, W.; Density-functional theory of atoms and molecules, Oxford Univ. Press, Oxford, **1989**.
7. Salahub, D. R. (*Eds.*) Zerner, M. C. (*Eds.*); *The Challenge of d and f Electrons*, ACS, Washington, D.C., **1989**.
8. Møller, C.; Plesset, M. S.; Note on an approximation treatment for many-electron systems. *Phys. Rev.*, **1934**, 46, 0618-0622.
9. Frisch, M. J.; Head-Gordon, M.; Pople, J. A.; Direct MP2 gradient method. *Chem. Phys. Lett.*, **1990**, 166, 275-280.
10. Frisch, M. J.; Head-Gordon, M.; Pople, J. A.; Semi-direct algorithms for the MP2 energy and gradient. *Chem. Phys. Lett.*, **1990**, 166, 281-289.
11. Head-Gordon, M.; Pople, J. A.; Frisch, M. J.; MP2 energy evaluation by direct methods. *Chem. Phys. Lett.*, **1988**, 153, 503-506.
12. Saebø, S.; Almlöf, J.; Avoiding the integral storage bottleneck in LCAO calculations of electron correlation. *Chem. Phys. Lett.*, **1989**, 154, 83-89.
13. Head-Gordon, M.; Head-Gordon, T.; Analytic MP2 Frequencies Without Fifth Order Storage: Theory and Application to Bifurcated Hydrogen Bonds in the Water Hexamer. *Chem. Phys. Lett.*, **1994**, 220, 122-128.
14. Pople, J. A.; Binkley, J. S.; Seeger, R.; Theoretical Models Incorporating Electron Correlation. *Int. J. Quantum Chem.*, **1976**, Suppl. Y-10, 1-19.
15. Pople, J. A.; Seeger, R.; Krishnan, R.; Variational Configuration Interaction Methods and Comparison with Perturbation Theory. *Int. J. Quantum Chem.*, **1977**, Suppl. Y-11, 149-63.
16. Raghavachari, K.; Pople, J. A.; Approximate 4th-order perturbation-theory of electron correlation energy. *Int. J. Quantum Chem.*, **1978**, 14, 91-100.

17. Raghavachari, K.; Frisch, M. J.; Pople, J. A.; Contribution of triple substitutions to the electron correlation energy in fourth-order perturbation theory. *J. Chem. Phys.*, **1980**, 72, 4244-4245.

18. Trucks, G. W.; Watts, J. D.; Salter, E. A.; Bartlett, R. J.; Analytical MBPT(4) Gradients. *Chem. Phys. Lett.*, **1988**, 153, 490-495.

19. Trucks, G. W.; Salter, E. A.; Sosa, C.; Bartlett, R. J.; Theory and Implementation of the MBPT Density Matrix: An Application to One-Electron Properties. *Chem. Phys. Lett.*, **1988**, 147, 359-366.

20. Raghavachari, K.; Pople, J. A.; Replogle, E. S.; Head-Gordon, M.; Fifth Order Møller-Plesset Perturbation Theory: Comparison of Existing Correlation Methods and Implementation of New Methods Correct to Fifth Order. *J. Phys. Chem.*, **1990**, 94, 5579-5586.

21. Bartlett, R. J.; Purvis III, G. D.; Many-body perturbation-theory, coupled-pair many-electron theory, and importance of quadruple excitations for correlation problem. *Int. J. Quantum Chem.*, **1978**, 14, 561-581.

22. Pople, J. A.; Krishnan, R.; Schlegel, H. B.; Binkley, J. S.; Electron Correlation Theories and Their Application to the Study of Simple Reaction Potential Surfaces. *Int. J. Quantum Chem.*, **1978**, 14, 545-60.

23. Cížek, J.; in Advances in Chemical Physics, Eds. Hariharan, P. C.; Vol. 14, Wiley Interscience, New York, **1969**.

24. Purvis III, G. D. ; Bartlett, R. J.; A full coupled-cluster singles and doubles model – the inclusion of disconnected triples. *J. Chem. Phys.*, **1982**, 76, 1910-1918.

25. Scuseria, G. E.; Schaefer III, H. F.; Is coupled cluster singles and doubles (CCSD) more computationally intensive than quadratic configuration-interaction (QCISD)? *J. Chem. Phys.*, **1989**, 90, 3700-3703.

26. Watts, J. D.; Gauss, J.; Bartlett, R. J.; Coupled-cluster methods with noniterative triple excitations for restricted open-shell Hartree-Fock and other general single determinant reference functions. Energies and analytical gradients. *J. Chem. Phys.*, **1993**, 98, 8718.

27. Grimme, S.; Antony, J.; Ehrlich, S.; Krieg, S.; A consistent and accurate ab initio parametrization of density functional dispersion correction (dft-d) for the 94 elements H-Pu, *J. Chem. Phys.*, **2010**, 132, 154104.

28. Grimme, S.; Ehrlich, S.; Goerigk, L.; Effect of the damping function in dispersion corrected density functional theory. *J. Comp. Chem.*, **2011**, 32, 1456.

29. Tkatchenko, A.; Scheffler, M.; Accurate molecular van der waals interactions from ground-state electron density and free-atom reference data. *Phys. Rev. Lett.*, 2009, 102, 073005.

30. Tkatchenko, A.; Di Stasio, R. A.; Car, R.; Scheffler, M.; Accurate and efficient method for many-body van der waals interactions. *Phys. Rev. Lett.*, **2012**, 108, 236402.

31. Becke, A. D.; Johnson, E. R.; Exchange-Hole Dipole Moment and the Dispersion Interaction. *J. Chem. Phys.*, **2005**, 122, 154104.

32. Johnson, E. R.; Becke, A. D.; A Post-Hartree-Fock Model of Intermolecular Interaction. *J. Chem. Phys.*, **2005**, 123, 024101.

33. Becke, A. D.; Johnson, E. R.; A Density-Functional Model of the Dispersion Interaction. *J. Chem. Phys.*, **2005**, 123, 154101.

34. Becke, A. D.; Johnson, E. R., Exchange-hole Dipole Moment and the Dispersion Interaction: High-Order Dispersion Coefficients. *J. Chem. Phys.*, **2006**, 124, 014104.

35. Johnson, E. R.; Becke, A. D.; A Post-Hartree-Fock Model of Intermolecular Interactions: Inclusion of Higher-Order Corrections. *J. Chem. Phys.*, **2006**, 124, 174104.

36. Becke, A. D.; Johnson, E. R.; Exchange-Hole Dipole Moment and the Dispersion Interaction Revisited. *J. Chem. Phys.*, **2007**, 127, 154108.

37. Steinberg, S.; Dronskowski, R.; The crystal Orbital Hamilton Population (COHP) Method as a Tool to Visualize and Analyze Chemical Bonding in Intermetallic Compounds. *Crystals*, 2018, 8, 225.

38. Bader, R. F. W. ; Matta, C. F.; Atomic charges are measurable quantum expectation values: a rebuttal of criticisms of QTAIM charges. *J. Phys. Chem. A*, **2004**, 108, 40, 8385.

39. Firme, C. L.; Antunes, O. A. C.; Esteves, P. M.; Relation between bond order and delocalization index of QTAIM. *Chemical Physics Letters*, **2009**, 468, 129–133.

40. Filho, E. B. A.; Moraes, I. A.; Weber, K. C.; Rocha, G. B.; Vasconcellos, M. L. A. A.; DFT/PCM, QTAIM, 1H NMR conformational studies and QSAR modeling of thirty-two anti-Leishmania amazonensis Morita–Baylis–Hillman Adducts. *Journal of Molecular Structure*, **2012**, 1022, 72.

41. Woińska, M.; Jayatilaka, D.; Dittrich, B.; Flaig, R.; Luger, P.; Woźniak, K.; Dominiak, P. M.; Grabowsky, S.; Validation of X-ray Wavefunction Refinement. *ChemPhysChem*, **2017**, 18 (23), 3334-3351.

42. Dunham, J. L.; The energy levels of a rotating vibrator *Phys. Rev.*, **1932**, 41, 721.

43. Tang, K. T.; Toennies, J. P.; The van der Waals potentials between all the rare gas atoms from He to Rn. *J. Chem. Phys.*, **2003**, 118, 4976.

44. Lippincot, E. R.; Schroeder, R.; One-dimensional model of the hydrogen bond. *J. Chem. Phys.*, **1955**, 23, 1099.

45. Glass, C. W., Oganov, A. R. & Hansen, N., Uspex: evolutionary crystal structure prediction. *Computer physics communications*, **2006**, 175, 713-720.

46. Zhu, Q., Li, L., Oganov, A. R.; Allen, P. B. Evolutionary method for predicting surface reconstructions with variable stoichiometry. *Physical Review B*, **2013**, 87, 195317.

47. Lyakhov, A. O., Oganov, A. R., Stokes, H. T. & Zhu, Q. New developments in evolutionary structure prediction algorithm uspex. *Computer Physics Communications*, **2013**, 184, 1172-1182.

48. Dess, D. B.; Martin, J. C.; Readily accessible 12-I-5 oxidant for the conversion of primary and secondary alcohols to aldehydes and ketones. *J. Org. Chem.* **1983**, 48, 4155.

49. Dess, D. B.; Martin, J. C.; A useful 12-I-5 triacetoxyperiodinane (the Dess-Martin periodinane) for the selective oxidation of primary or secondary alcohols and a variety of related 12-I-5 species. *JACS*, **1991**, 113, 7277.

7.0 ACKNOWLEDGMENT

First, I would like to thank my supervisor Prof. Dr. Artem R. Oganov and all members of Oganov’s lab at the Skolkovo Institute of Science and Technology.

Furthermore, I would like to thank people from different Institutions that collaborate with me: Dr. Adam A. L. Michalchuk (BAM Federal Institute for materials research and testing, Berlin, Germany); Dr. Alberto Otero-de-la-Roza (Universidad de Oviedo, Oviedo, Spain) Dr. Alexander S. Kil'met'ev (N. N. Vorozhtsov Novosibirsk Institute of Organic Chemistry, Novosibirsk, Russian Federation); Dr. Petr S. Sherin and Dr. Alexey S. Kiryutin (International Tomographic Center, Novosibirsk, Russian Federation); Dr. Sergey G. Arkhipov and Elena V. Boldyreva (Boreskov Institute of Catalysis, Novosibirsk, Russian Federation); Dr. Vladimir A. Lazarenko (National Research Center “Kurchatov Institute”, Moscow, Russian Federation); Prof. Dr. Enrico Benassi (Lanzhou Institute of Chemical Physic, Popular Republic of China) Dr. Davide Ceresoli (CNR, Istituto di Scienze e Tecnologie Molecolari, Milano, Italian Republic); Dr. Gabriele Saleh (Istituto Italiano di Technologia, Genova, Italian Republic); Prof. Dr. Lukas Buchinsky (Slovak University of Technology in Bratislava, Bratislava-Slovakia); Prof. RNDr. Robert Ponec (Academy of Sciences of the Czech Republic).